The Effect of Silica on the Reduction of Precipitated Iron-Based Fischer-Tropsch Catalysts

by

Matthew Coombes

Thesis submitted in fulfilment of the requirements for the degree

PHILOSOPHIAE DOCTOR

in

PHYSICS

in the Faculty of Science of the

Nelson Mandela Metropolitan University

Promoter:
Prof. J.H. Neethling

Co-Promoters:
Dr E.J. Olivier
Dr H.E. du Plessis

2016

Acknowledgements

I would like to thank the following people and organisations for their various contributions throughout the course of this thesis:

- My promoters: Prof Jan Neethling, Dr Jaco Olivier and Dr Esna du Plessis for their motivation, guidance and support.
- Dr Bruce Anderson for his guidance and support during the early stages of this thesis.
- Staff and students at the CHRTEM who contributed in so many different ways to all aspects of this work.
- Colleagues at Sasol for sharing their expertise in the wide variety of experimental techniques employed throughout this thesis.
- Staff and students from the NMMU Physics Department and NMMU Chemistry Department who gave up their time to assist with experiments.
- Staff at the University of Manchester for their assistance with the Protochips gas flow cell.
- Staff at Hummingbird Scientific for their assistance with the Hummingbird gas flow cell.
- Sasol, for financial support throughout the duration of these studies.
- The NMMU Postgraduate Research Scholarship and the Dormehl Cunningham Scholarship for additional funding.

Finally, I would like to thank all my friends and family for their unwavering support.

Declaration

In accordance with Rule G4.6.3:

4.6.3 A treatise/dissertation/thesis must be accompanied by a written declaration on the part of the candidate to the effect that it is his/her own work and that it has not previously been submitted for assessment to another university or for another qualification. However, material from publications by the candidate may be embodied in a treatise/dissertation/thesis.

I, Matthew John Coombes, student number 213317036, hereby declare that this thesis submitted for the degree ***Philosophae Doctor*** is my own original work and that I have not previously in its entirety or in part thereof submitted it to another university or for another qualification.

Signature: .....

Date: .....

Abstract

Iron Fischer-Tropsch (FT) catalysts are typically prepared as iron oxides which are reduced to FT-active iron metal and iron carbide prior to FT synthesis. The iron oxides contain a variety of different chemical and structural promoters to alter FT-activity. Silica is a common structural promoter which stabilises the formation of small crystallites and provides mechanical integrity to the catalyst. However, silica inhibits the reduction of the oxide precursor to the FT-active phases. This ultimately affects catalyst activity and product selectivity. It has been proposed that the silica interacts with the iron to form encapsulating shells of fayalite (Fe_2SiO_4), or fayalite rafts between the iron oxide and the silica support.

In this study, six silica-promoted iron oxide samples were prepared using a simple co-precipitation technique. Samples contain varying amounts of silica, and the samples are named $100/x$ **Fe/SiO$_2$**, where x is the weight of silica for 100 weight iron, with x taking on values of 0, 10, 25, 50, 100 and 200. The resulting iron oxides were characterised using scanning electron microscopy (SEM), transmission electron microscopy (TEM), X-ray powder diffraction (XRPD), Mössbauer spectroscopy (MS), magnetic susceptibility measurements (MM), Raman spectroscopy, thermal gravimetric analysis (TGA) and nitrogen physisorption. Their reduction in a hydrogen atmosphere was investigated using temperature programmed reduction (TPR), *in situ* XRPD and TEM. The reduction in hydrogen of **100/0 Fe/SiO$_2$** and **100/10 Fe/SiO$_2$** was also studied using *in situ* gas flow TEM cells. These cells allow the samples to be studied in the electron microscope at temperature and pressure conditions approaching those experienced in a real reactor environment.

In the absence of a silica promoter (**100/0 Fe/SiO$_2$**), hematite particles are formed with mean particle diameters of 39 $\pm$ 12 and 52.7 $\pm$ 0.2 nm determined using TEM and XRPD respectively. MM data reveals a magnetic transition (Morin transition) at $\approx$ 230 K, consistent with a mean particle size of $\approx$ 50 nm. In a hydrogen atmosphere, the hematite reduces to metallic iron

via a two-step process *viz.* hematite → magnetite → iron. The final iron particles have an average crystallite size of 68.0 ± 0.2 nm.

The presence of lower amounts of silica in the samples **100/10 Fe/SiO$_2$**, **100/25 Fe/SiO$_2$** and **100/50 Fe/SiO$_2$** results in the formation of silica-substituted 2-line ferrihydrite particles. Bands in the Raman spectra of these samples shift on increasing silica content, which indicates an increasing number of Fe-O-Si bonds within the ferrihydrite framework. MM reveals typical superparamagnetic (SPM) behaviour above a blocking temperature in the range 39 - 68 K which gives mean particle sizes of 4.2, 3.6 and 3.5 nm for **100/10 Fe/SiO$_2$**, **100/25 Fe/SiO$_2$** and **100/50 Fe/SiO$_2$** respectively, in good agreement with particle sizes determined using TEM (3.1±0.4, 2.4±0.3 and 2.4 ± 0.3 nm respectively). MS data at 300 K and 4.2 K were fitted with distributions of ΔE_Q and B_{hf} respectively. The median values of B_{hf} decrease with increasing silica content, indicating greater degrees of distortion in the Fe^{3+} environments induced by increased silica substitution.

The reduction to metallic iron occurs via a three-step process *viz.* hematite → magnetite → wüstite → iron, with the silica stabilising the wüstite phase. The increasing amount of Fe-O-Si bonds on increasing silica content shifts reduction to higher temperatures broadens each reduction step as a result of local Fe-O-Si concentration variations. Fractions of each sample are not completely reduced even at 1000°C, with the relative proportion increasing with increasing silica content.

In situ gas flow TEM studies reveal that the mechanism of reduction involves the liberation of atomic iron atoms from the silica-substituted iron oxides which agglomerate and grow into final iron particles. This leaves a poorly crystalline Fe-O-Si bonded framework behind. STEM-EDS and STEM-EELS reveal low concentrations of silicon at the surface of the resulting iron particles, however they do not form encapsulating shells of fayalite as previously suggested. The majority of the silica remains in the Fe-O-Si material which may crystallise into separate fayalite particles at elevated temperature.

The presence of silica in high proportions (**100/100 Fe/SiO_2** and **100/200 Fe/SiO_2**) results in the formation of a two-phase system consisting of silica-substituted 2-line ferrihydrite particles which are encapsulated in an iron-infused amorphous silica network. As with the other silica-bearing samples, there is an increase in Fe-O-Si bonds and an increase in the degree of distortion at Fe^{3+} sites with increasing silica content. The large amount of silica suppresses the blocking temperature of the SPM crystallites.

In a hydrogen atmosphere, the reduction to metallic iron follows the same three step process as the other silica-bearing samples. Reduction temperatures are further shifted to higher values and given reduction steps are considerably broader with increasing silica content. The fraction of iron not fully reduced also increases. Iron particle diameters are very small, since encapsulation by the silica matrix prevents growth of particles.

Key-words: Iron-silica interactions, *in situ* TEM, HRTEM, *in situ* X-ray powder diffraction, Mössbauer, catalyst characterisation, reduction

List of Figures

List of Tables

List of Terms and Abbreviations

BET Brunauer-Emmett-Teller.

BF bright-field.

BJH Barrett-Joyner-Halender.

BSE back-scattered electron.

CCD charge-coupled device.

CIF Crystallographic Information File.

DF dark-field.

DP-TEM differentially pumped TEM.

EDS energy dispersive X-ray spectroscopy.

EELS electron energy-loss spectroscopy.

FEG field-emission gun.

FT Fischer-Tropsch.

FTS Fischer-Tropsch synthesis.

HAADF high-angle annular dark-field.

HCDF hollow cone dark-field.

HRTEM high-resolution transmission electron microscopy.

ICSD Inorganic Crystal Structure Database.

MAS Mössbauer absorption spectroscopy.

MEMS microelectromechanical system.

MPMS magnetic and physical properties measurements.

SAED selected area diffraction patterns.

SEM scanning electron microscopy.

SMSI strong metal-support interaction.

SPM superparamagnetic.

SQUID superconducting quantum interference device.

STEM scanning transmission electron microscopy.

syngas a mixture of hydrogen and carbon monoxide gas.

TEM transmission electron microscopy.

TGA thermal gravimetric analysis.

TPR temperature programmed reduction.

WGS water-gas shift.

XRPD X-ray powder diffraction.

Contents

1 Introduction

Introduction

Iron, after aluminium, is the second most abundant metal found on Earth, and the fourth most abundant overall (silicon and oxygen occur in greater abundance)[1]. It is most commonly incorporated in one of the many forms of iron oxide, iron carbonate or iron silicate. Iron oxides in particular are an invaluable resource owing to their high natural abundance and the low relative cost of their production for use in a wide variety of applications. Natural iron oxides initially form through the aerobic weathering of magmatic rocks in both terestrial and marine environments, and are subsequently redistributed by a variety of processes such as wind/water erosion, reductive dissolution and oxidative precipitation, as well as through use by man[2]. Figure 1.1 provides a flow-chart overview of the redistribution processes of the iron oxides on Earth.

From prehistoric times, iron oxides have been employed in a wide variety of applications. This remains the case to the present day. Arguably their most obvious use is as a precursor material in the production of iron, the principle ingredient in any number of steels which serve as the fundamental structural and engineering material of our current age[3]. Apart from this, the variety of colours and hues that they exhibit, combined with their non-toxic nature and high UV absorbance make them excellent pigments and dyes for colouring applications ranging from foodstuffs to motor vehicle paints to art[4]. Some iron oxides possess excellent magnetic properties, making them perfect candidates in the manufacture of magnetic seals and inks, magnetic recording media, and ferrofluids as well as for use as contrast agents in magnetic resonance imaging and the subsequent treatment of cancer cells[5–8]. Their high surface area (iron oxides form very small crystallites as a result of the iron oxide's high energy of crystallisation[9]) and low solubility[10] make iron oxides suitable as a sorbent material for a variety of gases and dissolved molecules, and as drug delivery agents within the body[11–16]. Most relevant to this work is the ability of the iron oxides to serve as a catalyst in a diverse array of chemical reactions, either directly or by acting as the source of catalytically active iron[17–22].

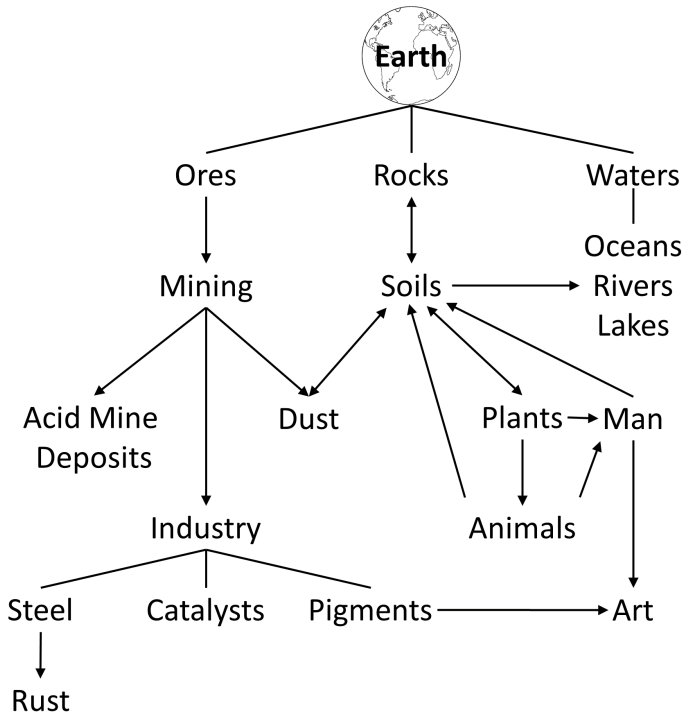

Figure 1.1: *The occurrence and redistribution relationships of the iron oxides on Earth*[2]

The Fischer-Tropsch (FT) reaction[23], which converts a mixture of hydrogen and carbon monoxide gas (syngas) to hydrocarbon products, is of enormous importance to the economy of South Africa. The balanced equation describing the production of paraffin products, which is only one such product that may be formed, is as follows:

$$(2n+1)\mathrm{H_2} + n\mathrm{CO} \xrightarrow{\Delta, catalyst} \mathrm{C_nH_{2n+2}} + n\mathrm{H_2O}$$

Iron is one of only two commercially viable metals (the other being cobalt) suitable for industrial-scale implementation of the FT process[24]. The iron catalysts are obtained by the reduction of an iron oxide precursor in hydrogen, carbon monoxide or syngas prior to Fischer-Tropsch synthesis (FTS). These iron oxide precursors are prepared via precipitation techniques, in the presence of copper and potassium oxide (K_2O), which act as chemical promoters, and silica (SiO_2) which serves the

role of structural promoter. The chemical promoters facilitate the reduction of the iron oxide to iron and the subsequent adsorption and dissociation of carbon monoxide. Structural promoters prevent the iron oxide crystallites from sintering while also providing the mechanical integrity needed to survive the turbulent conditions of the reactor[25].

An unfortunate consequence of silica addition as a structural promoter is the manifestation of an iron-silica interaction during reduction of the oxide precursor to metallic or carbidic iron. As a result of this interaction, it becomes difficult to achieve complete reduction of iron oxide to iron and the percentage of iron carbide, an important phase in FTS, formed during reaction is low. This causes undesirably low catalyst activity. The hydrocarbon selectivity of the reaction is also altered as a result of this interaction[26].

The interaction between iron and silica was first reported in 1981[27]. Mössbauer absorption spectroscopy (MAS) and X-ray powder diffraction (XRPD) showed that magnetite supported on silica yielded maghemite (γ-Fe_2O_3) rather than hematite (α-Fe_2O_3) when heated to 800 K in an oxidising environment. A model was proposed where Si^{4+} cations substitute for Fe^{3+} at tetrahedral sites near the surface of the magnetite.

Subsequent studies have further probed these interactions in silica-supported iron oxide catalysts, primarily through the use of MAS, XRPD and vibrational spectroscopy. The results of such studies lend support to a model in which silicon is substituting for iron in the iron oxide lattices. It has been proposed that there is often sufficient substitution of iron by silicon that small domains of fayalite (Fe_2SiO_4) begin to form at the surface of the particles. These silicon-containing iron oxides prove considerably more difficult to reduce compared to their unsubstituted counterparts.

However, the degree of substitution varies locally over the surface of the iron oxide particles, and the structural information obtained by techniques such as MAS and XRPD is limited owing to the bulk nature of such analyses. The degree of interaction is also heavily dependent on synthesis conditions, which makes comparison between different studies difficult owing to the different synthetic approaches used in preparation of the samples.

High resolution techniques, in particular aberration-corrected high-resolution transmission electron microscopy (HRTEM) and its associated structural and chemical techniques, are capable of providing a wealth of information about a particular sample, all at sub-ångstrom spatial resolutions. To date, no study has extensively employed aberration-corrected HRTEM to study the chemical and morphological effects of silica on both the precursor iron oxides and the reduced, active form of such co-precipitated iron-based catalysts. This study is conducted with the aim of studying a range of co-precipiated silica-promoted iron-based model catalysts, all prepared under the same reaction conditions. The influence of silica on the chemistry and morphology is of particular importance. The spatial resolution provided by HRTEM will deepen current understanding regarding initial distribution of silica within such samples, and the movement of silica- or silicon-bearing species during the reduction process. Additionally, the size and location of fayalite, or any other iron silicate domains, may easily be determined, should they form during reduction.

In this thesis, the characterisation results of co-precipitated, silica-promoted iron-based model Fischer-Tropsch catalyst materials are presented. The characterisation results include initial oxide precursors, their reduction in hydrogen, and the final reduction products.

Chapter 2 contains a review of the literature relevant to this work, with a particular emphasis on structure and properties of the iron oxides, the Fischer-Tropsch process and iron-silica interactions. Theoretical background required to follow the interpretation of data generated by each experimental technique is provided in Chapter 3.

The synthesis details are supplied in Chapter 4 together with the characterisation results for the as-synthesized silica-promoted iron oxide samples. The samples are characterised by numerous different techniques. BSE SEM and SEM-EDS was used to study the distribution of iron and silica within each sample and evaluate the initial success of the synthesis. The particle size and morphology was evaluated using TEM, and the distribution of silica within the particles evaluated using STEM-EELS and STEM-EDS.

Mössbauer spectroscopy and magnetic measurements were used to identify the

iron oxide phases present, along with XRPD and SAED patterns. This data was complemented by Raman, nitrogen physisorption and TGA measurements, giving insights into the iron oxide phase, the surface area and pore size distribution, and the thermal behaviour respectively.

Reduction of these samples in hydrogen atmosphere is reported in Chapter 5. TPR was used to study the effect of temperature on reduction and provides insight into the mechanism responsible for the reduction of the iron oxides. *In situ* XRPD data allowed the crystalline components formed during reduction to be studied. TEM/STEM data for the samples reduced *ex situ* gave further insight into the role that silica plays during reduction.

This thesis also incorporates *in situ* TEM data obtained using *in situ* gas flow cells. These results are presented in Chapter 6. The reduction of two of the prepared samples was studied in hydrogen at pressures of approximately 1 atmosphere and temperatures ranging from room temperature to 750°C. These results demonstrate the immense value of *in situ* gas flow cells for materials characterisation and offer insight into the reduction mechanism of silica-promoted iron oxides.

Finally, Chapter 7 summarises and discusses all the key results obtained in this thesis and the insights provided into the role silica plays in the reduction of co-precipitated, silica-promoted iron oxides.

2 Literature Review

The following section contains a literature review of all research relevant to the work in this thesis. It begins with a presentation of the structure and properties of the various iron oxides relevant to this thesis, followed by an outline of the Fischer-Tropsch process, with particular focus on iron-catalysed FT. Metal-support interactions are also described, with a focus on interactions in iron-silica samples and the influence that this has in their reduction behaviour and catalytic properties.

2.1 The Structure and Properties of Iron Oxides

The term "iron oxides" is used collectively when referring to any one of 16 different compounds of iron oxide, iron hydroxide and iron oxyhydroxide[2]. The iron species most commonly occur in the trivalent state (Fe^{3+} cations), while three of the iron oxides, namely wüstite (FeO), ferrous hydroxide ($Fe(OH)_2$) and magnetite (Fe_3O_4), contain iron species in the divalent state (Fe^{2+} cations).

Figure 2.1: *Octahedral and tetrahedral geometries of the iron centers in the iron-oxygen vertices.*

The iron oxides consist of close packed arrays of anions (most commonly in hexagonal or cubic arrangements) in which the interstices are partly filled with iron atoms. Iron species are more commonly found in a six-coordinate octahedral geometry, consisting of $Fe(O,OH)_6$ vertices, but may also exist in a four-coordinate tetrahedral geometry, consisting of $Fe(O,OH)_4$ vertices. The three-dimensional geometries of such vertices are illustrated in Figure 2.1. The differences between

the various iron oxides are a result of different arrangements of these vertices in space, and how the vertices are connected to one another. Each vertex within an iron oxide may be linked to another one by means of shared corners, edges or faces. Chloride, carbonate and sulfate anions may also participate in the structure of an iron oxide. The basic crystallographic details of each of the iron oxides is given in Table 2.1. All crystal structures visualised in the following paragraphs were constructed using data obtained from a Crystallographic Information File (CIF). These files were retrieved from the Inorganic Crystal Structure Database (ICSD) using FindIt version 1.9.6 software[28,29]. Visualisation of the structures is performed using VESTA version 3.3.2 software[30], while the literature source of the CIF is given in the caption with the ICSD reference number.

Table 2.1: *The 16 different iron oxides, as well as fayalite, and their basic crystallographic details*[2,31,32].

Compound	**Common Name**	**Crystal System**	**Space Group**
α-Fe_2O_3	Hematite	Hexagonal	$R\bar{3}c$
β-Fe_2O_3		Cubic	$Ia\bar{3}$
γ-Fe_2O_3	Maghemite	Cubic	$P4_332$
ϵ-Fe_2O_3		Orthorhombic	$Pna2_1$
Fe_3O_4	Magnetite	Cubic	Fd3m
FeO	Wüstite	Cubic	Fm3m
α-FeOOH	Goethite	Orthorhombic	Pnma
β-FeOOH	Akaganéite	Monoclinic	I2/m
γ-FeOOH	Lepidocrocite	Orthorhombic	Bbmm
δ-FeOOH		Hexagonal	P3m1
δ'-FeOOH	Feroxyhyte	Hexagonal	P3m1
HP FeOOH		Orthorhombic	$Pn2_1m$
$Fe_5HO_8 \cdot 4H_2O$	Ferrihydrite	Hexagonal	P31c
$Fe(OH)_3$	Bernalite	Orthorhombic	Immm
$Fe(OH)_2$		Hexagonal	$P\bar{3}1m$
Fe_2SiO_4	Fayalite	Orthorhombic	Pbnm

2.1.1 Hematite (α-Fe_2O_3)

α-Fe_2O_3 (Hematite) crystallises into the trigonal system (a = 5.0346 Å, c = 13.752 Å) with an $R\bar{3}c$ spacegroup[33,34] and is isostructural to the minerals corundum (α-Al_2O_3) and ilmenite ($FeTiO_3$)[2]. A total of six formula units are contained in a unit cell. It consists of hexagonally close-packed arrays of oxygen anions stacked along the [001] direction[2]. Two thirds of the sites are filled with Fe^{3+} ions which are arranged regularly with two filled sites followed by a vacant site in the (001) plane, thus forming sixfold rings. The arrangement of the Fe^{3+} cations produces pairs of FeO_6 octahedra. Each of these octahedra shares edges with three neighbouring octahedra in the same plane and one face with an octahedron in an adjacent plane. Face sharing occurs along the *c*-axis. This face-sharing feature results in the distortion of the cation sublattice from ideal packing: Fe^{3+} cations in the octahedron which share faces are repelled along the direction normal to the [001], causing these Fe^{3+} cations to shift closer to the unshared faces. This structure is illustrated in Figure 2.2.

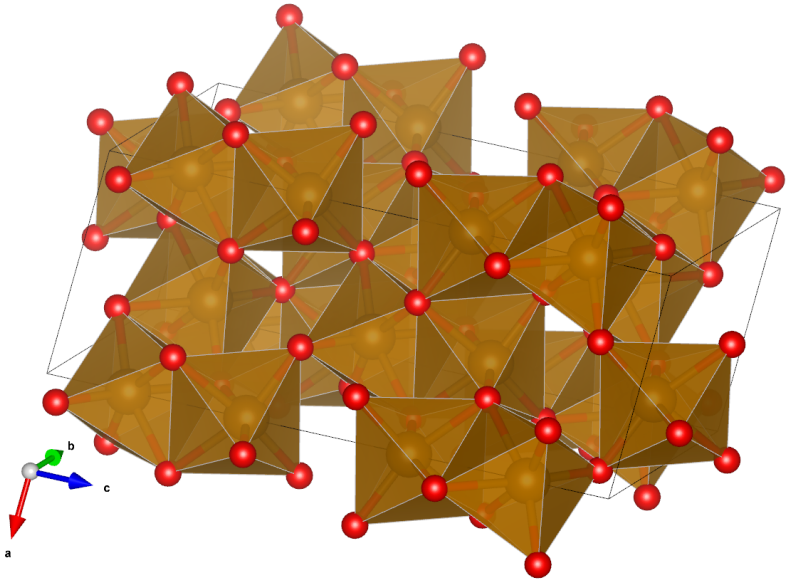

Figure 2.2: *Unit cell of hematite (ICSD: 415251)[35]. Iron atoms and iron-oxygen polyhedra are brown, oxygen atoms are red.*

Hematite is generally red in colour. This is a result of face sharing of octahedra

which produces an Fe-Fe distance of only 0.29 nm. This enhances electron pair transitions, resulting in a red hue.

At room temperature, hematite is weakly ferromagnetic, with a Curie temperature of 956 K. In its ferromagnetic state, the Fe^{3+} cations are antiferromagnetically coupled across the shared octahedral faces along the *c*-axis of the hematite crystal. The basal plane of the structure is comprised of two interpenetrating antiferromagnetic sublattices[36], with electron spins that are almost antiparallel, resulting in a weak ferromagnetic interaction. On cooling, hematite undergoes a transformation at a Morin temperature of 260 K to an antiferromagnetic state[37]. During this transformation, the electron spins reorient themselves at an angle of 7° to the basal plane. In this orientation, they are perfectly antiparallel, resulting in an antiferromagnetic state.

The magnetic properties of hematite are affected by the degree of crystallinity, as well as the presence of any substituent cations[38]. The particle size also plays a role, with nanoparticulate hematite demonstrating superparamagnetic behaviour[39].

2.1.2 Maghemite (γ-Fe_2O_3)

γ-Fe_2O_3 (Maghemite) is a second polymorph of Fe_2O_3. It is an inverse spinel structure with a cubic unit cell (a = 8.34 Å, Fd3m space group)[2]. Unlike hematite, which contains only octahedrally coordinated Fe^{3+}, maghemite contains a mixture of tetrahedral and octahedral Fe^{3+} cations. It has a similar structure to magnetite (see Section 2.1.4), with the difference being random vacancies of octahedral Fe^{3+} sites. This yields an alternative formula for maghemite, one that is perhaps more intuitive owing to its spinel structure: $Fe^{A}(Fe_{\frac{5}{3}}\square_{\frac{1}{3}})^{B}O_4$, where A represents tetrahedrally coordinated Fe^{3+}, B represents octahedrally coordinated Fe^{3+} and $\square$ represents vacancies. Synthetic maghemite may demonstrate superstructures in which the octahedral vacancy sites are ordered[40,41]. Vacancy ordering is not possible in a cubic unit cell with Fd3m symmetry. Instead, the unit cell is tripled along the *c*-axis, resulting in a tetragonal unit cell (a = 8.34 Å, c = 25.01 Å) with a $P4_22_12$ symmetry. This vacancy-ordered unit cell is illustrated in Figure 2.3.

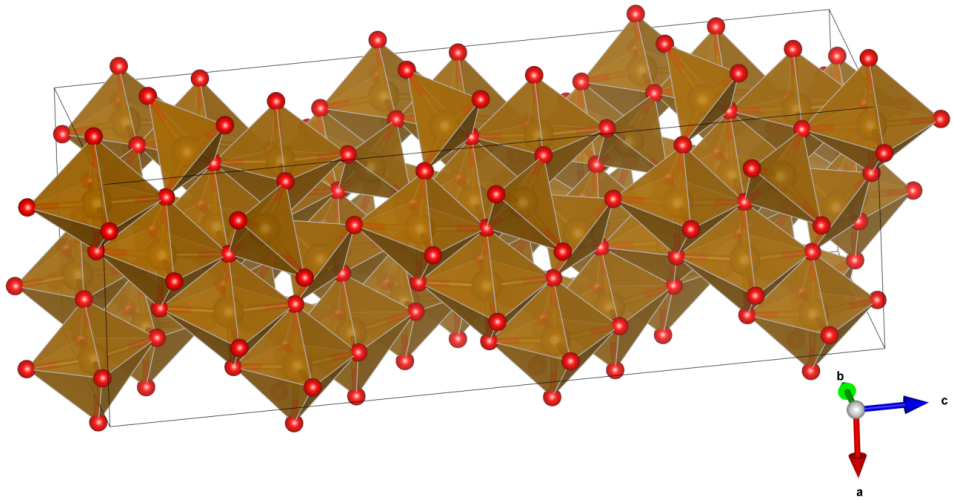

Figure 2.3: *The unit cell of the vacancy-ordered, tetragonal ($P4_22_12$ spacegroup) form of maghemite (ICSD: 172906)[42]. Iron atoms and iron-oxygen polyhedra are brown, oxygen atoms are red.*

Maghemite is ferrimagnetic at room temperature. It has proved difficult to measure the Curie temperature (T_C) of maghemite, since it transforms to hematite at lower temperatures. However, the Curie temperature has been estimated at approximately 950 K[43]. The magnetic structure consists of two sublattices corresponding to Fe^{3+} cations located at the A and B sites respectively. The electron spins at the A sites are parallel with each other, as are the spins at the B sites. However, the A site spins and B site spins are antiparallel to each other giving rise to the property of ferrimagnetism[44]. As with hematite, nanometer-sized particles of maghemite are superparamagnetic at room temperature[45].

2.1.3 Ferrihydrite ($Fe_5HO_8{\cdot}4H_2O$)

Ferrihydrite is a poorly nanocrystalline, short-range ordered oxyhydroxide of iron, with particles between 2 to 6 nm in size[46–49]. The unit cell of ferrihydrite is trigonal (originally determined unit cell: a = 5.1 Å, c = 9.4 Å, $P\bar{3}1c$ space group), however the exact contents of the unit cell vary depending on the degree of hydration of the ferrihydrite. This has led to a number of different proposed formulas

describing its contents, with the most common being $5Fe_2O_3{\cdot}9H_2O$, $Fe_5HO_8{\cdot}4H_2O$ and $Fe(OH)_3$. Ferrihydrite crystallises in a number of different forms depending on its degree of crystallinity[50,51]. The two commonly recognized forms are known as 2-line ferrihydrite (least ordered) and 6-line ferrihydrite (most ordered), with this number representing the number of reflections visible in their associated XRPD patterns. Owing to the nanoparticulate nature of ferrihydrite, all attempts to elucidate its structure via techniques that rely on long-range order have met with limited success. As such, the exact structure of ferrihydrite remains a topic of debate to this day. One of two structural models is generally agreed upon.

The first model, proposed by Drits *et al.*, suggests that ferrihydrite is a mixture of three separate components[52]. Firstly, a hexagonal (a = 2.96 Å, c = 9.40 Å, $P\bar{3}1c$ spacegroup) defect-free ferrihydrite phase consisting of hexagonally close packed anions. The anions are stacked according to the ABACA motif. Fe^{3+} cations occupy half the octahedral interstices. The second component is a defective ferrihydrite phase, which consists of two structural fragments in a hexagonal supercell (a = 5.126 Å, c = 9.40 Å). These structural fragments have their anions arranged with an Ac_1Bc_2A and Ab_1Cb_2A structural motif respectively. They occur with equal probability and alternate at random. The final component is ultra-dispersed hematite, consisting of crystallite domains not larger than two nanometres.

The second model was proposed by Michel *et al.* after real space modelling of the pair distribution function (PDF) which was derived from a direct fourier transform of the total X-ray scattering[53]. In this model, ferrihydrite is described as being a monophasic, hexagonal structure (a = 5.95 Å, c = 9.06 Å, $P6_3mc$ space group). The basic structural motif of the model consists of 13 iron cations and 40 oxygen anions. The central tetrahedrally coordinated iron(III) is connected by μ_4-oxo bridges to 12 octahedrally coordinated iron(III) cations arranged in edge-sharing groups of three. The 2- to 6-nm ferrihydrite nanoparticles can then be described as a three-dimensional packing of these clusters with adjacent clusters connected by a common pair of edge-shared octahedra, forming μ_4-oxo bridges from the three μ_2-OH groups *cis* to each of the μ_4-oxo centers in the bare cluster. In its ideal form, this structure contains 20% tetrahedrally and 80% octahedrally coordinated iron and has a basic structural motif closely related to the Baker-Figgis δ-Keggin cluster[54]. This structure is visualised in Figure 2.4.

The relationship between 2-line and 6-line ferrihydrite is another topic of debate in the literature, with some studies suggesting that they have identical atomic arrangement, the only difference being different sizes of their coherent scattering domains *viz.* 2 nm for 2-line and 6 nm for 6-line[52,53]. However, electron nano-diffraction studies that probed the structure of 2-line and 6-line ferrihydrite were able to show that the 2-line ferrihydrite has a higher fraction of disordered material compared to the 6-line variant[47–49].

The small crystallite sizes of the various forms of ferrihydrite and large surface areas ($> 200\ m^2.g^{-1}$) make it particularly useful as a precursor material for iron catalysts[46,55]. Ferrihydrite nanoparticles are superparamagnetic at room temperature[56], with a Néel temperature of 350 K[57].

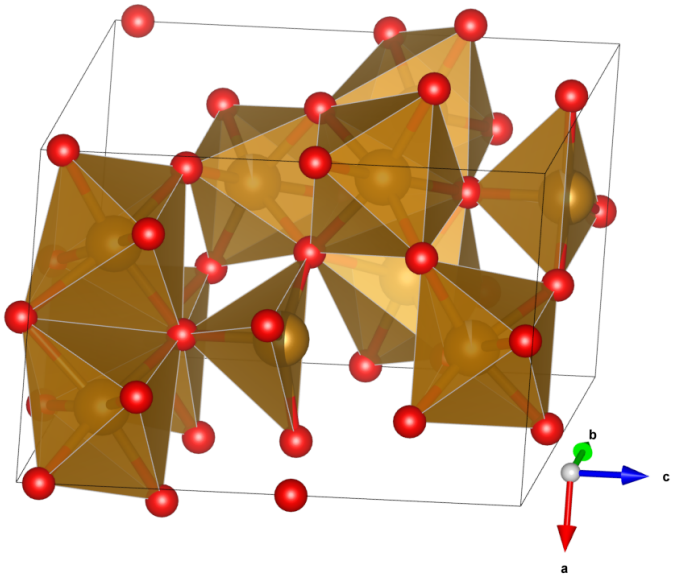

Figure 2.4: *The unit cell of ferrihydrite proposed by Michel et al. (ICSD: 158475[53]). Iron atoms and iron-oxygen polyhedra are brown, oxygen atoms are red.*

2.1.4 Magnetite (Fe_3O_4)

Magnetite's crystal structure is cubic (a = 8.39 Å, Fd3m space group) consisting of eight formula units per unit cell. Like maghemite, it is an inverse spinel structure[58]

and also one of the first minerals to be studied by X-ray diffraction[59], as such its structure has been known for some time. The unit cell, shown in Figure 2.5, is face-centered with the 32 oxygen anions regular cubic close-packed along the [111] direction[2]. It contains both Fe^{2+} and Fe^{3+} cations, with an ideal stoichiometric ratio of 1:2. The structure consists of octahedral and mixed tetrahedral/octahedral layers stacked along [111]. It is common for iron in magnetite to be found in non-stoichiometric amounts, in which case the Fe^{3+} sub-lattice is found to be deficient.

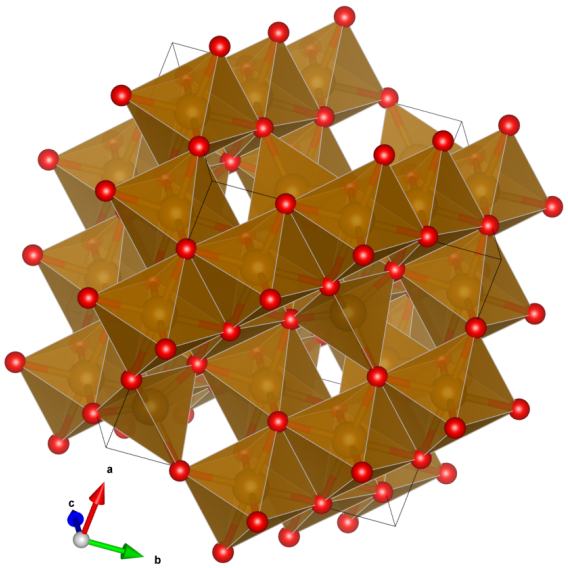

Figure 2.5: *The unit cell of magnetite (ICSD: 249047)[60]. Iron atoms and iron-oxygen polyhedra are brown, oxygen atoms are red.*

As with maghemite, magnetite is also ferrimagnetic at room temperature, possessing a Curie temperature of 850 K[2]. Not only does magnetite possess a similar crystal structure to maghemite: its magnetic lattice is similar as well, consisting of two interpenetrating sub-lattices (electron spins centered at the A and B sites respectively). The electron spins at the A and B sites are antiparallel to each each other as with maghemite, giving rise to the ferrimagnetism. Particles smaller than 6 nm in size are superparamagnetic at room temperature.

2.1.5 Wüstite (FeO)

Wüstite has a defective sodium chloride structure[61]. It may be regarded as two interpenetrating face-centered cubic structures of Fe^{2+} and O^{2-}. Alternatively, the structure of wüstite may be viewed as a cubic close-packed array of anions stacked along the [111] direction, with planes of anions alternating with planes of cations. Most of the Fe^{2+} cations occupy octahedral interstices within the structure, while the Fe^{3+} is usually found at vacant tetrahedral interstices. The FeO_6 octahedra share edges with one another. A unit cell of wüstite is shown in Figure 2.6.

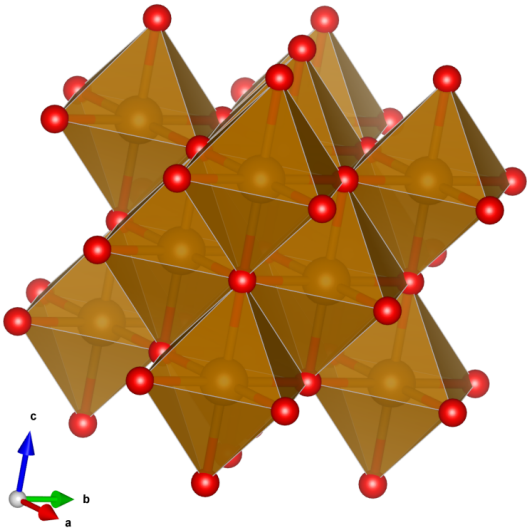

Figure 2.6: *The unit cell of wüstite (ICSD: 82233)[62]. Iron atoms and iron-oxygen polyhedra are brown, oxygen atoms are red.*

This compound, however, is found in a non-stoichiometric form at atmospheric pressure, but only at temperatures in excess of 567°C. Oxidation of Fe^{2+} to Fe^{3+} and cation vacancies account for this non-stoichiometry[2]. This leads to the chemical formula of wüstite commonly being written as $Fe_{1-x}O$. As a result of this oxidation and the presence of the cation vacancies, the unit cell varies in size from 4.28 Å to 4.31 Å, while the density of wüstite[63] ranges from 5.72 $g.cm^{-3}$ to 5.61 $g.cm^{-3}$. When wüstite is cooled below 567°C, it disproportionates to metallic iron and magnetite, according to the following equation:

$$4\,FeO \xrightarrow{T<567^{\circ}C} Fe_3O_4 + Fe$$

Wüstite is paramagnetic at room temperature, becoming antiferromagnetic below its Néel temperature, which varies from 203 K to 211 K, once again depending on the number of defect sites present[2]. The spins of the Fe^{2+} cations in the antiferromagnetic structure are ordered antiferromagnetically within (111) planes - their moments lie parallel to the [111] direction. Neighbouring (111) planes have opposite spin directions, resulting in a magnetic unit cell that is twice as large as the chemical unit cell[36,62,64].

2.1.6 Fayalite (Fe_2SiO_4)

While not strictly an iron oxide, fayalite is very relevant to this work and as such its structure is presented here. Fayalite is the iron end-member of the olivine mineral series[32,65–67]. Olivine is an iron-magnesium silicate having the structure $(Mg^{2+}, Fe^{2+})_2SiO_4$. It crystallises into an orthorhombic unit cell (a = 4.818 Å, b = 10.471 Å, c = 6.086 Å, Pbnm space group). It contains divalent iron cations.

Olivine consists of close packed oxygen anions, with iron and magnesium cations occupying half the interstices in two non-equivalent sites, namely M_I and M_{II}[67]. Both sites leave the cation in a six-coordinate, distorted octahedral environment. The M_I site is the more distorted of the two and slightly larger, with a point symmetry of m[66]. The less-distorted, smaller M_{II} site has a $\bar{1}$ point symmetry. There is a tendency for iron cations in fayalite to favour the M_I site over the M_{II} site. The structure of fayalite is illustrated in Figure 2.7.

Fayalite is paramagnetic at room temperature, but transforms into a colinear antiferromagnet below its Néel temperature of 65 K[68]. In its antiferromagnetic state, there is an antiferromagnetic ordering between corner sharing octahedra and a ferromagnetic ordering between edge sharing octahedra[69].

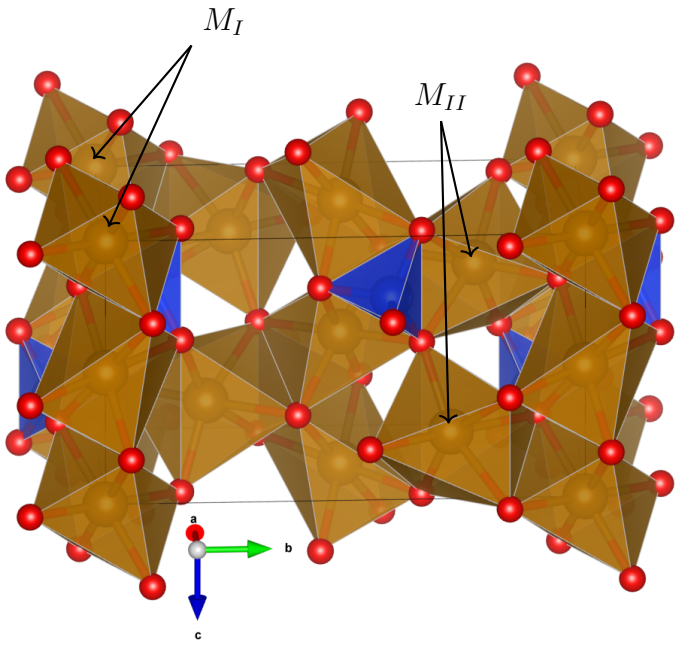

Figure 2.7: *The unit cell of fayalite (ICSD: 4353)*[32]*. Iron atoms and iron-oxygen polyhedra are brown, oxygen atoms are red, silicon atoms and silicon-oxygen polhedra are blue. M_I and M_{II} sites are labelled.*

2.2 Transformations of the Iron Oxides

The iron oxides exhibit a wide variety of transformations and interconversions. It is possible for almost any of the iron oxides to transform into at least two other iron oxide phases under the appropriate conditions[2]. One method of classification is from a chemical standpoint. If the transformation involves no chemical change, it is termed isochemical. Transformations involving chemical changes may be further subdivided into dehydrations (ones which involves the loss of water), dehydroxylations (ones involving the loss of hydroxy groups) and oxidation/reduction transformations (transformations which involve the oxidation or reduction of the iron cations within the iron oxide). In an oxidising environment, hematite and goethite are the most thermodynamically stable iron oxides, and as such are most often the end-members in any oxidative transformation series.

Apart from classifying the transformations in terms of their chemical change, the transformations may also be classified according to structural changes[70]. These

may be either topotactic, or reconstructive. Topotactic transformations occur in the solid state and involve an internal atomic rearrangement within a single crystal to another, different, single crystal phase. Should the transformation begin with a single crystal and result in a product that is not single crystalline, but where there is still a very clear relationship between the crystal axes of the initial and final product, it is termed pseudomorphic. These transformations require the atoms to be mobile, and since they only occur in the solid state, are only observed at elevated temperatures.

Reconstructive transformations involve dissolution of the initial phase into solution, followed by the subsequent precipitation of a new phase from the same solution[71]. Since the initial phase dissolves, there is not necessarily a structural relationship between it and the final, reconstructed phase. This process is governed by an energy gradient which is determined by the solubility and dissolution rate of the initial phase. Thus, unlike the topotactic transformations, the reconstructive transformations readily occur under ambient conditions. Some of the transformations are shown in Table 2.2.

Since this work is primarily concerned with the iron-silica interaction that manifests on reduction, the reduction behaviour of the iron oxides will be discussed in more detail. Particular emphasis is placed on the reduction pathways of hematite and ferrihydrite in a hydrogen atmosphere.

Table 2.2: *Various transformations of the iron oxides. This table is adapted from Cornell and Schwertmann[2]. DR = dissolution/reprecipitation, deOH = dehydroxilation, deH_2O = dehydration*

Initial Phase	**Final Phase**	**Type of Transformation**
Goethite	Hematite	Thermal or mechanical deOH
		Hydrothermal deOH
	Maghemite	Thermal deOH
Lepidocrocite	Maghemite	Thermal deOH
	Hematite	Thermal deOH
	Goethite	DR
	Magnetite	Reduction
Akaganéite	Hematite	Thermal deOH
	Goethite	DR
	Hematite	DR
	Magnetite	DR
δ-FeOOH	Hematite	Thermal deOH
Feroxyhyte	Goethite	DR
Ferrihydrite	Hematite	Thermal deH_2O/deOH
	Maghemite	Thermal deH_2O/deOH
	Goethite	DR
	Akaganéite	DR
	Lepidocroctie	DR
	Hematite	Aggregation
Hematite	Magnetite	Reduction
		Reduction DR
Magnetite	Maghemite	Oxidation
	Hematite	Oxidation
Maghemite	Hematite	Thermal conversion
Wüstite	Magnetite	Disproportionation

2.2.1 Reduction in Hydrogen

The reduction of hematite, both supported and unsupported, in hydrogen has been extremely well-studied in the literature. There are currently two accepted models which describe the reduction of hematite. The first involves a consecutive, two-step reduction process. Hematite is initially reduced to magnetite, which is subsequently reduced to metallic iron[72–76]. The equations describing the reduction process are:

$$3Fe_2O_3 + H_2 \longrightarrow 2Fe_3O_4 + H_2O$$
$$Fe_3O_4 + 4H_2 \longrightarrow 3Fe + 4H_2O$$

$$Fe_2O_3 + 3H_2 \longrightarrow 2Fe + 3H_2O$$

The first reduction step of hematite to magnetite occurs via a unimolceular reduction model[75], while the second step proceeds via two- or three-dimensional nucleation according to the Avarmi-Erofeev model at low partial pressures of H_2O[73,75]. The presence of just 3% H_2O in the reducing gas severely retards the reduction of magnetite to iron, with the rate-determining step being self-catalysed nucleation[73].

Alternatively, it has been proposed that the reduction of hematite to iron occurs via a three-step process. Hematite is initially reduced to magnetite, but this is followed by reduction of magnetite to wüstite, rather than directly to iron. The wüstite is in turn reduced to metallic iron[77–80]. The associated equations are:

$$3Fe_2O_3 + H_2 \longrightarrow 2Fe_3O_4 + H_2O$$
$$Fe_3O_4 + H_2 \longrightarrow 3FeO + H_2O$$
$$FeO + H_2 \longrightarrow Fe + H_2O$$

$$Fe_2O_3 + 3H_2 \longrightarrow 2Fe + 3H_2O$$

The difference between the two models occurs in the reduction pathway of magnetite. This is heavily dependent on the temperature of reduction[81]. At temperatures lower than 420°C, magnetite is reduced directly to metallic iron, giving rise to

the first model. At temperatures in excess of 570°C, the magnetite is fully reduced to wüstite which in turn is reduced to iron, since this temperature is capable of stabilising the wüstite particles that form. In fact, the reduction pathway is dependent on numerous other factors as well, including the water to hydrogen molar ratio (χ_{H_2O}/χ_{H_2})[82]. Should this value be large (> 0.35), the reduction occurs via the three-step pathway. Below this value, the reduction is expected to follow the two-step pathway. It is even possible at extremely low values of χ_{H_2O}/χ_{H_2} for hematite to reduce directly to iron.

The addition of supports and promoters to hematite alters the reduction behaviour, sometimes dramatically[78,83–85]. The presence of silica, in particular, causes reduction to shift to higher temperatures. This has been attributed to the iron-silica interaction that is the focus of this study. In these cases, copper is added as a chemical promoter, and greatly reduces the temperature of the first reduction step of hematite to magnetite. It does not affect the subsequent reduction steps however. The presence of silica also results in incomplete reduction, with the total hydrogen consumption measured during experiments being considerably less than that expected from theory. This points towards the formation of irreducible species during reduction[86].

It has been proposed that the reduction of ferrihydrite occurs via the thermal transformation of ferrihydrite to hematite, which in turn reduces in a manner described above[77]. However, more recent data suggests that the reduction of ferrihydrite is dependent on the form of ferrihydrite[87]. 2-line ferrihydrite is reduced to iron in a two-step process. During the first step of this reduction process, ferrihydrite is reduced directly to magnetite. The magnetite is then reduced directly to metallic iron, with no evidence for the formation of an intermediate wüstite phase:

$$6Fe_5HO_8 \cdot 4H_2O + 5H_2 \longrightarrow 10Fe_3O_4 + 32H_2O$$
$$Fe_3O_4 + 4H_2 \longrightarrow 3Fe + 4H_2O$$

$$2Fe_5HO_8 \cdot 4H_2O + 15H_2 \longrightarrow 10Fe + 24H_2O$$

The presence of silica results in a three-step reduction pathway, with magnetite first reducing to wüstite which itself is reduced to iron. It also proves considerably

more difficult to complete the reduction. While no explanation was given for this, it is likely the result of iron-silica interactions.

6-line ferrihydrite initially undergoes a thermal transformation to hematite. The reduction pathway then follows one of a hematite sample.

2.3 Fischer-Tropsch Synthesis

Crude oil has long been the staple source for petroleum products. However, the amount of crude oil available is rapidly decreasing, with some estimates suggesting all oil reserves will be depleted by the year 2042[88]. It is therefore important that an alternative fuel source for the production of petroleum products be employed. The Fischer-Tropsch (FT) process, discovered in 1927, is one such process capable of producing petroleum products from non-crude oil fuel stocks[23]. gasification of coal or oxidation of natural gas produces syngas, a mixture of carbon monoxide and hydrogen. The FT reaction primarily involves a polymerization reaction which, in the presence of a suitable metal catalyst, produces oligomers with varying carbon-chain lengths[89]. The principle chemical reactions that take place during FTS are olefin and paraffin synthesis, as well as the water-gas shift (WGS) reaction.

2.3.1 Fischer-Tropsch Chemistry

Balanced chemical equations for the primary FT reactions (olefin and paraffin formation, as well as the WGS reaction) are given below:

$$n\mathrm{CO} + (2n+1)\mathrm{H_2} \longrightarrow C_\mathrm{n}H_{2n+2} + n\mathrm{H_2O} \qquad \text{(Paraffin formation)}$$

$$n\mathrm{CO} + 2n\mathrm{H_2} \longrightarrow C_\mathrm{n}H_{2n} + n\mathrm{H_2O} \qquad \text{(Olefin formation)}$$

$$\mathrm{CO} + \mathrm{H_2O} \rightleftharpoons \mathrm{CO_2} + \mathrm{H_2} \qquad \text{(WGS reaction)}$$

The exact mechanism of hydrocarbon formation during FTS remains controversial, with many detailed mechanisms proposed[23,90–97]. Ignoring mechanistic details, the general process for hydrocarbon production may be described in four basic steps. The initial step involves the chemisorption of carbon monoxide onto the surface of

the catalyst. The carbon monoxide may chemisorb in various geometries, some of which are outlined in Figure 2.8. The linear CO molecule may lie perpendicular to the catalyst surface with the carbon bound to a metal site (a) or parallel, with carbon and oxygen chemisorbed to separate metal sites (b) or the same metal site (c).

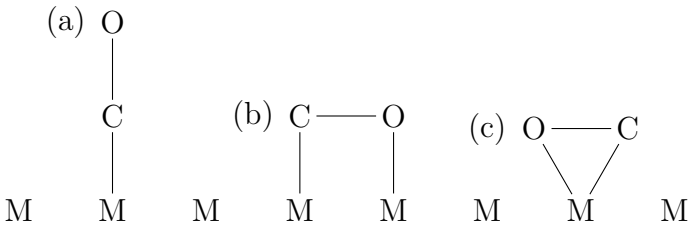

Figure 2.8: *Various geometries for chemisorbed CO species on an FT catalyst surface: (a) CO perpendicular to the catalyst surface (b) CO parallel to the catalyst surface with the carbon and oxygen chemisorbed to a separate metal site and (c) CO parallel to the catalyst surface with the carbon and oxygen chemisorbed to the same metal site.*

This is followed by hydrogenation of the chemisorbed carbon species to form primary CH_2 "building blocks". There are a number of possible pathways for this. Assuming chemisorption of CO in a perpendicular geometry, hydrogenation of the C-O bond results in the formation of an intermediate alcohol, which is followed by further hydrogenation to produce the primary CH_2 building block. Oxygen is released from the metal surface in the form of water molecules. This pathway is illustrated in Figure 2.9 (a). Figure 2.9 (b) suggests an alternate pathway in which each of the oxygen and carbon atoms of carbon monoxide is chemisorbed to a separate metal site. Cleavage of the C-O bond results in free carbon and oxgyen species on the surface of the metal. These then undergo direct hydrogenation to yield the primary CH_2 building block and water respectively. Of these two pathways, it is believed that the one outlined in (b) is more likely over iron and cobalt catalysts[91].

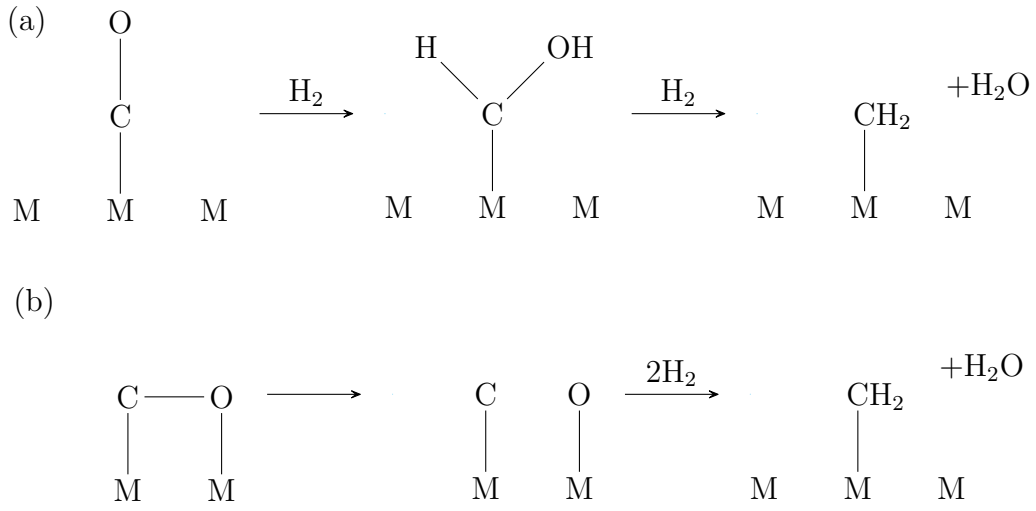

Figure 2.9: *Hydrogenation pathways for production of CH_2 primary building blocks from chemisorbed CO.*

The hydrocarbon products begin to form via chain growth of the primary CH_2 units. Two possible reaction pathways (amongst many) are outlined in Figure 2.10. It is believed that both these reactions are occurring simultaneously, with the relative extent of each reaction dependent on the catalyst type and reactor conditions. The first reaction pathway, shown in (a), involves the combination of two adjacent CH_2 units to create a chemisorbed ethyl. This in turn can further grow through continued insertion of CH_2 species. The second pathway (b) involves the combination of a surface alkyl species with a chemisorbed CO. Hydrogenation of this CO-alkyl intermediate results in chain growth and the release of water. It is of course possible for surface CH_2 species to be directly hydrogenated to methane, an undesired biproduct of FTS. Use of iron results in the lowest yield of methane, while nickel, and to a lesser extent cobalt, result in much higher levels of methane production[98].

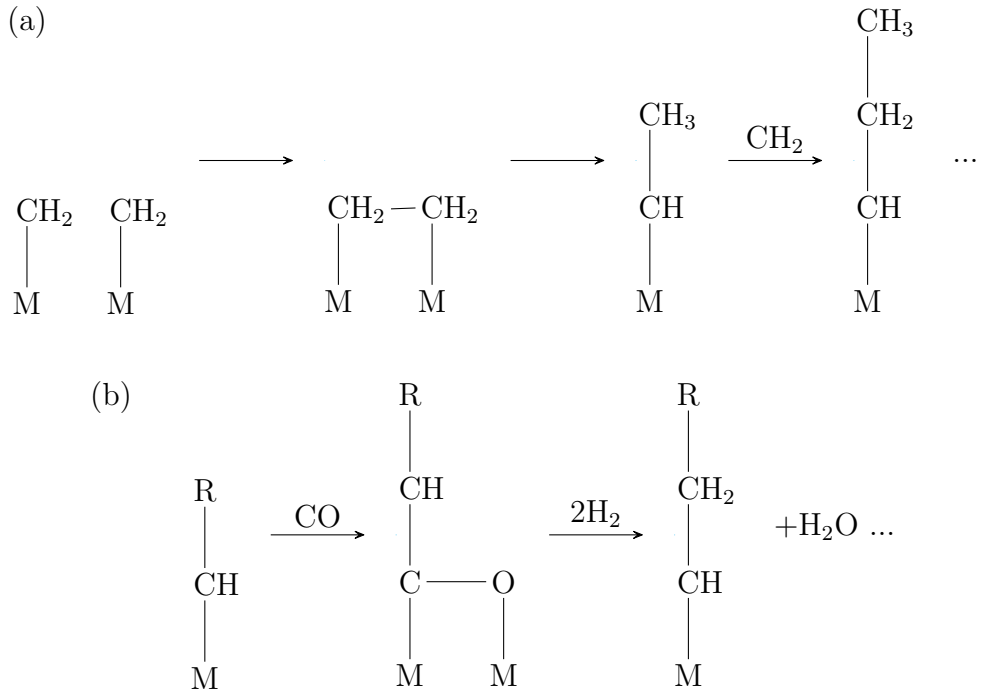

Figure 2.10: *Two possible pathways for chain growth during FT synthesis.*

Chain-growth of the hydrocarbon products is terminated through numerous possible routes, some of which include desorption, hydrogenation and insertion of oxygenated species. These are outlined in Figure 2.11. The desorption process is fairly straightforward: the alkyl species simply desorbs from the surface of the metal and is no longer able to participate in the chain growth process. Hydrogenation of the surface-bound alkyl radical creates a stable alkyl species, and as a result no more CH_2 insertion can occur. The formation of oxygenated species similarly prevents CH_2 insertion, thus terminating the chain growth process.

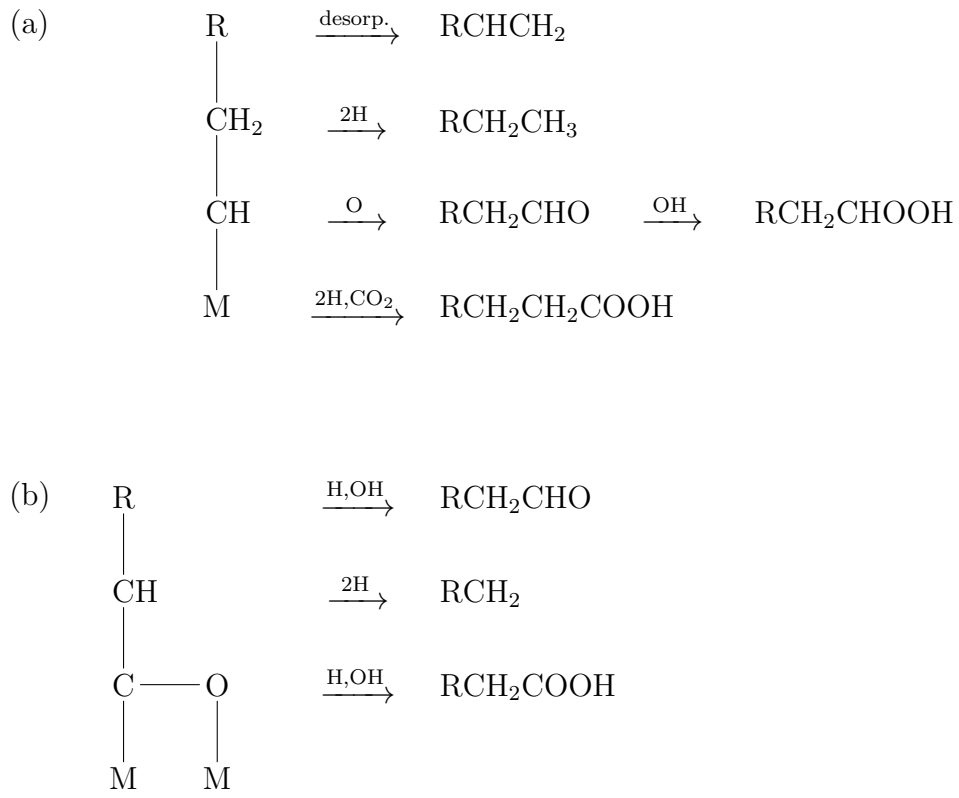

Figure 2.11: *Chain-growth termination during FT synthesis in the absence (a) and presence (b) of a surface-chemisorbed CO species.*

As can be seen, the FT process is a relatively complicated one and there are as yet no certainties regarding the mechanism nor the phases present in the reaction medium. Activated, C, CO, CO_2, H_2O, OH, H, H_2 species, amongst others, are all present on the surface of an FT catalyst at any given moment and could potentially participate in hydrocarbon chain growth and termination.

The FT-active catalysts are typically prepared in an oxide form and activated prior to FTS by reduction in hydrogen, carbon monoxide or syngas. These FT metals may in turn be transformed to metal carbides in the presence of carbon species present during reaction. The general reduction reactions in hydrogen and carbon monoxide, as well as the transformation to metal carbides, are as follows:

$$M_xO_y + yH_2 \longrightarrow yH_2O + xM$$
$$M_xO_y + yCO \longrightarrow yCO_2 + xM$$
$$yC + xM \longrightarrow M_xC_y$$

Of the transition metals, only iron, cobalt, nickel and ruthenium demonstrate appreciable activity towards FTS[24]. The methane selectivity of nickel is too high for it to be commercially viable, while the high cost of ruthenium also discounts its use. This leaves iron and cobalt as the only transition metals suitable for industrial-scale implementation of the FT process. Cobalt catalysts are usually activated with H_2 and the metallic cobalt produced is believed to be the active phase for FTS, with cobalt particle sizes playing a key role in catalytic performance[99]. Concerning iron, it has been reported that the reducing conditions (CO, H_2 and/or syngas) affect the FT activity and selectivity[100–105]. Reduction in hydrogen typically leads to the formation of metallic iron particles (α-Fe) while reduction in CO and syngas results to a mixed phase of α-Fe and various iron carbides. It is believed that ϵ-, γ- and χ-carbides are the active phases during FTS. It can be seen that understanding the reduction of FT catalyst metal oxide precursors, in particular iron, with its complex reduction behaviour, is essential to understand the resulting FT activity.

2.3.2 Iron-based Fischer-Tropsch Catalysts

Iron-based catalysts are typically less active than their cobalt counterparts, however they offer several significant advantages. Iron-based FTS catalysts have a relatively short lifetime on stream when compared to their cobalt counterparts, however they are considerably cheaper to produce[106,107]. They have the added advantage of simultaneously catalysing the WGS (described earlier) and FTS reactions[24,108]. By converting carbon monoxide and water to carbon dioxide and hydrogen, it allows for the use of syngas with a much lower hydrogen content and is particularly suited to syngas produced via the gasification of coal, which contains considerably less hydrogen than syngas derived from a methane source[24].

Iron-based FT catalysts are typically promoted with a number of different chem-

ical and structural promoters. The role of a structural promoter is to assist with metal dispersion and provide mechanical integrity to the catalyst, while chemical promoters affect the chemical behaviour of the catalyst in some way[25]. The most common structural promoter for iron-based catalysts is silica (SiO_2)[24], while the use of alumina, titania, manganese oxide and zeolitic materials have also been investigated[109–111]. Silica is also believed to interact chemically with the iron catalysts, inhibiting reduction and altering the hydrocarbon selectivity of the catalyst[105,112,113].

Chemical promoters employed in iron-based FT catalysts are typically copper and potassium[24]. The role of the copper is to facilitate the reduction of Fe^{3+} species to Fe^0. Copper may be substituted with a number of different metals, including platinum, ruthenium and palladium[114–116]. Copper is also believed to be responsible for an increased dispersion of iron carbides formed during FTS[107]. Potassium, an alkali metal, is an invaluable addition to the iron-based FT catalyst and is responsible for increasing the WGS reaction activity, suppressing methane formation and increasing hydrocarbon product selectivity[115,117–120].

2.4 Metal-Support Interactions

The interaction between metals and their supports in the field of catalysis has been observed in many metal/support systems and has been used to explain variations in, among other factors, changes in the rate of reactions, as well as the nature of the resulting products. The term strong metal-support interaction (SMSI) was coined to account for changes in catalytic activity of group VIII noble metals (Ru, Os, Rh, Pt, Pd, Ir) supported on titania[121]. The interaction is described as being a result of the formation of bonds between the noble metal atoms with titanium atoms on the surface of the support. Subsequent studies suggest that it is the migration of reduced titania (TiO_x) species onto the surface of the metal clusters that is responsible for the SMSI[122,123]. Using electron microscopy, these reduced titania layers have been directly observed in the case of Rh/TiO_2 and Ru/TiO_2[124,125]. They were present as amorphous layers approximately 2-4 Å thick surrounding each noble metal particle. TEM micrographs in Figure 2.12 demonstrate the partial (A) and complete (B) encapsulation of ruthenium particles

by partially reduced titania overlayers.

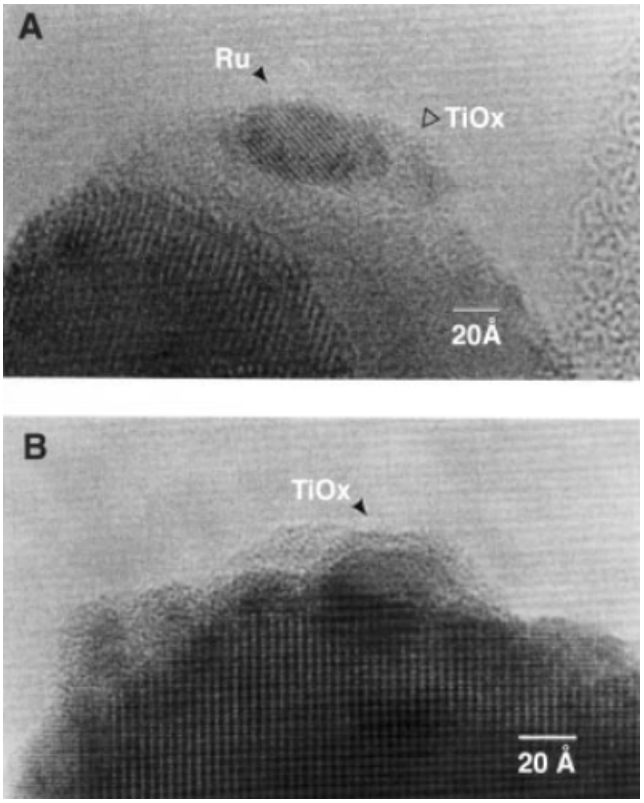

Figure 2.12: *Formation of partially reduced titania overlayers that partially (A) and fully (B) encapsulate ruthenium nanoparticles*[125].

While SMSI interactions were also evident in noble metal catalysts supported on ceria (CeO_2), electron microscope studies of both a Pt/CeO_2 system[126] and a Rh/CeO_2[127] system were unable to show similar reduced CeO_x layers on the metal particles, suggesting that the SMSI in this case is the result of a different underlying phenomenon to that of the group VIII metals on titania.

Alumina-supported catalysts have also demonstrated SMSIs. The underlying cause of this interaction has been reported as a charge transfer between the metal particles and the oxygen-deficient alumina support[128]. It is believed that the interaction is between the metal and aluminium of the alumina, rather than the oxygen atoms of the alumina[129].

2.4.1 The Iron-Silica Interactions

There have been numerous studies concerned with metal/SiO_2 systems. In all cases, these studies suggest the formation of silicide or silicate species forming at the interface between the particles and the silica support during the reduction of the metal-oxide precursor materials[130–134].

The first documented studies were concerned specifically with the particle-support interaction in magnetite (Fe_3O_4) supported on silica[27]. The interaction manifested in the high temperature oxidation of magnetite to maghemite, rather than to the more thermodynamically stable hematite. MAS data for octahedrally-coordinated Fe^{3+} atoms in the silica-supported structure exhibit parameters significantly different to those in unsupported magnetite. A model was proposed in which Si^{4+} cations substitute for tetrahedrally coordinated Fe^{3+} in the magnetite lattice, thus hindering the transformation to hematite. This silicon-substituted magnetite forms a shell around the core of unsubstituted magnetite[135] that is approximately 0.5 nm thick. This layer was not thick enough to inhibit the absorption of nitrous oxide onto the surface of these particles, however it was responsible for a decrease in activity of an order of magnitude towards the WGS reaction[136,137].

These iron-silica interactions were further probed by NO-adsorption studies on 1 wt% iron on silica samples[138]. MAS and infrared data were used to identify changes in the chemical environment of Fe^{2+} cations under different reducing conditions. It was concluded that with reduction, the Fe^{2+} cations interact with the silica support to form ultrathin rafts between the particles and support, or a surface iron-silicate phase that occurs between the iron and the silica support.

A MAS and infrared study, this time employing CO-adsorption and a 20 wt% iron on silica sample, has also been reported which lends further support to the idea of an iron-silicate phase forming during the reduction process[84]. In this study, goethite (α-FeOOH) particles were formed initially. Reduction led to the formation of an Fe^{2+}-containing phase which was not magnetite or wüstite, and was attributed to an iron-silicate phase. Once again, this phase was only observed on the surface of the particles, however in this case it was proposed that the layer encapsulated the entirety of each particle. One further study suggests the presence of magnetite and wüstite in the reduced iron sample (in this case a 5 wt% iron on

silica) alongside the iron-silicate phase[139].

More recently, the degree of interaction between the iron oxide and silica was investigated[25]. Model catalysts were prepared via a precipitation technique and silica was added at various stages of catalyst preparation. When silica was added during, or immediately after precipitation, the resulting iron oxide crystallites were small (approximately 3 nm) and exhibited strong interactions with the silica. This was evident in their resistance to reduction and carburisation. This resulted in very low CO conversion during FT catalysis. When silica was added after heat treatment, the resulting catalyst consisted of segregated iron- and silica-rich phases. It was less resistant to reduction, but ironically demonstrated even lower CO conversion. There was even evidence to suggest that the catalyst was reoxidised during FT activity.

Scanning electron microscopy (SEM) was used to identify this segregation in iron- and silica-containing phases. Figure 2.13 contains SEM micrographs of a catalyst with silica and iron co-precipitated, and a catalyst where silica was added after heat treatment of the iron oxide. Energy dispersive X-ray spectroscopy (EDS) maps of the area are able to show the elemental distribution across the surface. In the co-precipitated sample, the iron (from the iron oxide) and silicon (from the silica) maps are very similar, suggesting an intimate mixing between these two elements. In the sample where silica was added after heat treatment, there is a distinct segregation of iron- and silicon-containing phases. This is even evident in the backscatter micrograph (Figure 2.13 B) which contains darker gray silica regions. This intimate relationship between and iron- and silicon-species observed in the co-precipitated sample is responsible for the iron-silica interaction.

A study on two co-precipitated iron catalysts was conducted to further investigate the nature of this iron-silica interaction. A sample without silica, and one with 20 weight silica for 100 weight iron, was prepared[140]. The result of silica addition was the (reported) stabilisation of a maghemite precursor phase and reduction to small fayalite crystallites, versus hematite formation and reduction to α-Fe (in the silica-free sample). Evidence for the formation of fayalite was provided by XRPD. However, no other phases were identified using XRPD, and the relative amount of silica in the sample is insufficient to form only fayalite. Theoretically, only 37% of the iron could react with all the silica present to form fayalite, based on a 2:1

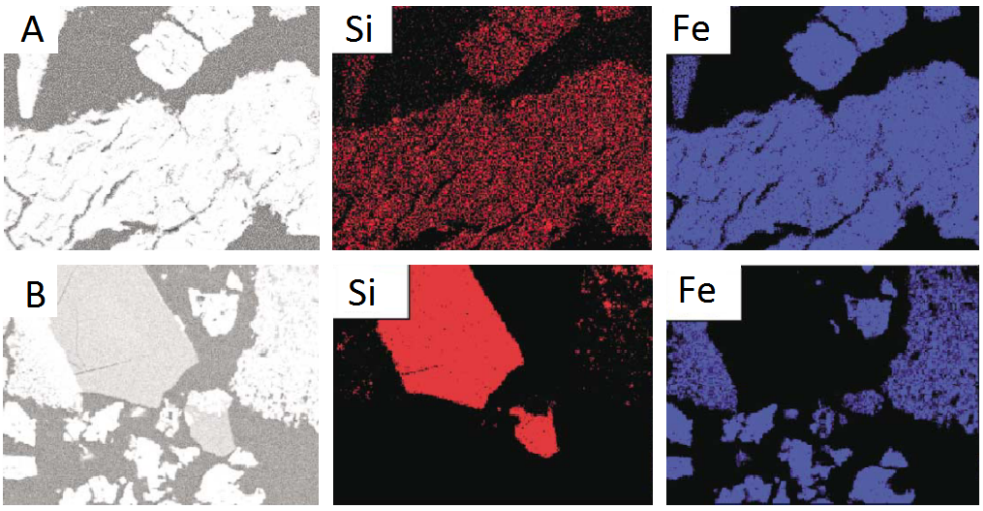

Figure 2.13: *BSE-SEM micrographs and EDS maps of two model iron/silica catalysts. In A, the iron and silica were co-precipitated, while in B, the silica was added after heat treatment of the iron oxide phase*[25].

Fe:Si stoichiometric ratio. This suggests very small, or poorly crystalline, iron or iron oxide particles must also be present after reduction. It has been shown that fayalite is extremely difficult to reduce in hydrogen[141], requiring temperatures in excess of 1000 K owing to its activation energy of 260 kJ.mol^{-1}.

A more recent study employed *in situ* scanning transmission X-ray microscopy to probe the nature of a working, silica-copper-potassium-promoted iron-based FT catalyst[142]. Complex phase changes were observed, and the X-ray absorption spectra provided further evidence (both through the iron L_2- and L_3-edge spectra as well as the oxygen K-edge spectrum) of the presence of the Fe_2SiO_4 phase. The atomic-scale location of the iron-silicate phase was not determined, likely a result of the 15 nm spatial resolution of this technique. The researchers were also able to show the formation of carbidic iron species during FTS as well as an increased number of reactant carbon species in iron-deficient areas. This suggests that the promoters play a role in the spillover of hydrocarbon species from iron to promoter, thereby preventing blocking of the FT-active sites.

The most recent study investigated silica-promoted iron catalysts with silica contents ranging from 0 to 50 atomic percent silicon for 100 atomic percent iron[86]. Using X-ray photoelectron spectroscopy (XPS), and probing the Fe 3*p* and Si 2*p*

peaks, it was shown that there is a net transfer of electrons from iron to silicon, resulting in an electron-deficient iron species which is more difficult to reduce.

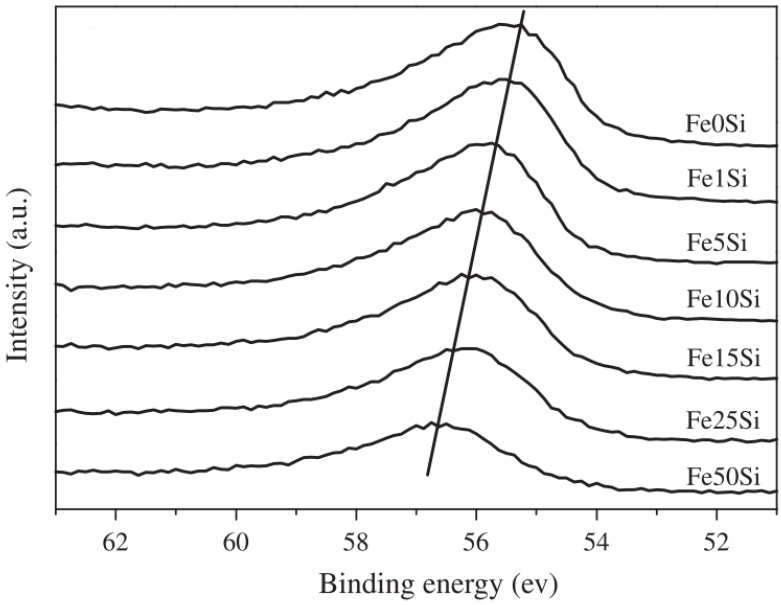

Figure 2.14: *Fe 3p XPS peaks for silica-promoted iron catalysts with varying silica content. The Fe:Si ratio is 100Fe:xSi (atomic), where* $x = 0, 1, 5, 10, 15, 25, 50$ [86].

The Fe 3*p* spectra are shown in Figure 2.14. This shift in binding energy of Fe 3*p* electrons to higher values with increasing silica content suggests a transfer of electron density from iron sites to silicon species, causing the remaining electron density to be more tightly bound, hence increasing its binding energy. The regular trend that is oberved also leads to the hypothesis that the transfer is a long range phenomenon, as opposed to a localised, near-neighbour effect. This electron transfer has been observed in similar iron-silica catalyst systems [143,144]. This study also showed that the addition of silica alters the adsorption sites of the catalyst material *viz.* it decreases the number of weak H-adsorption sites but improves the adsorption strengths of H, C, and O on reduced or carburized catalysts.

The addition of zirconia (ZrO_2) to silica-promoted iron catalysts has also been investigated [143]. The presence of zirconia species in the catalyst matrix is able to weaken the Fe-O-Si bonds that form, thus enhancing the reduction of the catalyst as well as its carburisation. This is a result of Zr-O-Si linkages that form. The

presence of zirconia also resulted in the formation of more stable iron carbide species and increased the C_5^+ hydrocarbon selectivity.

The study of iron-silica interactions is not limited to research in the field of catalysis. Analysis of high silica-content iron-silica xerogels demonstrates the formation of various iron species, ranging from individual tetrahedrally substituted Fe^{3+} atoms incorporated in a silica matrix to complete iron oxide nanoclusters[145]. Separate $Fe_2O_3-SiO_2$ nanocomposites prepared by a sol-gel technique were studied using infrared (IR) and nuclear magnetic resonance (NMR) spectroscopies and once again demonstrated the formation of Fe-O-Si bonds between iron and silica species[146].

In fact, this chemical affinity between iron and silica is evident in natural environments as well, and is responsible for many different ecologically important phenomena[147–150]. During the formation of ferrous oxyhydroxides in the presence of silica, such as ferrihydrite, these compounds adsorb large quantities of silica, part of which is unpolymerized, forming Fe-O-Si structures within the oxide framework, and part of which is polymerized[151]. The formation of the iron-silica species (in whatever form it is found) begins immediately during the hydrolysis of Fe^{3+} ions in solution. Since this study is concerned with co-precipitated iron-based catalysts, this is very likely the mechanism by which initial iron-silica interactions occur.

In solution, at low pH and in the absence of silica, Fe^{3+} is hexa-coordinated with 6 oxygens of H_2O- and/or OH-groups in the first coordination sphere of the metal, at an Fe-O distance of 2.00 ± 0.01 Å. With increasing pH, these groups are rapidly replaced by bridging hydroxyls (-OH-) or oxygens (-O-), and polymerized Fe^{3+} hydroxide complexes form via Fe-(O/OH)-Fe bonds[152–154]. In these polymers, the first atomic shell of iron represents a distorted octahedron with six O/OH groups and Fe-O distances ranging from 1.92 Å to 2.07 Å. The iron octahedra are linked together by their edges (Fe-Fe distance 2.92 Å to 3.12 Å) and corners (Fe-Fe distance 3.47 ± 0.03 Å).

In the presence of silica, important differences are observed. At lower concentrations, the corner linkages between iron octahedra in the polymeric complexes disappear, and the Fe-Fe distances corresponding to the edge linkages slightly in-

crease to values between 3.12 Å and 3.14 Å. At higher silica concentrations, the Fe-Fe bond disappears and Fe-Si bonds are formed instead. Some Fe^{3+} species are also found to be tetrahedrally coordinated, suggesting the iron substitutes for silicon in the tetrahedral network of silica polymers (which would be observable in silica-rich environments). The net result is an inhibition of iron polymerisation, which explains the smaller particle sizes formed during precipitation of iron-based catalysts in the presence of silica. This process is summarised in Figure 2.15.

An alternative view has been proposed for the formation of silica-bearing ferrihydrite[155]. Three principle steps are responsible for the formation of the ferrihydrite and silica species that result from hydrolysis of Fe^{3+} in the presence of silica:

1. Rapid hydrolysis of Fe^{3+} results in precipitation of ferrihydrite. This is subsequently followed by a rapid drop in the concentration of free Fe^{3+} species in solution.
2. Silicate anions are adsorbed onto the ferrihydrite surfaces. This prevents further crystal growth.
3. Surface-adsorbed silicate species polymerise and dehydrate to form silica.

Finally, siliceous ferrihydrites have been studied by synchroton X-ray scattering and X-ray absorption near edge (XANES) spectroscopies[156]. Linear combination fits and principal component analysis (PCA) carried out on the pair distribution functions (PDFs) obtained suggest that iron partitions between two phases in the resulting products that form *viz.* ferrihydrite and an iron-bearing amorphous silica phase. A mechanism of co-precipitation is proposed, in which silicate binds to Fe^{3+} polymers and ferrihydrite particles, thus inhibiting particle growth at low silica content. At higher silica content, ${SiO_4}^{4-}$ polymerization traps significant quantities of Fe^{3+}, thus limiting the further availability of Fe^{3+} species for the formation and development of ferrihydrite particles. This study was not able to determine whether there was any substitution of Si^{4+} for Fe^{3+} in the ferrihydrite crystal lattice.

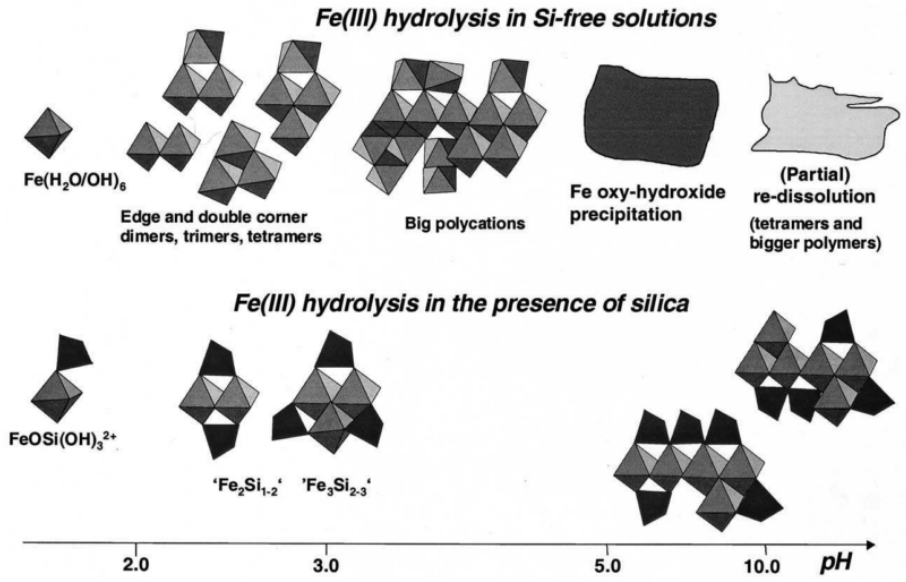

Figure 2.15: *Schematic illustration of Fe^{3+} hydrolysis in Si-free aqueous solution, and structures of Fe-Si complexes formed in moderately concentrated silica-containing solutions, as functions of pH*[154].

3 Theory

This chapter contains a brief summary of the fundamental theory needed to follow and interpret the data generated by each technique used in this study. It is in no way complete and the reader is encouraged to refer to the cited literature at the start of each technique section for a more comprehensive presentation of each subject.

3.1 Fundamental Crystallography

A solid material is referred to as crystalline when its atoms are arranged in a periodic, geometrical structure in space[157–161]. It is often convenient, when considering crystalline structures, to ignore the actual atoms composing the crystal and their periodic arrangement in space and instead consider a set of imaginary points which has a fixed relation in space to the atoms of the crystal and which may be regarded as a framework or skeleton on which the actual crystal is built. These identical points form a lattice, a simplified example of which is illustrated in Figure 3.1. The vectors between any element of this lattice and its two nearest neighbours are given by **a** and **b** respectively. Each other point in the lattice may be reached by translating by a vector **R** given by

$$\mathbf{R} = n_1\mathbf{a} + n_2\mathbf{b} \tag{3.1}$$

where n_1 and n_2 are any two integers. The vectors **a** and **b** thus form a basis for the lattice shown in Figure 3.1. Assuming an infinite lattice, a translation by this vector **R** leaves the lattice invariant. This translational symmetry is an intrinsic property of crystals. This is easily extended to three dimensions through the addition of a third, unique basis vector **c** which lies outside the plane determined by **a** and **b**. The translational vector, **R**, is then given by

$$\mathbf{R} = n_1\mathbf{a} + n_2\mathbf{b} + n_3\mathbf{c} \tag{3.2}$$

where n_3 is also an integer. The vectors **a**, **b** and **c** describe a parallelepiped known as the unit cell. This unit cell is the fundamental building block of any crystalline

system. The choice of **a**, **b** and **c** to be the vectors connecting nearest neighbours is not unique, however they are typically chosen to produce a unit cell that is as small as possible with the highest possible symmetry.

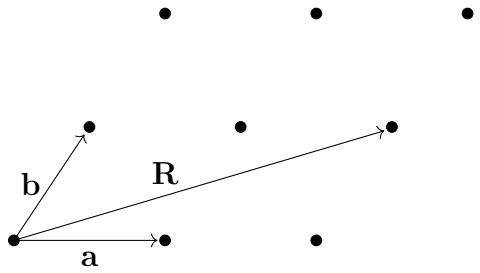

Figure 3.1: *Two-dimensional illustration of a crystal lattice. Any point in the lattice may be reached by translating by a vector* $\boldsymbol{R}$*, which has the form* $\boldsymbol{R}=n_1\boldsymbol{a}+n_2\boldsymbol{b}$*.*

a, **b** and **c** are known as the crystallographic axes of the unit cell. The lengths of these axes (a, b, c) and the angles between them (α, β, γ) are collectively known as the lattice constants. A unit cell in three-dimensions is shown in Figure 3.2. A total of only seven unit cells is necessary to describe any lattice type in three dimensions. These are known as the seven different crystal systems. They are cubic (a=b=c, α=β=γ=90°), tetragonal (a=b, α=β=γ=90°), orthorhombic (a≠b≠c, α=β=γ=90°), hexagonal (a=b, γ=120°), rhombohedral (a=b=c, α=β=γ≠90°), monoclinic (α,γ=90°, β≠90°), and triclinic (α,β,γ≠90°).

Seven different point lattices may be obtained by simply putting points at the corners of each unit cell of the seven crystal systems. However, there are other arrangements of points which fulfill the requirements of a point lattice *viz.* that each point have identical surroundings. This gives rise to a further 7 point lattices, bringing the total number of possible point lattices to 14. These lattices are referred to as Bravais lattices.

Any crystal structure may be created by adding a basis of atoms at every point of a given Bravais lattice. The positions of the constituent atoms within a unit cell are typically expressed as fractions of the basis vectors **a**, **b** and **c** with the origin typically taken as one corner of the unit cell.

It is often necessary and useful to refer to directions in a crystal. The direction of any line in a lattice may be described by first drawing a line through the origin

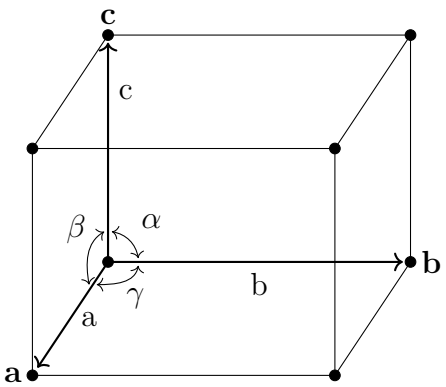

Figure 3.2: *Unit cell in three dimensions. The lattice constants a, b and c and α, β and γ are shown. Adapted from Cullity 1978*[161].

parallel to the given line and then giving the coordinates of any point on the line through the origin. Let the line pass through the origin of the unit cell and any point having coordinates u, v and w ($u, v, w \in \mathbb{R}$, $\mathbb{R}$ is the set of real numbers), then $[uvw]$ is the direction of the given line. Negative numbers are typically indicated by a bar over the number e.g. -2 is written as $\bar{2}$ and, by convention, u, v and w are converted to a set of smallest integers, whilst maintaining the same ratio.

In unit cells with certain symmetry, e.g. a cubic unit cell (a=b=c, α=β=γ=90°), it is possible that two or more directions are equivalent. For example, the [100] direction in a cubic unit cell is equivalent to the [010] direction. These sets of equivalent directions are denoted by $<uvw>$.

Planes within the crystal may also be described symbolically. This is done using a set of three numbers, known as the Miller indices, given by h, k and l. These are defined as the reciprocal of the fractional intercept values of a given plane with the crystallographic axes **a**, **b** and **c** respectively. The method for determining the Miller indices of a given plane is as follows, with two examples shown in Figure 3.3:

1. Determine the intersection of the plane with the crystallographic axes in terms of a, b and c.

2. Take the reciprocal of these values i.e. $\frac{1}{a}$, $\frac{1}{b}$ and $\frac{1}{c}$ and reduce them to a set of smallest possible integers having the same ratio. If the plane is parallel

to an axis, the intercept is at ∞ and the reciprocal is $\frac{1}{\infty} = 0$.

3. The resulting integers are written (hkl). Negative values are similarly denoted by a bar above the number.

As with crystallographic directions, crystallographic planes that are related by symmetry i.e. (110), (011), $(\bar{1}01)$ etc. in a cubic system, are equivalent to each other, and the set of such equivalent planes is written as $\{hkl\}$.

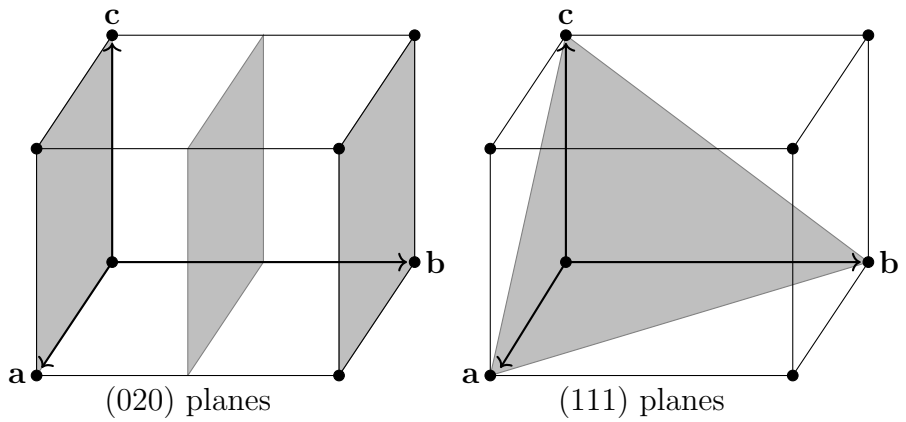

Figure 3.3: *Two examples of planes in a crystal structure: on the left are (020) planes, while on the right is a (111) plane.*

If a set of different crystallographic planes all lie parallel to a particular crystallographic direction, these planes are said to be part of a zone, and this direction is referred to as a zone axis. The set of lattice planes that form part of a given zone axis may have very different miller indices, since the only requirement for a plane with indices (hkl) to lie on a zone axis with direction $[uvw]$ is

$$hu + kv + wl = 0 \tag{3.3}$$

One final concept of fundamental crystallography that is critical to this work is the spacing between adjacent, parallel crystallographic planes having the same Miller indices, known as the d-spacing (d_{hkl}). These are a function of the Miller indices of the planes, as well as the lattice constants of the unit cell. For a given set of lattice parameters, higher indices correspond to smaller values of d_{hkl} and vice versa for low values of (hkl). This calculation for cubic systems with a unit cell of length a

is relatively simple and is given by:

$$\frac{1}{d_{hkl}^2} = \frac{h^2 + k^2 + l^2}{a^2} \tag{3.4}$$

3.2 Transmission Electron Microscopy

A transmission electron microscope (TEM) is a device used to reveal the internal fine structure in solid materials, typically in the sub-micron range[162–165]. The TEM technique directs a beam of electrons, accelerated by a potential difference, through a thin specimen and it is the interaction of these electrons with the atoms of the specimen that provide a wealth of valuable information. These interactions are summarised graphically in Figure 3.4 and are discussed in more detail in the relevant sections that follow.

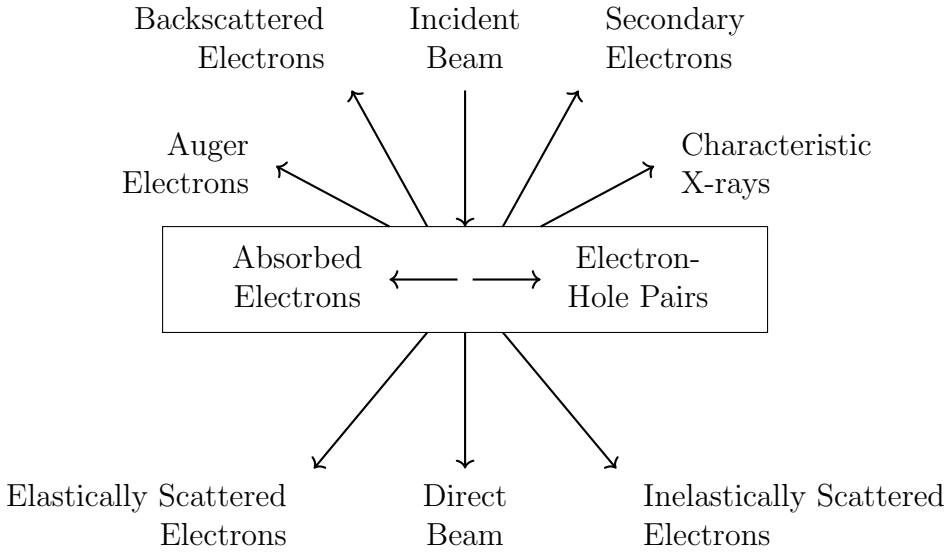

Figure 3.4: *The various signals generated through the interaction of a high energy electron beam with a thin specimen. Adapted from Williams and Carter (1996)*[162].

3.2.1 Electron Scattering

The concept of electron scattering is fundamental to any form of electron microscopy. Electrons that impinge on a thin sample are referred to as the incident beam, while those that come through the sample are referred to as the transmitted beam. Transmitted electrons may further be divided into those that are not deviated from their original trajectory, referred to as the direct beam, and those that deviate to measurable angles.

The incident beam typically consists of a uniform distribution of electrons. As the electrons travel through the specimen they interact with it via Coulomb forces (electrons are negatively charged particles), and are scattered by numerous different processes. The final result is a transmitted beam that has a non-uniform distribution of electrons, and it is this non-uniformity which contains all the structural and chemical information of a particular sample.

It has been shown that electrons exhibit both wave and particle properties. Visualising the electrons as either a wave or a particle is useful for understanding different aspects of electron scattering. Scattered electrons may either be elastically (same energy as incident electrons) or inelastically scattered. When referring to the wave nature of electrons, which are typically coherent in the source (in phase and of the same wavelength), electrons may be coherently or incoherently scattered.

Electrons incident on a sample have a characteristic wavelength which is determined by the accelerating voltage, V, at the source. The potential difference accelerates the electrons to a particular speed and imparts on them a kinetic energy of eV, where e is the elementary charge. Electron speeds are sufficiently high that relativistic effects must be taken into account, which gives the electron wavelength, λ, as

$$\lambda = \frac{h}{\left[2\mathrm{m}_0 eV\left(1+\frac{eV}{2\mathrm{m}_0\mathrm{c}^2}\right)\right]^{\frac{1}{2}}} \tag{3.5}$$

where m_0 is the rest mass of the electron, c is the speed of light in a vacuum and h is planck's constant. By increasing the accelerating voltage, the electron wavelength may be decreased which improves the theoretical resolution of the electron micro-

scope. The classic Rayleigh criterion for light microscopes defines this resolution as the smallest distance, δ, which can be resolved and is approximately

$$\delta = 1.22\frac{\lambda}{\beta} \tag{3.6}$$

where β is the collection semi-angle of the objective lens. For a microscope operating at 200 kV (a typical accelerating voltage), the corresponding electron wavelength is 2.5 pm. However a variety of aberrations and astigmatisms, caused by lens defects and the electron source, result in the transformation of point objects to circular disks. This significantly reduces the working resolution of the microscope compared to the theoretical resolution.

The wave function of a beam of electrons, moving in the z direction, is given by

$$\Psi = Ae^{2\pi i(kz-\nu t)} \tag{3.7}$$

where $k = \frac{1}{\lambda}$ is the wavenumber and ν is its frequency. The probability of finding an electron in a volume $d\tau$ is given by $|\Psi|^2 d\tau$. With the accelerating voltage being constant in an electron microscope, the probability density is independent of time, which allows the wave function to be written more simplistically as

$$\Psi = Ae^{2\pi i\mathbf{k}\cdot\mathbf{r}} \tag{3.8}$$

where $\mathbf{k}$ is the wave vector in three dimensions and $|\mathbf{r}|$ the distance the wave has propagated.

All scattering from an atom is governed by a term known as the scattering cross section of the atom. This is a measure of the probability that scattering will occur. The cross section of a single atom may be defined in terms of an effective radius, r, such that the cross section, σ_{atom} is given by:

$$\sigma_{\text{atom}} = \pi r^2 \tag{3.9}$$

Of particular interest in transmission electron microscopy (TEM) is whether the incident beam electrons are scattered outside a particular angular range or not. This requires knowledge of the differential cross section, $\frac{d\sigma}{d\Omega}$. Electrons scattered

through an angle θ into a solid angle Ω are related by

$$\Omega = 2\pi(1 - \cos\theta) \tag{3.10}$$

Some mathematical manipulation allows the single-atom scattering cross section for electrons scattered at angles greater than θ to be written as

$$\sigma_{\text{atom}} = 2\pi \int_{\theta}^{\pi} \frac{d\sigma}{d\Omega} \sin\theta d\theta. \tag{3.11}$$

The differential cross section is related to the atomic scattering factor $f(\theta)$, a measure of the efficiency of a particular atom in scattering electrons, by

$$|f(\theta)|^2 = \frac{d\sigma(\theta)}{d\Omega} \tag{3.12}$$

where the atomic scattering factor is usually defined as

$$f(\theta) = \frac{\left(1 + \frac{E_0}{\mathrm{m_0 c^2}}\right)}{8\pi^2 a_0} \left(\frac{\lambda}{\sin\frac{\theta}{2}}\right)^2 (Z - f_x) \tag{3.13}$$

where E_0 is the accelerating voltage, a_0 is the Bohr radius of the atom, Z its atomic number and f_x is the scattering factor for X-rays.

A real specimen consists of a number of atoms per unit volume, N. This allows a total cross section for scattering from the specimen to be written as

$$\sigma_{\text{total}} = N\sigma_{\text{atom}} = \frac{\mathrm{N_0}\sigma_{\text{atom}}\rho}{A} \tag{3.14}$$

where ρ is the density of the specimen, $\mathrm{N_0}$ is Avogadro's number and A is the atomic mass of the scattering atoms. For a sample of thickness t, the probability of scattering is simply a product of the scattering cross section and the thickness:

$$\sigma_{\text{total}} t = N\sigma_{\text{atom}} = \frac{\mathrm{N_0}\sigma_{\text{atom}}(\rho t)}{A} \tag{3.15}$$

The product ρt is known as the mass thickness of a sample. This indicates that a sample that is lighter than another may still scatter as much, provided it is appropriately thicker.

When atoms in a sample are arranged in a regular, crystal structure, the structure factor, $F(\theta)$ may be introduced. It is a measure of the amplitude scattered by a unit cell of a crystal structure. It may be defined as the sum of all atomic scattering factors within the unit cell, multiplied by a phase factor. This phase factor accounts for the difference in phase between electron waves scattered from atoms on different but parallel atomic planes with Miller indices (hkl) and is given by

$$F(\theta) = \sum_{i=1}^{\infty} f_i e^{2\pi i(hx_i + ky_i + lz_i)} \tag{3.16}$$

where f_i is the i^{th} atom in the crystal and x_i, y_i, z_i are the relative positions of atom i within the unit cell. The amplitude of scattering is thus not only influenced by the type of atom present, but also its relative position.

3.2.2 Electron Diffraction

This rather complicated process is more simplistically explained through the use of Bragg's Law. Bragg's Law formulated in real space is relevant to both electron diffraction and X-ray diffraction, and is discussed in more detail in Chapter 3.7.

Reformulation of Bragg's law in terms of reciprocal space leads to the Ewald Sphere, a construct that is particularly useful when discussing electron diffraction. Just as the lattice vector was defined in real space (Equation 3.2), it may similarly be defined in reciprocal space as

$$\mathbf{r}^* = m_1\mathbf{a}^* + m_2\mathbf{b}^* + m_3\mathbf{c}^* \tag{3.17}$$

where $\mathbf{a}^*$, $\mathbf{b}^*$ and $\mathbf{c}^*$ are the unit cell lattice vectors in reciprocal space and m_1, m_2 and m_3 are integers. The directions of these vectors are determined by

$$\mathbf{a}^* \cdot \mathbf{b} = \mathbf{a}^* \cdot \mathbf{c} = \mathbf{b}^* \cdot \mathbf{c} = \mathbf{b}^* \cdot \mathbf{a} = \mathbf{c}^* \cdot \mathbf{a} = \mathbf{c}^* \cdot \mathbf{b} = 0 \tag{3.18}$$

i.e. $\mathbf{a}^*$ is normal to $\mathbf{b}$ and $\mathbf{c}$ etc. There lengths are defined as the reciprocal value of the length in real space e.g. $a^* = \frac{1}{a}$.

Consider an electron with momentum $\mathbf{p} = h\mathbf{k}$ that is incident on a scattering atom

at angle θ lying at a point O on an atomic plane with indices (hkl). It is then elastically scattered by an angle θ and its new momentum is given by $h\mathbf{k}'$. This is shown in Figure 3.5 (a). $\mathbf{g}$ is the reciprocal lattice vector, whose value is the reciprocal of d_{hkl} and direction is parallel to the normal of the plane with indices (hkl). By rearranging the vectors $\mathbf{k}$ and $\mathbf{k}'$ tail-to-tail at a point C, as shown in Figure 3.5 (b), the following relation may be obtained.

$$\mathbf{k}' = \mathbf{k} + \mathbf{g} \tag{3.19}$$

By taking the projection of this equation on $\mathbf{g}$ it may be shown to be equivalent

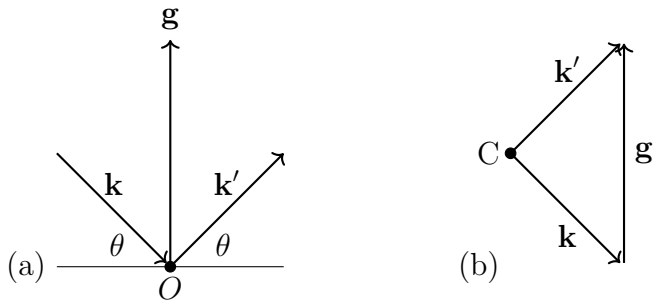

Figure 3.5: *Incident and diffracted wave vectors with reciprocal lattice vector* $\boldsymbol{g}$ *(a) and redrawn vector construction (b).*

to Bragg's Law. This shows that Bragg's Law is satisfied whenever this point C falls on the perpendicular bisector plane of the vector $\mathbf{g}$. The perpendicular bisector plane to the vector $\mathbf{g}$ consists of all points that are at the same distance from the origin of reciprocal space and the reciprocal lattice point hkl. This leads to a simple geometric construction for the direction of a diffracted wave when the incident wave vector and crystal orientation are given. This is known as the Ewald sphere and is shown in Figure 3.6.

It is constructed as follows:

1. Draw the reciprocal lattice with origin O.
2. Draw the incident wave vector $\mathbf{k}$ such that its end point coincides with O, leaving C as the center of a sphere with radius $|\mathbf{k}|$.

Whenever a reciprocal lattice point falls on the sphere, Bragg's Law is satisfied

and the diffracted vector $\mathbf{k}'=\mathbf{k}+\mathbf{g}$ is allowed. Since more than one reciprocal lattice point may lie on the Ewald sphere, a number of crystal planes ($\mathbf{g}$ vectors in reciprocal space) may satisfy Bragg's Law for a given crystal orientation.

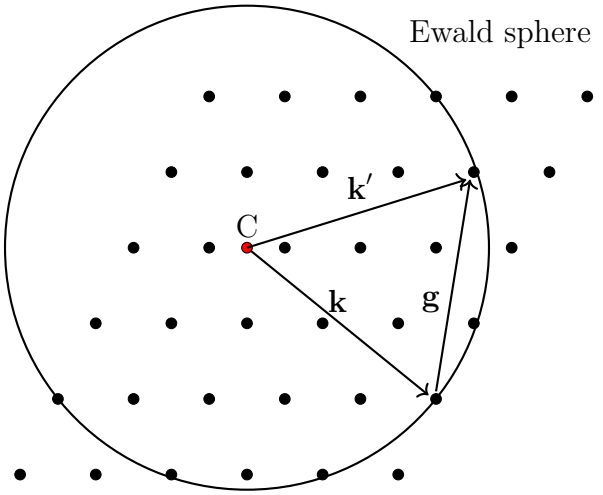

Figure 3.6: *The Ewald sphere. Dots indicate reciprocal lattice points.*

In a TEM, the crystal under investigation is usually in the form of a thin foil normal to the beam direction. This results in an elongation of the reciprocal lattice points normal to the crystal. Since the Ewald sphere is much larger than the reciprocal lattice vectors, the Ewald sphere will intersect a plane section of the reciprocal lattice at numerous points. As a result, Bragg's Law is relaxed and considerably more diffracted beams are generated than would otherwise be expected. This diffracted intensity is projected onto a camera, and a diffraction pattern may be recorded. The distance between the diffraction spots and the transmitted beam on the camera (R) are related to the interplanar spacings, d_{hkl} by the electron wavelength according to the equation

$$\mathrm{R} = \frac{\lambda L}{d_{hkl}} \tag{3.20}$$

where L is the camera length, or distance from the specimen to the screen.

3.2.3 TEM Instrumentation

A TEM typically consists of an electron gun, a complex arrangement of electromagnetic lenses, apertures, a specimen stage, a fluorescent viewing screen and a charge-coupled device (CCD) camera. It may also be equipped with a variety of analytical attachments. The main lenses and apertures are shown in a ray diagram in Figure 3.7.

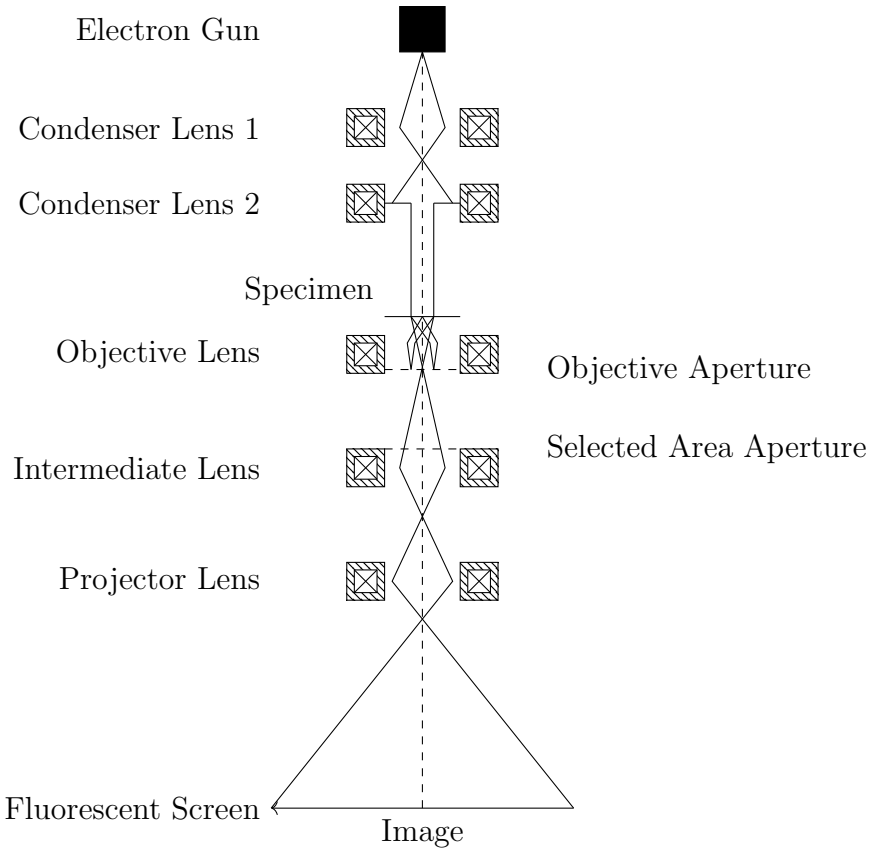

Figure 3.7: *Schematic ray path of a conventional TEM. Adapted from Reimer and Kohl (2005)*[164].

The electron gun is responsible for the emission of electrons, and these are accelerated into the high-vacuum microscope column. This produces a stable electron beam with sufficiently high brightness and good spatial and temporal coherence. These are important factors for producing high quality TEM data. An electron gun may be either thermionic (typically LaB_6 crystals) or a field-emission gun (FEG).

Thermionic sources are heated to sufficiently high temperatures (T) to allow electrons to overcome the work function (Φ) of the material, thus being emitted into the vacuum. The current density (J) of emitted electrons is given by

$$J = AT^2 e^{-\frac{\Phi}{kT}} \tag{3.21}$$

where k is Boltzman's constant and A is Richardson's constant. FEGs employ a very high electric field at the source, which has the effect of lowering the work function barrier, thus allowing electrons to tunnel out at much lower temperatures than thermionic sources. FEG sources generate more monochromatic electrons than their thermionic counterparts as well as a finer probe. These emitted electrons are then accelerated towards an anode by a potential difference, typically between 80 kV and 300 kV in TEMs.

To ensure these emitted electrons travel down the microscope column, the anode contains a central hole through which electrons may pass. A Wehnelt cylinder is attached between the gun and anode, and applies a small negative voltage between it and the accelerating cathode. This aids in the extraction of electrons from the source and is also responsible for the formation of a beam crossover, which is a very fine point in the electron beam.

The condenser lens system, including the apertures, are responsible for manipulating the beam into the desired size, position and convergence angle. These depend upon the magnification required and the mode of operation. The objective lens system, which follows immediately after, is responsible for focusing the beam onto the sample. The beam then interacts with the sample and is projected towards the viewing area (CCD camera or fluorescent screen) by a set of projector lenses to form a magnified image. The magnification in a TEM is determined by the ratio of the distances between the specimen and the objective lens' image plane which may be controlled electronically.

The projection lenses can be adjusted to project the back focal plane of the lens rather than the image plane, which allows diffraction patterns to be observed.

Electromagnetic lenses employ electric and magnetic fields to alter the direction of electrons down the electron column using electromagnetic coils. They consist of

wire coiled around a soft-iron pole piece. Current through these wires magnetizes the pole piece. This magnetic field is inhomogeneous along the length of the lens, but axially symmetric. It is the strength of the field in a magnetic lens that controls the electron trajectories or ray paths. Electrons with charge -e passing through an magnetic field **B** experience a force **F** known as the Lorentz force, which depends on the velocity **v** of the electron. This force is calculated as

$$\mathbf{F} = -\mathrm{e}(\mathbf{v} \times \mathbf{B}) \tag{3.22}$$

As a result, the Lorentz force always acts perpendicular to the direction of travel, causing the electrons to precess about the optic axis as they travel through the lens.

Apertures are often inserted into various lenses. The aperture controls the collection angle (β) of a lens and affects factors such as resolution, depth of field, depth of focus, image contrast, and angular resolution of an electron diffraction pattern. They are typically circular holes in metal disks (referred to as diaphragms) of platinum or molybdenum.

Unlike glass lenses, which may be fabricated to perfection, electromagnetic lenses are very far from perfect. These imperfections limit the achievable resolution of the microscope, but conversely allow for better depth of focus and depth of field to be achieved. The three primary lens defects are astigmatism, chromatic aberration and spherical aberration.

Spherical aberration is a defect which occurs when the lens field behaves differently for off-axial rays. With electromagnetic lenses, the further off axis an electron is, the more strongly it is bent back towards the axis. As a result, a point object is imaged as a disk of finite size, limiting the ability to magnify details in a specimen. This defect may be corrected for in TEMs through the use of a spherical-aberration corrector, which is a complex system of quadrupole and hexa- or octupole lenses[166,167]. The corrector has the effect of creating a diverging lens which spreads out the off axis beams such that they re-converge to a point, rather than a disk, in the Gaussian image plane.

Chromatic aberrations arise from the fact that electron sources are not monochro-

matic (i.e. all electrons having exactly the same wavelength). Instead, the electrons have an energy spread of between 0.3 and 1.2 eV, depending on the source. As a result of their different energies (velocities) they are bent by different amounts in an electromagnetic lens, which once again causes a point object to be imaged as a disk and degrades the image resolution.

Astigmatism occurs when the electrons enter a non-uniform magnetic field as they spiral around the optic axis. This defect arises because it is not possible to produce the soft-iron polepieces with perfect cylindrical symmetry down the entirety of the lens bore. Astigmatism is comparatively easy to correct for, at least when considering chromatic and spherical aberrations. This is done using stigmators, which are small octupoles that introduce a compensating field to balance the inhomogeneities responsible for the initial stigmation.

3.2.4 TEM Sample Holders

For TEM analysis, a specially prepared sample of a standardized size (approximately 3 mm in diameter) is placed on the tip of a sample holder. A standard sample holder is shown in Figure 3.8. The sample holder is then inserted through the specimen stage through a series of airlocks into the TEM. These airlocks ensure minimal fluctuation in vacuum pressure during insertion of the holder. Once inserted, the sample can be manipulated in the electron beam using the specimen holder through mechanisms which allow for the movement of the sample in the horizontal (xy) plane, z-height adjustment, and at least one rotational degree of freedom. This manipulation of the sample position and orientation allows the user to move the sample to a specific site of interest and tilt it to a suitable crystallographic direction (using diffraction mode) for analysis.

One key component of a conventional side-entry holder described here and shown in Figure 3.8 is the O-ring, which assists with the seal of the holder and provides a point of mechanical attachment to the microscope. By having multiple O-rings, the gap between the O-rings can be pumped separately to improve the vacuum in the electron column. A cup at the tip of the holder is responsible for holding the specimen and provides the immediate environment seen by stray electrons and X-rays. As a result, it is typically manufactured using beryllium to minimise the

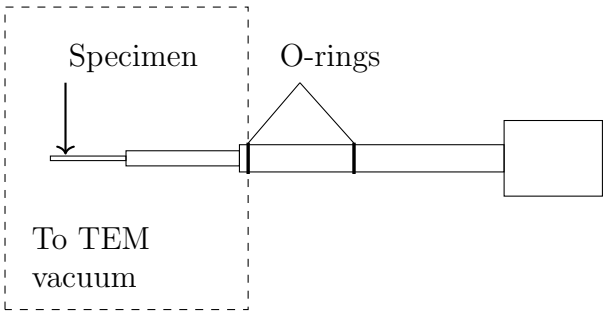

Figure 3.8: *Basic design of side-entry TEM holder. Adapted from Williams and Carter (1996)*[162].

generation of X-rays. Finally, a clamping ring, or screw, holds the specimen in the cup.

3.2.5 Image Formation in a TEM

Before discussing imaging in a TEM, a brief discussion of the two important mechanisms producing image contrast is necessary. Contrast (C) is defined quantitatively as the difference in intensity between two adjacent areas in an image:

$$\mathrm{C} = \frac{I_2 - I_1}{I_1} = \frac{\Delta I}{I} \tag{3.23}$$

where I_1 and I_2 are the intensities in region 1 and 2 respectively. In a TEM image, this contrast results from changes in phase and amplitude of the incident electron wave as it interacts with the specimen. In conventional TEM imaging, amplitude contrast is principally employed, while HRTEM employs phase contrast.

Amplitude contrast is produced as a result of loss of electrons from the incident beam. It comes in two forms *viz.* mass-thickness contrast and diffraction contrast. Mass-thickness contrast arises from a fraction of the imaging electrons not being collected by the lenses/camera as a result of scattering to large angles. As was shown in Equation 3.15, this is affected by the atomic number of the specimen atoms (with heavier atoms scattering more, resulting in a greater loss in intensity) and the thickness of the specimen. In crystalline specimens, Bragg-diffracted beams are able to create diffraction contrast in a TEM image.

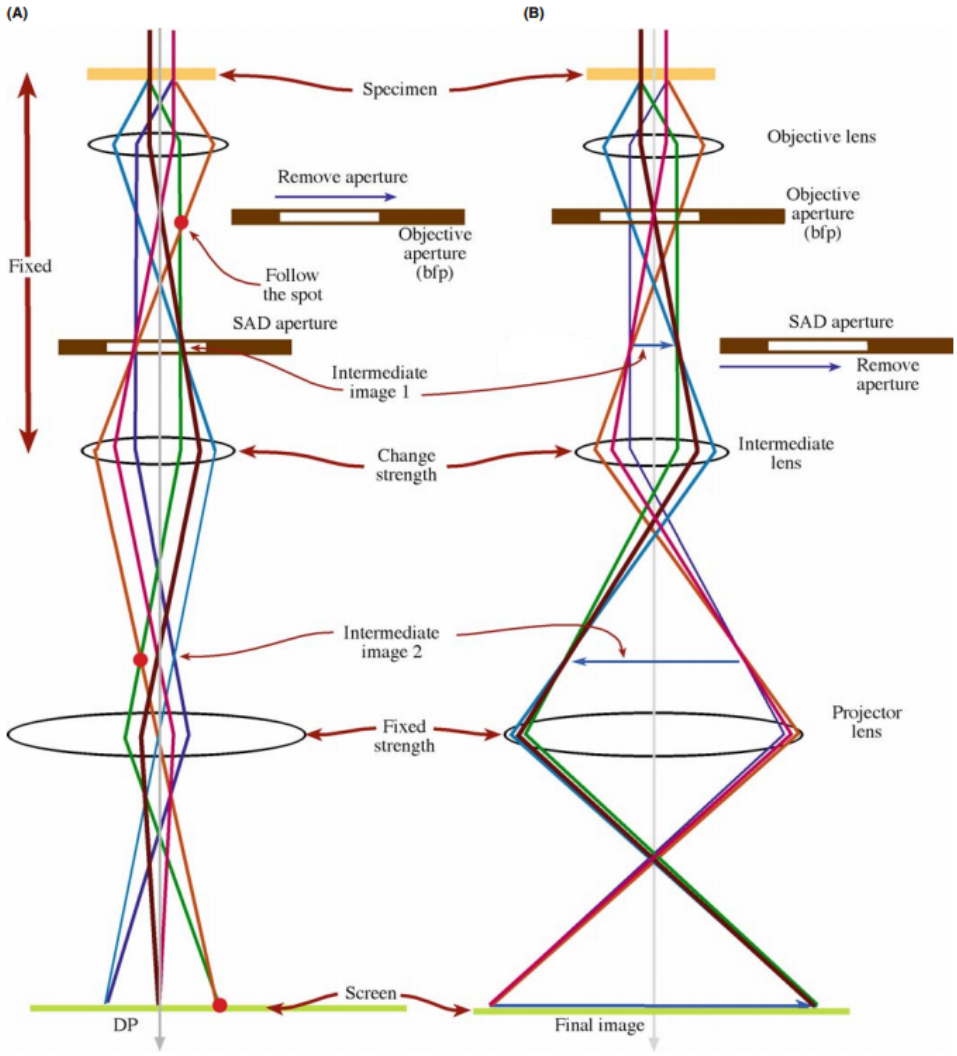

Figure 3.9: *The two basic imaging modes in a TEM. (A) The formation of a diffraction pattern (B) The formation of a magnified image of the specimen. Image taken from Williams and Carter (1996)*[162].

As mentioned, directly transmitted and scattered electrons form the basis of image formation in a TEM. After the illuminating uniform plane wave electron interacts with the specimen, it gets diffracted and transmitted through the specimen. The transmitted wave is focused onto the back-focal plane of the objective lens and a Fourier transformed image of the specimen is produced. This is the diffraction pattern of the specimen. This may be again Fourier transformed to produce a

magnified, inverted image of the specimen at the image plane.

The two basic operations of the TEM imaging system involve the production of a diffraction pattern and a conventional dark-field or bright field TEM image. Simplified schematics of these are shown in Figure 3.9. The basic difference between the two modes is the excitation of the intermediate lens system. To produce a diffraction pattern, the intermediate lens is excited to a strength such that the back-focal plane of the objective lens is chosen as its "object". For conventional TEM image, the "object" of the intermediate lens is the image plane of the objective lens.

When operating in imaging mode, an objective aperture is inserted into the back-focal plane of the objective lens. The size and position of this aperture selects which diffracted beams are used in the subsequent Fourier transform to produce the TEM image. In the case where only the transmitted beam is allowed to pass through, this is a bright-field (BF) image. This is shown in Figure 3.10 (a).

A dark-field (DF) image is produced when the objective aperture is positioned so that only diffracted beams may pass through it. There are two methods for doing this. The first method, shown in Figure 3.10 (b), involves a displacement of the objective aperture off axis, thus blocking the direct beam and allowing a diffracted beam through. In the second method, referred to as centered dark-field, the objective aperture remains centered on the optic axis, but the incident beam is tilted off axis. This is shown in Figure 3.10 (c). In a DF image, regions of the specimen that give rise to the diffraction spots used to generate the image appear bright, while the remaining regions appear dark.

A TEM can also be operated in scanning TEM mode (STEM). In this mode of operation, the electron probe formed is convergent and extremely small. It is then rastered (scanned) across the specimen. As with TEM images, STEM images can also be DF or BF. A BF STEM image is formed by placing a BF electron detector onto the optical axis of the TEM instrument. Any direct electrons and electrons scattered to very small angles will be detected. STEM DF images may be produced by collecting electrons scattered at higher angles. An entire angular range of electrons is collected, hence DF STEM images are called angular dark-field (ADF) images.

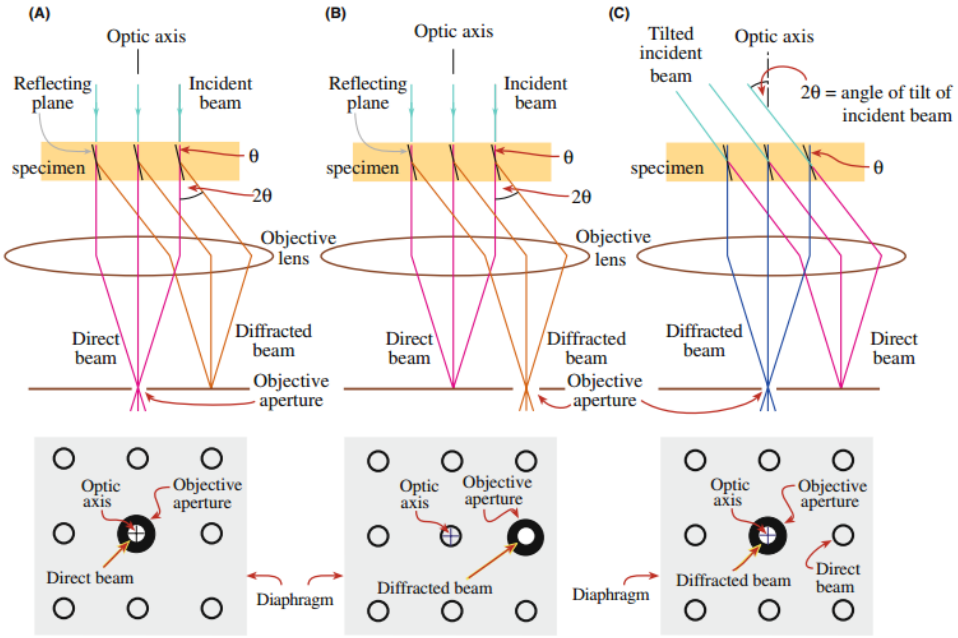

Figure 3.10: *Ray diagrams showing how the objective lens and objective aperture are used in combination to produce a BF image (A), a displaced-aperture DF image (B), and a centered DF image (C). Image taken from Williams and Carter (1996)*[162].

.

A specific form of ADF STEM image, referred to as high-angle annular dark-field (HAADF) STEM imaging is particularly useful. When collecting electrons scattered through angles greater than ≈ 50 mrad, any Bragg effects are avoided. As a result, the contrast observed is purely a result of mass-thickness. Thus, for a uniformly thin sample, the contrast will be almost entirely a result of the square of the atomic number of the scattering atoms. Thus HAADF imaging is often termed Z-contrast imaging. BF, ADF and HAADF STEM detectors are shown in Figure 3.11.

3.3 *In Situ* Gas Flow TEM

In situ gas flow TEM has circumvented the need for high vacuum conditions throughout the column of an electron microscope. It allows materials to be studied under temperature and gaseous conditions more applicable to those experienced

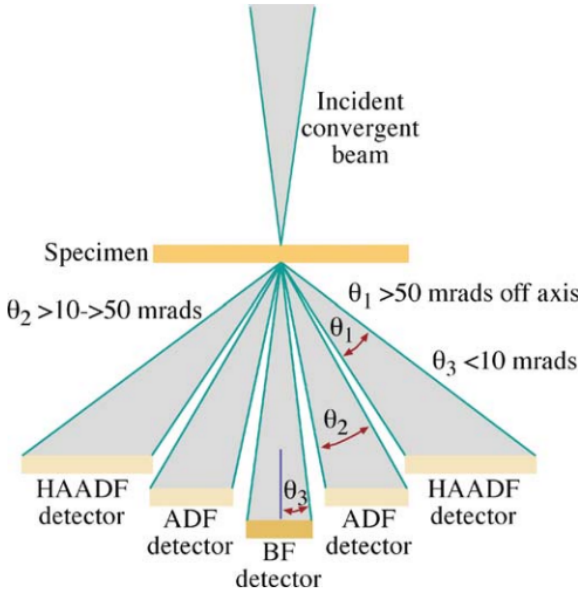

Figure 3.11: *Schematic of the BF, ADF and HAADF detector setups in a TEM operating in STEM mode, together with their typical collection angles. Image taken from Williams and Carter (1996)*[162].

.

in its conventional operating environment. The practical implementation of this takes on one of two forms: a differentially-pumped gas system in the vicinity of the objective lens of a microscope or through the use of windowed gas flow cells.

The presence of gas in a microscope column results in electrons being scattered not only in the eucentric plane, but above and below this plane as well. As a result, the scattering geometry becomes ill-defined in relation to the objective lens and the rest of the imaging lens system. The end result of this complicated system of trajectories is a loss in intensity as electrons scattered above and below the sample are captured by apertures or the column itself[168].

The high current density in the electron beam is able to damage the samples in a number of ways[169–171]. Interaction between the electron beam and the gas molecules present may also lead to ionization of the gas molecules. This changes the normal reactivity of the gas present, thus altering the experimental conditions.

3.3.1 Differentially-Pumped TEM

In a differentially pumped TEM (DP-TEM), also referred to as an environmental-TEM (ETEM), the entire area of the column around the objective lens is filled with a low pressure of gas, typically not more than 30 mbar with the limit dictated by the molecular mass of the gas being used[172,173]. This region is referred to as an environmental cell (E-cell). A schematic of such a column is shown in Figure 3.12.

The experimental gas is leaked into the E-cell, located between the upper and lower objective pole pieces. The flow of gas to the remainder of the column (towards the gun and camera) is heavily restricted by using a set of apertures and differentially pumping the gas leaked through each of these apertures using turbo molecular pumps (TMPs). The E-cell is thus fully incorporated within the microscope column, which allows a regular holder to be used, including those for heating, cooling and tilting of the sample[173].

Since the electrons are scattered by the experimental gas, in addition to scattering by sample, it is critical that the gas path length be as small as possible to minimise the loss in resolution. While reducing the gap between the two apertures will reduce the gas path length, it also restricts the tilting capability of the specimen holders. As a result, a compromise must be made, with ideal values of the gas path length being in the range of 4 to 7 mm[174]. The sizes of the apertures control the leak rate and hence the pressure in the sample area. In order to obtain high gas pressures around the sample, these apertures must be small. However, the lower aperture also eliminates some of the diffraction information as it acts as an objective aperture. The top aperture should be as small as possible to minimise the gas flow to the electron gun, since this is the most critical part of an electron microscope, requiring a high vacuum.

Another advantage for E-cells is that, apart from the gas, there are no physical objects interfering with the electron beam. Therefore, under a sufficiently low pressure, light-element materials may be imaged with excellent resolution and contrast[175].

Disadvantages of such a system include the limited pressure range in which the E-

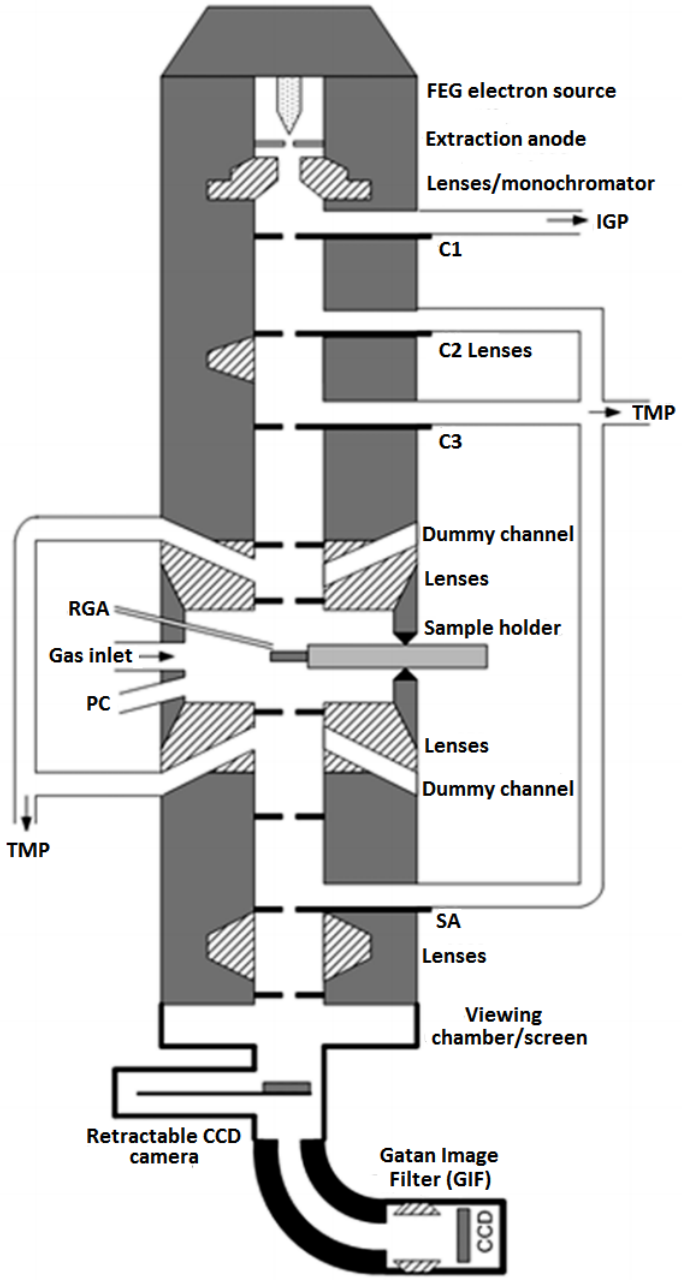

Figure 3.12: *Schematic diagram of a DP-TEM column. FEG: field emission gun; IGP: ion getter pump; TMP: turbo molecular pump; RGA: residual gas analyser; PC: plasma cleaner; C1/C2/C3: first/second/third condenser aperture; SA: selected area aperture. Image from Wagner et al.*[168].

cell may operate. Since the post-specimen (lower) differential pumping apertures eliminate electrons scattered to high angles, any dark-field (DF) micrographs are restricted to collection angles lower than might otherwise be desired. As a result, DF micrographs are subject to a certain amount of diffraction contrast.

3.3.2 Gas Flow Cells

The other approach to *in situ* gas flow TEM involves the use of a windowed gas flow cell. With these gas flow cells, the gas of interest is sandwiched between two silicon chips with electron-transparent silicon nitride membranes, typically 50 nm thick each[176,177]. This confines the gas to a very small region defined by the gap between the two silicon chips. This is generally of the order of 10^2 μm[168]. The high fracture strength of silicon nitride membranes allows them to withstand differential pressures of just over one bar, whilst providing a reasonable size viewing window[178]. The gas flow cell is contained entirely on the sample holder.

As the electrons are scattered off the experimental gas, so too are they scattered by the silicon nitride membranes. This results in a slight degradation of image resolution and detection sensitivity, especially when considering lighter-element materials. It also hinders the ability to perform reliable EDS measurements.

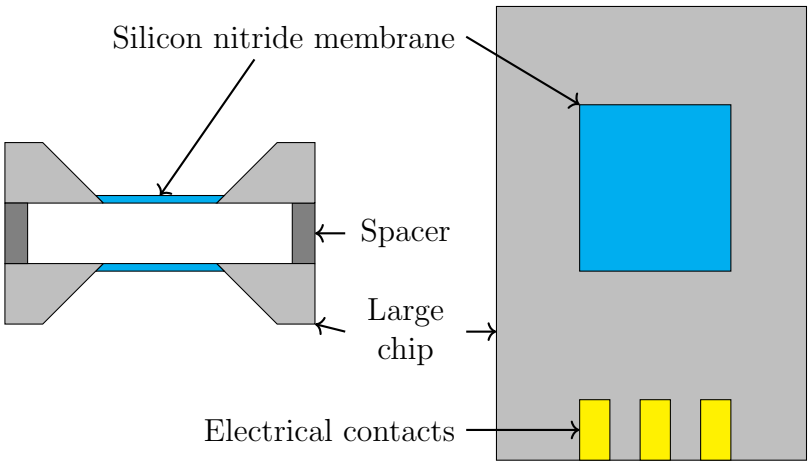

Figure 3.13: *Simplistic side view of a gas flow cell (left), composed of two silicon chips separated by a spacer. A top view (right) of an individual chip, containing electrical contacts and silicon nitride window, is also shown.*

The gas flow cell is a microelectromechanical system (MEMS) consisting of two separate silicon chips, a large chip and a small chip, which are separated by a spacer. The height of this spacer can be selected and defines the height of the flow channel within the gas cell. Both chips contain a thin, electron transparent silicon nitride membrane. The sample of interest is supported on or across one of these silicon nitride membranes. An example of such a chip is shown in Figure 3.13. The experimental gas flows through the channel created by the spacer units. One of the chips, typically the large chip, contains electrical contacts, as well as some form of heating device (not shown) which is connected to these electrical contacts.

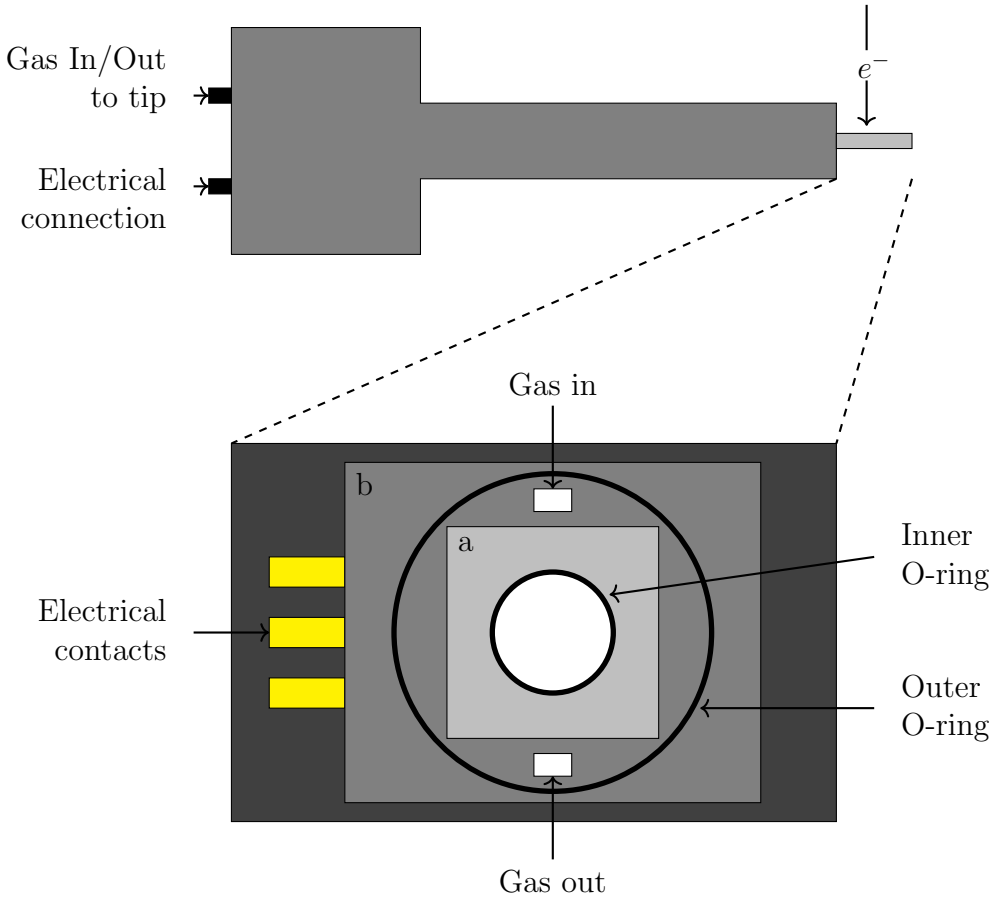

Figure 3.14: *A simplified schematic of the top view tip of a gas flow holder (bottom). The holder is shown in side view (top).*

The TEM holder, custom designed to accommodate the gas cells on the tip, contains a gas inlet and outlet channel through which the experimental gas can flow.

These are connected to gas lines which flow to the tip of the holder. A simplified side view of such a holder is shown in Figure 3.14. The tip of the holder consists of grooves (or indents) that are designed to accommodate the two silicon chips. The central hole through which the electron beam passes is surrounded by an inner O-ring. The small chip is placed on top of this in the groove labeled 'a'. This is in turn surrounded by an outer O-ring. The gas inlet and outlet is contained between these two O-rings. The large chip is then placed on top of the small chip in the groove labeled 'b'. It is placed in such a way that the electrical contacts of the chip line up with the electrical contacts on the tip of the holder. Finally a clamp is used to provide a small amount of pressure, squeezing the two chips together and creating a seal for the cell. Once the gas cell has been assembled, it must be tested for leaks, since these can compromise the integrity of the vacuum within the microscope column[168,176].

Gas lines carrying the experimental gas are connected to the appropriate inlet/outlet valves on the holder. The holder also contains an electrical connection which runs to a computer with control software installed. This supplies current, allowing for heating of the gas cell.

When compared to a DP-TEM, the disadvantages and advantages almost mirror each other. The gas cell, being self-contained, allows *in situ* experiments to be performed in any microscope, provided it can accommodate the custom holder (the need for a custom holder may be seen as a disadvantage). Additionally, imaging of light-element materials is difficult as a result of the silicon nitride membrane. However, the absence of post-specimen apertures allows high-angle scattered electrons to be collected for HAADF-STEM micrographs, which provides excellent contrast in high-Z materials. The gas flow cell also permits the use of gas pressures in excess of 1 atmosphere, orders of magnitude greater than the 30 mbar limit of a DP-TEM.

3.4 Electron Energy-Loss Spectroscopy

Analysis of the energy distribution of electrons after they have interacted with a specimen is known as electron energy-loss spectroscopy (EELS)[162,179–181]. Specif-

ically in a TEM, where electrons are very energetic and the sample is very thin, almost all electrons are transmitted through the specimen. These electrons lose energy as a result of interactions with the specimen.

In a TEM, the beam of incident electrons interact with the atoms of a specimen through electrostatic (Coulomb) forces and are transmitted through it. The transmitted beam is directed into a high-resolution energy loss spectrometer, which separates the electrons according to their kinetic energy. It produces an electron energy-loss spectrum, which shows the number of electrons versus the amount of energy that they have lost through interaction with the specimen. A typical EEL spectrum is shown in Figure 3.15. This example was recorded from a thin specimen of the high temperature superconductor $YBa_2Cu_3O_7$ and it demonstrates some of the key features that are observable in typical EEL spectra. These are discussed in more detail below.

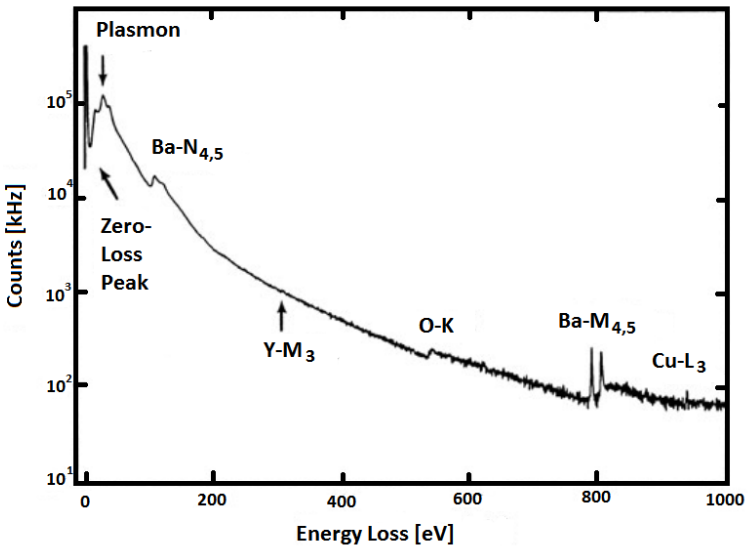

Figure 3.15: *EELS spectrum of $YBa_2Cu_3O_7$ showing key features observable in typical spectra. Image adapted from Egerton (2011)*[179].

The zero-loss peak (ZLP) consists of those electrons that are transmitted through the specimen without any appreciable energy loss. This includes elastically scattered electrons and those which excite phonon modes. Even though these phonon modes do correspond to a slight decrease in energy, the losses are considerably lower than the resolution limit of an EEL spectrometer.

The second series of peaks in an EEL spectrum occurs within several 10s of eV after the ZLP. They arise from inelastic scattering of incident electrons from the outer electron shells of the specimen and are referred to as plasmon peaks. When a high-energy electron passes through a specimen, the nearby atomic electrons are displaced by Coulomb repulsion, forming a region of net positive potential, known as a correlation hole, that trails behind the electron. If the electron velocity exceeds the Fermi velocity, the response of the atomic electrons is oscillatory, resulting in regions of alternating positive and negative space charge along the electron trajectory. The spatial periodicity (λ_w) of this alternating positive and negative charge is given by

$$\lambda_w = v/f_p \tag{3.24}$$

where v is the velocity and f_p is the plasma frequency given by

$$2\pi f_p = \omega_p = \left[\frac{ne^2}{\epsilon_0 m}\right]^{\frac{1}{2}} \tag{3.25}$$

n being the density of the outer-shell and m the electrons relativistic mass. As the electron moves through the specimen, the backward attractive force of the positive correlation hole results in energy loss through the generation of a pseudoparticle, known as a plasmon, with energy E_p.

As the energy loss increases, the total number of electron counts decreases rapidly in a continuous fashion. Superimposed on this continuous decreasing intensity are sharp edges which correspond to inner-shell electron excitations. This sharp edge occurs at the ionization threshold of a particular inner-shell electron, and the associated electron energy loss is approximately the binding energy of this inner-shell electron. Since these binding energies are unique for each element and for each shell, they can be used to identify which elements are present in the specimen. When viewed in high detail, fine structure may be observed in regions surrounding the core-loss edges. They exhibit distinct features that are characteristic of the local environment of the scattering atom.

3.4.1 EELS instrumentation

TEM-EELS instrumentation is based on the magnetic prism in which a uniform magnetic field (B) is generated by an electromagnet with precisely engineered polepieces. A schematic of such a spectrometer is shown in Figure 3.16. When entering this field, electrons follow a circular path (Equation 3.22) with radius R. This radius is equal to

$$R = \frac{m_e B v}{e} \tag{3.26}$$

where v is the speed of the electron, m_e its mass and e the fundamental charge.

Electrons that deviate from the optic axis in a direction perpendicular to the magnetic field experience an increase or decrease in their path length within the field. If the beam of electrons entering the spectrometer originates from a point (O), electrons of a given energy are returned to a single image point (I). Since the electrons all have different energies (as a result of losses), this results in a focused spectrum in a plane passing through this point. In addition, the fringing field at the polepiece edges focuses electrons that deviate in a direction y parallel to the magnetic field (Figure 3.16 (b)). By adjusting the angles of the polepiece edges, the focusing power in these two perpendicular directions can be made equal, producing a spectrum of small width in the direction of the applied magnetic field

The energy loss spectrometer is most commonly located below the viewing chamber of a TEM. By tilting this screen to a vertical position, electrons may enter the spectrometer, where they are dispersed according to their energies. The spectrometer object point (O) is an electron-beam crossover produced just below the bore of the final TEM projector lens. A spectrometer entrance aperture limits the range of entrance angles and ensures adequate energy resolution. Alternatively an EEL spectrometer may be incorporated directly into the TEM imaging column.

Modern EEL spectra may be digitally recorded using a serial-recording system. In this setup, a narrow slit is placed in the spectrum plane (I) and the spectrum is scanned past this slit by varying the strength of B in the magnetic prism. An electron detector behind the slit produces an electrical signal which is directly proportional to the intensity of electrons at each energy loss. The detector typically consists of a scintillator and a photomultiplier tube. This system has a low signal

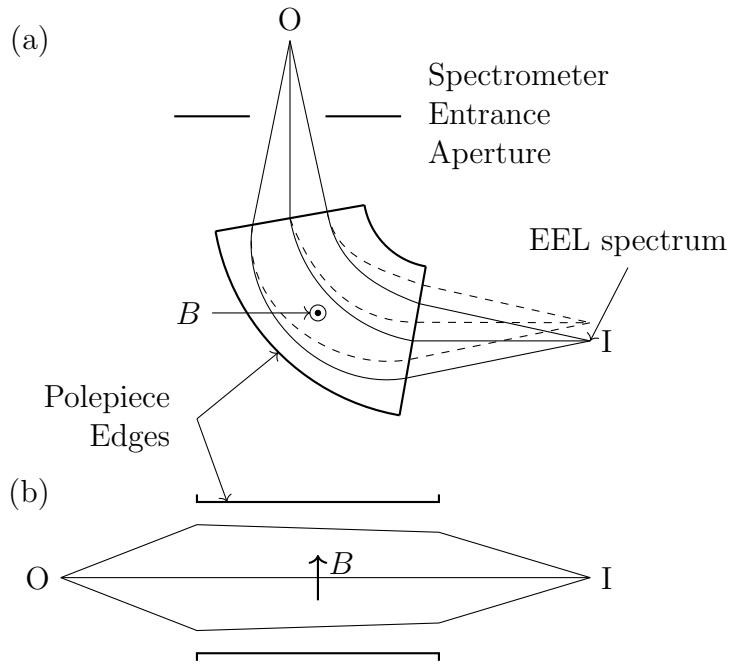

Figure 3.16: *Schematic of an EEL magnetic prism in a plane perpendicular to B (a) and parallel to B (b). It demonstrates the dispersive and focusing properties of the prism. Solid lines are zero-loss electrons, while dashed lines are electrons that have lost some energy during interaction with the specimen. Adapted from Egerton (2009)*[181]*.*

to noise ratio, since many electrons are lost as a result of the slit.

To circumvent this, parallel-recording detectors may be employed. These do not employ a slit, so no electrons are wasted. In this setup, an extended range of the EEL spectrum is projected by an electron lens onto a fluorescent screen coupled to a CCD camera, the output of which is read by a computer.

3.5 Scanning Electron Microscopy

A SEM is an electron microscope that images the surface of a sample through the scanning of a high-energy beam of electrons across the sample surfaces in a raster pattern[165,182–185]. The electrons then interact with the atoms at or near the sample surface to produce secondary electrons, back-scattered electrons (BSE),

characteristic X-rays and light (cathodoluminescence) through a variety of secondary processes. The signals from these types of interactions can then be used to obtain information about the sample's surface topography, composition and various other properties such as electrical conductivity.

In a conventional SEM, shown in Figure 3.17, an electron probe (generated by an electron gun and formed using a condenser lens system) containing electrons accelerated to between 1 and 30 keV is focused by an objective lens onto the surface of a sample and this probe is scanned using a set of scan coils in a raster across the surface. The signal from the sample surface is collected by a detector and displayed in a similar raster on a cathode ray tube (CRT) or frame store. Hence scanning the probe over a smaller region on the sample, while maintaining the same size raster on the CRT, will lead to magnification. However there is a limit to the minimum size of the probe, and hence the achievable resolution for a given probe current.

The signals generated in an SEM all originate from scattering and absorption events that occur in a region of the sample referred to as the interaction volume. The size of the interaction volume depends primarily on the electron beam energy, the atomic number of the sample's constituent atoms and the sample density.

Through elastic scattering interactions of the primary beam with the electrons of the sample, reflected electrons known as backscattered electrons may be produced. The intensity of the backscattered signal is strongly related to the atomic number of the scattering atoms, hence images produced using the backscattered signal reveal contrast based on the chemical composition of the specimen.

Inelastic scattering of the primary electrons is capable of producing secondary electrons. These are relatively low energy and as such, only those generated near the surface of the specimen escape into the vacuum. As a consequence, imaging with secondary electron signals is capable of providing highly detailed scans of the specimen surface topography.

X-rays are also generated from within the interaction volume, and these give information regarding the elemental composition of the specimen. This is discussed in more detail in Chapter 3.6.

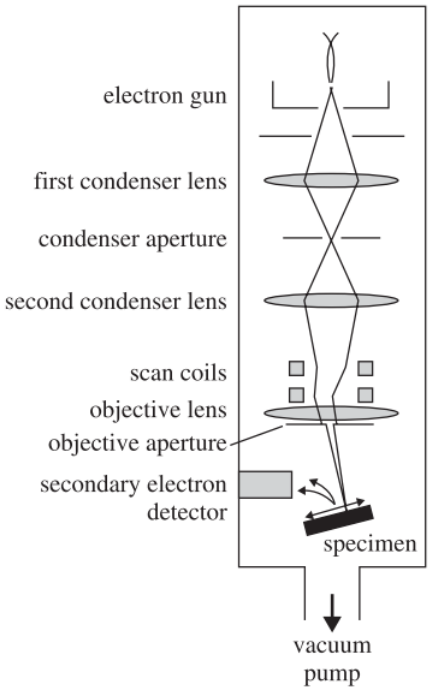

Figure 3.17: *Basic schematic of a conventional SEM. Image taken from Brydson (2011)*[165].

3.6 Energy Dispersive X-ray Spectroscopy

When high energy electrons interact with a specimen, X-rays are emitted from the sample due to interaction of the electrons with the atoms of the specimen. These X-rays are characteristic of the element from which they are released and, when combined with the small probe offered by SEM and STEM instruments, allow elemental distributions within a specimen to be mapped out.

3.6.1 Characteristic X-rays

The energy levels within an atom are arranged in shells labeled K, L, M etc, with the highest binding energy being for an electron in the K-shell and the lowest for an electron in the N-shell. These correspond to the principle atomic quantum number (n = 1,2,3,...) and are shown in Figure 3.18. Each shell (with the exception of K)

may be divided into a number of different sub-shells e.g. L_1, L_2 etc.

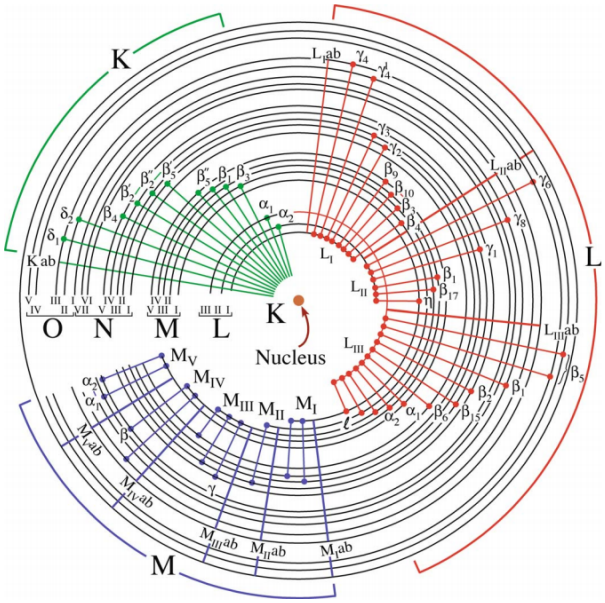

Figure 3.18: *Illustration of the electron orbital shells around a nucleus showing the full range of possible X-ray transitions responsible for K, L and M X-ray generation. Taken from Williams and Carter (1996)*[162]*.*

The characteristic X-rays are produced when incident electrons collide with the inner orbital electrons of a specimen's constituent atoms. If there is sufficient energy transfer to the orbital electron during this collision, it may be ejected from its orbital, leaving a hole. This leaves the atom in an excited state, and an electron from a higher shell will fill this hole, returning the atom to a more energetically stable state and potentially releasing a photon of energy in the process. This photon is the characteristic X-ray. This is demonstrated in Figure 3.19. Alternatively, an Auger electron may be emitted during this process. The probability of X-ray versus Auger emission is described by the fluorescence yield, ω, which is the ratio of X-ray emissions to inner-shell ionizations[162]. The fluorescence yield is a strong function of atomic number, decreasing at a rate proportional to Z^4, where Z is the atomic number. A common expression for ω is:

$$\omega_i = \frac{Z^4}{A_i + Z^4} \tag{3.27}$$

where ω_i is the fluorescence yield of the i$^{\text{th}}$ shell and A_i is a constant for the i$^{\text{th}}$

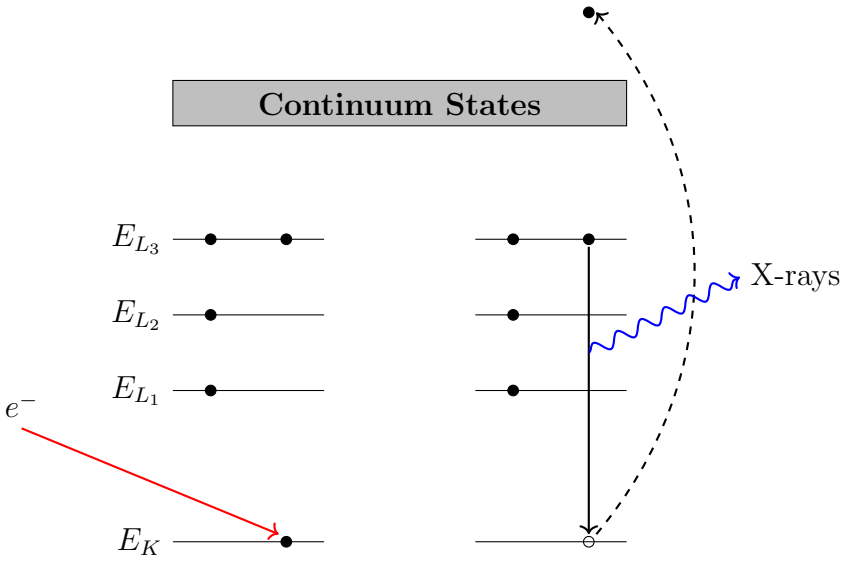

Figure 3.19: *The production of characteristic X-rays by electrons. Adapted from Williams and Carter (1996)*[162].

shell. Thus for low-Z elements, the probability of observing an X-ray is relatively low. As such, EELS (Section 3.4) might be better suited for the analysis of low-Z elements.

The various characteristic X-rays of an element are uniquely described using three symbols. The first is the shell that is filled when an X-ray is produced and is the same as the shell from which an electron was ejected e.g. K, L etc. The second symbol refers to the shell from which the electron which filled the hole originated from. If it originated from the shell immediately above the hole (e.g. a L-electron filling a hole in the K shell) it is termed α, if it is from two shells above, it is termed β etc. Finally, a number after the second term denotes which sub-shell the α, β etc. electron originated from, with 1 corresponding to the outermost subshell (e.g. L_3, M_5 etc.). Thus if a K-shell electron is ejected from an atom, and the resulting hole is filled by an electron from the L_3 subshell, the resulting X-ray is described as a $K_{\alpha 1}$ X-ray.

The energy of this emitted X-ray is equal to the difference in energies of the two subshells and it its associated wavelength is given by Moseley's law:

$$\lambda = B(Z - C)^{-2} \tag{3.28}$$

where Z is the atomic number of the element involved and B and C are constants dependent on the family of electronic transitions (e.g. K_α, L_β,...).

3.6.2 EDS Detectors

An EDS detector consists of three basic components. Firstly, the detector itself (shown in Figure 3.20) is a semiconductor which collects the emitted X-rays. In the intrinsic silicon region, the incoming X-rays generate electron-hole pairs which are separated by an applied bias. The number of electron-hole pairs (and hence the current) produced is directly proportional to the X-ray energies. A positive bias attracts the electrons to the rear ohmic contact and this charge pulse is amplified by a field effect transistor and converted to a voltage.

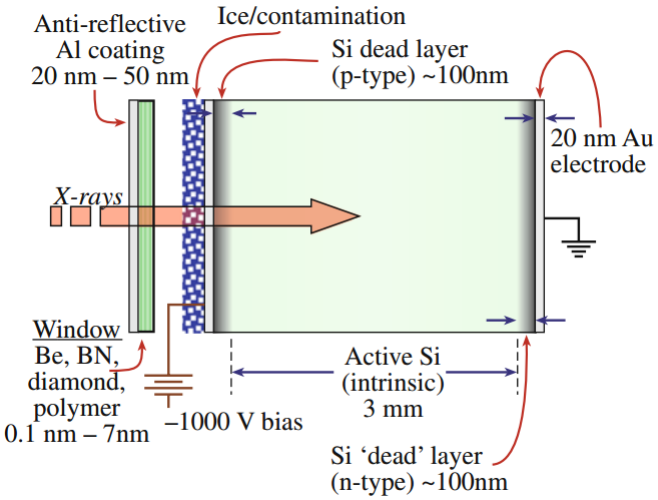

Figure 3.20: *Cross section of a Si(Li) EDS-detector with dimensions indicated. Image taken from Williams and Carter (1996)*[162].

A pulse processor then measures the electronic voltage signals to determine the energy of each X-ray detected. This information is fed into an analyzer which is able to display and interpret the signal.

3.7 X-ray Powder Diffraction

X-ray diffraction (XRD) is an extremely powerful technique for studying crystalline samples and relies on the interaction of X-rays with the electronic structure of the atoms in such samples[159–161]. X-rays are scattered by periodic crystal lattices and reflections are observed when X-rays scattered from different atoms interfere constructively.

X-rays form part of the electromagnetic spectrum and as such have both wave and particle properties. For the purposes of XRD, the wave nature of X-rays is assumed. Depending on the X-ray source, they have wavelengths between 1 Å and 2 Å. This is approximately the spacing between lattice planes in crystals, which makes X-rays perfectly suitable for probing the structure of crystalline materials.

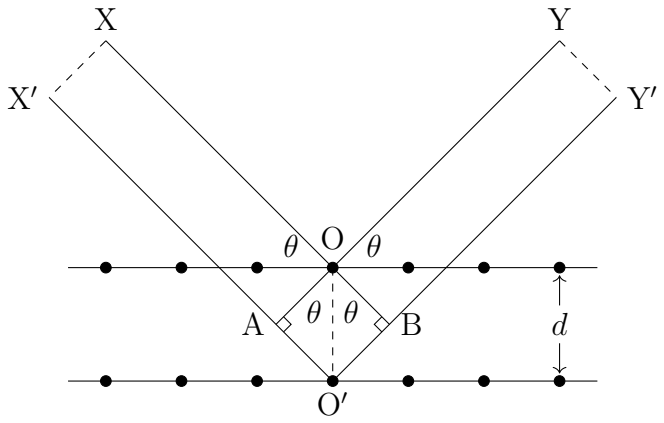

Figure 3.21: *Diffraction of monochromatic, parallel X-rays from two parallel lattice planes of a crystal. Adapted from Cullity (1978)*[161].

The principle of diffraction arises as a result of certain phase relationships between two or more waves. If two waves are in phase, then they add constructively, yielding a total wave with a greater amplitude. Similarly, if two waves are completely out of phase, the two waves will cancel each other, resulting in zero amplitude. Any intermediate differences in phase will produce an amplitude between these two extremes.

Consider a beam of perfectly parallel, monochromatic X-rays of wavelength λ striking a crystal at an angle θ, as in Figure 3.21. The lattice planes shown

are separated by a distance d. Consider the X-ray originating from X which is scattered by the atom at O at an angle θ to point Y. The distance it travels is given by XO+OY. Consider a second X-ray from X′, which is scattered by the atom at O′ (also at an angle θ) to point Y′. The lattice plane containing O′ is the lattice plane below (but parallel) to the plane containing the atom at O. The distance it travels is thus X′O′+O′Y′. By constructing perpendiculars from this X-ray path to the point O, the difference in path length may be given as AO′+O′B. From Figure 3.21 it can be seen that:

$$\mathrm{AO'} = \mathrm{O'B} = d\sin\theta \tag{3.29}$$

For these X-rays to interfere constructively (in phase), the path length difference must be an integer (n) number of wavelengths. This gives rise to the following relation, which is known as Bragg's law.

$$n\lambda = 2d\sin\theta \tag{3.30}$$

From Figure 3.21, two important relationships may be seen. Firstly, the incident beam, the normal to the lattice plane and the diffracted beam are always coplanar. Secondly, the angle between the incident beam and and the diffracted beam is 2θ. This angle is known as the diffraction angle and is measured experimentally.

From Bragg's law, and the fact that $\sin\theta$ cannot exceed 1, the following condition is imposed:

$$\frac{n\lambda}{2d} < 1 \tag{3.31}$$

This leads to the condition that

$$\lambda < 2d \tag{3.32}$$

For most crystal planes, d is 3 Å or less, which means λ cannot exceed 6 Å. It is for this reason that X-rays are suited for the study of crystal structures. Ultraviolet radiation ($\lambda \approx 500$ Å) is too large, while smaller wavelength radiation will result in diffraction angles that are too small to accurately measure.

In a typical X-ray experiment, a powder (consisting of a very large number of crystallites) is placed in the X-ray beam and the angle 2θ between source and detector is varied within a certain 2θ angular range. Owing to the large number

of crystallites in the powder, some will be in an orientation allowing Bragg's law to be satisfied. As a result, reflections from all lattice planes with d-spacings in the range dictated by 2θ will be observed.

3.7.1 X-ray Powder Diffractometer

A spectrometer used to produce X-ray powder patterns is known as a diffractometer. It employs X-rays of known wavelength to determine the lattice spacings of unknown crystals. A typical X-ray powder diffractometer operating in reflection mode is shown in Figure 3.22. It is also possible to operate a powder diffractometer in transmission mode.

It consists of an X-ray source which produces a divergent X-ray beam. The focal point of these X-rays (F) is located at the circumference of a circle (radius R) with center at the center of the sample. This is known as the goniometer. The incident beam passes through several Soller slits (DS) which elimate highly divergent X-rays, causing a minimally divergent beam to strike the sample. Since the sample is irradiated by a divergent beam, it converges (self-focuses) at the receiving slit (RS) of the detector (D), which is also located on the goniometer circumference. The receiving slit is the entrance of the detector. By rotating either (or both) of the X-ray source and the detector around this goniometer, a full range of Bragg angles may be probed, and the detector is able to record the X-ray intensity as a function of 2θ.

X-rays are typically produced by the source using an X-ray tube. High-energy electrons (with energies of several 10s of keV) bombard a metal target, producing X-rays as described in Chapter 3.6.1. This is a very inefficient process, with a large portion of the electron energy simply heating the metal target. This requires the target to be constantly cooled. Since a number of characteristic X-rays are given off by a given metal target, a filter is used to eliminate unwanted X-ray wavlengths, thus producing a monochromatic beam.

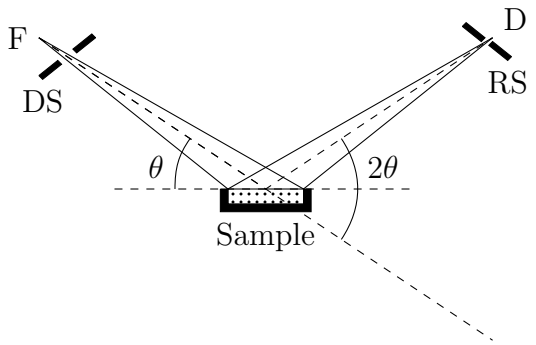

Figure 3.22: *Schematic of a Bragg-Brentano focusing geometry using a flat sample in reflection mode. Adapted from Cullity (1978)*[161].

3.7.2 X-ray Powder Diffractograms

The X-ray powder patterns recorded are unique to a specific crystal structure and are characterised by three main features. These are the shape of the reflection peaks, their intensities and their positions.

In a perfect crystal, using a perfect diffractometer, very sharp Bragg reflection peaks will be observed. However, sample and instrument imperfections cause reflections to broaden. The shape of the reflections are influenced by three different factors:

1. Ω - the instrumental broadening. This depends on the location and geometry of the source, any monochromators, the slits and the sample.
2. Λ - the wavelength (spectral) dispersion. This accounts for the distribution of the wavelengths in the source and varies according to the nature of the source.
3. Ψ - the specimen. This originates from several effects including dynamical scattering of X-rays, crystallite size effects and microstrains in the crystal lattice.

The convolution of these gives the peak-shape function (PSF) which describes the

shape of the reflections:

$$PSF(\theta) = \Omega(\theta) * \Lambda(\theta) * \Psi(\theta) + b(\theta) \tag{3.33}$$

where $b(\theta)$ is the background function which results from non Bragg scattered X-rays and $*$ is the convolution operation. The specimen broadening effects are of particular interest in materials characterisation, since they give insight into the average crystallite size (τ) and microstrain of a lattice plane responsible for a particular Bragg reflection. τ may be calculated using the Scherrer equation:

$$\tau = \frac{k\lambda}{\beta \cos\theta} \tag{3.34}$$

where β is the reflection halfwidth at half maximum intensity after subtraction from broadening that arises from any other effect, θ is the Bragg angle and k a dimensionless shape factor equal to 0.9 for spherical particles.

Numerous factors are responsible for the observed intensity of Bragg reflections. These may be loosely divided into structural factors, which are determined by the crystal structure, specimen factors which arise from particle size and strain, and instrumental factors such as polarization of the X-ray radiation, properties of the detector, and the slit and monochromator geometry. The latter two factors are less critical, with the primary factor affecting peak intensity being the actual crystal structure of the specimen. This intensity, I_{hkl} is related to the structure factor (F_{hkl}, given in Equation 3.16) by:

$$I_{hkl} \propto |F_{hkl}|^2 \tag{3.35}$$

As shown by Equation 3.30, the position of reflections are influenced solely by the X-ray wavelength and the spacing, d, between lattice planes. The spacing between various lattice planes is dependent on the type of unit cell and the value of its lattice parameters (see Equation 3.4 for the calculation for a cubic cell).

However, other factors also affect the peak position. These are known as systematic aberrations and they are usually collectively described using a single parameter $\Delta 2\theta$, so that the observed position, $2\theta_{obs}$, is the sum of the theoretical position ($2\theta_{calc}$) and $\Delta 2\theta$. For the Bragg-Brentano focussing geometry shown above in

Figure 3.22, this correction is described as the sum of six factors:

$$\Delta 2\theta = \frac{p_1}{\tan 2\theta} + \frac{p_2}{\sin 2\theta} + \frac{p_3}{\tan \theta} + p_4 \sin 2\theta + p_5 \cos \theta + p_6 \tag{3.36}$$

where p_1 and p_2 account for the axial divergence of the incident beam, p_3 accounts for the zero-curvature of flat samples, p_4 accounts for the thickness of the sample, p_5 describes the displacement of the specimen from the goniometer axis and p_6 accounts for improper calibration of the zero-angle of the diffractometer.

3.8 Mössbauer Absorption Spectroscopy

Mössbauer spectroscopy (MS) is a nuclear spectroscopic technique which is based on the Mössbauer effect, first observed in 1958 [186]. It involves the recoilless emission and resonant absorption of γ-rays by identical nuclei [187–191]. MS is widely used as an analytical tool in the fields of chemistry, minerology and physics to provide a wide range of information on structural properties, valence state, bonding and site occupancies, magnetic properties, cation distribution and the coordination environment of Mössbauer-active elements [187–190].

3.8.1 The Mössbauer Effect

Radioactive nuclides emit γ-rays when they undergo transitions from excited nuclear states to the ground state during nuclear decay. It is possible for these γ-rays to be absorbed by identical nuclei which then undergo a transition from the ground state to an excited nuclear state [187–191]. This is illustrated in Figure 3.23, where the emitter (red) undergoes a transition from a state of energy E_e to the ground state, E_g. The energy difference between these two states is E_0, referred to as nuclear transition energy.

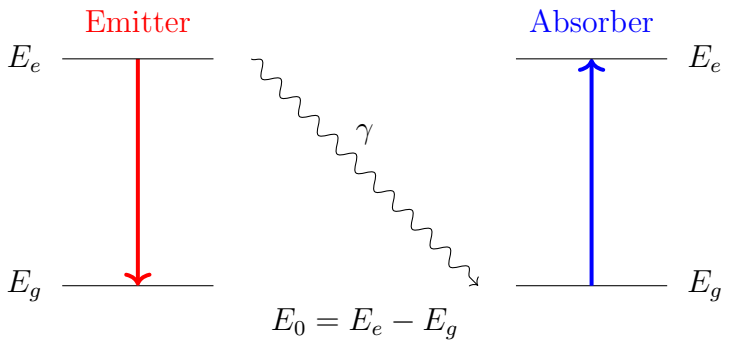

Figure 3.23: *Emitting nucleus decays to the ground state, giving off a γ-photon which is absorbed by an absorber nucleus of the same species.*

During a nuclear transition, γ-rays are emitted which possess a certain momentum, $\vec{p}_\gamma$. Momentum conservation dictates that the emitting nucleus must recoil with the same momentum: $\vec{p}_{nucleus} = -\vec{p}_\gamma$. The kinetic energy of recoil (E_R) is given by Equation 3.37.

$$E_R = \frac{\vec{p}^{\,2}_{nucleus}}{2M_n} = \frac{\vec{p}^{\,2}_\gamma}{2M_n} = \frac{E_\gamma^2}{2M_n c^2} \tag{3.37}$$

where c is the speed of light, M_n is the mass of the nucleus and E_γ is the energy of the emitted γ photon. The energy of the emitted γ-rays is

$$E_\gamma = E_0 \pm E_R \tag{3.38}$$

Hence, as a result of these recoils during nuclear emission (and absorption), this resonance emission/absorption behaviour does not occur for free nuclei, since a portion of incident γ-ray energy is converted to recoil energy, leaving insufficient energy for resonance absorption[192].

However, if a nucleus is bound in a crystal lattice, the recoil energy is negligibly small. If the entire lattice recoils, rather than an individual nucleus, the M_n value in Equation 3.37 gets replaced by the mass of the entire lattice, M. Since $M >> M_n$, it follows that $E_r \approx 0$. This means emission and absorption of the γ-rays may occur with virtually no loss of energy. This is referred to as the Mössbauer effect. The spectroscopic technique based on this effect i.e. Mössbauer spectroscopy, is used to measure very small changes in nuclear energy levels that arise from interactions with the nucleus of interest and its surrounding environment.

3.8.2 Mössbauer Parameters

In most situations, nuclei in the emitter and absorber are not isolated, but exist in different chemical and physical environments, interacting with their nearest neighbours through electro-magnetic interactions. This results in different shifts or splittings of the nuclear energy levels of the emitter and absorber, dependent on the local environment. Information such as the valence state of the atom, coordination environment, symmetry and magnetic field at the Mössbauer nucleus may be determined by measuring these shifts/splittings in the Mössbauer spectra.

There are three principal hyperfine interactions that may be observed during an MS experiment *viz.* the isomer shift (δ), the quadrupole hyperfine splitting (ΔE_Q) and the hyperfine magnetic field (B_{hf}).

The isomer shift is an increase or decrease in the nuclear energy levels of the emitter and absorber. It arises as a result of electric monopole interactions between the surrounding, negatively-charged electrons and the positively-charged nucleus. The different chemical environments of the sample and source result in an absorption at a different energy to the emitted γ-photon. As a result, the centroid of the absorption spectrum shifts from zero velocity, as shown in Figure 3.24 (a). This shift is proportional to the total electronic charge densities of the source and the absorber ($|\psi_s(0)|^2$ and $|\psi_a(0)|^2$ respectively)[190]:

$$\delta = C\left[|\psi_s(0)|^2 - |\psi_a(0)|^2\right]\frac{\Delta R}{R} \tag{3.39}$$

where R is the average radius of the nucleus, ΔR represents the radius difference between the nuclear excited state and the nuclear ground state, and C is a constant.

Any nuclei with a nuclear spin quantum number, I, greater than one half ($I > \frac{1}{2}$) possess nuclear electric quadrupole moments, Q[192–194]. It describes the effective shape of the ellipsoid of nuclear charge distribution. A positive value of Q indicates a prolate distribution, while a negative value indicates an oblate distribution, with reference to the z-axis. The magnitude of Q describes the deviation of the distribution from perfect sphericity.

The nuclear electric quadrupole moment can interact with an electric field gradient

(EFG) at the nucleus (electric-quadrupole interactions). This splits the nuclear energy levels into $\left(I + \frac{1}{2}\right)$ sublevels. In the case of iron, the effect of the electric-quadrupole interaction is to split the excited nuclear level with $I{=}\frac{3}{2}$ into two degenerate substates with magnetic spin quantum numbers $m_I = \pm\frac{3}{2}$ and $m_I = \pm\frac{1}{2}$. The ground state of ^{57}Fe has $I{=}\frac{1}{2}$, thus this energy level is not split. The energy difference, ΔE_Q, is observed in the Mössbauer spectrum (Figure 3.24 (b)) as the separation between two resonance lines. The magnitude of the quadrupole splitting may be expressed as[192,194]

$$\Delta E_Q = \frac{1}{2} e^2 Q V_{zz} \left(1 + \frac{\eta^2}{3}\right)^{\frac{1}{2}} \tag{3.40}$$

where η is the asymmetry parameter and V_{zz} is the principle EFG tensor component. η may be calculated by

$$\eta = \frac{|V_{xx} - V_{yy}|}{V_{zz}} \tag{3.41}$$

where V_{xx} and V_{yy} are the other diagonal components of the EFG tensor. In systems with an axial symmetry, such as tetragonal and trigonal systems, the values of V_{xx} and V_{yy} are equivalent, meaning the asymmetry parameter tends to 0.

The degeneracy of both the $I{=}\frac{3}{2}$ and $I{=}\frac{1}{2}$ nuclear energy levels may be lifted by the Zeeman effect if the nucleus possesses a magnetic dipole moment (true for any nucleus with $I > 0$). The magnetic dipole moment of a nucleus is given by

$$\mu = gI\mu_N \tag{3.42}$$

where μ_N is the nuclear magneton and g is the gyromagnetic ratio[192–194]. The interaction of this nuclear magnetic dipole moment, μ, and the magnetic field, H, at the nucleus leads to a splitting of the nuclear energy levels into $(2I{+}1)$ sublevels. The Hamiltonian of the hyperfine magnetic interaction is given by[188,190]

$$H_m = -\mu H = -g\mu_N I H \tag{3.43}$$

with the energy eigenvalues being calculated as

$$E_n = -\frac{\mu H m_I}{I} = -g\mu_N m_I H \ (m_I = I, (I-1), ..., -(I-1), -I) \tag{3.44}$$

For ^{57}Fe, the $I = \frac{3}{2}$ excited state splits into 4 sublevels (with $m_I = -\frac{3}{2}, -\frac{1}{2}, \frac{1}{2}$ and $\frac{3}{2}$) while the $I = \frac{1}{2}$ ground state splits into 2 sublevels (with $m_I = -\frac{1}{2}$ and $\frac{1}{2}$). This gives rise to 6 transitions, dictated by selection rules ($\Delta I = \pm 1$, $\Delta m_I = 0, \pm 1$), between the ground and excited state of the nucleus. As a result the Mössbauer spectrum contains a sextet of resonance lines, seen in Figure 3.24 (c).

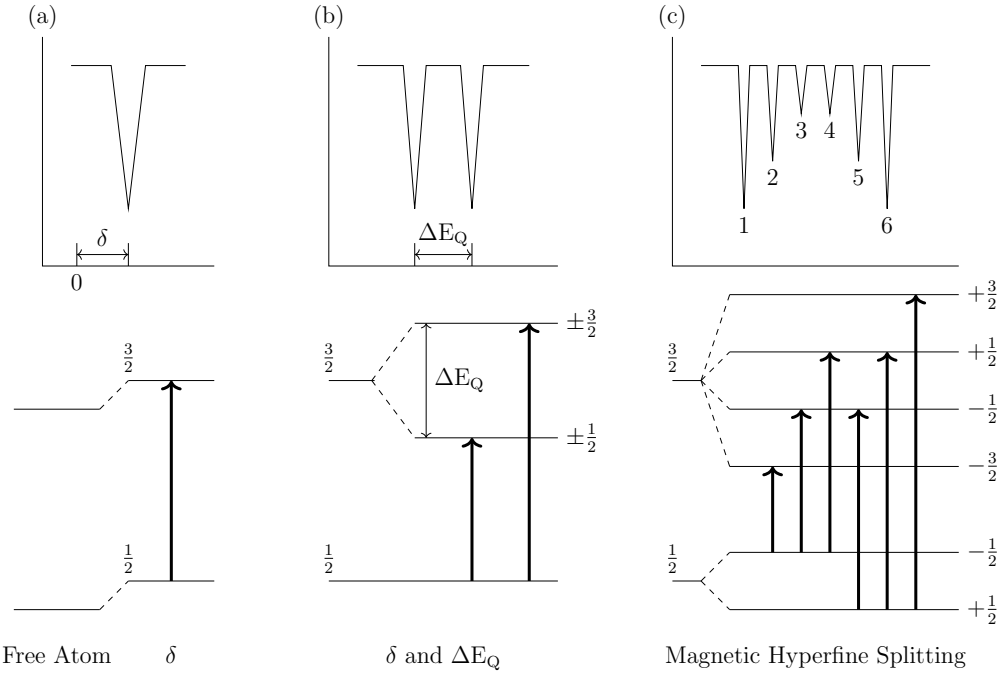

Figure 3.24: *Energy level diagrams for Mössbauer hyperfine interactions (bottom) and change in the Mössbauer spectra (top). (a) Isomer Shift (δ), (b) quadrupole splitting (doublet - ΔE_Q) and (c) magnetic hyperfine splitting (sextet - B_{hf}). Adapted from Darby Dyar et al. 2006*[194].

In this figure, the six resonance lines in the sextet are labeled 1 to 6. The relative intensities of these lines, from 1 to 6, is given by 3:2:1:1:2:3 if the sample is a random powder or unmagnetized foil[190]. Additionally, the overall splitting of the spectrum is proportional to the magnetic field experienced by the nucleus, as well as the moment at the iron site.

This behaviour changes when an external magnetic field is applied. The hyperfine magnetic field determined during MS measurements is the result of a number of contributions:

$$\vec{B}_{\mathrm{hf}} = \vec{B}_c + \vec{B}_{sn} + \vec{B}_{ln} + \vec{B}_{cc} \tag{3.45}$$

where B_c is the Fermi contact term, B_{sn} and B_{ln} are dipole-dipole interactions between the nucleur magnetic moment with the spin and orbital components of the electron magnetic moment respectively, and B_{cc} is the contribution from conduction electrons and is only applicable to metallic systems[195]. The magnetic field (B_{meas}) measured during MS experiments in an applied field (B_{A}) is the vector sum of B_A and B_{hf}:

$$\vec{B}_{\mathrm{meas}} = \vec{B}_{\mathrm{hf}} + \vec{B}_{\mathrm{A}} \tag{3.46}$$

thus the magnitude of the hyperfine field in the presence of a magnetic field reads

$$B_{\mathrm{hf}}^2 = B_{\mathrm{meas}}^2 + B_{\mathrm{A}}^2 - 2B_{\mathrm{meas}}B_{\mathrm{A}}\cos\theta \tag{3.47}$$

The observed MS spectra are significantly altered in an applied field. Diamagnets and paramagnets have no noticable B_{hf} and therefore B_{A} has no significant effect on them. Ferromagnetic (FM), antiferromagnetic (AFM) and ferrimagnetic (FiM) materials are more interesting. The changes in the MS spectra for each of FM, AFM and FiM materials when a magnetic field ($\vec{B}_{\mathrm{A}}$) is applied parallel to the direction of the γ-rays may be summarised as follows[196]:

- FM: $B_{\mathrm{meas}} \approx B_{\mathrm{hf}} - B_{\mathrm{A}}$
  Lines 2 and 5 cancel out

- AFM: $B_{\mathrm{meas}} \approx B_{\mathrm{hf}}$
  Line ratio of 3:4:1:1:4:3

- FiM: $B_{\mathrm{meas}} \approx B_{\mathrm{hf}} + B_{\mathrm{A}}$ (A sites)
  $B_{\mathrm{meas}} \approx B_{\mathrm{hf}} - B_{\mathrm{A}}$ (B sites)
  Lines 2 and 5 cancel out

For FM and FiM materials, any factor (e.g. the presence of defects) that prevents a full alignment of the spins on $\vec{B}_{\mathrm{A}}$ will result in lines 2 and 5 not canceling out

completely.

Apart from changes in the measured magnetic field, MS measurements in an applied field also allow the angle (θ) between the measured field and the gamma rays to be determined[196]. It is related to the relative areas of lines 2 and 5 ($A_{2,5}$) with respect to lines 1 and 6 ($A_{1,6}$) according to the equation

$$\frac{A_{2,5}}{A_{1,6}} = \frac{4}{3}\frac{\sin^2\theta}{(1+\cos^2\theta)} \tag{3.48}$$

These three magnetic hyperfine values, isomer shift, quadrupole splitting and hyperfine magnetic field, can readily be determined from MS spectra through least-squares fitting of a number of Lorentzian profiles, each corresponding to a unique iron site (using iron as an example). The values of these parameters are unique to the particular phase under investigation and comparison with literature values allows for the identification of unknown material.

3.8.3 Mössbauer Measurements

A typical Mössbauer experiment consists of three components: a radioactive source, an absorber and a detector. The source typically consists of a radioactive isotope that decays to an energetic nuclear state of the isotope of interest. The source used for Fe-based MS is the radioactive ^{57}Co, which decays to ^{57}Fe via electron capture (the half-life of this process is 270 days[197]), summarised graphically in Figure 3.25. The 136 keV nuclear level of ^{57}Fe is initially populated, with nuclear spin quantum number $I = \frac{5}{2}$. This excited state decays to a 14.4 keV excited state with $I = \frac{3}{2}$ (85% probability) by emitting a 122 keV γ-photon, or directly to the ground state with $I = \frac{1}{2}$ (15% probability) by emitting a 136 keV photon. The decay between the the first excited state (I=$\frac{3}{2}$) and the ground state (I=$\frac{1}{2}$) occurs through the emission of a 14.4 keV photon with a half life of 100 nanoseconds. Both the half life and the energy of the emitted γ-photon are ideally suited for ^{57}Fe MS.

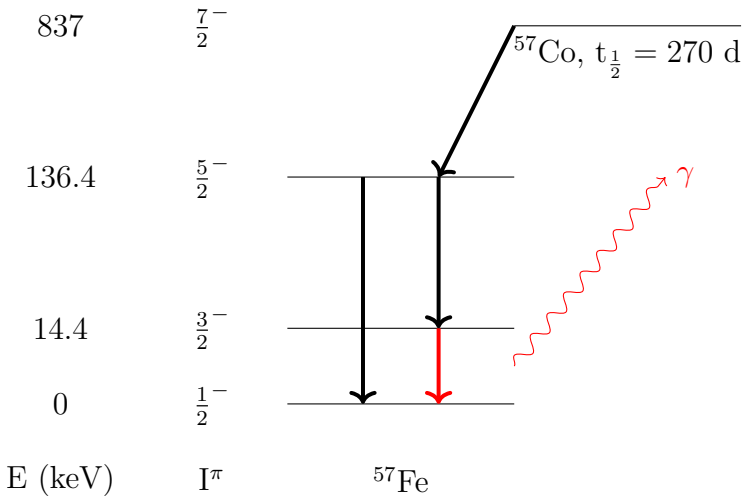

Figure 3.25: *Simplified decay scheme for ^{57}Co to ^{57}Fe, which produces the 14.4 keV γ-photon (red) used in ^{57}Fe MS.*

However, the subtle changes in the nuclear energy levels between the source and absorber requires the energy of the emitted γ-photons be modified. This is achieved by using small Doppler shifts of the source relative to the absorber, allowing all the transition energies, that arise as a result of the hyperfine effects described in Chapter 3.8.2, to be accounted for. This is typically performed by mounting the source on a transducer. By moving the source at a velocity v relative to the source, the energy of the emitted γ-photon is modified to a value E':

$$E' = E_\gamma \left(1 + \frac{v}{c}\right) \tag{3.49}$$

where v is the relative velocity of the source, c is the speed of light and E_γ is the γ-photon energy from the stationery source. The transducer moves the source using a signal supplied by a digital function generator. This is typically a triangular wave-form, which results in a linear Doppler-velocity scale.

The emitted, Doppler-shifted γ-ray photons are collimated in the drive direction to form a beam. The absorber (sample) is placed in this beam, and the γ-ray photons may be either absorbed or transmitted. The transmitted γ-photons are detected using the detector system. This typically consists of a pre-amplifier, an amplifier, a multi-channel analyser for data storage device and a computer for

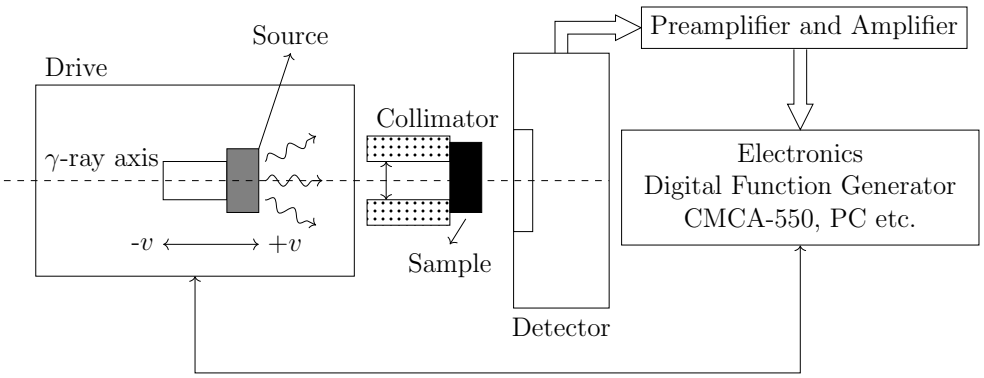

Figure 3.26: *Schematic diagram of a typical transmission Mössbauer spectrometer setup, adapted from Subramanian 2010*[198].

data display. The motion of the transducer is synchronised with the opening of the various channels of the multichannel analyser such that each velocity (γ-photon energy) corresponds to only one channel.

A basic schematic of a Mössbauer spectrometer is shown in Figure 3.26.

3.9 Magnetic Properties Measurements

3.9.1 Fundamentals of Magnetism

Magnetism in materials arises from two sources. The first is the orbital and spin motions of electrons about the nucleus of an atom, while the second is the spin magnetic moments of elementary particles, particularly nuclei. The spin magnetic moments of nuclei are neglible when compared to the electron spin magnetic moments, however they are of importance in nuclear resonance techniques such as nuclear magnetic resonance (NMR) and Mössbauer spectroscopy (MS) [199–202].

The orbital motion of the electron gives rise to the magnetic moment, μ_l

$$\vec{\mu}_l = -\frac{|e|}{2m_e}\hbar\vec{l} = -\mu_B\vec{l} \tag{3.50}$$

where m_e is the electron rest mass, $\hbar$ is the reduced Planck constant, $\vec{l}$ is the orbital

angular momentum of the electron and μ_B is called the Bohr magneton and has a value of

$$\mu_B = \frac{e\hbar}{2m_e} = 9.27 \times 10^{-24}\text{J.T}^{-1} \tag{3.51}$$

The magnitude of the magnetic moment, and its projection along the direction of an applied magnetic field (taken as the z-direction by convention) are given by Equation 3.52 and 3.53 respectively.

$$\mu_l = \mu_B\sqrt{l(l+1)} \tag{3.52}$$

$$\mu_{lz} = -m_l\mu_B \tag{3.53}$$

The situation is different for magnetism arising from the spin angular momentum of an electron. In this case, the associated magnetic moment is

$$\vec{\mu}_s = -g_e\frac{|e|}{2m_e}\hbar\vec{s} = -g_e\mu_B\vec{s} \tag{3.54}$$

where g_e is the spectroscopic splitting factor for a free electron, and is equal to 2.0022907. The component of the magnetic moment in the direction of an applied field is

$$\mu_{sz} = -g_e m_s\mu_B \tag{3.55}$$

When describing the atomic origin of magnetism within a material, both the orbital and spin contributions must be taken into account, as well as any interactions between them. For a given atom with i electrons, the total orbital angular momentum, $\vec{L}$, and the total spin angular momentum, $\vec{S}$, are given by

$$\vec{L} = \sum_{i=1}\vec{l_i} \tag{3.56}$$

$$\vec{S} = \sum_{i=1}\vec{s_i} \tag{3.57}$$

The contribution to $\vec{L}$ of a completely-filled electron shell is 0, hence only partially filled shells contribute to the total orbital momentum. This also applies for the total spin, $\vec{S}$ of an atom, with spin-paired electrons contributing 0 to $\vec{S}$. Coupling of the resultant $\vec{L}$ and $\vec{S}$ through the spin-orbit interaction gives the resultant total

angular momentum $\vec{J}$:

$$\vec{J} = \vec{L} + \vec{S} \tag{3.58}$$

This is referred to as Russel-Saunders coupling or strong coupling, and is generally applicable for lighter atoms and hydrogen-like atoms. For heavier atoms, jj coupling is a better approximation for the total angular momentum. This is given by

$$\vec{J} = \sum_{i=1} \vec{j}_i = \sum_{i=1} \left(\vec{l}_i + \vec{s}_i \right) \tag{3.59}$$

The total dipole moment from such a situation, $\vec{\mu}_{\text{tot}}$, is given by the vector sum of $\vec{\mu}_S$ and $\vec{\mu}_L$. It is not collinear with $\vec{J}$, but is tilted towards the spin (owing to its larger g-factor). $\vec{\mu}_{\text{tot}}$ makes an angle θ with $\vec{J}$, and also precesses around $\vec{J}$. This is a result of $\vec{L}$ and $\vec{S}$ exerting a torque on each other as a result of the spin-orbit interaction. This causes them to precess about $\vec{J}$. The precession frequency is higher than measurement times. This process is illustrated in Figure 3.27.

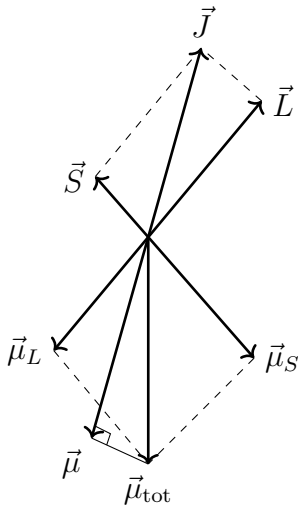

Figure 3.27: *Spin-orbit coupling between $\vec{L}$ and $\vec{S}$, and the relationship between $\vec{J}$ and $\vec{\mu}_{tot}$.*

As a result of this precession, only the component of $\vec{\mu}_{\text{tot}}$ along $\vec{J}$ is observed, since the other components average to zero. The magnetic properties of an atom are thus determined by the quantity $\vec{\mu}$ which may be calculated as follows:

$$\vec{\mu} = \vec{\mu}_{\text{tot}} \cos\theta = -g_J \vec{\mu}_B J \tag{3.60}$$

The factor g_J is known as the Landé spectroscopic g-factor, and is calculated by

$$g_J = 1 + \frac{J(J+1) + S(S+1) - L(L+1)}{2J(J+1)} \tag{3.61}$$

These values may be predicted for a free atom in its ground state by using Hund's rules[201].

3.9.2 Magnetic Ordering

Magnetism is present in all materials and in varying degrees[199–202]. Substances are classified magnetically by their behaviour in an eternally applied magnetic field, $\vec{H}$. When a substance is placed in such a field, a field $\vec{B}$, referred to as magnetic induction, is induced inside the substance. It is given by:

$$\vec{B} = \vec{H} + 4\pi\vec{M} = \mu\vec{H} \tag{3.62}$$

The quantity $\vec{M}$ is known as the magnetisation of the substance, and μ its permeability*. The magnetisation arises as a result of an external magnetic field $\vec{H}$. To a good approximation, $\vec{M}$ is a linear function of $\vec{H}$, with the constant of proportionality being referred to as the magnetic susceptibility, χ:

$$\vec{M} = \chi\vec{H} \tag{3.63}$$

Susceptibility is a parameter that is characteristic of a particular substance and in general it depends on the substance's temperature. Depending on the value of χ, the substance may be divided into one of several groups.

For $\chi < 0$, the substance is termed diamagnetic. These substances are repelled in an applied field $\vec{H}$ and χ is temperature independent. Diamagnetic materials comprise the majority of known substances[200]. It originates from shielding currents induced by an applied magnetic field in fully-filled electron shells. This produces a magnetic field which opposes the applied magnetic field. As a result, it is present in all substances, however the contribution to the net magnetisation is very small such that it is not observed if another form of magnetism is present

*The μ discussed here is different to the magnetic dipole moment, $\vec{\mu}$, discussed above.

in the substance.

For samples with $\chi > 0$, the substance is termed paramagnetic, and the relationship between the susceptibility and the sample temperature, T, is given by Curie's law:

$$\chi = \frac{C}{T} \tag{3.64}$$

where C is known as the Curie constant. These substances all contain unpaired electrons in an electron shell such that the sample has a net magnetic dipole moment $\vec{\mu}$.

In solid, crystalline materials, the fixed arrangement of atoms in space allows for local short-range interactions between neighbouring magnetic dipole moments below certain characteristic temperatures in certain materials. These are termed ferromagnetic (FM), antiferromagnetic (AFM) or ferrimagnetic (FiM), depending on their behaviour below this characteristic temperature. Above this temperature, they all exhibit paramagnetic behaviour.

In FM substances, the magnetic moments tend to strongly align along the direction of the applied magnetic field, as with paramagnetic materials. They continue to remain aligned when this applied field is removed, unlike paramagnets which orient themselves randomly as a result of thermal fluctuations. The characteristic temperature below which a material enters a FM state is known as the Curie temperature (T_C).

AFM substances may be most easily visualized as containing two separate sublattices (A and B). In the magnetically ordered AFM state, which arises below the Néel temperature, T_N, the atomic magnetic moments are ordered in an FM state within A and B. However, the magnetic moments of A are alligned antiparallel with those in B. Since the magnetic moments in each sublattice are equal, the net magnetic moment of the substance is zero, at least at zero Kelvin. At higher temperatures, there is a small net magnetisation in an applied magnetic field.

FiM substances are similar to AFM substances. The only distinction is that the magnetic moments of the sub-lattices are unequal. The characteristic temperature at which a substance goes from a paramagnetic state to a FiM state is also referred to as the Curie temperature.

The Curie-Weiss law describes the temperature behaviour of χ above T_C or T_N and is given by

$$\chi = \frac{C}{T - \theta_P} \tag{3.65}$$

where θ_p is the paramagnetic Curie temperature. Negative values of θ_p are observed in AFM systems, while positive values of θ_P are indicative of FM or FiM systems. θ_p may be determined experimentally by plotting χ^{-1} versus T. At high temperatures, this plot will be linear. Extrapolation of this linear region to the T-axis allows θ_p (the intercept) to be read off directly. The value of C may also be used to determine the magnetic moment per molecule (μ_{eff}) in a material. These two quantities are related by[203]

$$C = \frac{N_A \mu_{eff}^2}{3Ak_B} \tag{3.66}$$

where N_A is Avogadro's number, k_B is Boltzman's constant, A is the molar mass of the material and C has been determined from mass susceptibility data. This allows μ_{eff} to be calculated by

$$\mu_{eff} = \sqrt{\frac{3Ak_BC}{N_A}} \tag{3.67}$$

Both diamagnetism and paramagnetism are referred to as linear magnetism, since the susceptibility varies linearly with respect to an applied field, while ferromagnetism, ferrimagnetism and antiferromagnetism are reffered to as non-linear or collective magnetism.

An additional magnetic phenomenon that is exhibited only by systems of nanoparticles is superparamagnetic (SPM) behaviour. They exhibit collective magnetism (FM, AFM or FiM) below the characteristic T_C or T_N, but above an additional critical temperature known as the blocking temperature, T_B. It is cause by thermal energy (k_BT) which is sufficient to destroy the collective ordering of an assembly of FM, FiM or AFM nanoparticles and induces a spontaneous reversal of the direction of magnetisation when the crystallite size is small enough. The threshold diameter for this effect is between the range of 10 - 30 nm for the iron oxides[5].

The dynamic response of an assembly of nanoparticles depends on the measuring

time (τ_m) of the experimental technique used. As the reversion of the magnetic moment in a single-domain particle over the anisotropy energy barrier $E_a = KV$ is assisted by thermal phonons, the relaxation time for the single-domain particles exhibits an exponential dependence on temperature characterized by the Néel-Brown equation[204]:

$$\tau = \tau_0 \exp \frac{KV}{k_B \mathrm{T}} \tag{3.68}$$

K is the anisotropy constant, V the volume of the magnetic domain (nanoparticle), T the absolute temperature, k_B is Boltzman's constant and τ_0 is an attempt time, typically in the range 10^{-12} to 10^{-9} seconds. By considering $\tau_0 \approx 10^{-9}$ s and $\tau_m \approx$ 100 s (typical of magnetometry measurements), Equation 3.68 may be rearranged to yield:

$$k_B \mathrm{T} = 25\mathrm{KV} \tag{3.69}$$

3.9.3 Magnetic Measurement Techniques

The magnetisation of a material in a magnetic field may be measured using a number of different techniques[203]. These include a fluxmeter, based on the flux change when a sample is extracted from within a coil. A vibrating sample magnetometer (VSM) is based on the flux change in a coil when the magnetised sample is vibrated near it. An alternative field gradient magnetometer (AFGM) works similar to a VSM, but affixes the sample to a fibre. By matching the frequency of vibration to the resonance frequency of the fibre, the vibration amplitude may be increased by the quality factor of the vibrating system. A superconducting quantum interference device (SQUID) (as used in this study) may also be used as a magnetometer and is discussed below.

A SQUID is based on the tunneling of superconducting electrons across a very narrow insulating gap, called a Josephson junction, between two superconductors. A basic schematic of such a device is shown in Figure 3.28. A superconducting measuring current flows into the ring at A and divides so that an equal current passes through the Josephson junctions on either end of the ring, and recombines at B where it exits the ring. A changing magnetic flux through the ring induces a voltage and a current in the ring. This induced current adds to the measuring current in one junction, and subtracts in the other. The wave nature of the

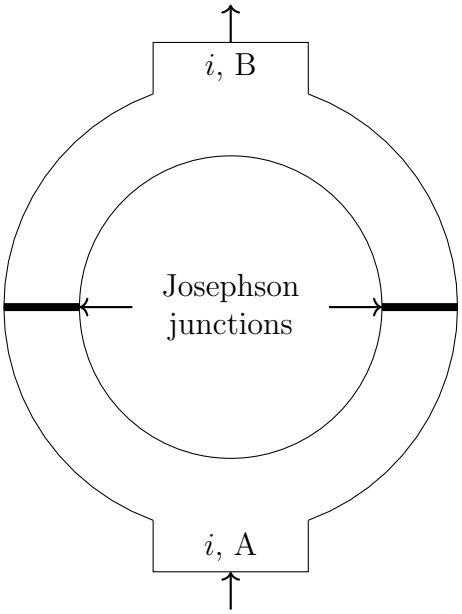

Figure 3.28: *SQUID flux sensor, adapted from Cullity and Graham*[203].

superconducting current results in a periodic appearance of resistance in the superconducting circuit and the creation of a potential difference between points A and B. Each voltage step corresponds to the passage of a single flux quantum across the boundary of the ring. The SQUID is most commonly linked to a coil to measure the flux from a small sample, and thus the sample magnetization.

The Josephson junctions require low temperatures to operate, therefore they are often used in conjunction with a superconducting solenoid. The magnetic field produced by the superconducting magnet is held exactly constant by a superconducting shield, and the sensitivity of a SQUID magnetometer can be as low as 10^{-8} emu[203].

3.10 Physisorption

The term physisorption (physical adsorption) refers to the phenomenon of gas molecules adhering to a surface at a pressure less than the vapour pressure[205,206]. The attraction forces between adsorbent molecules and the surface are relatively weak. By measuring the amount of adsorbed gas as a function of pressure, prop-

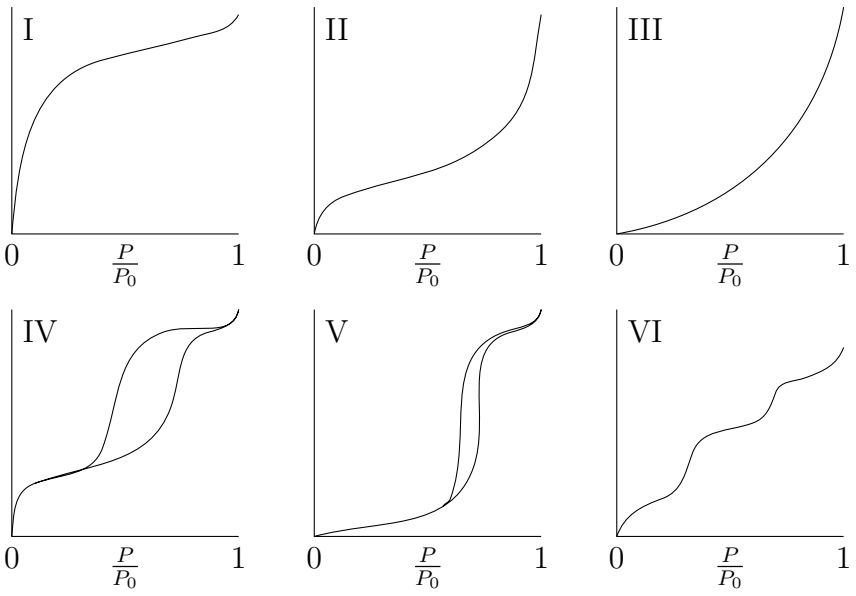

Figure 3.29: *The six different gas adsorption isotherms obtained from physisorption measurements, adapted from Condon*[205].

erties of the adsorbent material such as surface area and porosity may readily be measured.

3.10.1 Theory of Physisorption

The adsorbent provides a net attraction for the adsorbate molecules. The attraction is generally delocalised across the surface. As such, the adsorbed molecules are able to move freely over the surface of the adsorbent. For most adsorption models, the adsorbate is believed to behave similar to a liquid, where adsorbate molecules can roll over one another and an adsorptive molecule can adsorb upon another adsorbate molecule.

Most physisorption experiments keep the temperature below the triple point of the gas being used, but above its freezing point. The primary measurement performed during such an experiment is that of the adsorption isotherm, which is the amount of gas adsorbed versus the pressure, while keeping the temperature constant. The pressure is typically expressed as a ratio of the adsorptive pressure, P, to the saturated vapour pressure of the bulk liquid, P_0.

The shape of measured isotherms already reveals a great deal about the sample. The general shape of an isotherm may be classified into one of six different types. These are shown in Figure 3.29. A type I isotherm is characteristic of either a chemisorption process or physisorption on an absorbent that has extremely small pores, called micropores[†]. Samples with isotherms of type II or type III are characteristic of a non-porous (or macroporous) material with a high energy of adsorption (II) and a low energy of adsorption (III). Type VI and V isotherms are characteristic of mesoporous materials with high (IV) and low (V) energies of adsorption. This hysteresis effect in the adsorption isotherm is characteristic of mesoporous materials. Finally, type VI isotherms arise from a number of different scenarios, including multiple pore sizes, steps on the adsorbate surface, multiple energies of adsorption and that the adsorbed gas behaves more like a solid (rather than a liquid).

The determination of a material's surface area is simple in theory. If the molar amount of gas adsorbed, n_m is known, and monolayer coverage of the surface by the gas is assumed, then the surface area, A, may be determined by

$$A = n_m N_A a \tag{3.70}$$

where N_A is Avogadro's number and a is the molecular cross section of the adsorbed gas. The difficulty arises in determining when monolayer coverage is achieved (ie what the value of n_m is) and what the value of a is for a particular gas. The mostly popular theory for the determination of n_m is that developed by Brunauer, Emmett and Teller, commonly referred to as the BET theory[208]. It assumes that the adsorbate molecules settle on two types of sites: the surface atoms of the material, or on top of another adsorbed gas molecule. The spaces between these sites are the same as those in the close packing of the adsorbent molecules, thus a is determined from the solid phase spacing of the adsorbate gas. The BET equation, in its most common form, is

$$\frac{P}{n_{ad}(P_0 - P)} = \frac{1}{n_m C} + \frac{C-1}{n_m C}\frac{P}{P_0} \tag{3.71}$$

[†]Pores are classified as being micro- meso- or macropores according to IUPAC definitions. Pores with diameter, d, below 2 nm are micropores, between 2 nm and 50 nm are mesopores, while any pores greater than 50 nm in diameter are clasified as macropores[207].

where $n_a d$ is the amount of adsorbate and C the BET constant. By plotting the quantity on the left of this equation versus P/P_0, the result should be linear and allows for the calculation of n_m. The plot is typically performed in the P/P_0 range of 0.05-0.35, although this does depend on the adsorbate-adsorbent system.

The total pore volume, V_p, is often derived from the amount of vapour adsorbed at a relative pressure close to unity by assuming that the pores are then filled with condensed adsorptive in the normal liquid state. If the solid contains no macropores, the isotherm remains nearly horizontal over a range of P/P_0 approaching unity and the total pore volume is well-defined. In the presence of macropores the isotherm rises rapidly near $P/P_0 = 1$. The limiting adsorption at the top of the steep rise can be identified reliably with the total pore volume only if the temperature on the sample is very carefully controlled and there are no cold areas on the apparatus[205–207].

Not only is it possible to determine the total pore volume of a material, but it is also possible to determine the mean pore diameter, as well as the volume associated with a distribution of pore diameters. The calculations are presented elsewhere[205,206,209].

3.10.2 Physisorption Instrumentation

Two principle techniques are used to determine the amount of gas adsorbed *viz.* a volumetric and a gravimetric method. The gravimetric method is simple, but requires very expensive, high precision balances which limit its use. The volumetric technique is far simpler, and a basic schematic is shown in Figure 3.30.

Using this volumetric technique, a known quantity of pure gas is usually admitted to a tube containing the adsorbent sample. This entire system is maintained at a constant temperature, often by immersion in a liquid bath. As adsorption takes place, the pressure in the confined volume falls until an equilibrium is reached. The amount of gas adsorbed at the equilibrium pressure is given as the difference between the amount of gas admitted and the amount of gas required to fill the space around the adsorbent. This space is known as the dead space, V_d, and is typically measured prior to the experiment beginning. The adsorption isotherm is

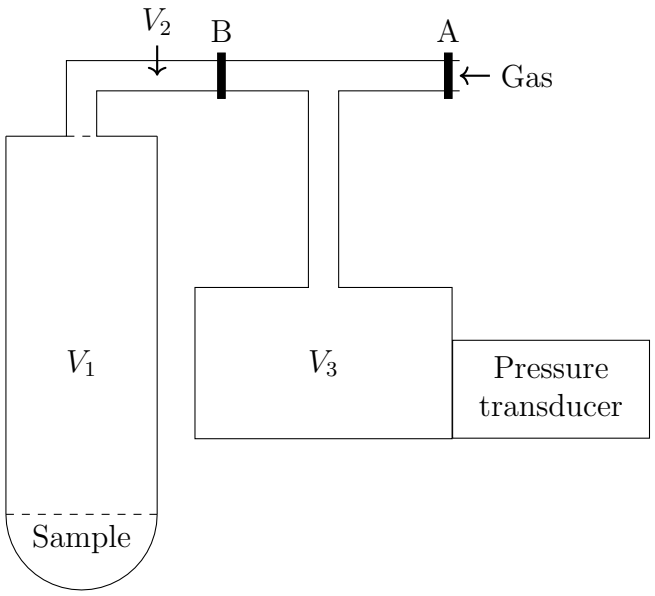

Figure 3.30: *Basic schematic of a volumetric physisorption instrument, adapted from Condon*[205].

usually constructed point-by-point by the admission to the adsorbent of successive charges of gas with the aid of a volumetric dosing technique and application of the gas laws. The pressure is usually measured with a Bourdon (or similar) pressure transducer[205–207].

When introducing the gas, three volumes, labeled V_1, V_2 and V_3 in Figure 3.30 must be considered. V_2 and V_3 are collectively referred to as the manifold, and V_3 is precalibrated, and known for the instrument. The volume V_1 and V_2 are unknown, and the dead space mentioned above is an average of these two volumes, weighted by their inverse temperatures. For an individual dosing step, gas is introduced at valve A, while leaving valve B closed, and the pressure, P_i, measured. Valve A is closed and valve B opened. Once equilibrium has been reached, the pressure, P_f, is measured. The total amount of gas adsorbed is then determined by

$$n_{ad} = \frac{P_i V_1 - P_f \left(V_d + V_1\right)}{RT} \tag{3.72}$$

This process is typically repeated over the full range of P/P_0 from 0 to 1. The incremental amount of gas adsorbed during each dosing step is added to that of previous steps to determine the total volume adsorbed.

3.11 Raman Spectroscopy

Raman spectroscopy is a fundamental molecular spectroscopy based on the inelastic scattering of laser light. It is used to probe the structure and properties of molecules using transitions between their various vibrational modes[210–213]. A Raman spectrum can be analyzed in terms of the molecular components or functional groups present in a molecule, providing a unique "fingerprint".

3.11.1 The Raman Effect

Raman scattering is a two-photon event and was first reported by Raman and Krishnan[214]. The interaction of the polarizability of the molecule being investigated with incoming radiation (light) creates an induced dipole moment in the molecule, and the photon promotes the molecule to a virtual energy state. On returning to the ground state, radiation that is emitted by this induced dipole contains the Raman scattered photons. The scattered radiation consists of two parts: Rayleigh scattered radiation and Raman scattered radiation.

Assuming a simple diatomic molecule, the binding effect of the electronic charge distribution is approximated by a spring between pointlike nuclei[213]. If the excitation is a vibration, then the dynamical variable is the vibrational displacement q. Expanding the polarizability of the molecule, α, as a Taylor series yields:

$$\alpha = \alpha_0 + \left(\frac{\partial \alpha}{\partial q_k}\right)_0 q_k + \left(\frac{\partial^2 \alpha}{\partial q_k^2}\right) \frac{q_k^2}{2} + ... \tag{3.73}$$

Here, q_k is the displacement of the kth normal coordinate. If the molecule is oscillating with a frequency ω_m and the incoming monochromatic electromagnetic wave is oscillating as $E = E_0 \cos(\omega t)$, then the induced dipole moment, P, may be written as

$$P = \alpha_0 E_0 \cos(\omega t) + \left(\frac{\partial \alpha}{\partial q_k}\right)_0 E_0 q_k^0 \frac{1}{2}[\cos(\omega + \omega_m)t + \cos(\omega - \omega_m)t] \tag{3.74}$$

The first term in Equation 3.74 describes the Rayleigh scattering, while the second and third terms correspond to frequency (energy) shifted light, referred to as anti-

Stokes and Stokes-Raman scattering. These scattering events are simplified in Figure 3.31. An incoming photon, of energy $\hbar\omega$, excites a molecule from any of the vibrational ground states to a higher energy, virtual excited state. The molecule returns to a vibrational level in the ground state, emitting a photon in this process. If the energy of the emitted photon is the same as the incoming photons, this is Rayleigh (elastic) scattering. If the molecule returns to a higher energy vibrational ground state, the emitted photon has lower energy (frequency) and is termed Stokes-Raman scattering. For molecules returning to a lower vibrational energy state, the emitted photon has a higher energy than the incident photons, and is termed anti-Stokes scattered. This change in energy, ΔE, is related to the frequency of the characteristic vibrational modes of a molecule by $\Delta E = \hbar\omega_m$.

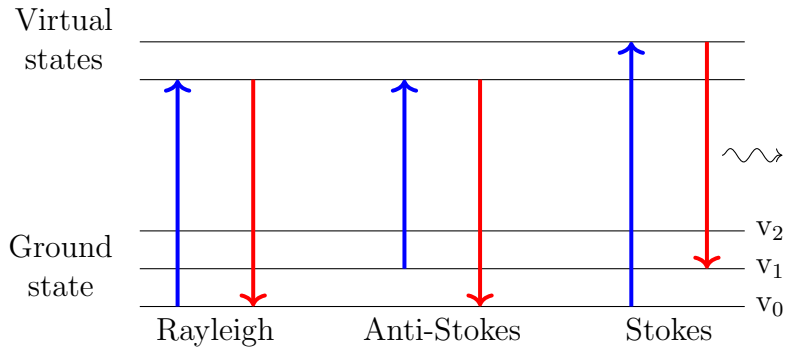

Figure 3.31: *Energy level diagram showing the origin of Rayleigh (left), Stokes-Raman (right) and Anti-Stokes Raman scattering (middle).*

It is the measurements of these frequency shifts that constitutes Raman spectroscopy. The challenge in the collection of Raman spectra is to collect the Raman-scattered radiation without including the Rayleigh scattered radiation, which is significantly more intense.

3.11.2 Raman Instrumentation

A typical Raman instrument is shown in Figure 3.32. The Raman scattering is excited by a laser source. By combining the Raman instrument with an optical microscope, the laser source can be focused to a spot in the micron range. This allows it to provide molecular information at a very high spatial resolution. The laser

photons impinge on the sample and the scattered light is collected with a low f-number lens and focused onto the entrance slit of a single-grating spectrometer[211]. Prior to entry into the spectrograph, the radiation passes through a Rayleigh filter to eliminate all Rayleigh-scattered light. The signal is detected using a Si-based CCD detector.

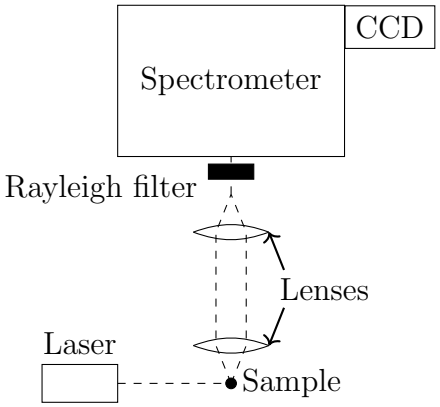

Figure 3.32: *Basic schematic of a Raman spectrometer, adapted from Vij*[211].

3.12 Thermal Gravimetric Analysis

Thermal gravimetric analysis (TGA) is a technique in which the mass of a sample is measured against time (or temperature) while the temperature of the sample, in a controlled atmosphere, is programmed[215]. By following all the effects of heat on the changing mass of the sample, it is possible to obtain information on the various stages of analysis and the temperatures required to bring about their completion. The ability of TGA to characterise, both quantitatively and qualitatively, a huge variety of materials over a considerable temperature range sees it being widely used in basic research and other applications by scientists and engineers across multiple disciplines[216–219].

It is not possible to detect thermal events that are not responsible for a mass change within the sample, such as melting, crystallization and glass transitions in polymer materials. This information must be obtained using alternative thermal analysis techniques, such as differential scanning calorimetry (DSC).

In the field of catalysis, TGA is particularly useful for studying catalyst precursor transformations, dehydration/dehydroxylation reactions, determination of the porous structure of catalysts by adsorption measurements and studies of the adsorption/desorption properties of gases frequently used in heterogeneous catalytic processes.

Bulk- and supported-metal oxide catalysts usually contain variable amounts of water. Quantitative determination of the water content using TGA is critical, since several surface characteristics of the catalysts depend largely on the population of molecular water and hydroxyl groups retained by the oxides[218].

3.12.1 TGA Instrumentation

A TGA apparatus is essentially a thermobalance, which consists of an electronic microbalance, a furnace, a temperature programmer, an atmospheric controller and a recording instrument, such as a PC[217]. A basic schematic of such an instrument is shown in Figure 3.33.

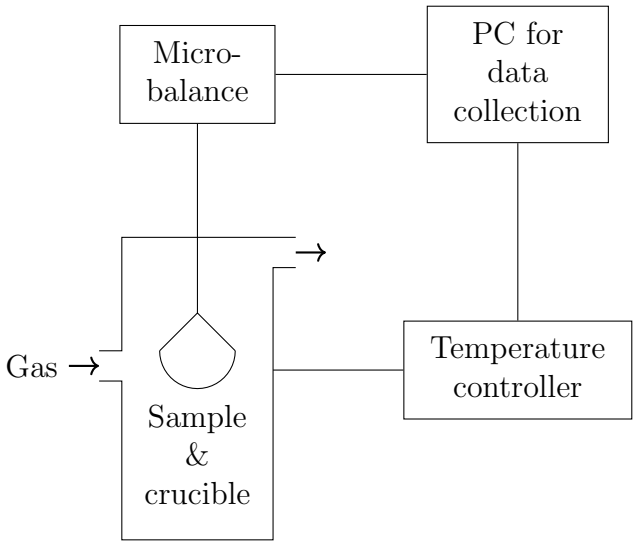

Figure 3.33: *Basic schematic of a conventional TGA instrument, adapted from Hatekeyama & Liu*[217].

The balance employed may be either mechanical or electronic, however, modern instruments tend to favour electronic balances. These come in single pan and dual

pan varieties. The furnace is heated by a coil which is wound non-inductively to avoid magnetic interactions between the coil and the sample, which would otherwise give false mass changes within the samples. These coils are manufactured using various high temperature materials, such as nichrome, platinum and silicon carbide. The Curie point (T_C) of a number of ferromagnetic materials is typically used to calibrate the temperature.

The sample is suspended on the balance by placing it in a crucible, and may be placed below the balance (as shown in Figure 3.33), above the balance or parallel to the balance. The below-balance placement is typically used for TGA, while the other two placements are more common for dual-mode instruments, such as TGA-DTA (differential thermal analysis). The choice of crucible is crucial. It must not demonstrate mass loss in the experimental temperature range, nor must it react chemically with the sample over the entirety of the temperature range. The crucibles are typically constructed of quartz, platinum or aluminium.

TGA is measured under a variety of atmospheric conditions including static and flowing atmospheres. The gas composition in a static atmosphere experiment varies around the sample when a gas generating reaction occurs. As a result, the reaction rate of the sample varies as a function of the partial pressure of the gas. A flowing atmosphere is typically employed for TGA experiments, with most common gases employed being air, Ar, Cl_2, CO_2, H_2, HCN, H_2O, N_2, and SO_2.

3.13 Temperature Programmed Reduction

Temperature programmed reduction (TPR) is a widely used technique for characterising the reduction of reducible materials[220–222]. In short, a reducible sample is placed in a reactor and exposed to a flow of reducing gas, most commonly hydrogen or carbon monoxide, and the temperature of the sample increased linearly with time. The rate of reduction is constantly monitored by measuring the composition of the reducing gas at the outlet of the reactor. A typical TPR profile plots the amount of reducing gas consumed against the time or temperature.

The position of peaks in the TPR profile, a result of gas consumption (reduction) is determined by the chemical nature and environment of the reducing species

present within the sample. The area under each peak corresponds to the total amount of gas consumed for the reduction. Knowledge of the starting mass and chemical identity allows reduction pathways to be determined through quantitative analysis of the total gas consumption.

TPR experiments are especially useful in the field of catalysis, where catalyst materials are prepared as oxidic precursors. It is able to provide very important information regarding optimum reducing conditions of these precursors and also allows for identification of different precursor phases in the initial precursor catalyst, how they interact with each other, as well as any chemical or structural support materials[223].

3.13.1 TPR Theory

For a simple, one-step reduction process, the rate of reduction may be expressed as[224]

$$\frac{d\alpha}{dt} = k(T)f(\alpha)\phi(C) \tag{3.75}$$

where α is the degree of reduction (S/S_0, with S_0 being the initial amount of reducible species and S its amount at time t), C is the mean gas concentration, $k(T)$ the rate constant, $\phi(C)$ a function that accounts for the dependence of the rate on the gas concentration and $f(\alpha)$ is a function that accounts for the dependence of the rate on the degree of reduction. Various reduction models are proposed, leading to different forms of $f(\alpha)$. These are summarised in Table 3.1.

The hydrogen mass balance for the reduction is given by

$$FC_0 = FC + S_0\left(\frac{d\alpha}{dt}\right) \tag{3.76}$$

where F is the gas flow rate and C_0 is the gas concentration at the reactor inlet. If the reduction kinetics are first order with respect to the gas concentration, then $\phi(C) = C$ and Equation 3.75 becomes

$$\frac{d\alpha}{dt} = \frac{C_0 k(T)f(\alpha)}{1 + (S_0/F)k(T)f(\alpha)} \tag{3.77}$$

Table 3.1: *Various reduction models and the associated forms of* $f(\alpha)$ [75,225–228].

Reduction Model	$f(\alpha)$
Nucleation according to Avarmi-Erofeev	$n(1-\alpha)[-\ln(1-\alpha)]^{1-\frac{1}{n}}$
n^{th}-order reaction	$(1-\alpha)^n$
1D diffusion	$\frac{1}{2\alpha}$
2D diffusion	$\frac{1}{-\ln(1-\alpha)}$
3D diffusion according to Jander	$\frac{3}{2}(1-\alpha)^{\frac{1}{3}}((1-\alpha)^{-\frac{1}{3}}-1)^{-1}$
Phase boundary controlled reaction[a]	$(1-\alpha)^{\frac{1}{2}}$
Phase boundary controlled reaction[b]	$(1-\alpha)^{\frac{1}{2}}$
Prout-Tompkins	$\alpha(1-\alpha)$
Sestak-Berggren	$\alpha^n(1-\alpha)^m[-\ln(1-\alpha)]^p$

[a] contracting area
[b] contracting volume

Introducing a linear heating programme with a heating rate of β:

$$T = T_0 + \beta t \tag{3.78}$$

and applying the Arrhenius law to the rate constant:

$$k(T) = A\exp(-E_a/RT) \tag{3.79}$$

where E_a is the activation energy of the reduction process and A is the pre-exponential factor, the final rate equation, true for any reduction process that is first-order with respect to the gas concentration, becomes

$$\frac{d\alpha}{dt} = \frac{A\exp(-E_a/RT)f(\alpha)}{(\beta/C_0) + PA\exp(-E_a/RT)f(\alpha)} \tag{3.80}$$

where P is the quantity $\beta S_0/FC_0$. A similar process may be applied to multi-step reduction processes. Equation 3.80 also demonstrates the influence of β/C_0 and P on the reduction profile. Both of these factors are determined by experimental conditions. As such, the profile of a given reduction process can vary significantly

based on the experimental conditions employed.

3.13.2 TPR Instrumentation

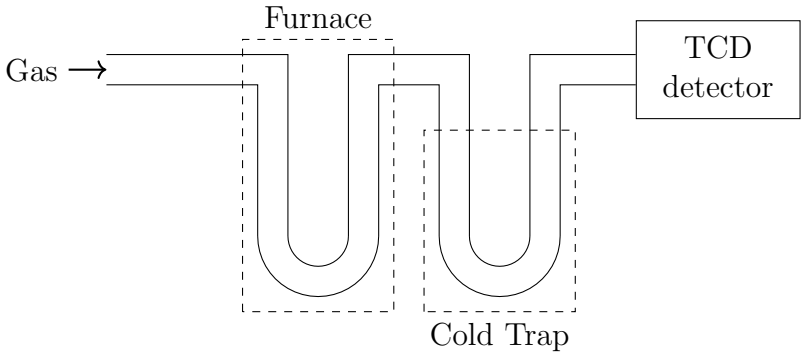

Figure 3.34: *Basic schematic of a TPR instrument, adapted from Pinna*[223].

A basic schematic for a standard TPR instrument is detailed in Figure 3.34. The sample is contained in a reactor tube, typically made of an inert material capable of withstanding high temperatures. This is located inside a furnace that is responsible for heating the sample at the prescribed heating rate. The gas flows over the sample to a TCD detector, which measures the amount of gas consumed by comparing it to a reference stream. A cold trap is typically placed between the reactor and the TCD detector to remove any reduction byproducts (such as water which forms when oxides are reduced in hydrogen)[223].

The TCD detector signal is typically calibrated to give quantitative hydrogen consumption values by running a standard with a well-defined reduction pathway. An example is the reduction of copper(II) oxide in hydrogen:

$$CuO + H_2 \rightarrow Cu + H_2O$$

indicating that 1 mole of hydrogen is consumed for every mole of copper. Knowledge of the initial mass of copper(II) oxide allows the TCD signal to be calibrated against the expected hydrogen consumption.

4 Synthesis and Characterisation of Iron Oxide Precursors

4.1 Synthesis

Silica-promoted iron oxide catalyst precursor samples were prepared using a simple co-precipitation technique, involving rapid hydrolysis of iron(III) nitrate in aqueous medium, adapted from several different sources[25,86,112,140]. The details are as follows:

An appropriate amount of iron(III) nitrate nonahydrate ($Fe(NO_3)_3 \cdot 9H_2O$) and sodium metasilicate pentahydrate ($Na_2SiO_3 \cdot 5H_2O$) were each dissolved in approximately 50 mL of deionised water in separate beakers. The exact masses are dependent on the desired iron/silica ratio and are given in Table 4.1. These two solutions were heated to 80°C. A third beaker was filled with approximately 75 mL distilled water, and the pH corrected to 8.0 using a 25% ammonium hydroxide solution. This was also heated to 80°C. The iron(III) nitrate and sodium metasilicate solutions were added dropwise with vigorous stirring over a period of 40 minutes to the pH-adjusted solution. The addition was slow, and the pH maintained at 8.0 throughout the dropwise addition of ammonium hydroxide. During this process the iron and silica were simultaneously precipitated out of solution.

After precipitation was complete, the samples were filtered and washed several times with deionised water. They were subsequently dried for 24 hours at 90°C. The solid cakes obtained after drying were ground to fine powders using a pestle and mortar, and the resulting powders calcined at 400°C for 4 hours in air.

In total five silica-promoted samples and one silica-free sample (to serve as a control) were prepared. They are labeled according to their iron/silica ratios (by mass), with the iron content always being given in 100 parts. The six samples are: **100/200 Fe/SiO_2**, **100/100 Fe/SiO_2**, **100/50 Fe/SiO_2**, **100/25 Fe/SiO_2**, **100/10 Fe/SiO_2** and **100/0 Fe/SiO_2**.

Table 4.1: *Mass of reagents used in the preparation of co-precipitated iron-silica samples.*

Sample	Mass [g]	
	$Fe(NO_3)_3 \cdot 9H_2O$	$Na_2SiO_3 \cdot 5H_2O$
100/200 Fe/SiO$_2$	18.08	17.66
100/100 Fe/SiO$_2$	18.08	8.83
100/50 Fe/SiO$_2$	18.08	4.42
100/25 Fe/SiO$_2$	18.08	2.21
100/10 Fe/SiO$_2$	36.16	1.77
100/0 Fe/SiO$_2$	36.16	0.00

The calcined samples vary in colour. **100/0 Fe/SiO$_2$** is a dark red colour, while **100/10 Fe/SiO$_2$**, **100/25 Fe/SiO$_2$** and **100/50 Fe/SiO$_2$** are all a similar dark brown. **100/100 Fe/SiO$_2$** is a slightly lighter brown than the lower silica-content samples, while **100/200 Fe/SiO$_2$** is light brown. These differences in colour already suggest different iron oxide and/or silica phases being present within each of the samples.

4.2 Experimental Details

4.2.1 Scanning Electron Microscopy

BSE SEM micrographs and EDS data were obtained using a JEOL JSM-7001F operating at 15 kV and using the equipped secondary and inline backscattered electron detectors and Oxford Instruments XMax 20 EDS detector. Samples were prepared by embedding the powders in resin. Resin blocks were polished to 1 μm and carbon coated to prevent charging. EDS data was analysed using Oxford Aztec software.

4.2.2 Transmission Electron Microscopy

TEM micrographs, selected area diffraction patterns (SAED), BF and HAADF scanning transmission electron microscopy (STEM) micrographs, EDS and EELS data were obtained using a STEM- and TEM-C_s-corrected JEOL JEM-ARM-200F operated at 200 kV and equipped with an Oxford Instruments XMax 80 EDS detector and Gatan GIF 965ERS with dual EELS capability. Supplementary TEM micrographs, SAED patterns, BF and HAADF STEM micrographs and EDS data were obtained using a JEOL JEM-2100 operated at 200 kV and equipped with an Oxford Instruments XMax 80 EDS detector and a Gatan Quantum EELS system. Samples were prepared by placing a small amount of sample in ethanol and dispersing it by ultrasonicating for approximately 15 minutes. A drop of dispersed solution was placed on an amorphous carbon film supported by a copper grid. Data was analysed using a combination of Gatan Digital Microscopy Suite with the PASAD tools add-in[229], Oxford Aztec Software and ImageJ[230].

4.2.3 X-Ray Powder Diffraction

X-ray powder diffraction (XRPD) analyses were performed on a Bruker D8 advance spectrometer using a cobalt radiation source ($\lambda = 0.178897$ nm). Samples were prepared in standard polycarbonate sample holders using standard loading techniques to minimise preferred-orientation effects at the sample surface. The sample was scanned from $2\theta = 5^\circ$ to $2\theta = 135^\circ$ in steps of 0.014325° 2θ. Crystalline phases present in the sample were identified using Bruker AXS DIFFRAC.EVA software, while average crystallite sizes were determined using Rietveld refinement, the fundamental parameter, full pattern refinement approach and Topas version 4.1 software.

4.2.4 Raman Spectroscopy

Raman spectra were collected using a Renishaw inVia Raman Spectrometer (514 nm laser at 15% power, 1800 l/mm diffraction grating). The powder sample was deposited on a glass slide and a Leica microscope (20X objective lens) was used

to focus the laser and identify sites on the sample used to collect spectra. Each spectrum collected is the result of 5 accumulations at 30 seconds per accumulation. Three spectra were collected per sample from different sites to account for local inhomogeneities. These spectra were averaged.

4.2.5 Physisorption

Nitrogen physisorption measurements were performed using a Micromeritics ASAP 2420. The samples were initially degassed by heating to 300°C for 12 hours under vacuum prior to analysis. This ensured the removal of surface contaminants. The samples were back-filled with dry nitrogen and transferred to the analysis port. The volume of nitrogen adsorbed was determined as a function of nitrogen relative pressure (P/P_0) in the range $2.0 \cdot 10^{-5}$ to 1.0 at a temperature of 77 K. Normalised surface area was determined by applying the Brunauer-Emmett-Teller (BET) method to the nitrogen adsorption isotherm data[208], while total pore volume and pore size distribution were calculated by applying the Barrett-Joyner-Halender (BJH) method to the desorption arm of the same isotherm data[231].

4.2.6 Mössbauer Absorption Spectroscopy

MAS measurements were performed at room temperature (RT) using a conventional constant acceleration spectrometer operating in absorption mode equipped with a ^{57}Co/Rh source. Zero-field (ZF) low temperature (LT) measurements and applied field (AF) low temperature measurements, with an applied field of 10 T, were performed at 4.2 K for each sample using an Oxford Instruments Spectromag SM4000-10 cryomagnet. The Mössbauer absorption spectra were analysed using Normos software, a least-squares program that models the peaks as a combination of quadruple doublets and sextets based on a Lorentzian line-shape profile[232]. The individual absorption features were identified based on their hyperfine parameters i.e. the isomer shift (δ), quadrupole splitting (ΔE_Q) and magnetic hyperfine field (B_{hf}) values. All isomer shift and magnetic hyperfine field values are reported relative to metallic iron (α-Fe).

4.2.7 Magnetic Measurements

Magnetic measurements were performed using a magnetic and physical properties measurements (MPMS) XL-7 SQUID magnetometer from Quantum Design, Inc. Samples were loaded at room temperature and aligned (centred) in the magnetic field by means of a 100 Oe applied field. Thereafter, the samples were cooled to 2 K in zero magnetic field. The following procedure was then followed:

1. A magnetic field of 100 Oe was applied and the samples were heated from 2 K to 400 K at a rate of 5 K.min^{-1}. The magnetisation as a function of temperature (M(T) curves) was recorded at temperature intervals of 2 K. This is referred to as zero-field cooled (ZFC) mode.
2. Still in a 100 Oe magnetic field, the samples were cooled from 400 K to 2 K at a rate of 5 K.min^{-1}. M(T) data was recorded in 2 K intervals. This is referred to as field cooled (FC) mode.
3. The magnetic field was set to 0 Oe and the samples were heated from 2 K to 400 K at a rate of 5 K.min^{-1}. M(T) data was recorded in 2 K intervals. This is referred to as thermal remanence magnetisation (TRM).

4.2.8 Thermogravimetric Analysis

Thermogravimetric analysis was performed for each sample using a TA 2050 Thermogravimetric Analyser. A small mass of powder sample was placed in a platinum pan and heated from room temperature to 700°C at a heating rate of 10°C.min^{-1}. Nitrogen was continually flowed over the sample at a rate of 10 mL.min^{-1}. The resulting mass loss data was analysed using Universal Analysis 2000 version 4.2 software.

4.3 Scanning Electron Microscopy

The initial success of the synthesis was gauged using SEM. It is crucial that a homogeneous distribution of iron- and silica-bearing phases occurs within each

sample. This ensures a very intimate mixing between the two, resulting in the strongest iron-silica interaction as explained by Dlamini *et al.*[25].

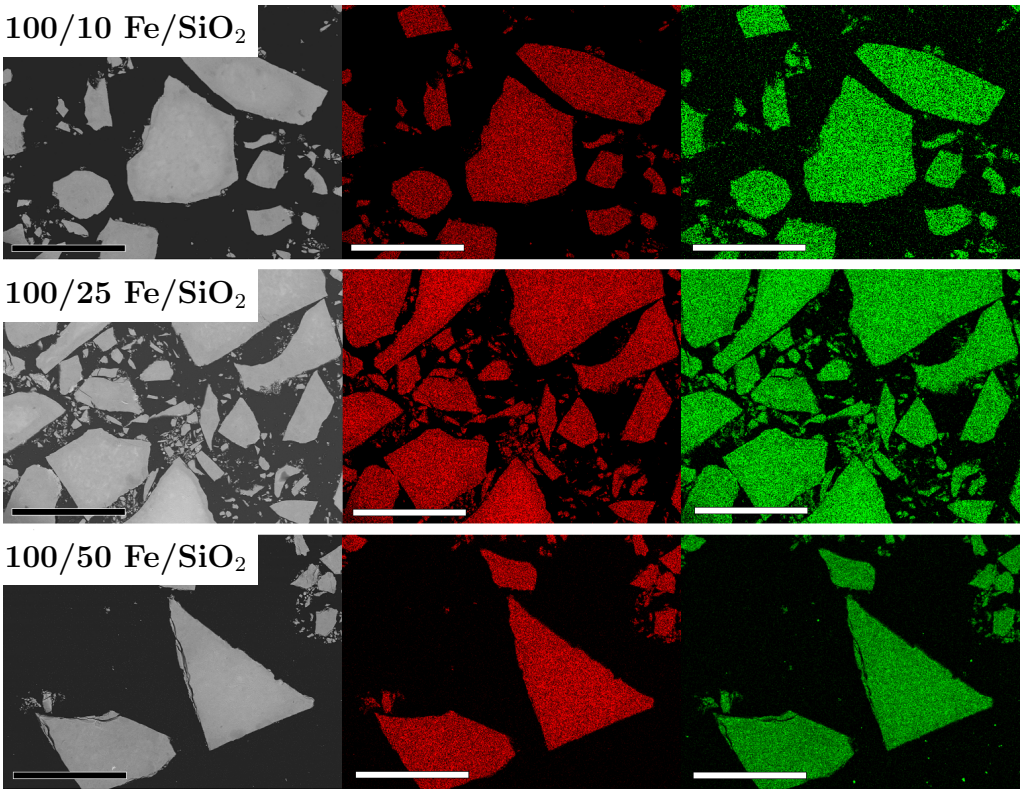

Figure 4.1: *BSE SEM micrographs (left), Fe- (center, red) and Si-EDS (right, green) maps for* ***100/10 Fe/SiO$_2$****,* ***100/25 Fe/SiO$_2$*** *and* ***100/50 Fe/SiO$_2$*** *showing homogeneous distribution of iron and silicon. Scale bars are 200µm.*

Back-scattered electron (BSE) SEM micrographs, together with the corresponding iron- and silicon-EDS maps of **100/10 Fe/SiO$_2$**, **100/25 Fe/SiO$_2$** and **100/50 Fe/SiO$_2$** are shown in Figure 4.1. Since BSE micrographs are sensitive to the average atomic density of the sample, the iron particles appear bright, while the carbon-based resin matrix appears dark. All three samples demonstrate slight variations in contrast on the sample surface, which might suggest some regions are slightly richer in silicon (darker areas) than others.

Alternatively, this contrast might simply be a result of voids within the interaction volume of the particular region being probed. It is also possible that the particular region of interest is thinner than the interaction volume at that point, resulting

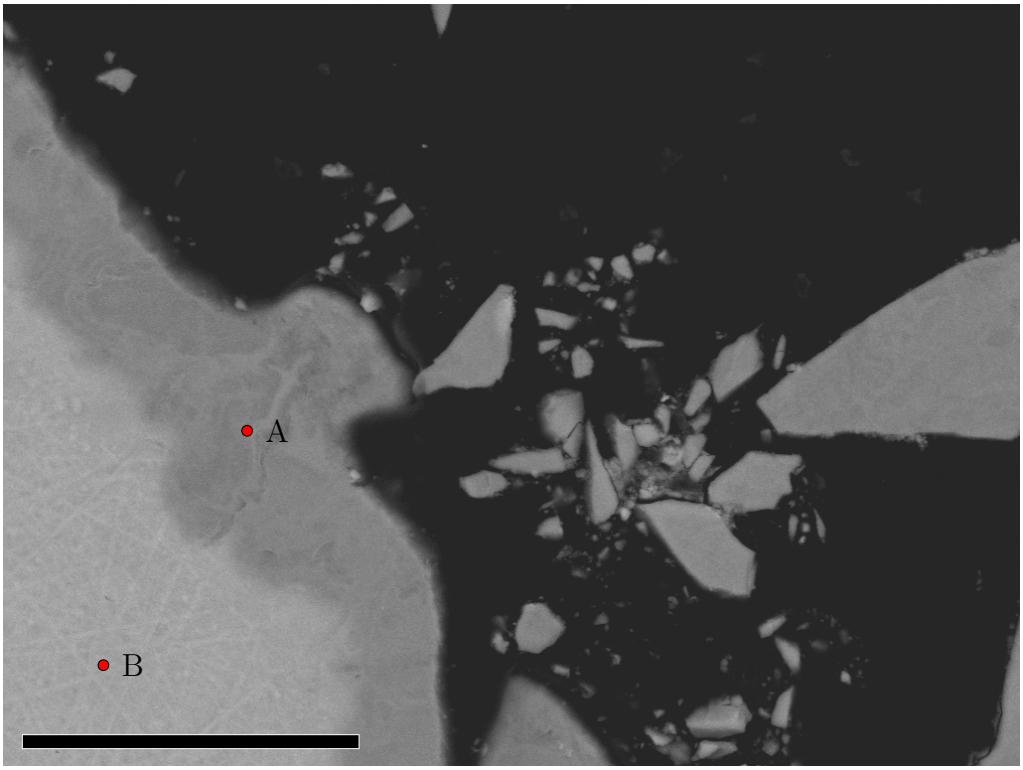

Figure 4.2: *BSE SEM micrograph of* ***100/10 Fe/SiO$_2$*** *indicating regions probed for EDS spot analysis. Scale bar is 200µm.*

in some contribution of the resin matrix to the BSE signal. Both scenarios would result in a slightly lower average atomic number and hence appear slightly darker in the corresponding BSE micrographs. Indeed, quantitative EDS spot analysis on the darker and lighter regions reveals no difference in iron and silicon concentrations, suggesting that the presence of voids is the more likely explanation for the observed contrast difference.

Figure 4.2 is a BSE SEM micrograph of **100/10 Fe/SiO$_2$**. EDS spot analyses were performed at the regions marked A and B. Spot A, a darker region, has an Fe:Si composition (by weight) of 100:5.1 (±0.2), while spot B, taken from a brighter region in the same particle, has an Fe:Si composition of 100:5.2 (±0.2). These statistically similar values lend support to the idea that this contrast is simply the result of different average atomic number within the interaction volume. Based on the location of spot A (the edge of a large particle) it is likely that the sample

is very thin at this point, resulting in a contribution to the total BSE from the resin below. Similar spot analyses on **100/25 Fe/SiO$_2$** and **100/50 Fe/SiO$_2$** also revealed statistically insignificant differences in the Fe:Si weight ratio between dark and light regions.

Iron- and silicon-EDS maps (Figure 4.1) also reveal a homogeneous distribution of iron and silicon across the surface of the sample, supporting the idea of voids being responsible for the observed contrast difference.

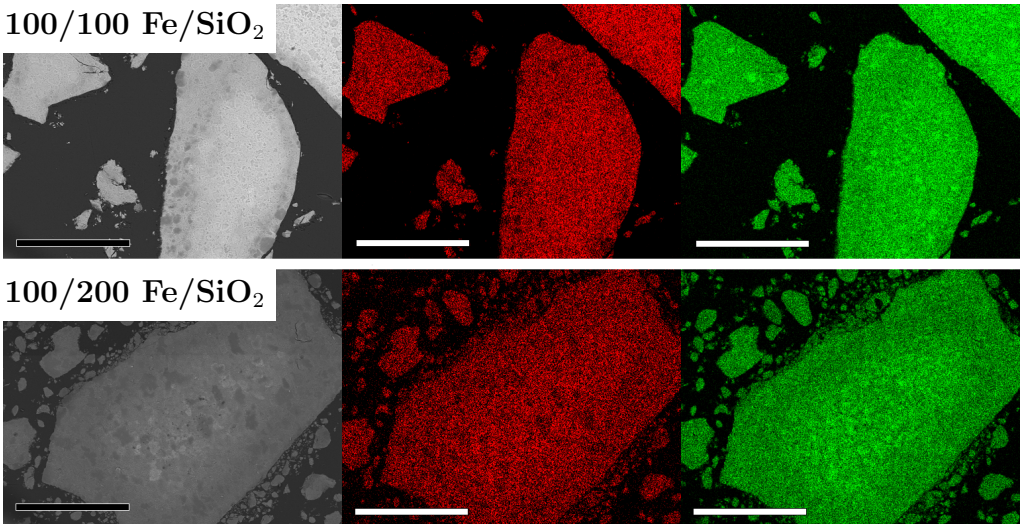

Figure 4.3: *BSE SEM micrographs (left), Fe- (center, red) and Si-EDS (right, green) maps for* ***100/100 Fe/SiO$_2$*** *and* ***100/200 Fe/SiO$_2$*** *showing heterogeneous distribution of iron and silicon. Scale bars are 200µm.*

BSE SEM micrographs of **100/100 Fe/SiO$_2$** and **100/200 Fe/SiO$_2$**, together with the corresponding iron- and silicon-EDS maps, are shown in Figure 4.3. Both samples demonstrate considerably more contrast in the BSE micrographs than the lower silica-content samples. Comparison with the corresponding EDS maps reveals that this is not entirely the result of voids, but also differences in iron and silicon concentrations. Darker regions do contain less iron than the lighter regions. Figure 4.4 is a BSE SEM micrograph of **100/100 Fe/SiO$_2$**. EDS spot analyses were performed at the regions marked A and B. Spot A, a darker region, has an Fe:Si composition (by weight) of 100:64.6 (±0.8), while spot B, one of the brighter regions, has an Fe:Si weight ratio of 100:45.0 (±0.5). This confirms that this contrast is not simply the result of voids within the sample. However, there

are no regions which contain only iron or only silicon.

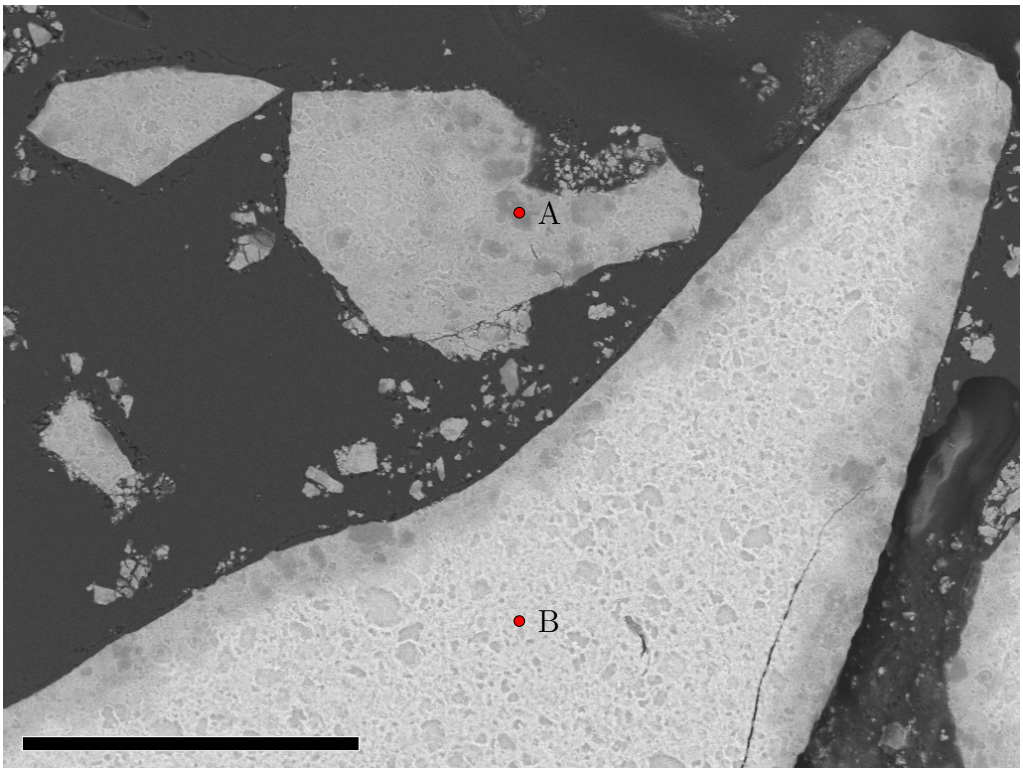

Figure 4.4: *BSE SEM micrograph of* ***100/200 Fe/SiO$_2$*** *indicating the regions probed for EDS spot analysis. Scale bar is 200µm.*

EDS was also used to determine the amount of iron and silicon present in each sample. Using this information, the iron to silicon weight ratio was determined. This data is presented in Table 4.2. In all cases, the average silicon content is slightly higher than theoretically expected, but falls within one standard deviation of the expected value. There is a significant increase in error as the silica content increases. This is a result of inhomogeneities in the iron and silicon concentrations and suggests that even in **100/50 Fe/SiO$_2$** there is some inhomogeneity present. This concentration inhomogeneity becomes more pronounced as the silica content is increased to 100 and 200 parts for every 100 parts iron.

Based on this data, it is concluded that there is an intimate mixing between the iron and silicon-bearing phases within each of the samples, although the Fe:Si ratio is not homogeneous. This conclusion is valid to within the resolution dictated by the

X-ray interaction volume. Monte Carlo simulations were performed using Casino v2.4.8.1 software to approximate this resolution[233]. Pure iron oxide (hematite, α-Fe_2O_3) and silica (SiO_2) were used as substrates for the simulations, since they form the two extremes within each of the samples. The simulation results are illustrated in Figure 4.5.

α-Fe_2O_3 suggests an electron interaction volume having a corresponding surface diameter of approximately 1.2 μm, while this value rises to approximately 2.3 μm for silica. Thus this iron-silicon intimacy observed in the SEM analyses is valid down to a resolution of 2 μm, since the generation of emitted X-rays occurs within a smaller subvolume of the full interaction volume[234]. This interaction volume will of course vary from sample to sample, being largest for **100/200 Fe/SiO_2** and smallest for **100/10 Fe/SiO_2**.

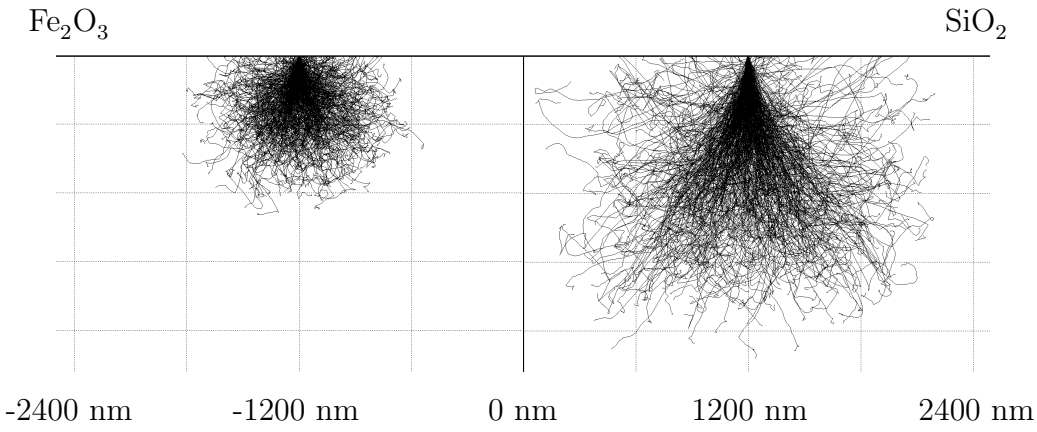

Figure 4.5: *Monte Carlo simulation showing simulated electron trajectories within Fe_2O_3 and SiO_2 with an incident eletron energy of 30 keV. X-rays collected for EDS analysis are generated by these electrons.*

Table 4.2: *Theoretical and experimental iron and silicon weight ratios determined using EDS within each sample. The standard error is given in brackets.*

Sample	$\mathbf{Fe:Si}_{Theoretical}$	$\mathbf{Fe:Si}_{EDS}$
100/10 Fe/SiO$_2$	100 : 4.7	100 : 5.3 (0.9)
100/25 Fe/SiO$_2$	100 : 11.7	100 : 13.3 (0.7)
100/50 Fe/SiO$_2$	100 : 23.4	100 : 25.4 (3.9)
100/100 Fe/SiO$_2$	100 : 46.7	100 : 52.7 (9.7)
100/200 Fe/SiO$_2$	100 : 93.5	100 : 101 (16)

4.4 Transmission Electron Microscopy

Transmisison electron microscopy (TEM) micrographs of **100/0 Fe/SiO$_2$** reveal that it is comprised of irregular-shaped nanoparticles and SAED identified this phase as hematite. One such micrograph is shown on the left of Figure 4.6. An SAED pattern of this area is shown on the right. It exhibits a large number of diffraction spots located in concentric rings, which is characteristic of a collection of crystalline nanoparticles. The SAED pattern was rotationally averaged and the resulting line pattern is overlaid. The position of the reflections correspond to those expected for hematite. All spots have been indexed, suggesting **100/0 Fe/SiO$_2$** does not contain any other phases.

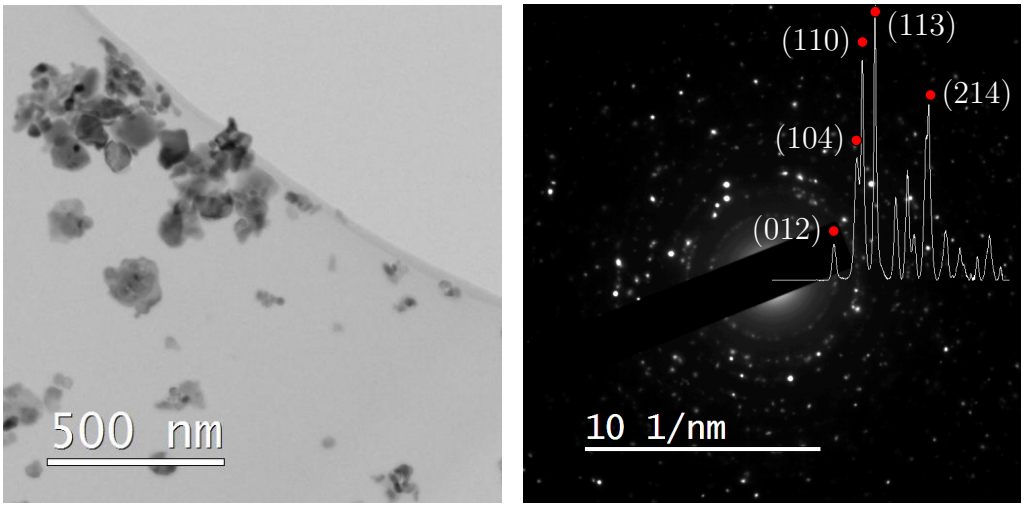

Figure 4.6: *TEM micrograph of* ***100/0 Fe/SiO$_2$*** *(left) and corresponding SAED pattern (right). The rotationally averaged SAED pattern is superimposed and major reflections of hematite annotated.*

The addition of 10 weight silica during synthesis results in a dramatic difference in the resulting iron oxide phase. TEM (with its corresponding SAED pattern) and high resolution HAADF STEM micrographs of **100/10 Fe/SiO$_2$** are shown in Figure 4.7. Very small particles have been stabilized by the presence of silica, with HRSTEM revealing a poorly crystalline material. The SAED pattern exhibits two broad rings at d-spacings of approximately 2.5 Å and 1.5 Å. This is characteristic of the poorly-crystalline iron oxide known as 2-line ferrihydrite.

Ferrihydrite, particularly the 2-line variety, is notoriously susceptible to electron beam damage[87,235]. 2-line ferrihydrite has been shown to transform when exposed to sufficiently high electron doses[87]. The use of low-dose techniques in combination with a liquid nitrogen-cooled holder is thus recommended for TEM analysis of ferrihydrite. However, the presence of silica in these samples appears to inhibit beam-induced transformations, as noted by the continued presence of two broad diffraction rings even after continued exposure.

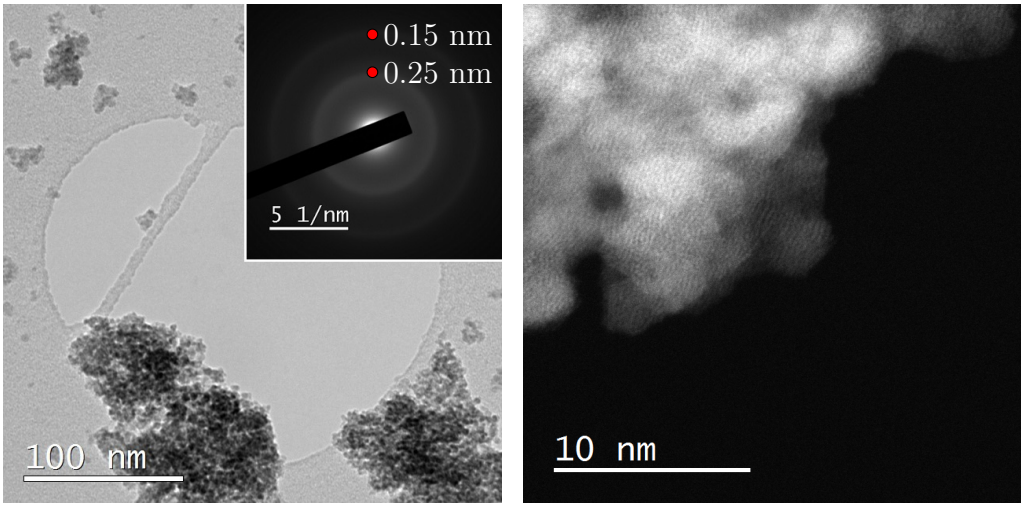

Figure 4.7: *TEM micrograph of* ***100/10 Fe/SiO$_2$*** *(left), corresponding SAED pattern (left inset) and HAADF STEM micrograph (right).*

The HAADF STEM micrograph exhibits some variations in contrast. There are two possible explanations for this. Firstly, any segregation between iron- and silica-bearing phases would result in contrast in the corresponding HAADF micrograph (Z-contrast). Secondly, variation in sample thickness will also result in such a contrast variation.

Figure 4.8 shows STEM-EELS compositional maps for oxygen and iron within the region indicated. Should silica and iron oxide be segregated, it is expected that a higher concentration of oxygen (and no iron) would be observed in the corresponding elemental map. The iron and oxygen distributions, however, correspond with each other. This suggests that the silicon is homogeneously distributed throughout the iron oxide. The silicon EELS signal is too weak to generate a silicon compositional map, however STEM-EDS compositional maps also indicate that the silicon is homogeneously distributed. **100/10 Fe/SiO$_2$** is thus a silicon-substituted ferrihydrite and the contrast observed in the HAADF STEM micrographs is simply a result of thickness variations.

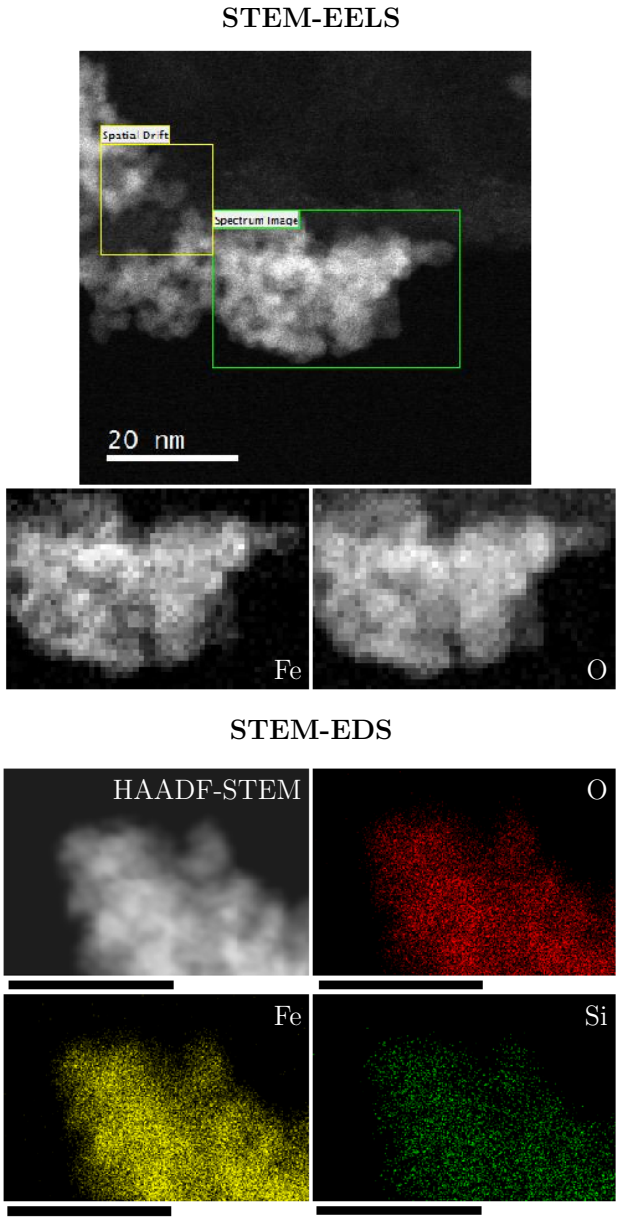

Figure 4.8: *STEM-EELS and STEM-EDS compositional maps showing the distribution of iron and oxygen (EELS) and iron, oxygen and silicon (EDS) in* ***100/10 Fe/SiO$_2$****. EELS data was collected from the region inscribed by the green rectangle, while EDS data was obtained from the HAADF STEM micrographs shown. The scalebar for the STEM-EELS data is 50 nm.*

It is also possible that only a portion of the silica has been incorporated within the iron oxide structure of **100/10 Fe/SiO$_2$**, while the remaining silica has formed larger chunks which (owing to the sample preparation method) have been been selectively excluded during the preparation of the TEM grid. Quantification of EDS signals obtained from a number of different areas of **100/10 Fe/SiO$_2$** indicates the contrary *viz.* all the silica is incorporated within the iron oxide structure.

Increasing the silica content from 10 to 25 weight parts for every 100 weight iron in **100/25 Fe/SiO$_2$** leaves the final particle morphology largely unchanged. TEM (with the correpsonding SAED pattern) and HAADF STEM micrographs are shown in Figure 4.9. As with **100/10 Fe/SiO$_2$**, very small nanoparticles have formed, which exhibit two broad rings in their SAED pattern corresponding to the 2-line variety of ferrihydrite. The HAADF STEM micrograph illustrates the crystalline disorder within the particles, and exhibits a similar contrast to **100/25 Fe/SiO$_2$**. There is no evidence in any of the TEM or STEM micrographs for the formation of a segregated silica phase.

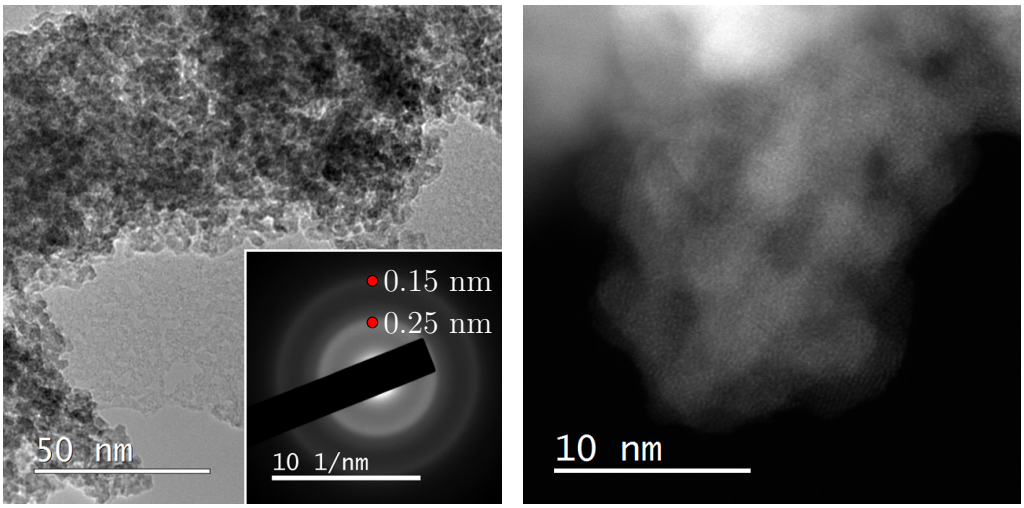

Figure 4.9: *TEM micrograph of **100/25 Fe/SiO$_2$** (left), corresponding SAED pattern (left inset) and HAADF STEM micrograph (right).*

STEM-EELS compositional maps (Figure 4.10) once again show correlation between the iron and silicon distributions, suggesting a silicon-substituted ferrihydrite has once again formed. As with **100/10 Fe/SiO$_2$**, quantification of EDS

spectra suggests all of the silicon is contained within the ferrihydrite structure.

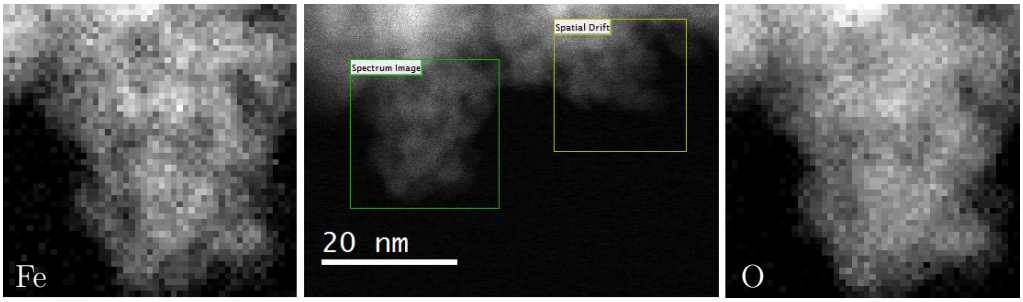

Figure 4.10: *STEM-EELS compositional maps showing the distribution of iron and oxygen in* ***100/25 Fe/SiO$_2$****. EELS spectra were collected from the region inscribed by the green rectangle.*

Further doubling the silica content to 50 weight silica for 100 weight iron in **100/50 Fe/SiO$_2$** reveals very little structural change. TEM (with the correpsonding SAED pattern) and HAADF STEM micrographs are shown in Figure 4.11. As with **100/10 Fe/SiO$_2$** and **100/25 Fe/SiO$_2$**, very small iron oxide nanoparticles have formed, which exhibit two broad rings in their SAED pattern corresponding to the 2-line variety of ferrihydrite. The HAADF STEM micrograph illustrates the crystalline disorder within the particles, and exhibits a similar contrast to **100/25 Fe/SiO$_2$**. There is no evidence in any of the TEM or STEM micrographs for the formation of segregated silica or iron phases.

STEM-EELS compositional maps once again show correlation between the iron and silicon distributions, suggesting a silicon-substituted ferrihydrite has formed. Furthermore, the quantity of silicon was significantly high to allow a silicon compositional map to be extracted from the EELS data. This data is shown in Figure 4.12. It corresponds to the iron and silicon distributions, suggesting a homogeneous silicon-substitution of the ferrihydrite structure has occurred. Once more, quantification of EDS spectra suggest all of the silicon is contained within the ferrihydrite structure.

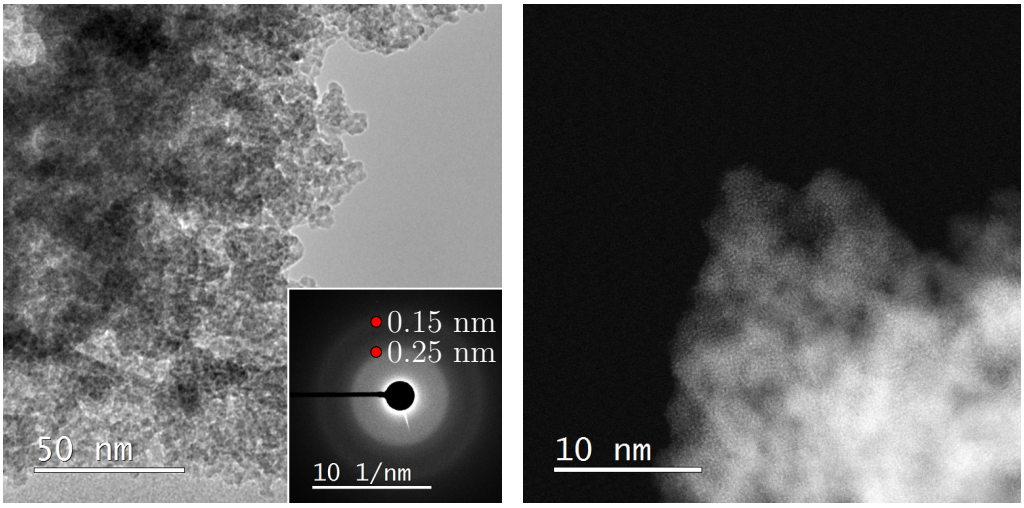

Figure 4.11: *TEM micrograph of* ***100/50 Fe/SiO$_2$*** *(left), corresponding SAED pattern (left inset) and HAADF STEM micrograph (right).*

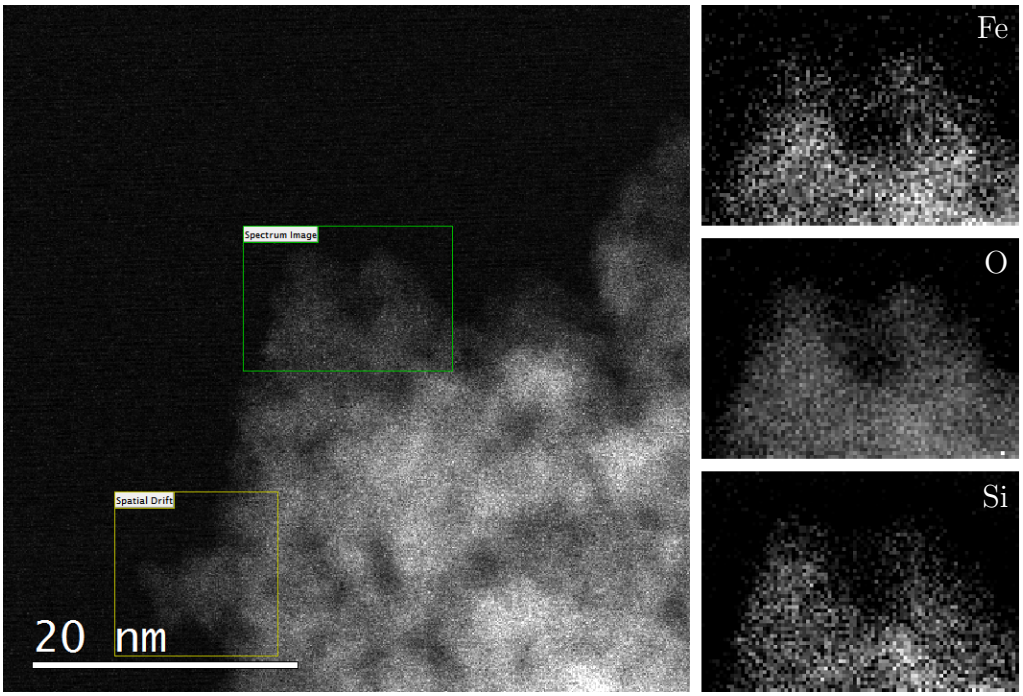

Figure 4.12: *STEM-EELS compositional maps showing the distribution of iron, oxygen and silicon in* ***100/50 Fe/SiO$_2$****. EELS spectra were collected from the region inscribed by the green rectangle.*

BF and HAADF STEM micrographs of **100/100 Fe/SiO$_2$** are shown in Figure 4.13. Unlike the samples with a lower silica content, no individual particles are clearly visible. The SAED pattern does, however, exhibit the same broad-ring pattern corresponding to 2-line ferrihydrite, which indicates that this iron oxide phase is present. Additionally, a large degree of contrast variation is apparent in the HAADF STEM micrographs, which is indicative of some segregation between the iron- and silicon-bearing phases.

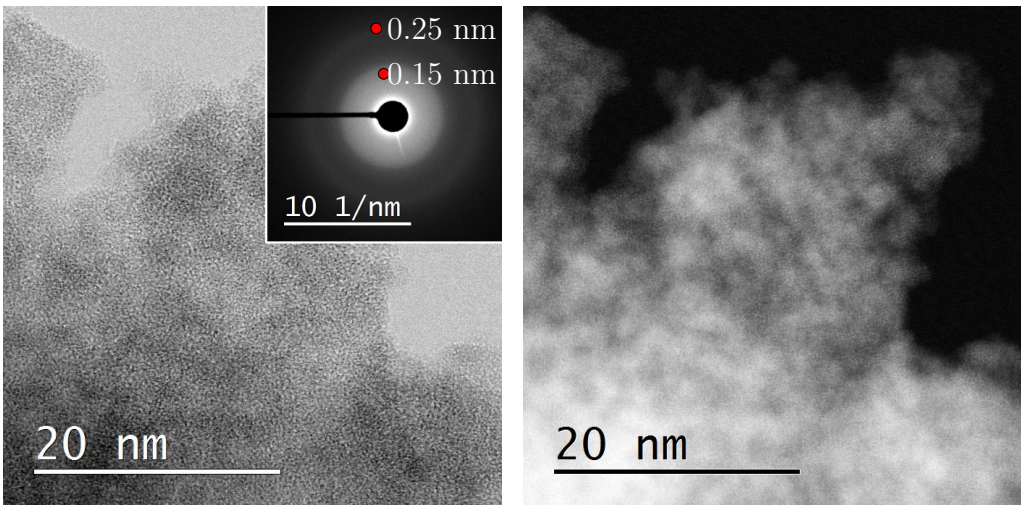

Figure 4.13: *BF STEM micrograph of* ***100/100 Fe/SiO$_2$*** *(left), corresponding SAED pattern (left inset) and HAADF STEM micrograph (right).*

A similar STEM-EELS compositional map confirms this segregation. While the distribution of oxygen corresponds to the entirety of the sample in the region probed, the iron and silicon distributions do not correspond. The iron appears to be distributed in two distinct environments. There are concentrations of iron (and oxygen) in regions where the silicon content is low, suggesting the formation of silicon-substituted 2-line ferrihydrite particles, similar to those in **100/10 Fe/SiO$_2$**, **100/25 Fe/SiO$_2$** and **100/50 Fe/SiO$_2$**. The other regions contain iron that does not appear concentrated into any particulate form, and also corresponds to regions of high silicon and oxygen content. This is a vitreous silica which contains iron domains as part of its amorphous structure. There is thus some critical amount of silica between 50 and 100 weight parts (for 100 weight iron) after which no additional silica can be incorporated in the ferrihydrite structure. Instead, the

silica encapsulates the iron, forming a vitreous network and preventing it from interacting with additional iron dimer/trimers during synthesis. As a result, larger iron oxide particles are unable to form.

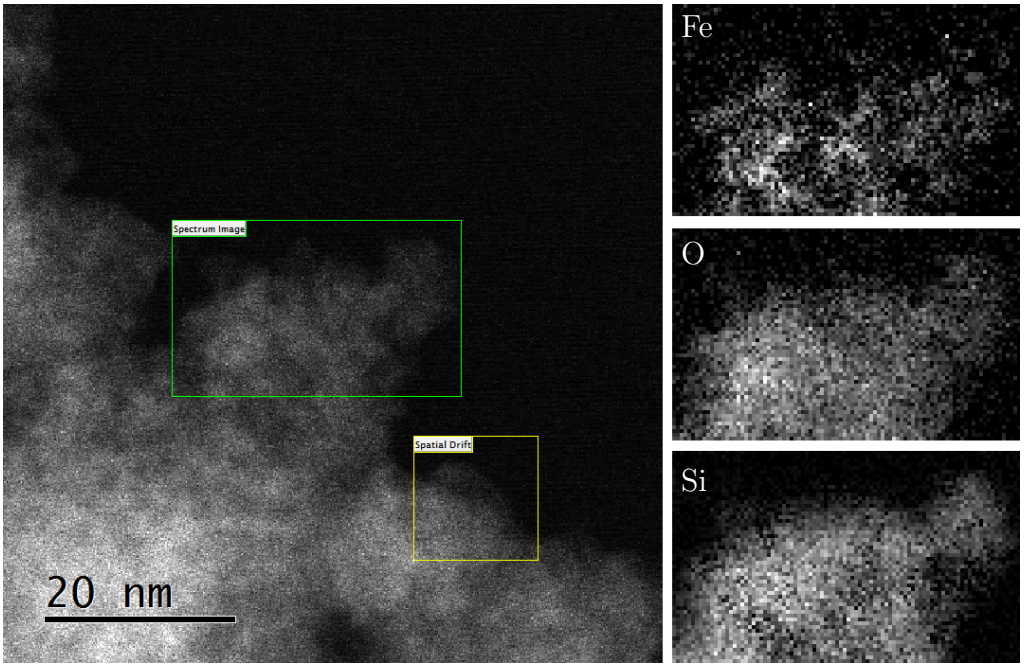

Figure 4.14: *STEM-EELS compositional maps showing the distribution of iron, oxygen and silicon in* ***100/100 Fe/SiO$_2$****. EELS spectra were collected from the region inscribed by the green rectangle.*

This trend continues with **100/200 Fe/SiO$_2$**. BF and HAADF STEM micrographs of **100/200 Fe/SiO$_2$** are shown in Figure 4.15. As with **100/100 Fe/SiO$_2$**, the bright field micrograph does not exhibit individual, clearly-defined particles, but the SAED pattern still exhibits the 2-line pattern characteristic of the silicon-substituted two-line ferrihydrites. Furthermore, the contrast in the HAADF micrographs is even more apparent than with the samples containing less silica.

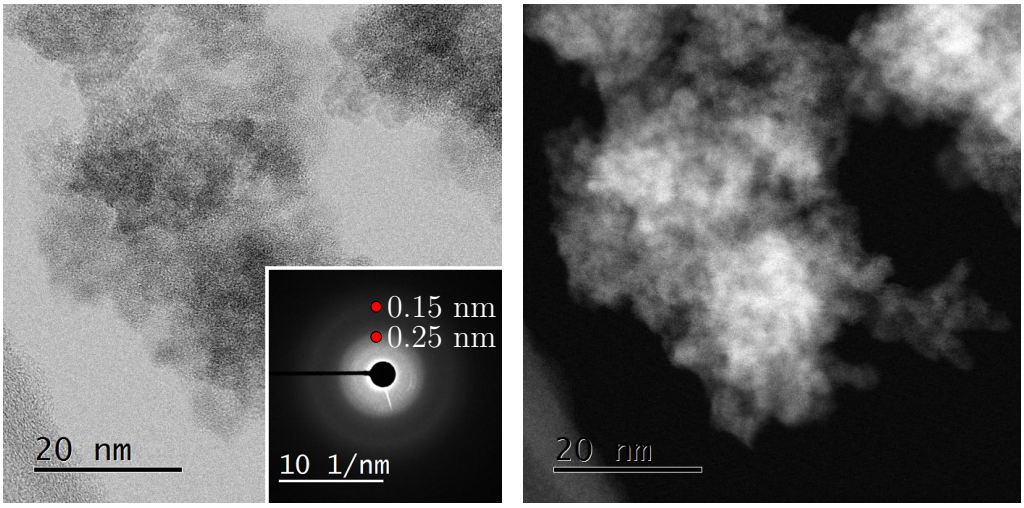

Figure 4.15: *BF STEM micrograph of* ***100/200 Fe/SiO$_2$*** *(left), corresponding SAED pattern (left inset) and HAADF STEM micrograph (right).*

STEM-EELS compositional maps in Figure 4.16 confirm this segregation. As with **100/100 Fe/SiO$_2$**, the distribution of oxygen corresponds to the entirety of the sample in the region probed, while the iron and silicon distributions do not correspond. The iron also exists in two environments corresponding to encapsulated silicon-substituted ferrihydrite and iron-bearing vitreous silica. The relative amount of this silica phase is however greater than **100/100 Fe/SiO$_2$**, as would be expected with double the silica amount employed in the synthesis of **100/200 Fe/SiO$_2$**.

Average particle sizes were also determined for **100/0 Fe/SiO$_2$**, **100/10 Fe/SiO$_2$**, **100/25 Fe/SiO$_2$** and **100/50 Fe/SiO$_2$**. The diameters, d, of 100 to 200 particles were counted for each sample, and the resulting distribution of diameters fitted with a log-normal distribution bearing the following probability density function typical of nanoparticle assemblies[236,237]:

$$f(d) = \frac{1}{\sqrt{2\pi}\sigma d} \exp\left(-\frac{(\ln d - \mu)^2}{2\sigma^2}\right) \tag{4.1}$$

Where μ and σ are respectively the location and scale parameters of the distribution. The mean diameter, d_0, and diameter standard deviation, Δd, of the

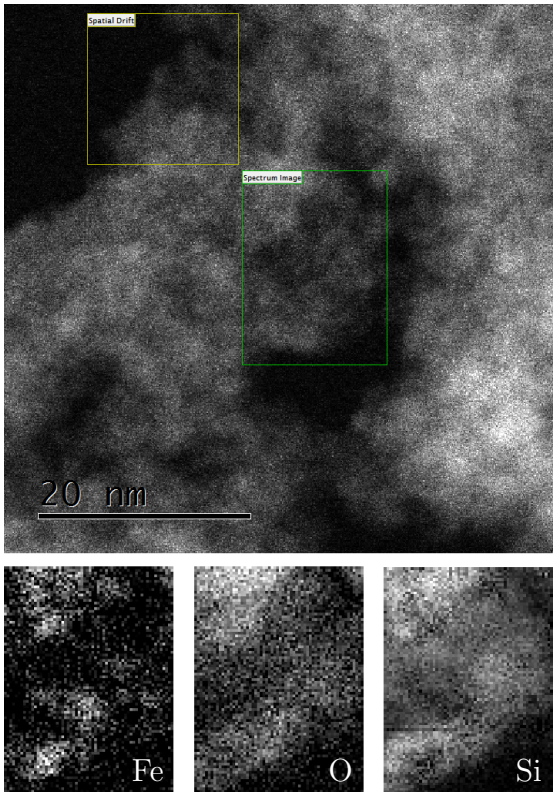

Figure 4.16: *STEM-EELS compositional maps showing the distribution of iron, oxygen and silicon in* ***100/200 Fe/SiO$_2$****. EELS spectra were collected from the region inscribed by the green rectangle.*

diameter may be calculated using equation 4.2 and 4.3:

$$d_0 = e^{\mu}\sqrt{e^{\sigma^2}} \tag{4.2}$$

$$\Delta d = d_0\sqrt{e^{\sigma^2} - 1} \tag{4.3}$$

The particle diameter distributions are shown in Figure 4.17, while the mean diameter (and standard deviation) are summarised in Table 4.3.

Table 4.3: *Mean particle diameter, d_0, and corresponding standard deviation, Δd_0, of* ***100/0 Fe/SiO$_2$****,* ***100/10 Fe/SiO$_2$****,* ***100/25 Fe/SiO$_2$*** *and* ***100/50 Fe/SiO$_2$****.*

Sample	$d_0 \pm \Delta d_0$ **[nm]**
100/0 Fe/SiO$_2$	39 ± 12
100/10 Fe/SiO$_2$	3.1 ± 0.4
100/25 Fe/SiO$_2$	2.4 ± 0.3
100/50 Fe/SiO$_2$	2.4 ± 0.3

100/0 Fe/SiO$_2$ has a mean particle diameter of 39 ± 12 nm. This large standard deviation is a result of the broad range of particle sizes observed in the TEM micrographs. The ferrihydrite particles in **100/10 Fe/SiO$_2$** are 3.1 ± 0.4 nm in diameter, while **100/25 Fe/SiO$_2$** particles possess particle diameters of 2.4 ± 0.3 nm. This decrease in particle size is evidence of the effect silica has in stabilising small iron crystallites. Interestingly, this trend does not continue with **100/50 Fe/SiO$_2$**, which exhibits the same mean particle diameter as **100/25 Fe/SiO$_2$**. The composition of **100/100 Fe/SiO$_2$** and **100/200 Fe/SiO$_2$** being a mixture of iron-bearing vitreous silica encapsulating extremely small domains of iron oxide, prevents the identification of individual particles, hence sizing was not performed for these two samples.

The ability of silica, even in small quantities, to stabilise the formation of poorly crystalline ferrihydrite nanoparticles is clearly evident and consistent with previous studies[2,25,84–86,112,140,238]. Particle sizes determined in other studies are very similar to those determined here. Suo *et al.* reported the formation of particles 16.9 nm, 7.5 nm and 4 nm in diameter for iron:silica ratios similar to **100/10 Fe/SiO$_2$**, **100/25 Fe/SiO$_2$** and **100/50 Fe/SiO$_2$** respectively[86]. However, that study employed tetraethylorthosilicate (TEOS) as the silica precursor, rather than sodium metasilicate as was used here. Zhang *et al.* conservatively estimated particle sizes below 15 nm for a 20 weight part silica sample, although the X-ray powder diffractograms they present suggest poorly crystalline material below 5 nm[140]. Dlamini *et al.*, employing a similar precipitation technique, obtained particle sizes below

3 nm, also for a sample bearing 20 weight parts silica[25]. Finally, Masina *et al.* reported a mean particle diameter of 3.5 nm for a sample containing 10 weight parts silica[239].

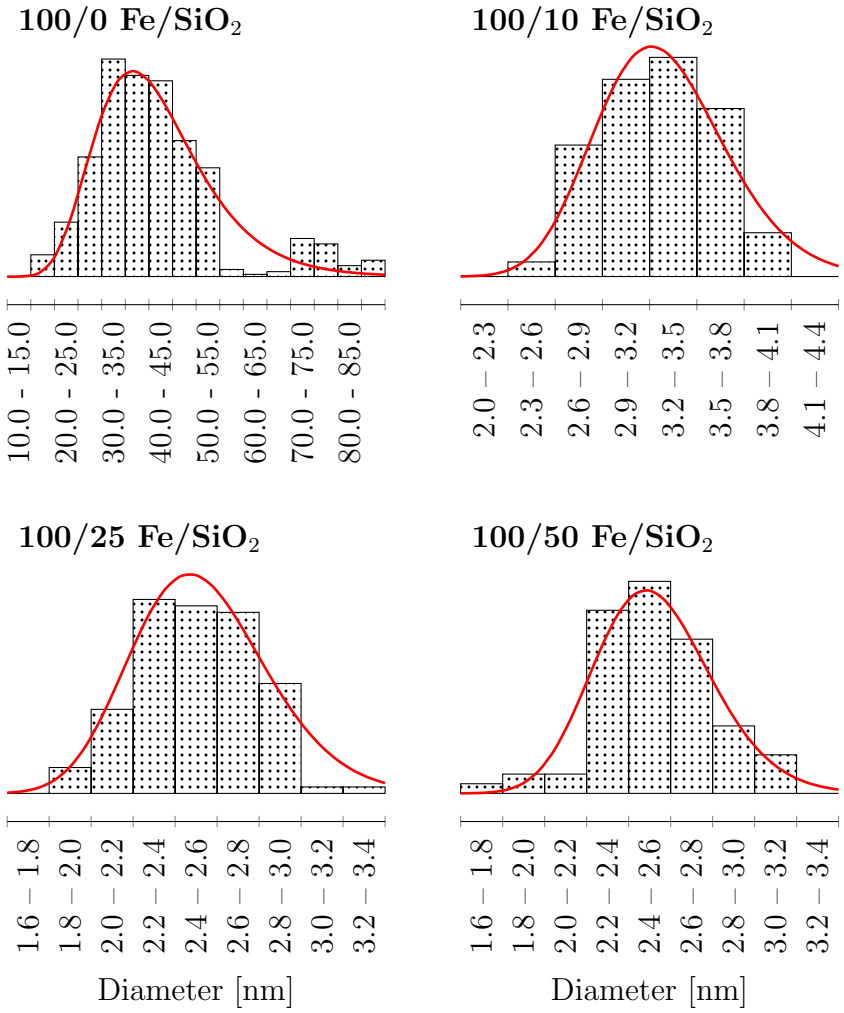

Figure 4.17: *Particle size distributions of* ***100/0 Fe/SiO$_2$****,* ***100/10 Fe/SiO$_2$****,* ***100/25 Fe/SiO$_2$*** *and* ***100/50 Fe/SiO$_2$****. Owing to the non-spherical shape of* ***100/0 Fe/SiO$_2$*** *particles, a circle-equivalent diameter was used.*

The formation of poorly ordered ferrihydrite which exhibits decreased crystallinity on increasing silica content is also documented[240], as is the formation of bulk silica phase upon reaching a critical concentration[151,155,156]. There does, however, appear to be uncertainty on whether the silica is incorporated within the iron oxide

material itself or binds only to the surface of the iron oxide particles, preventing their further growth.

The data obtained in this TEM analysis reveals that the silica is fully incorporated within the iron oxide of the framework, since the resolution of the micrographs are sufficient to resolve a significant difference in surface and bulk concentrations that would be the case should the silica be entirely located at the surface of the ferrihydrite particles. The co-precipitation of iron oxide and silica allows for maximum interaction between the two species, thus resulting in a very homogeneous silicon substitution within the iron oxide crystal structure.

4.5 Raman

The Raman spectrum for **100/0 Fe/SiO$_2$** is shown in Figure 4.18, while the Raman spectra for the silica-bearing samples are shown in Figure 4.19. The silica-bearing samples demonstrate very similar spectra, while the silica-free **100/0 Fe/SiO$_2$** exhibits a distinctly different Raman spectrum.

100/0 Fe/SiO$_2$ demonstrates eight unique bands in its Raman spectrum, located at 227, 245, 295, 299 412, 502, 614 and 1320 cm^{-1}. Comparison with the literature suggests that this sample is hematite[241]. The intense transition located at 1320 cm^{-1} (literature: 1320 cm^{-1}) is a two-magnon scattering which arises from the interaction of two magnons created on the antiparallel close spin sites in the antiferromagnetic hematite. The other seven bands are a result of the hematite structure, which is a member of the D^6_{3d} crystallographic space group. The bands at 227 and 502 cm^{-1} (literature: 225 and 498 cm^{-1}) are A_{1g} modes, while the five remaining bands at 245, 295, 299, 412 and 614 cm^{-1} (literature: 247, 293, 299, 412 and 613 cm^{-1}) are A_g modes.

The similarity between the Raman spectra of the silica-bearing samples suggests they are all very similar in terms of their composition. Four broad bands are visible in all the samples in the ranges 1388-1368, 957-915, 716-703 and 355-338 cm^{-1}. The bands located between 338-355, 703-716 and 1368-1388 cm^{-1} all appear to decrease in relative intensity (compared to the peak at 915-957 cm^{-1} which increases in intensity).

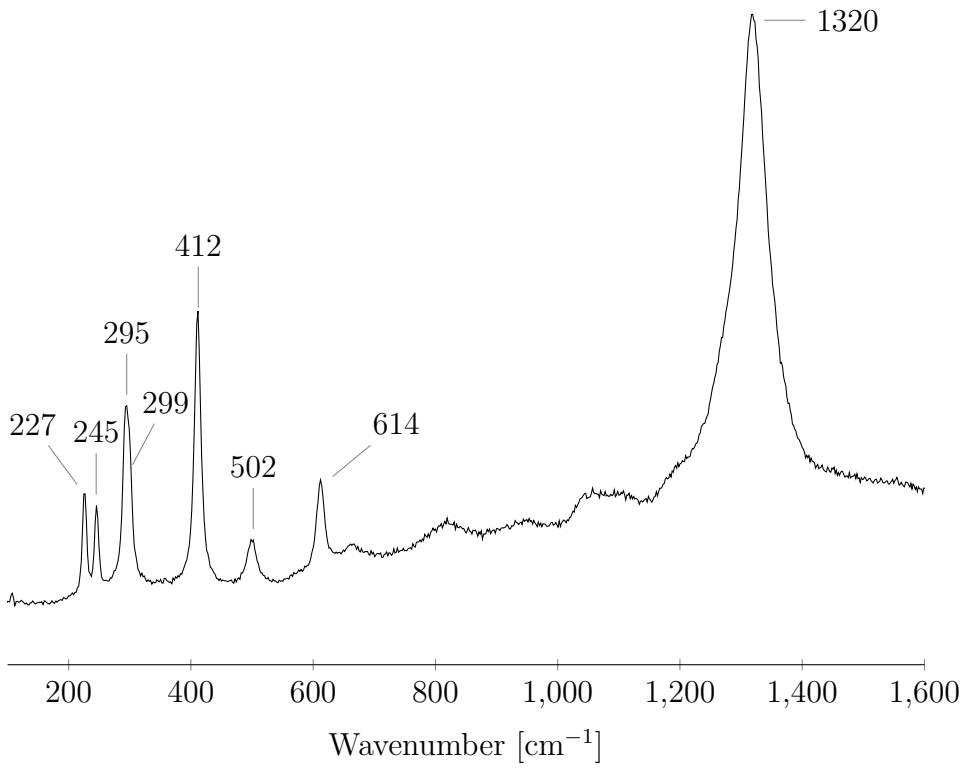

Figure 4.18: *Raman spectrum of* ***100/0 Fe/SiO$_2$****.*

While Raman spectroscopy is not a quantitative technique, it does seem reasonable to conclude that the three peaks which decrease on increasing silica content are a result of Fe-O vibrational modes, while the other peak involves a vibrational mode associated with silica. This change in peak intensity with increasing silica content is illustrated by the arrows in Figure 4.19.

The peaks at 338-355, 703-716 and 1368-1388 cm^{-1}, as well as the shape of the Raman spectra, agree with literature spectra obtained for 2-line ferrihydrite[242,243]. The literature values for these peaks are 370, 710 and 1340 cm^{-1} respectively, slightly lower than those observed. However, a trend is noticeable, with a higher silica content resulting in a slight blue-shift in the location of peak maxima. The presence of some silicon atoms in Fe-O linkages would decrease the reduced mass of Fe-O oscillations, thus resulting in the observed shift to higher wavenumbers. Similarly, the vibrational band occurring at 915-957 cm^{-1} is ascribed to a ν_3 asymmetric vibrational mode of silicate anions (SiO_4^{4-})[244]. As the silica content

decreases, this band is red-shifted, suggesting it contains some Fe-character. Both these trends provide evidence of iron-silica interactions present even prior to reduction.

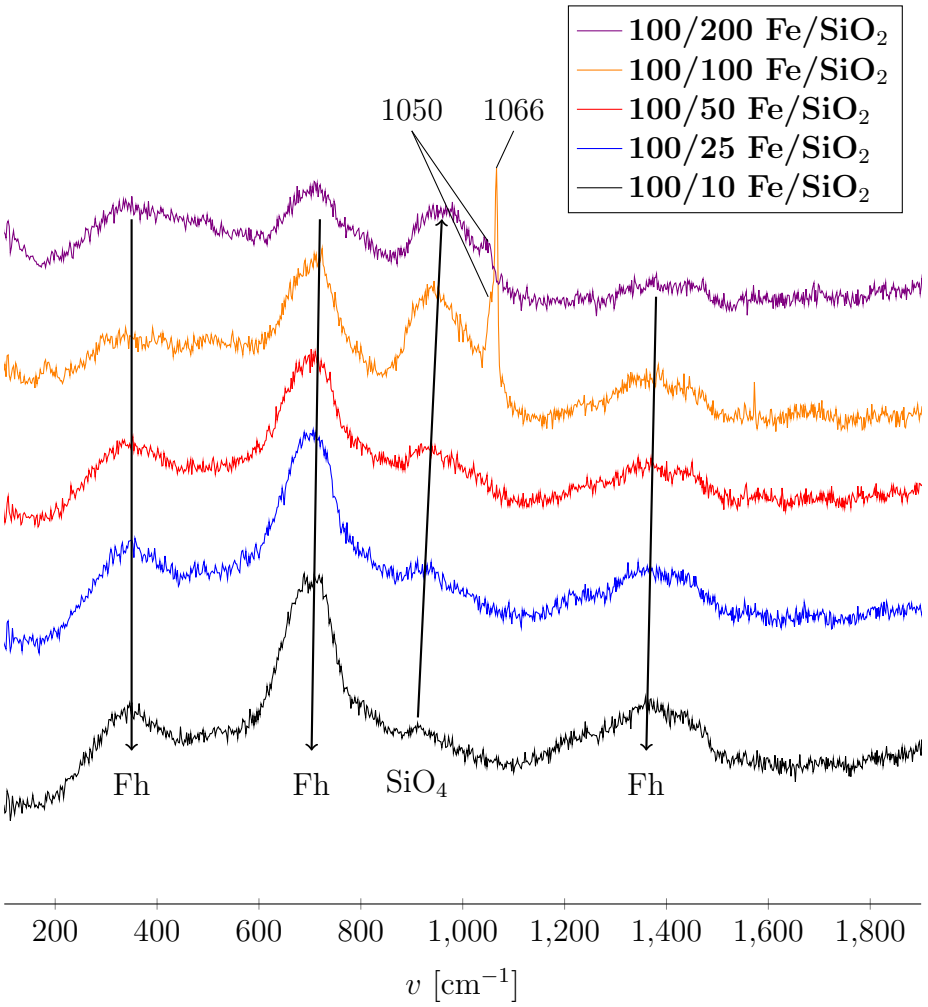

Figure 4.19: *Raman spectra of (a)* ***100/10 Fe/SiO$_2$****, (b)* ***100/25 Fe/SiO$_2$****, (c)* ***100/50 Fe/SiO$_2$****, (d)* ***100/100 Fe/SiO$_2$*** *and (e)* ***100/200 Fe/SiO$_2$****. The changes in peak intensity with an increase in silica content are indicated by the arrows.*

It is also of interest to note that the samples with the two highest silica contents (**100/100 Fe/SiO$_2$** and **100/200 Fe/SiO$_2$**) both present an additional absorption band at 1050 cm^{-1}. This is a vibrational mode of vitreous silica, suggesting that these two samples contain a significant amount of silica glass[245]. The absence

of this band in the lower silica-content samples suggests that the silica is very homogeneously mixed amongst the iron oxide until a critical silica content (somewhere between 50 and 100 weight parts) is reached. Finally, **100/100 Fe/SiO$_2$** exhibits a very intense band at 1066 cm^{-1}. This is ascribed to a symmetric N-O vibration of the nitrate anion, an indication that nitrate salt is still present in the sample, even after washing[246].

4.6 X-Ray Powder Diffraction

The X-ray powder diffractogram for **100/0 Fe/SiO$_2$** is shown in Figure 4.20. It exhibits sharp reflections characteristic of a crystalline material. Pattern matching reveals that only a single crystalline phase is present *viz.* hematite. The experimental pattern was fitted with the hematite structure using the Rietveld method and the resulting average crystallite size, determined using the fundamental parameter approach and full pattern refinement, was 52.7 ± 0.2 nm.

Figure 4.21 contains the X-ray powder diffractograms of the silica-containing samples. The addition of silica has significantly altered the resulting samples, as evidenced by the vastly different diffractograms. **100/10 Fe/SiO$_2$**, **100/25 Fe/SiO$_2$** and **100/50 Fe/SiO$_2$** contain two broad reflections at d-spacings of approximately 2.55 Å and 1.50 Å, while only one reflection is visible in **100/100 Fe/SiO$_2$** and **100/200 Fe/SiO$_2$**. These are consistent with the 2-line form of ferrihydrite[51–53,247,248]. The broad reflections are a result of extremely low crystallinity within the sample. The relatively high diffuse intensity on the low-angle side of the 2.55 Å reflection, which results in an asymmetric peak, is characteristic of two-line ferrihydrite[52].

As the silica content increases to 50 weight parts for 100 weight iron in **100/50 Fe/SiO$_2$**, there is an apparent shift in the 2.55 Å reflection to a higher d-spacing (lower 2θ). However, vitreous silica exhibits very broad reflections in the d-spacing interval of 4.0 Å to 3.6 Å[249]. This corresponds to 2θ values between 25° and 29°. The formation of vitreous silica in this sample explains this apparent shift in degrees two-theta, as the observed reflection is the sum of two broad overlapping reflections. A further increase in silica content with **100/100 Fe/SiO$_2$** and

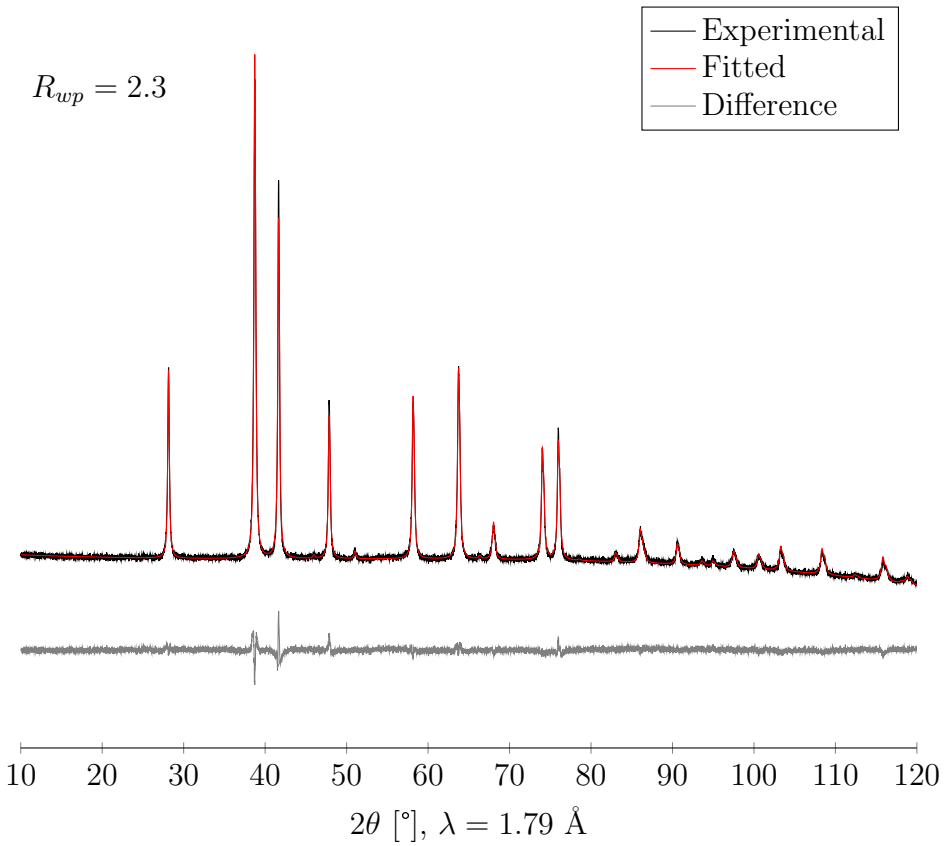

Figure 4.20: *Experimental and fitted XRPD pattern of* ***100/0 Fe/SiO$_2$****. The crystalline phase present is hematite.*

100/200 Fe/SiO$_2$ results in an even greater shift of this peak as an increasing amount of vitreous silica is formed and scattering from these domains has a greater contribution to the shape of the measured reflection. This is especially apparent in **100/200 Fe/SiO$_2$**, where there is a maximum in intensity at 3.7 Å ($2\theta = 28°$).

Increasing the silica content also results in a broadening of the two reflections, with the reflection at 1.50 Å disappearing completely in **100/100 Fe/SiO$_2$** and **100/200 Fe/SiO$_2$**. The increasing concentration of silica during synthesis further reduces the already-poor crystallinity observed in 2-line ferrihydrite. TEM data suggests that the mean particle diameters in **100/25 Fe/SiO$_2$** and **100/50 Fe/SiO$_2$** are the same, however the reflections for **100/50 Fe/SiO$_2$** are broader. This is the result of a decrease in coherent scattering domain size within **100/50 Fe/SiO$_2$** and further supports the idea of a homogeneous substitution of silicon

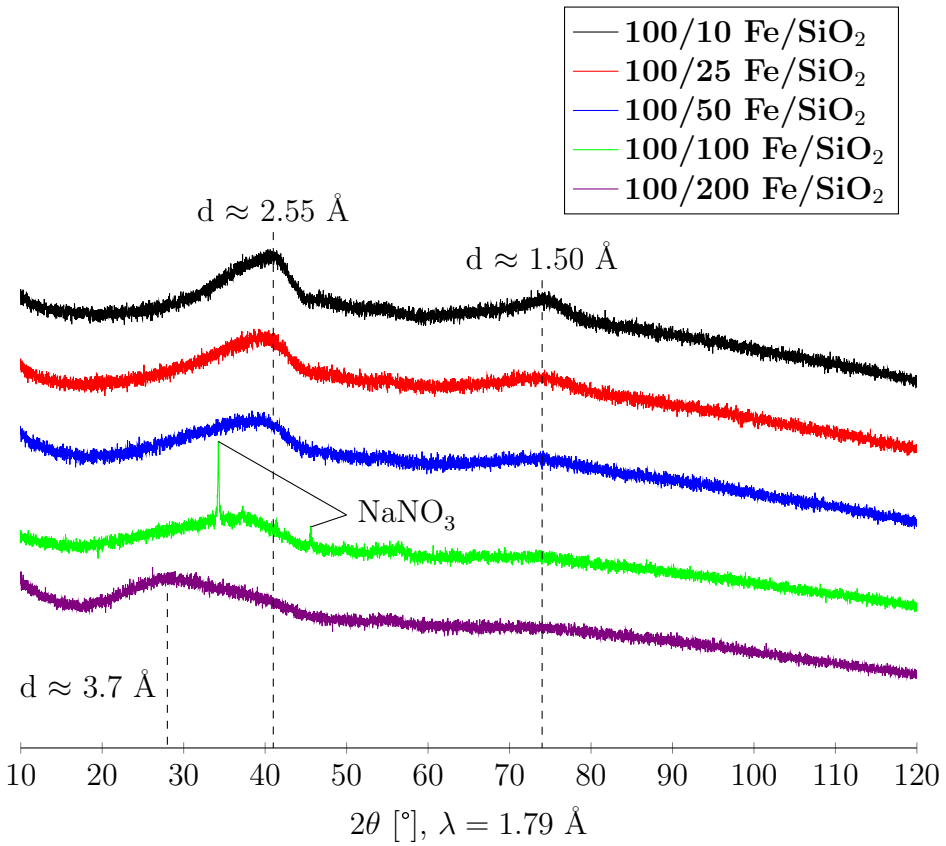

Figure 4.21: *XRPD patterns of* ***100/10 Fe/SiO$_2$****,* ***100/25 Fe/SiO$_2$****,* ***100/50 Fe/SiO$_2$****,* ***100/100 Fe/SiO$_2$*** *and* ***100/200 Fe/SiO$_2$****.*

within the ferrihydrite lattice, resulting in increased strain and disorder which contributes to the increased peak width[250].

Finally, **100/100 Fe/SiO$_2$** exhibits several sharp reflections which have been matched to crystalline sodium nitrate, despite the fact that the precipitate was thoroughly washed. During precipitation, the silica has likely encapsulated large amounts of sodium and nitrate ions (present as a result of sodium metasilicate and iron(III) nitrate respectively), thus preventing their removal during the washing step of the synthesis.

4.7 Nitrogen Physisorption

The BET surface area, total pore volume and average pore diameter for all six samples obtained from nitrogen physisorption measurements are summarised in Table 4.4, while the adsorption isotherms and pore-size distribution data (obtained by applying the BJH method on the desorption isotherm) are summarised in Figures 4.22 and A.1 - A.6 in Appendix A.

Table 4.4: *BET surface area (S_{BET}), total pore volume (TPV) and average pore diameter ($\bar{D}_{pore}$) of the iron oxide samples.*

Sample	$S_{\mathbf{BET}}$ **[m^2.g^{-1}]**	**TPV [cm^3.g^{-1}]**	$\bar{D}_{pore}$ **[nm]**
100/0 Fe/SiO$_2$	22.87	0.158	22.7
100/10 Fe/SiO$_2$	233.6	0.387	5.5
100/25 Fe/SiO$_2$	324.0	0.531	5.8
100/50 Fe/SiO$_2$	312.6	0.370	5.1
100/100 Fe/SiO$_2$	86.18	0.258	8.6
100/200 Fe/SiO$_2$	142.2	0.532	17.4

100/0 Fe/SiO$_2$ has the lowest surface area of all the samples with a value of 22.87 m^2.g^{-1}. The pore size distribution in Figure 4.22 indicates that most pores are between 18 and 32 nm in diameter, slightly skewed towards the lower side of this range. The iron oxide particles present in this sample are considerably larger than in the other samples, resulting in the lower measured surface area.

100/10 Fe/SiO$_2$, **100/25 Fe/SiO$_2$** and **100/50 Fe/SiO$_2$** all demonstrate considerably higher surface areas, with respective values of 233.6, 324.0 and 312.6 m^2.g^{-1}. This is a result of the silica structural promoter stabilising small iron oxide crystallites. Increasing the silica content from 10 to 25 weight parts results in an almost 50 % increase in surface area, a result of even smaller iron oxide crystallites being formed. A further increase to 50 weight parts silica results in a slight decrease in surface area. This suggests the particles in **100/50 Fe/SiO$_2$** are approximately the same size as **100/25 Fe/SiO$_2$**, but that there is likely larger

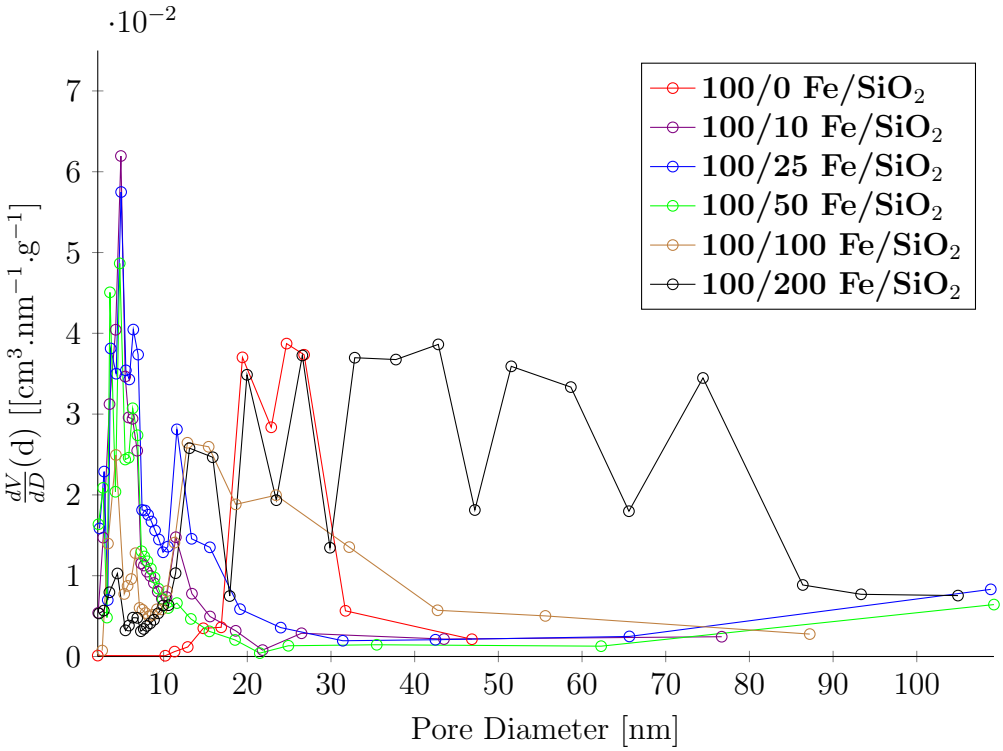

Figure 4.22: *Pore size distributions calculated from the desorption isotherm.*

particles of silica forming, resulting in the slight surface area decrease. The pore size distributions, shown in Figure 4.22, are similar for all three samples, with majority of the pores being below 10 nm in size.

100/100 Fe/SiO$_2$ exhibits a vastly different isotherm to the lower silica content samples. The surface area is also lower at 86.18 m^2.g^{-1} . **100/100 Fe/SiO$_2$** has considerably lower total pore volume. The pore size distribution, Figure 4.22, shows the same shape as the lower silica content samples below 10 nm pore diameter, but it also demonstrates a very large number of pores having a diameter between 10 and 40 nm. This suggests the sample is a mix of dispersed oxide particles as with the lower silica content sample, but also contains mesoporous silica in significant quantities. TEM data confirms that **100/100 Fe/SiO$_2$** contains a large amount of silica dispersed between the iron oxide particles, as well as iron oxide particles dispersed in silica glass.

100/200 Fe/SiO$_2$ has a surface area of 142.2 m^2.g^{-1}. The pore size distribution

in Figure 4.22 shows less pores below 10 nm in diameter and majority of pores with diameters ranging from 15 to 80 nm. The distribution of these pore diameters is fairly uniform. This suggest that **100/200 Fe/SiO$_2$** is largerly a silica sample. Any iron oxide particles that have formed are most likely encapsulated within the silica matrix. TEM data confirms that **100/200 Fe/SiO$_2$** consists largely of small iron oxide domains encapsulated within an iron-substituted silica glass.

If it is assumed that the particles are solid spheres with a smooth surface, and all of the same size, the surface area may be related to the average equivalent particle diameter by the following equation[251]:

$$D_{\mathrm{BET}} = \frac{6000}{\rho S_{\mathrm{BET}}}$$

where D_{BET} is the average diameter of a spherical particle, S_{BET} represents the measured surface area of the powder in $\mathrm{m^2.g^{-1}}$ and ρ is the theoretical density of the sample in $\mathrm{g.cm^{-3}}$. Based on XRPD, TEM and Raman data, it was assumed that **100/0 Fe/SiO$_2$** is hematite (ρ = 5.30 $\mathrm{g.cm^{-3}}$) and the remaining samples were ferrihydrite (ρ = 2.85 $\mathrm{g.cm^{-3}}$).

The resulting particle sizes are shown in Table 4.5. As expected, the low surface area of **100/0 Fe/SiO$_2$** is a result of large particles, while the addition of silica has stabilised the formation of small nanoparticles. The particle size of **100/100 Fe/SiO$_2$** and **100/200 Fe/SiO$_2$** was not calculated since the large amount of silica will have too large an effect on calculated particle sizes.

It is important to note that the particle size obtained using BET surface area is likely slightly larger than the true size, since a small amount of surface area is lost due to the nanoparticles forming aggregates.

Table 4.5: *The average particle size calculated using the BET surface area measured for* ***100/0 Fe/SiO$_2$****,* ***100/10 Fe/SiO$_2$****,* ***100/25 Fe/SiO$_2$*** *and* ***100/50 Fe/SiO$_2$****.*

Sample	Particle Size [nm]
100/0 Fe/SiO$_2$	49.5
100/10 Fe/SiO$_2$	9.01
100/25 Fe/SiO$_2$	6.50
100/50 Fe/SiO$_2$	6.73

4.8 Mössbauer Absorption Spectroscopy

Mössbauer spectra recorded at 300 K (RTMS) for each sample are shown in Figure 4.23 and Figure 4.24. The RTMS spectrum of **100/0 Fe/SiO$_2$** (Figure 4.23 (a)) consists of a sextet with hyperfine parameters of δ = 0.39 mm.s^{-1}, ΔE_Q = -0.20 mm.s^{-1}, B_{hf} = 51.7 T, consistent with those reported for hematite.[2,43,252–257].

The RTMS spectra of the silica-bearing samples (Figure 4.23 (b)-(c) and Figure 4.24 (a)-(c)) all presented themselves as doublets and were fitted with distributions of ΔE_Q. The fitting of such spectra with distributions of hyperfine parameters has been used extensively to characterise poorly crystalline iron oxides[43,258,259]. This takes into account the defective nature of such materials. It is believed that these distributions of ΔE_Q result from the varied environment surrounding the Fe atoms.

For the silica-bearing samples, $\delta \approx 0.35$ mm.s^{-1}. The ΔE_Q values are part of a right-skewed distribution in the range 0-2 mm.s^{-1}, with maximum probabilities in each distribution located at $\Delta E_Q \approx 0.9$ mm.s^{-1}, and distribution half widths of 1.2 mm.s^{-1}. These values are consistent with high-spin, Fe^{3+} ions in an octahedral environment. The higher the ΔE_Q value, the larger the degree of distortion at octahedral Fe^{3+} sites, while the halfwidths give an indication of the variation in Fe^{3+} site geometry[43,258,260].

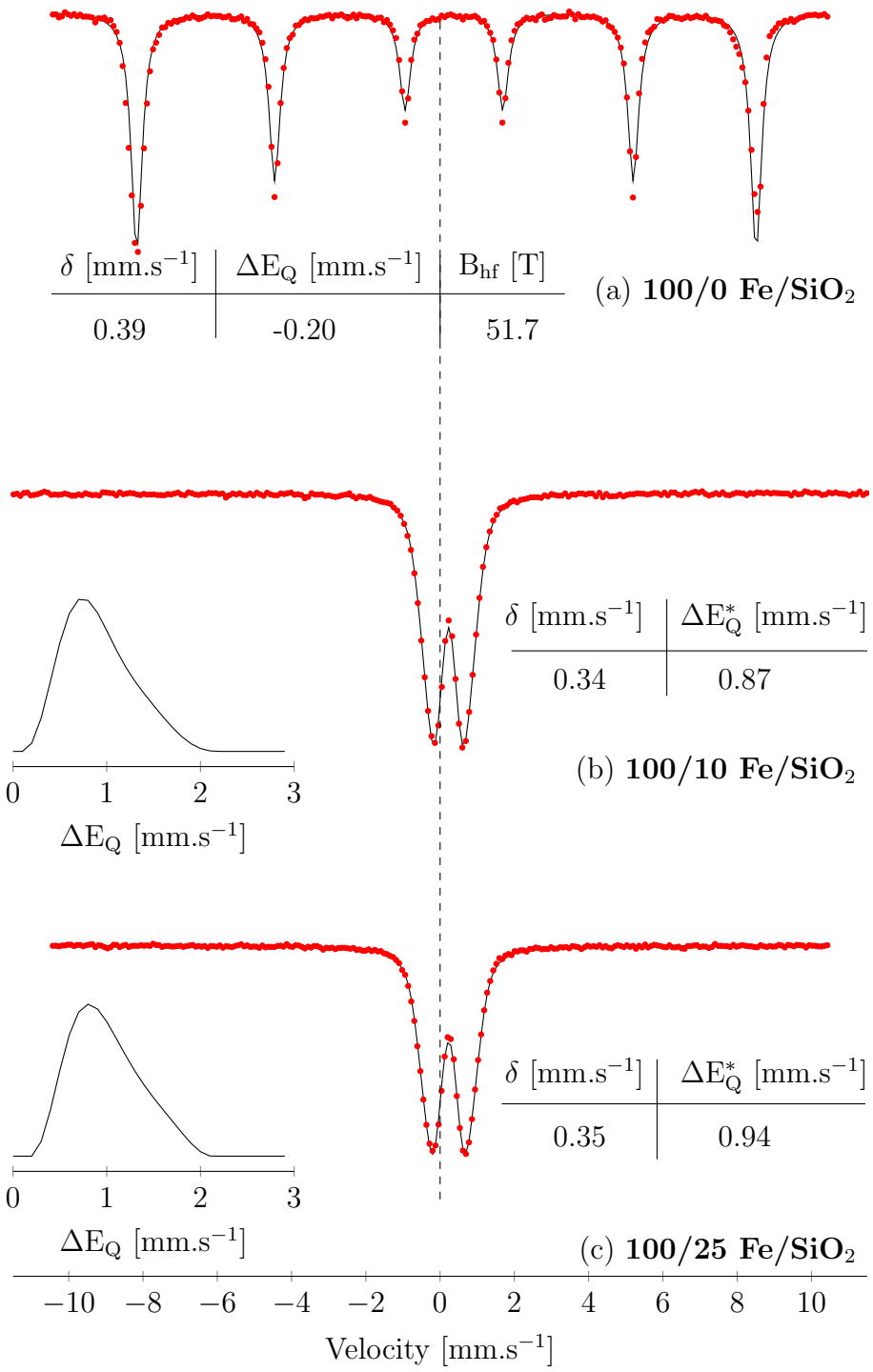

Figure 4.23: *RTMS spectra of* ***100/0 Fe/SiO$_2$****,* ***100/10 Fe/SiO$_2$*** *and* ***100/25 Fe/SiO$_2$****. The distribution of ΔE_Q for the fitted distributions and key magnetic hyperfine values are shown as insets. *Median value of the distribution.*

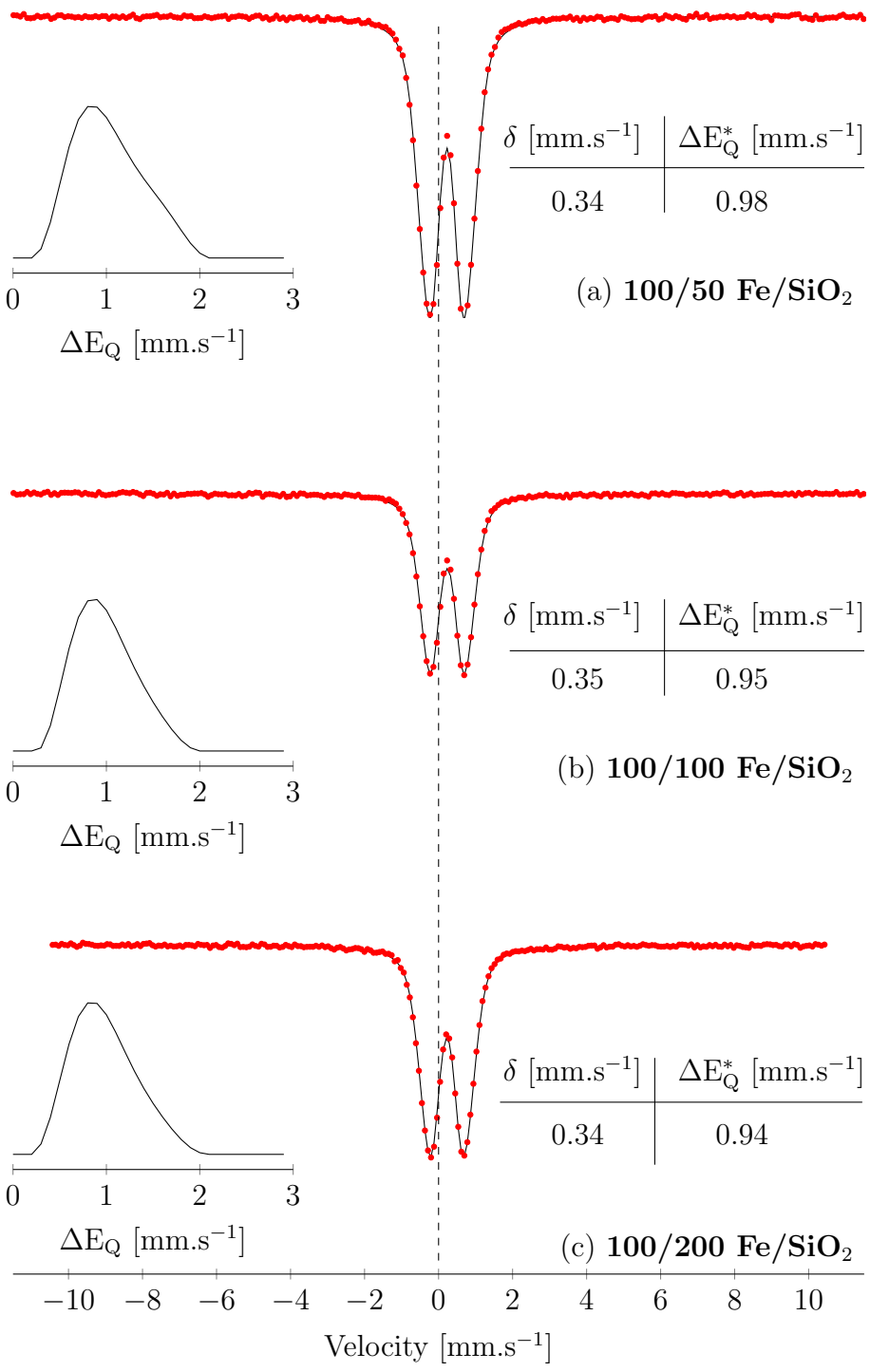

Figure 4.24: *RTMS spectra of* ***100/50 Fe/SiO$_2$****,* ***100/100 Fe/SiO$_2$*** *and* ***100/200 Fe/SiO$_2$****. The distribution of quadrupole splitting for the fitted distributions and key magnetic hyperfine values are shown as insets. *Median value of the distribution.*

In comparison, the distribution of quadrupole splitting for pure synthetic two-line ferrihydrite exhibits a median value of $\Delta E_Q \approx 0.78$ mm.s^{-1} and a distribution half width of 0.86 mm.s^{-1}. These are both lower than the data reported for the silica-bearing particles, suggesting that the presence of silica results in an increased distortion in the octahedral environment of Fe^{3+} ions[43].

The presence of doublets in the silica-bearing samples are most likely due to the presence of SPM crystallites within the sample. Measurement of Mössbauer spectra of SPM particles at temperatures well above the blocking temperature, in which case the magnetic relaxation frequency is significantly greater than the Mössbauer measurement frequency, causes the usual 6-line spectrum to collapse into a quadrupole-doublet[261–263]. This effect is related to the particle volume (particle diameter) and indicates that very small crystallites are present in these samples.

In order to identify the iron oxide phase present in the silica-bearing samples, it was necessary to perform Mössbauer measurements at 4.2 K (LTMS), since the spectra obtained at room temperature were not resolved and therefore the associated phases present in each sample could not be unambiguously identified. MS spectra recorded at 4.2 K are capable of removing all effects of superparamagnetic relaxation and collective magnetic excitations and, where applicable, mitigate variations of recoil-free fractions ensuing from small particle sizes[43].

The LTMS spectrum of **100/0 Fe/SiO$_2$** is shown in Figure 4.25. It was fitted with a single sextet, and the corresponding hyperfine values of $\delta = 0.49$ mm.s^{-1}, $\Delta E_Q = 0.40$ mm.s^{-1} and $B_{hf} = 53.9$ T are in excellent agreement with those reported for hematite[2,43,252–257].

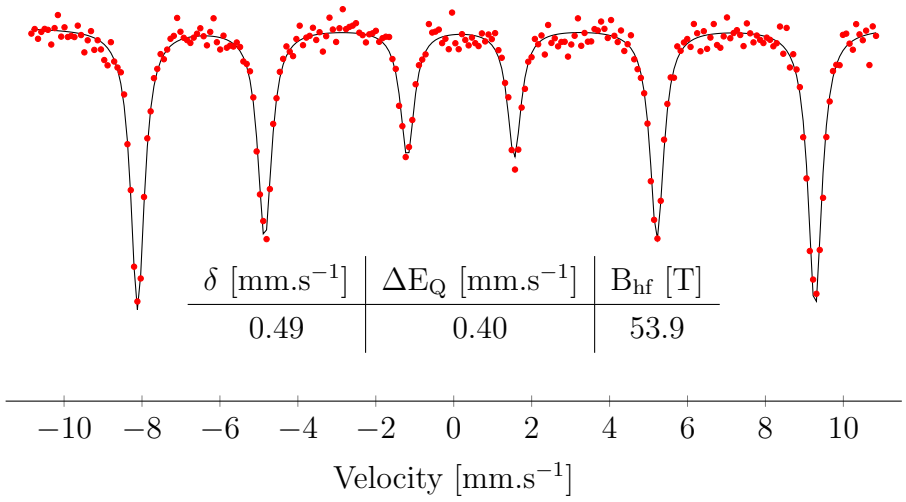

Figure 4.25: *LTMS spectrum of* ***100/0 Fe/SiO$_2$****.*

The LTMS spectra of **100/10 Fe/SiO$_2$**, **100/25 Fe/SiO$_2$** and **100/50 Fe/SiO$_2$**, shown in Figure 4.26, all exhibit fully resolved sextets and were also fitted with a distribution of the hyperfine magnetic field. The need for a distribution arises from a range of crystallite sizes present in the sample and distortions in the Fe-site geometry. Fitting gives a value of $\delta \approx 0.48$ mm.s^{-1} for all three samples. In all cases, $\Delta E_Q \approx 0$ mm.s^{-1}. These values are consistent with those obtained for 2-line ferrihydrite[153,196,236,264]. The magnetic hyperfine distributions are all left-skewed and exhibit median B_{hf} values at 49.0 T, 48.0 T and 46.9 T for **100/10 Fe/SiO$_2$**, **100/25 Fe/SiO$_2$** and **100/50 Fe/SiO$_2$** respectively, i.e. the median value of B_{hf} decreases with increasing silica content. This decrease in B_{hf} has in the past been attributed to a decrease in particle size[43], however it also seems likely that the increased amount of silica within the ferrihydrite framework is contributing to this observed decreasing trend in the B_{hf} values.

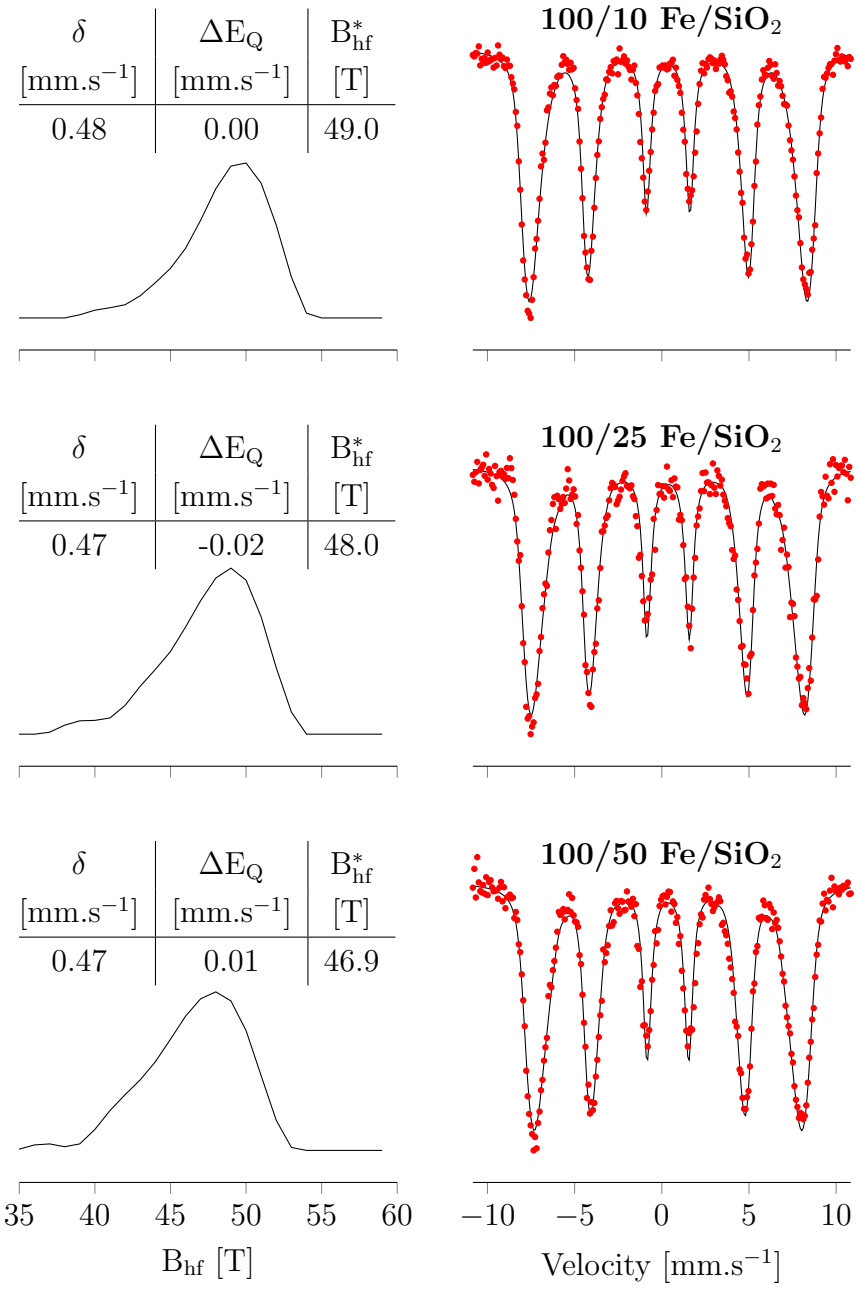

Figure 4.26: *LTMS spectra of* ***100/10 Fe/SiO$_2$****,* ***100/25 Fe/SiO$_2$*** *and* ***100/50 Fe/SiO$_2$*** *on the right, with the distributions of B_{hf} and a table of hyperfine parameters on the left. *Median value of the distribution.*

The LTMS spectra of **100/100 Fe/SiO$_2$** and **100/200 Fe/SiO$_2$** (Figure 4.27) also exhibit magnetically-resolved sextets, however they are more complex. They were best fitted with two distributions of the hyperfine magnetic field. Fits using a doublet (representing a diamagnetic iron silicate species within the sample) and a distribution of B_{hf} were investigated, however this gave relatively poor fits.

The first distribution for **100/100 Fe/SiO$_2$** and **100/200 Fe/SiO$_2$** (shown in blue on both spectra in Figure 4.27) has $\delta \approx 0.45$ mm.s^{-1} for **100/100 Fe/SiO$_2$** and **100/200 Fe/SiO$_2$**. They both have $\Delta E_Q \approx 0$ mm.s^{-1}, and median B_{hf} of 44.8 T. These are consistent with small silicon-substituted ferrihydrite particles that were observed in the lower silica-content samples. The decrease in B_{hf} compared to **100/50 Fe/SiO$_2$** confirms the above observed trend between silica content and median B_{hf}.

The second distributions for **100/100 Fe/SiO$_2$** and **100/200 Fe/SiO$_2$** (shown in orange on both spectra in Figure 4.27) exhibit a very broad range of hyperfine field values, but isomer shifts and quadrupole splittings that are consistent with Fe^{3+} cations. They have thus been attributed to very small, isolated Fe^{3+} domains present within the vitreous silica network, consistent with the TEM data discussed in Chapter 4.4. The relative areas of these distributions may be related to their phase-abundance within the samples. They are 33% and 35% for **100/100 Fe/SiO$_2$** and **100/200 Fe/SiO$_2$** respectively. This suggests that approximately two-thirds of the iron is contained as ferrihydrite particles within the silica matrix, while the remaining third exists as Fe^{3+} domains encapsulated by the silica.

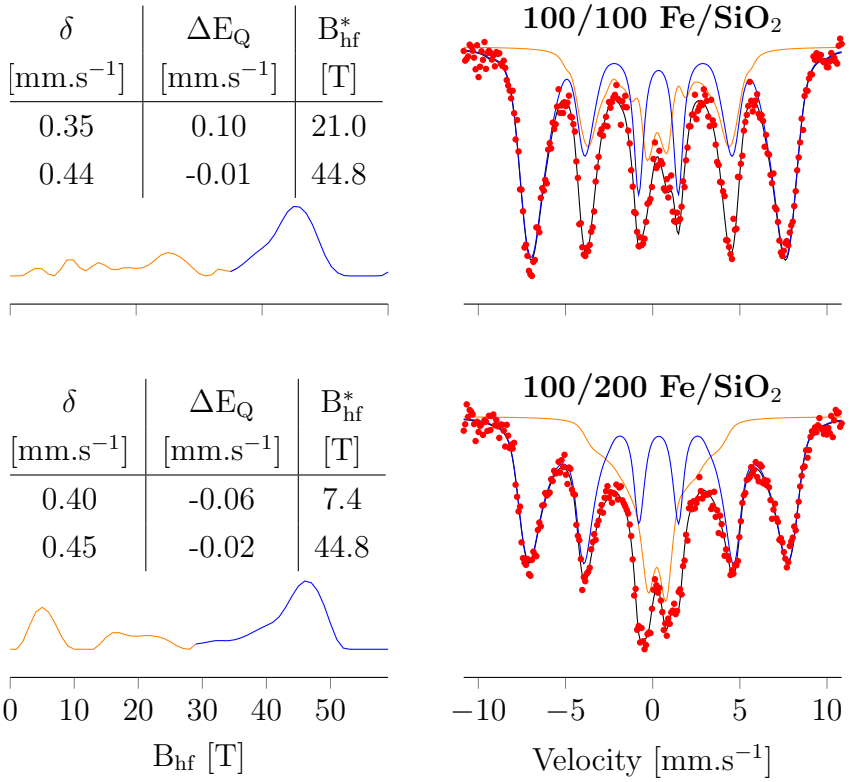

Figure 4.27: *LTMS spectra of* ***100/100 Fe/SiO$_2$*** *and* ***100/200 Fe/SiO$_2$*** *shown on the right, with the distributions of B_{hf} and a table of hyperfine parameters on the left. *Median value of the distribution.*

While **100/0 Fe/SiO$_2$** has been unambiguously identified as hematite at room temperature already, it was necessary to perform MS measurements at 4.2 K in a 10 T magnetic field applied parallel to the gamma rays (AFMS) in order to confirm the presence of a ferrihydrite phase present in these samples.

The iron oxides are generally either FM, AFM or FiM. As a result, changes are observed in their applied field MS spectra, as discussed in Chapter 3.8.2. However, it has been reported that ferrihydrite is different and demonstrates a unique form of magnetism termed speromagnetism in which the moments are aligned in random, isotropic directions[265]. This translates to an unusual broadening of the line width, particularly for lines 1 and 6 (the outer lines), while there is a slight increase in the intensity of lines 2 and 5, similar to what is expected for AFM materials.

The AFMS spectra for **100/10 Fe/SiO$_2$**, **100/25 Fe/SiO$_2$** and **100/50 Fe/SiO$_2$** are shown in Figure 4.28 and were fitted with a single distribution of the measured magnetic field, B_{meas}. The median value of B_{meas} was 48.9, 47.8 and 47.1 T for **100/10 Fe/SiO$_2$**, **100/25 Fe/SiO$_2$** and **100/50 Fe/SiO$_2$** respectively i.e. B_{meas} decreasing with increasing silica content. These are very similar to the values obtained from ZFMS measurements (49.0, 48.0 and 46.9 T respectively). Pure 2-line ferrihydrite has a median B_{meas} between 46 and 50 T[266].

The area ratios of lines 2 and 5 to lines 3 and 4 ($A_{2,5}/A_{3,4}$) of the fits from ZFMS and AFMS measurements are shown in Table 4.6. In zero field, all three samples have an area ratio of approximately 2. This value is 2 for **100/10 Fe/SiO$_2$** and increases slightly to 2.16 for **100/25 Fe/SiO$_2$** and **100/50 Fe/SiO$_2$**, a result of increasing intensity of lines 2 and 5. Lines 1 and 6 also broaden considerably in each sample. These changes were also observed for pure 2-line ferrihydrite samples in an applied field[196,267].

Table 4.6 also shows the B_{meas} distribution widths from ZFMS and AFMS measurements. The distribution width of B_{meas} is approximately 5.5 T for each sample, which is much broader than those in zero field, as expected for particles randomly orienting themselves in the applied field. Broadening of the distribution in an applied field has been observed for pure 2-line ferrihydrite particles[43,267].

These three observations from the AFMS measurements *viz.* the similar median B_{meas} values, slightly increasing line intensities of lines 2 and 5 and the broadening of lines 1 and 6, as well as the B_{meas} distribution widths are all consistent with the values observed for ferrihydrite[196,265].

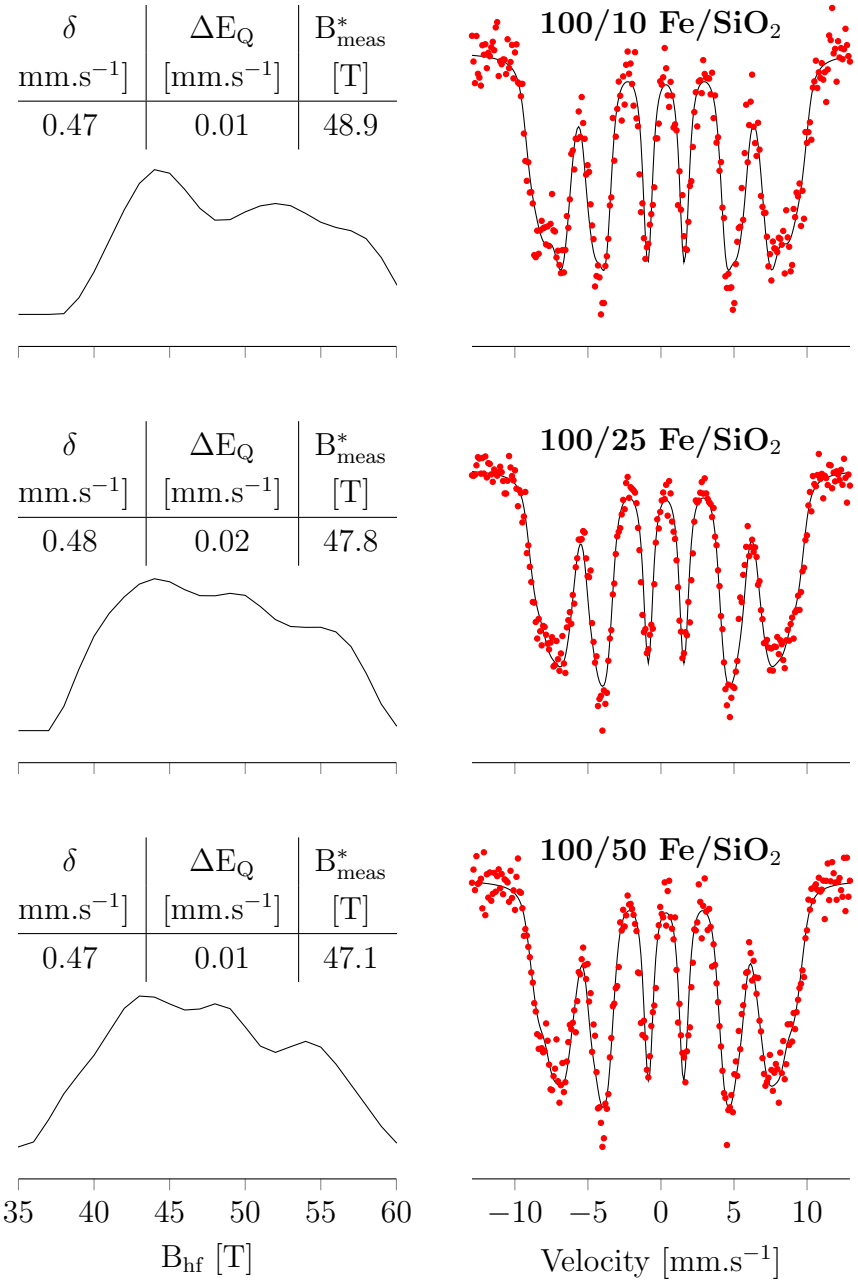

Figure 4.28: *LTMS spectra of* ***100/10 Fe/SiO$_2$****,* ***100/25 Fe/SiO$_2$*** *and* ***100/50 Fe/SiO$_2$*** *in a 10 T applied magnetic field on the right, with distributions of B_{meas} and a table of hyperfine parameters on the left. *Median value of the distribution.*

Table 4.6: *Area ratios ($A_{2,5}/A_{3,4}$) of lines 2 and 5 to lines 3 and 4 and the distribution widths of B_{hf} and B_{meas} for the iron-silica samples measured in zero-field and in applied field MS experiments. The values shown for* ***100/100 Fe/SiO$_2$*** *and* ***100/200 Fe/SiO$_2$*** *are for the high-field distributions corresponding to the ferrihydrite-phases. The widths are given by the standard deviation of each distribution.*

Sample	$A_{2,5}/A_{3,4}$		**Std. Dev. [T]**	
	0 T	10 T	0 T	10 T
100/10 Fe/SiO$_2$	1.98	2.04	2.81	5.54
100/25 Fe/SiO$_2$	1.99	2.16	3.22	5.42
100/50 Fe/SiO$_2$	1.99	2.16	3.54	5.51
100/100 Fe/SiO$_2$	2.12	1.86	3.74	6.43
100/200 Fe/SiO$_2$	1.07	1.09	4.99	5.68

The outer lines (lines 1 and 6) in the AFMS spectra of **100/100 Fe/SiO$_2$** and **100/200 Fe/SiO$_2$**(Figure 4.29) also broaden. As with the zero-field spectra, these were fitted with two distributions of the measured magnetic field each. The median values of the high-field distribution are 44.0 and 43.0 T respectively. These are lower than those measured at zero-field (44.8 T for both samples). If it is assumed that the magnetic moments have randomly oriented themselves, it is likely that there is some heavy overlap of the two distributions, thus causing the median values to be slightly different than those in zero-field.

The median of the measured magnetic field for the low-field distribution corresponding to the Fe^{3+} domains in silica is largely unchanged in **100/100 Fe/SiO$_2$** (21.0 T to 19.3 T), however it increases from 7.4 T to 20.7 T in **100/200 Fe/SiO$_2$**. This increase of 13.3 T in **100/200 Fe/SiO$_2$** seems unreasonably high, since the applied field is only 10 T and hence the maximum increase in the measured field magnitude should not exceed this. However, this is readily explained by considering an overlap of the two distributions. This would shift the median to a higher than expected value owing to some contribution from the high-field distribution.

The low-field distribution accounts for only 12% of the sample in **100/100 Fe/SiO$_2$** (compared to 33% in zero-field). This suggests that the high-field distribution con-

tains a significant amount of the silica-incorporated Fe^{3+} species in addition to the ferrihydrite, indicating that the measured field for the low-field distribution has increased on application of a magnetic field.

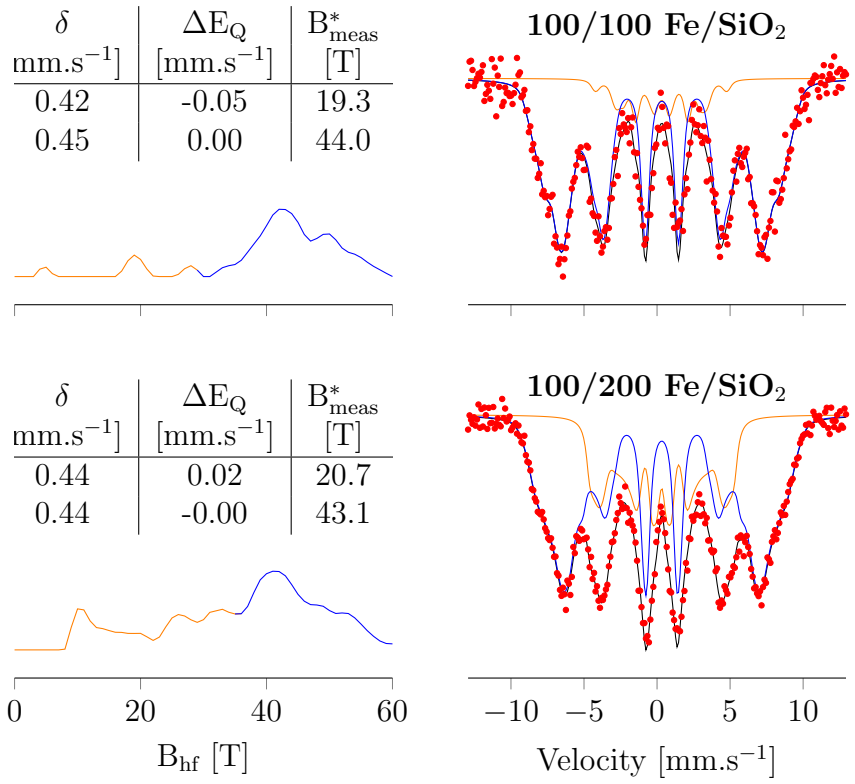

Figure 4.29: *LTMS spectra of* ***100/100 Fe/SiO$_2$*** *and* ***100/200 Fe/SiO$_2$*** *in a 10 T applied magnetic field on the right, with distributions of B_{meas} and a table of hyperfine parameters on the left. *Median value of the distribution.*

The low-field distribution in **100/200 Fe/SiO$_2$** accounts for 32% of the total distribution of magnetic fields, in good agreement with the zero-field measurement (35%).

These data suggest that the applied magnetic field does not alter the position of the high-field distribution, merely broaden it as the particles randomly orientate themselves with respect to the applied field. This confirms the presence of silicon-substituted ferrihydrite particles within these two samples. The shift to higher magnetic fields in the low-field distributions on application of a magnetic field suggests that the magnetic moments of the Fe^{3+} domains within the silica matrix

align parallel to the applied field. This is similar to the behaviour of very small Fe^{3+} domains (several atoms at most) observed in iron-spin-glass materials which also exhibit this behaviour in applied magnetic field[268,269].

Table 4.7: *MS hyperfine parameters for* ***100/x Fe/SiO$_2$*** *recorded at 300 K, 4.2 K and 4.2 K in a 10 T applied magnetic field.*

Sample	300 K			4.2 K			4.2 K 10 T		
	δ^*	ΔE_Q^{**}	B_{hf}^{***}	δ^*	ΔE_Q^{**}	B_{hf}^{***}	δ^*	ΔE_Q^{**}	B_{hf}^{***}
100/0 Fe/SiO$_2$	0.39	-0.20	51.7	0.49	0.40	53.9	-	-	-
[a]**100/10 Fe/SiO$_2$**	0.34	0.87	-	0.48	0.00	49.0	0.47	0.01	48.9
[a]**100/25 Fe/SiO$_2$**	0.35	0.94	-	0.47	-0.01	48.0	0.48	0.02	47.8
[a]**100/50 Fe/SiO$_2$**	0.34	0.98	-	0.47	0.01	46.9	0.47	0.01	47.1
[a]**100/100 Fe/SiO$_2$**	0.35	0.95	-	0.35	0.10	21.0	0.44	0.02	20.7
				0.44	-0.01	44.8	0.44	-0.00	43.1
[a]**100/200 Fe/SiO$_2$**	0.35	0.95	-	0.40	-0.06	7.4	0.42	-0.05	19.3
				0.45	-0.02	44.8	0.45	0.00	44.0

$^*\delta$ in mm.s^{-1}, $^{**}\Delta E_Q$ in mm.s^{-1}, $^{***}B_{hf}$ in T.

[a] ΔE_Q (at 300 K) and B_{hf} (at 4.2 K) values reported are the medians of the respective distributions.

4.9 Magnetic Measurements

The magnetisation (M) in zero-field cooled (ZFC), field cooled (FC) and magnetic thermal remanence (TRM) modes for all samples was recorded versus temperature. The magnetisation measurements were converted to mass susceptibility (χ_{DC}), defined as

$$\chi_{DC} = \frac{M}{H} \tag{4.4}$$

where H is the applied magnetic field. χ_{DC} as a function of temperature (χ_{DC}(T) curves) for all the samples are shown in Figure 4.30. For **100/0 Fe/SiO$_2$** (Figure 4.30 (a)), χ_{DC}(T) curves reveal a magnetic transition between 220 and 230 K ascribed to the Morin transition (T_M). It is a structural transition typically found to occur between 250 K and 260 K for large grains of hematite[255]. It induces a change in the magnetic ordering in hematite from weakly ferromagnetic (WFM) above T_M to a canted antiferromagnetic ordering below T_M. Below T_M the spins lie along the *c*-axis of the rhombohedral lattice, equal numbers in either orientation. The spins rotate 90° to the basal *c*-plane, within which they are canted out of exact antiparallelism by a fraction of a degree[270,271]. As a result, T_M is also known as a spin-flop transition.

Many factors contribute to lowering the value of T_M, including a decrease in particle size, changes in morphology and the presence of impurities[253,272–274]. This decrease in T_M with decreasing particle size is attributed to a change in the dipolar magnetic field as a result of lattice dilation in nanoparticles that accompanies a decrease in particle size[253]. Jacob and Abdhul Khadar reported a T_M value of 229 K for 54 nm particles[253], while Zysler *et al.* reported T_M = 200 K for 40 nm particles and T_M = 243 for 83 nm particles[275]. The value of T_M in **100/0 Fe/SiO$_2$** is 232 K, 223 and 220 K when measured from the ZFC, FC and TRM curves respectively. This suggests the hematite particles present in **100/0 Fe/SiO$_2$** have a mean particle diameter between 50 and 60 nm, in fairly good agreement with TEM (Chapter 4.4) which suggested a particle size of 39 ± 12 nm.

The χ_{DC}(T) curves in ZFC, FC and TRM modes for the silica-containing samples (Figure 4.30 (b)-(f)) are typical of an assembly of SPM nanoparticles. When individual SPM nanoparticles are cooled in the absence of an applied magnetic field their magnetic moments become frozen but remain randomly aligned such

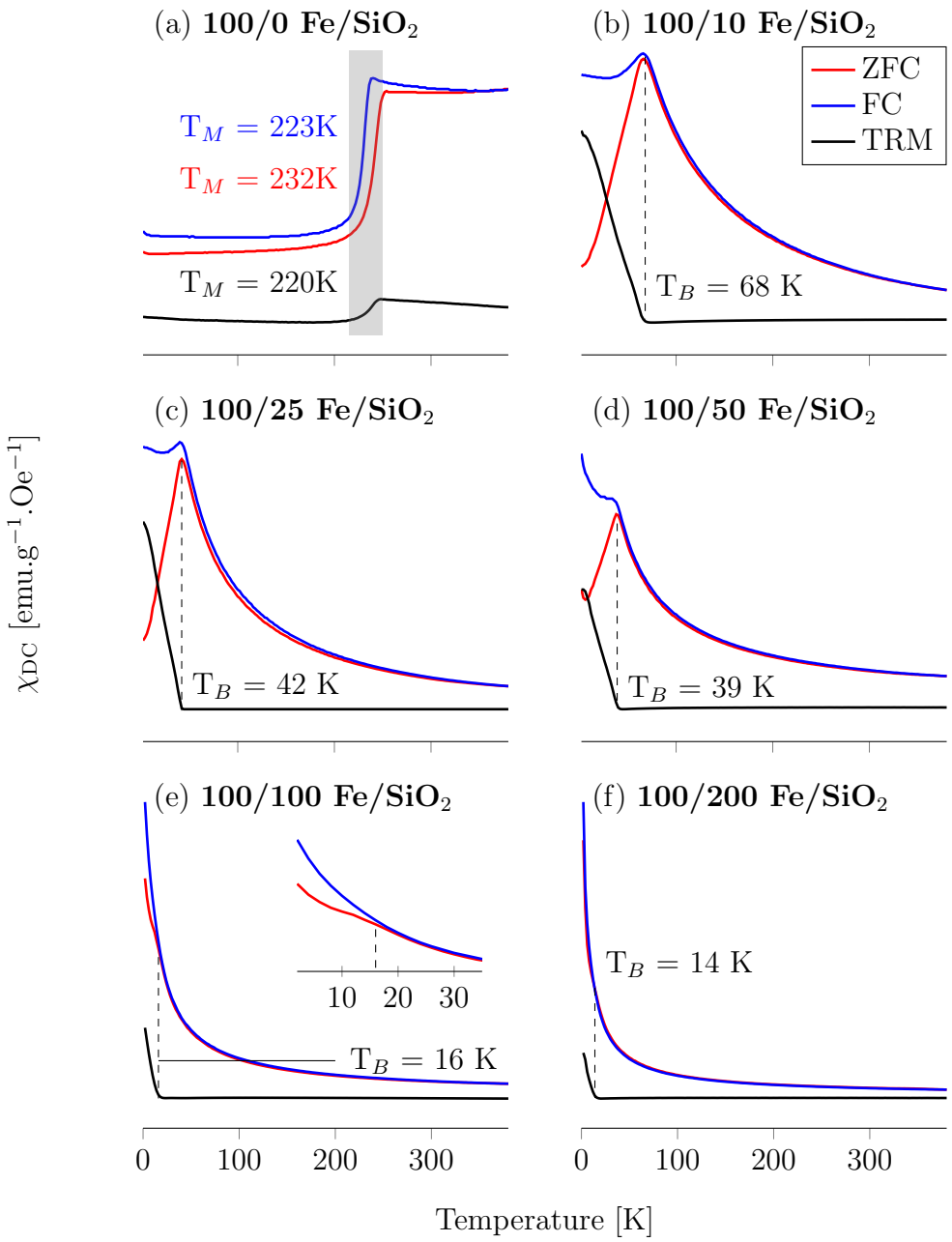

Figure 4.30: *Zero-field cooled (ZFC), field cooled (FC) and thermal remenant magetisation (TRM) DC magnetisation measurements for* ***100/0 Fe/SiO$_2$****,* ***100/10 Fe/SiO$_2$****,* ***100/25 Fe/SiO$_2$****,* ***100/50 Fe/SiO$_2$****,* ***100/100 Fe/SiO$_2$*** *and* ***100/200 Fe/SiO$_2$****. In each case, the applied field (H) has a value of 100 Oe.*

that the resulting magnetisation should average to zero at 0 K[276]. A magnetic field, H, is then applied and kept constant while heating up the sample (ZFC mode). The ordering energy associated with the magnetic field forces an alignment of the magnetic moments along H, while the opposing thermal energy (k_BT) causes their directions to fluctuate, forcing a random distribution of magnetic moments. Magnetisation increases as long as the ordering energy exceeds the thermal energy. Magnetisation reaches a maximum value when these two energies are balanced.

The temperature at which maximum χ_{DC} is reached in ZFC mode is referred to as the blocking temperature (T_B)[204,276]. **100/10 Fe/SiO$_2$**, **100/25 Fe/SiO$_2$** and **100/50 Fe/SiO$_2$** exhibit very clear maxima in their χ_{DC}(T) curves, giving blocking temperatures of 68 K, 42 K and 39 K respectively. The high amounts of silica in **100/100 Fe/SiO$_2$** and **100/200 Fe/SiO$_2$** suppress these maxima at T_B. Instead, the maxima are replaced by small curbs after which χ_{DC} continues to decrease as T increases. The TRM curves for both **100/100 Fe/SiO$_2$** and **100/200 Fe/SiO$_2$** exhibit some thermal magnetic remenance, likely a result of SPM particles initially in a blocked state which rapidly become unblocked as the sample is heated. This tends to suggest that the addition of silica is related to a supression of the blocking temperature. Above T_B, the thermal energy exceeds the ordering energy, causing χ_{DC} to gradually decrease until the highest temperature of the measurements.

At high temperatures, the FC curves for each sample closely follow the ZFC curves, until temperatures close to the blocking temperature, where χ_{DC} increases to a higher value than that measured in the corresponding ZFC curve. This lack of complete reversibility implies that the blocking temperature is not a single, well-defined value but rather consists of a distribution of T_B values as a result of distributions in particle size. Below T_B, the magnetic moments are blocked and almost all aligned along H. In the case of **100/10 Fe/SiO$_2$**, **100/25 Fe/SiO$_2$** and **100/50 Fe/SiO$_2$**, further cooling results only in a small increase in the measured magnetisation[276]. However, χ_{DC} increases sharply at low temperatures for both **100/100 Fe/SiO$_2$** and **100/200 Fe/SiO$_2$** in an apparent hyperbolic fashion.

Using the values of T_B determined for **100/10 Fe/SiO$_2$**, **100/25 Fe/SiO$_2$** and **100/50 Fe/SiO$_2$**, the mean particle sizes were determined using Equation 3.69 and a value for the anisotropy constant equal to $5.9 \cdot 10^5$ J.m^{-3}, previously de-

termined for a co-precipitated silica-ferrihydrite sample[87]. The calculated mean particle diameters are shown in Table 4.8 and compared with the particle diameters obtained using TEM. The calculated particle sizes are 4.2 nm, 3.6 nm and 3.5 nm for **100/10 Fe/SiO$_2$**, **100/25 Fe/SiO$_2$** and **100/50 Fe/SiO$_2$** respectively. These are in good agreement with those measured using TEM, with an increase in silica content stabilising the formation of smaller particles.

Table 4.8: *Blocking temperature (T_B), average crystallite size determined using TEM (D_{TEM}) and average crystallite size determined using T_B (D_{MM}) for* ***100/10 Fe/SiO$_2$****,* ***100/25 Fe/SiO$_2$*** *and* ***100/50 Fe/SiO$_2$****.*

Sample	T_B [K]	D_{TEM} [nm]	D_{MM} [nm]
100/10 Fe/SiO$_2$	68	3.1 ± 0.4	4.2
100/25 Fe/SiO$_2$	42	2.4 ± 0.3	3.6
100/50 Fe/SiO$_2$	39	2.4 ± 0.3	3.5

Correlation with the structural data obtained using TEM, presented in Chapter 4.4, provides some insight into the magnetisation behaviour of **100/100 Fe/SiO$_2$** and **100/200 Fe/SiO$_2$**. Both samples consist of very small iron oxide nanoparticles encapsulated by a bulk silica matrix. In many cases, these domains are no more than several atoms in size. **100/100 Fe/SiO$_2$** does however contain a larger number of iron oxide nanoclusters than **100/200 Fe/SiO$_2$**, which corresponds to the small observable local maximum in its measured ZFC curve. These tiny iron oxide clusters give rise to a broad range of magnetic domain volumes that explains such a distribution of T_B. TEM data for **100/10 Fe/SiO$_2$**, **100/25 Fe/SiO$_2$** and **100/50 Fe/SiO$_2$** instead reveals larger nanoparticles within a much narrower size range, hence resulting in a much narrower distribution of T_B and the pronounced maxima in the magnetisation curves.

The χ_{DC}^{-1} versus T curves for all silica-bearing samples are shown in Figure 4.31. All samples exhibit convex-shaped curves. Extrapolation of the linear region to the temperature axis reveals values of θ_p = 143, -50, -266, -248 and -100 K for **100/10 Fe/SiO$_2$**, **100/25 Fe/SiO$_2$**, **100/50 Fe/SiO$_2$**, **100/100 Fe/SiO$_2$** and **100/200**

Fe/SiO$_2$ respectively. The negative values of θ_p for all samples barring **100/10 Fe/SiO$_2$** suggest an AFM interactions are present, consistent with ferriihydrite. The positive value of θ_p for **100/10 Fe/SiO$_2$** indicates FM/FiM interactions are present, however, the shape of the curve (Figure 4.31 (a)) is similar to that of **100/25 Fe/SiO$_2$** (Figure 4.31 (b)) between 100 and 300 K. It is possible that the χ_{DC}^{-1}(T) curve of **100/10 Fe/SiO$_2$** will similarly change at temperatures above 380 K, as **100/25 Fe/SiO$_2$** did between 300 and 380 K. This would give rise to a linear region that would also indicate AFM interactions in **100/10 Fe/SiO$_2$**.

Finally, the magnetic moment per atom (μ_{eff}) was calculated from the linear plots using Equation 3.67 and a molar mass of ferrihydrite equal to 168.7 g.mol^{-1}. This yielded μ_{eff} values (summarised in Table 4.9) of 5.42, 5.32 and 5.42 μ_B for **100/10 Fe/SiO$_2$**, **100/25 Fe/SiO$_2$** and **100/50 Fe/SiO$_2$** respectively. These are lower than reported values for pure 2-line ferrihydrite of ≈ 5.75 μ_B[87,277], likely a result of the silica. **100/100 Fe/SiO$_2$** has a lower μ_{eff} of 5.14 μ_B while **100/200 Fe/SiO$_2$** is drastically lower at 3.86 μ_B.

Table 4.9: *Effective magnetic moment (μ_{eff}) calculated from χ_{DC}^{-1} vs T data.*

Sample	$\mu_{\mathbf{eff}}$ [μ_B]
100/10 Fe/SiO$_2$	5.42
100/25 Fe/SiO$_2$	5.32
100/50 Fe/SiO$_2$	5.42
100/100 Fe/SiO$_2$	5.14
100/200 Fe/SiO$_2$	3.86

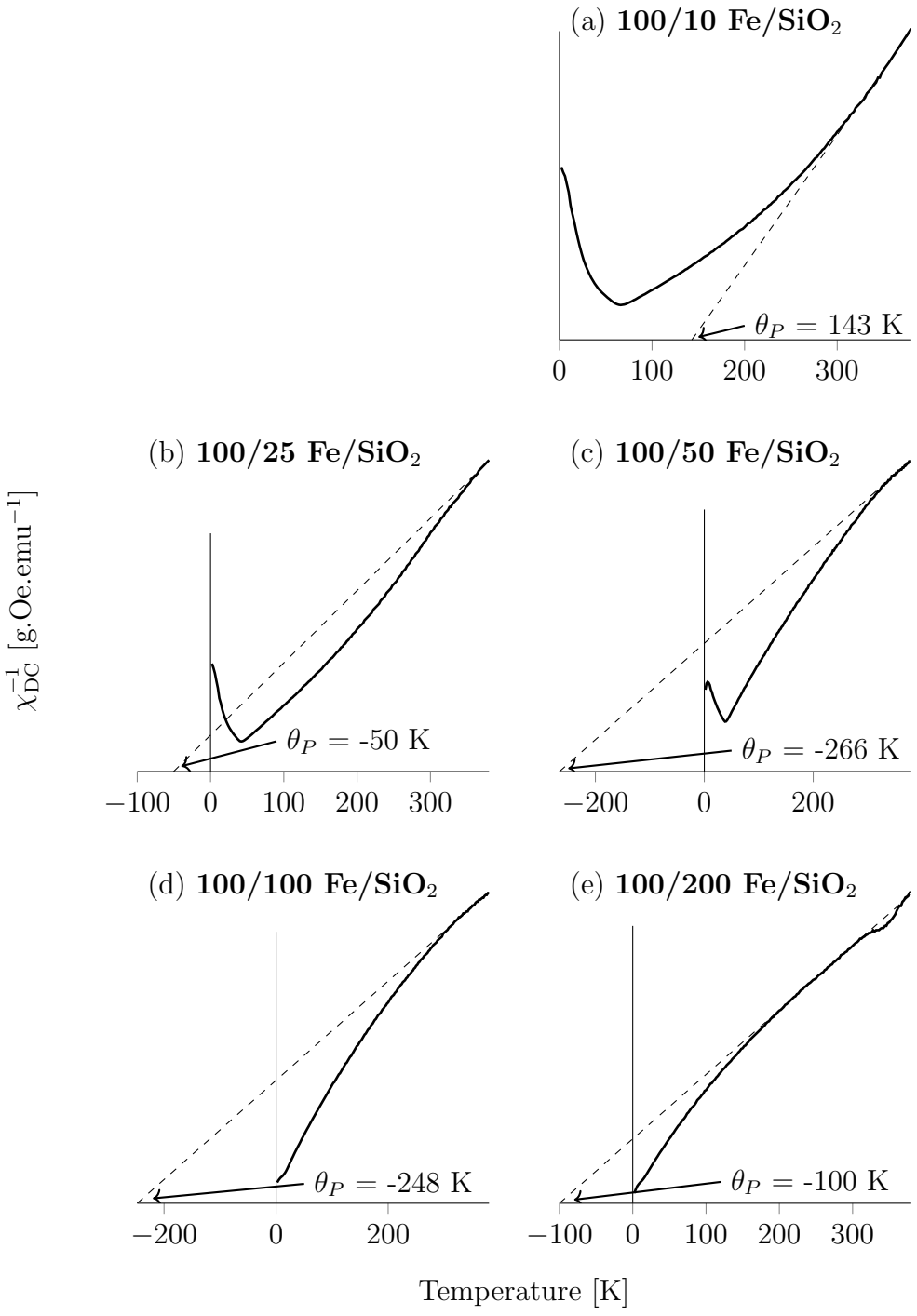

Figure 4.31: *χ_{DC}^{-1} versus T for silica-bearing samples.*

4.10 Thermogravimetric Analysis

Owing to the variable water content of ferrihydrite crystallites[2], thermogravimetric analysis was used to determine nominal chemical formulae for the silica-bearing samples[‡]. The TGA mass loss curves recorded from room temperature up till 700°C in nitrogen for **100/10 Fe/SiO$_2$**, **100/25 Fe/SiO$_2$**, **100/50 Fe/SiO$_2$**, **100/100 Fe/SiO$_2$** and **100/200 Fe/SiO$_2$** are shown in Figure 4.32.

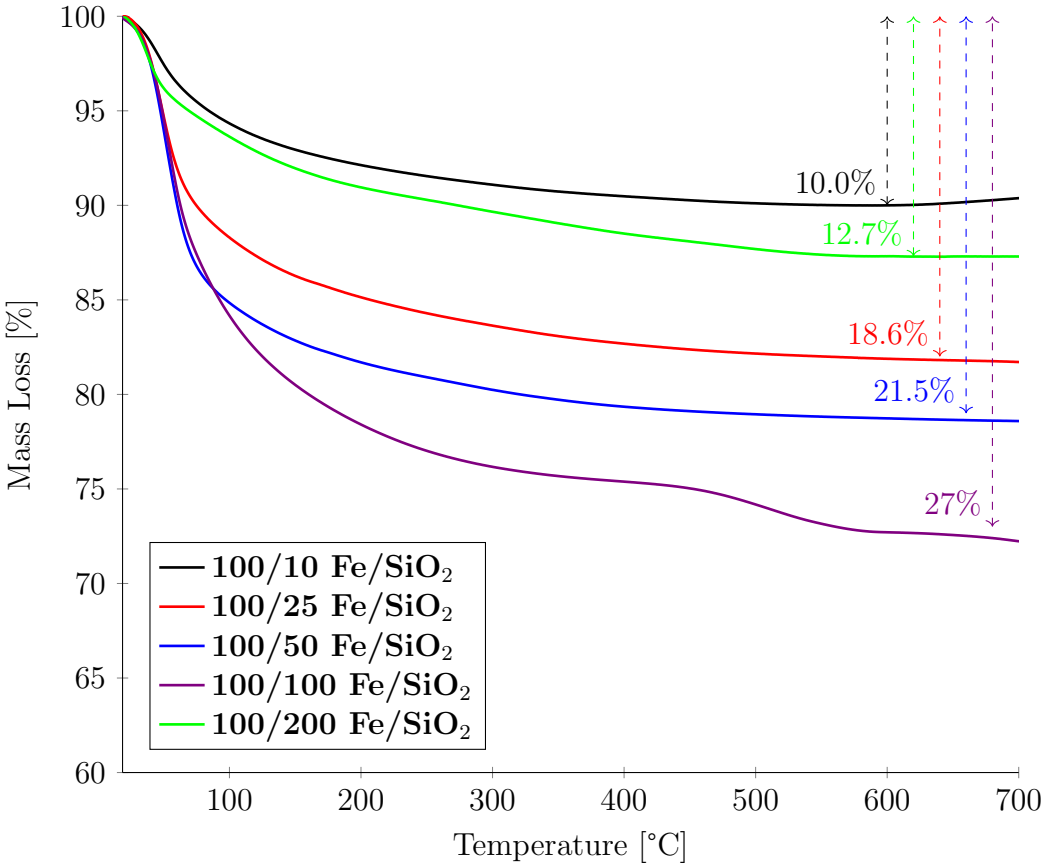

Figure 4.32: *TGA mass loss curves for* ***100/10 Fe/SiO$_2$****,* ***100/25 Fe/SiO$_2$****,* ***100/50 Fe/SiO$_2$****,* ***100/100 Fe/SiO$_2$*** *and* ***100/200 Fe/SiO$_2$*** *in nitrogen. The total mass loss for each sample is indicated.*

100/10 Fe/SiO$_2$, **100/25 Fe/SiO$_2$** and **100/50 Fe/SiO$_2$** exhibit very similar,

[‡]**100/0 Fe/SiO$_2$**, known to be hematite, was shown to have a negligible amount of surface adsorbed water.

single-step mass-loss curves, with a higher silica content resulting in a greater total loss, suggesting an increase in water content. There is initially a sharp decrease in mass, likely a result of weakly bound surface water molecules, followed by a much slower mass loss corresponding to structural water. The total mass loss by 700°C in each of the samples is 10.0%, 18.6% and 21.5% respectively. **100/100 Fe/SiO$_2$** demonstrates very different mass-loss behaviour. It consists of a two-step mass loss. The first mass loss corresponds to the loss of water from the iron oxide particles, while the second mass loss is likely the decomposition of the sodium nitrate known to be present in this particular sample. The presence of this nitrate salt makes determination of a nominal chemical formula for **100/100 Fe/SiO$_2$** subject to a significant error. Finally, **100/200 Fe/SiO$_2$** reveals very a low total mass loss of 12.7%, since a large portion of the sample is vitreous silica. Since all the samples have been calcined at 400°C, any mass loss prior to this temperature is water that has been absorbed from the moist laboratory air, while any mass loss after this point is from other events, such as nitrate decompositions and dehydroxylations which did not occur below 400°C.

If a nominal formula of $Fe_2O_3 \cdot xH_2O \cdot ySiO_2$ is assumed for each of the samples at the start of the run and the only mass loss is a result of water leaving, then the difference in mass may be used to determine the relative amount of water in each sample. These results are shown in Table 4.10. The water content increases as the particle size decreases (silica content increase) in **100/10 Fe/SiO$_2$**, **100/25 Fe/SiO$_2$** and **100/50 Fe/SiO$_2$**, an indication that the water is bound predominantly to the surface of the particle. This has been observed previously[278]. The value obtained for **100/100 Fe/SiO$_2$** of 5.6 formula water per Fe_2O_3 unit is an over estimate as a result of the nitrate decomposition. **100/200 Fe/SiO$_2$** demonstrates a drop in water content. Correlating this with TEM data would suggest that this is simply a result of less iron oxide surface being available for adsorption as a result of iron-encapsulation by the vitreous silica matrix.

Table 4.10: *Water content of each sample determined using TGA mass loss curves. Water content is given as x moles, assuming a formula of* $Fe_2O_3 \cdot xH_2O \cdot ySiO_2$.

Sample	Mass Loss [%]	Calculated x
100/10 Fe/SiO$_2$	10.0	1.1
100/25 Fe/SiO$_2$	18.6	2.4
100/50 Fe/SiO$_2$	21.5	3.3
100/100 Fe/SiO$_2$	27.0	5.6
100/200 Fe/SiO$_2$	12.7	3.1

4.11 Chapter Conclusions

Iron oxide was precipitated from solution at pH 8.0 in the presence of varying amounts of silica using an ammonium hydroxide precipitating agent. All samples were subject to the same drying and calcination steps The resulting powders were characterised using a combination of SEM, TEM, XRPD, Raman, nitrogen physisorption, MS, magnetic measurements and TGA.

The precipitation of iron nitrate at pH 8.0 in the absence of silica, followed by the subsequent drying and calcination treatments, results in the formation of irregular-shaped hematite nanoparticles with a mean particle diameter of 39 ± 12 nm in **100/0 Fe/SiO$_2$**. *d*-spacing information obtained from XRPD and SAED, as well as vibrational modes from Raman spectroscopy, are consistent with hematite and suggest that the sample is phase pure. Nitrogen physisorption reveals surface area and pore size distribution characteristic of hematite nanoparticles. The MS spectra at room temperature and 4.2 K of **100/0 Fe/SiO$_2$** were fitted with a single sextet each and the hyperfine parameters (δ_{RT} = 0.39 mm.s^{-1}, $\Delta E_{Q,RT}$ = -0.20 mm.s^{-1}, $B_{hf,RT}$ = 51.7 T, δ_{LT} = 0.49 mm.s^{-1}, $\Delta E_{Q,LT}$ = 0.40 mm.s^{-1}, $B_{hf,LT}$ = 53.9 T) are consistent with pure hematite. The Morin transition ($T_M \approx$ 230 K) observed in themagnetic measurements data is different to bulk hematite, but consistent with hematite in the nano-regime.

The addition of 10, 25 and 50 weight parts silica to 100 parts iron in **100/10 Fe/SiO$_2$**, **100/25 Fe/SiO$_2$** and **100/50 Fe/SiO$_2$** results in the formation of silicon-substituted 2-line ferrihydrite nanoparticles within a very narrow size range. SEM-EDS and STEM-EELS reveal the substitution to be homogeneous, while SEM-EDS and TEM-EDS also confirms that all the silica is incorporated within the iron oxide structure. TEM and nitrogen physisorption reveal mean particle diameters of 3.1 ± 0.4 nm, 2.4 ± 0.3 nm and 2.4 ± 0.3 nm for **100/10 Fe/SiO$_2$**, **100/25 Fe/SiO$_2$** and **100/50 Fe/SiO$_2$** respectively. While the mean diameter of **100/50 Fe/SiO$_2$** is the same as **100/25 Fe/SiO$_2$**, the corresponding XRPD diffraction pattern exhibits broader reflections as a result of the increased structural disorder resulting from the higher degree of silicon substitution. Raman spectra of the three samples exhibit peaks characteristic of 2-line ferrihydrite, as well as an additional peak consistent with a ν_3 SiO_4^{4-} vibrational mode. Shifts in these peaks with increasing silica content is a result of changes in the reduced mass, which is an indication of Fe-O-Si bonds forming even prior to reduction. The relative proportion of these Fe-O-Si bonds also increases with increasing silica content.

The MS spectra of these samples all exhibited a doublet at room temperature and were fitted with a distribution of the quadrupole splitting. The isomer shift values (δ = 0.34 - 0.35 mm.s^{-1}) are consistent with super paramagnetic Fe^{3+} cations in an octahedral environment, while the large values of the quadrupole splitting distributions (maximum intensity greater than 0.90 mm.s^{-1} for all samples) is indicative of a large amount of distortion in the octahedral environment. At 4.2 K, each sample exhibited a broad sextet which was fitted with a distribution of the magnetic hyperfine field. There was a regular decrease in the median position of the hyperfine field distribution on increasing silica content (49.0 T, 48.0 T and 46.9 T for **100/10 Fe/SiO$_2$**, **100/25 Fe/SiO$_2$** and **100/50 Fe/SiO$_2$** respectively). These hyperfine values are characteristic of ferrihydrite particles, with a decrease in the field distribution indicative of a decrease in particle size or an increase in disorder. Additionally, in a 10 T applied field, the distribution merely broadened as a result of particles randomly orienting themselves in the field. This behaviour is characteristic of ferrihydrite.

The temperature-dependent magnetisation of each of these samples are characteris-

tic of an assembly of superparamagnetic nanoparticles. The blocking temperature decreased with increasing silica content with T_B=68 K for **100/10 Fe/SiO$_2$**, 42 K for **100/25 Fe/SiO$_2$** and 39 K for **100/50 Fe/SiO$_2$**. Using these blocking temperatures, the mean particle sizes for each sample were calculated as 4.2 nm for **100/10 Fe/SiO$_2$** and 3.6 nm for **100/25 Fe/SiO$_2$** and 3.5 nm for **100/50 Fe/SiO$_2$**. These are in excellent agreement with those obtained from the TEM micrographs.

The addition of 100 and 200 weight parts silica (for 100 weight part iron) in **100/100 Fe/SiO$_2$** and **100/200 Fe/SiO$_2$** is too high to be fully incorporated within the ion oxide structure. As a result, two distinct phases are formed. The first phase is small, silicon-substituted ferrihydrite particles, while the second is a vitreous silica infused with very small iron domains. The presence of a broad reflection in XRPD data at $\approx$ 3.7 Å and a Raman vibrational mode at 1050 cm^{-1} confirm the presence of amorphous, vitreous silica. The excess silica encapsulates the iron during precipitation, preventing its complete growth to defined iron oxide particles. The presence of macropores common in silica is also confirmed by nitrogen physisorption measurements.

The MS spectra of these samples all exhibited a doublet at room temperature and were fitted with a distribution of the quadrupole splitting. The isomer shift values (δ = 0.34 - 0.35 mm.s^{-1}) are consistent with super paramagnetic Fe^{3+} cations in an octahedral environment, while the large values of the quadrupole splitting distributions (maximum intensity greater than 0.90 mm.s^{-1} for all samples) is indicative of a large amount of distortion in the octahedral environment. The LTMS spectra are complex and best fitted with two distributions of the magnetic hyperfine field. The high field distribution in both has a median value of 44.8 T and is attributed to ferrihydrite domains within each sample. The low-field distribution (whose contribution to the total spectrum is greater in **100/200 Fe/SiO$_2$** than **100/100 Fe/SiO$_2$**) is attributed to isolated Fe^{3+} domains encapsulated in a silica matrix. In a 10 T applied field, the high-field distribution merely broadens as the ferrihydrite domains orient themselves randomly with respect to the field, while the low-field distribution is shifted to higher values as the magnetic moments of the isolated Fe^{3+} domains orient themselves parallel to the applied field.

The temperature-dependent magnetisation of these samples is distinctly different

to those with lower silica content. **100/100 Fe/SiO$_2$** exhibits a small bump corresponding to the blocked state of the larger iron oxide domains, while this is not even evident in the χ_{DC}(T) curve for **100/200 Fe/SiO$_2$**. The presence of this increased amount of silica results in a much broader particle size distribution which results in a very broad distribution of blocking temperatures.

5 Reduction in Hydrogen

5.1 Experimental Details

5.1.1 Temperature Programmed Reduction

H_2-TPR measurements were performed using a Micromeritics Autochem 2950 HP chemisorption analyzer. Approximately 50 mg of sample was loaded into a quartzU-tube reactor. Samples were initially dried at 120°C in argon. A 10% H_2/90% Ar gas mixture was used for the reduction and the temperature was heated from room temperature to 1000°C at a rate of 10°C.min^{-1}. A cold trap employing an isopropyl alcohol in dry ice slurry was used to trap water formed during the reduction process. Hydrogen consumption was measured using a TCD detector calibrated with a Ag_2O standard.

5.1.2 *In Situ* X-Ray Powder Diffraction

In situ X-ray powder diffractograms were obtained using a PANalytical Excellerator detector with a cobalt radiation source (λ=0.178897 nm). Samples were packed into a stainless steel sample holder. Hydrogen gas with a flow-through configuration was introduced at 1 bar pressure at a flow rate of 100 mL.min^{-1}. A 2 hour scan was performed initially at 40°C, with a 20 min scan after every 20°C step increase, beginning at 80°C and ending at 360°C. The heating rate between scans was 10°C.min^{-1}. Four consecutive 2 hour scans were performed at a final temperature of 380°C. All scans were performed from $2\theta_{\text{start}}$= 5° to $2\theta_{\text{end}}$= 105°, with a step size = 0.017° 2θ. Crystalline phases present in the diffractograms were identified using Bruker AXS DIFFRAC.EVA software, while average crystallite sizes were determined using Rietveld refinement, the fundamental parameter, full pattern refinement approach and Topas4.1 software.

5.1.3 Transmission Electron Microscopy

TEM micrographs, SAED, BF and HAADF STEM micrographs, EDS and EELS data were obtained using a JEOL JEM-ARM-200F operated at 200 kV. A small amount of oxide powder was placed on a glass slide on a metal susceptor, which was itself placed in a quartz reactor tube. The samples were reduced at 400°C for 20 hours in ultrahigh purity hydrogen gas at a flow rate of 500 mL.min^{-1}. The reduced samples were immediately placed into ethanol and ultrasonicated to ensure they were well dispersed. A drop of dispersed solution was placed on an amorphous carbon film supported by a copper grid and immediately mounted on the sample holder and inserted into the microscope. The work was performed as quickly as possible to minimise oxidation of the sample from exposure to atmospheric oxygen and moisture. Data was analysed using a combination of Gatan Microscopy Suite version 2.11, Oxford Aztec Software and ImageJ.

5.2 Temperature Programmed Reduction

The hydrogen consumption as a function of temperature during the temperature programmed reduction experiments for each sample is shown in Figure 5.2 to Figure 5.7. All six TPR profiles are also shown on the same set of axes in Figure 5.1. It is readily seen that on increasing the silica content, there is a shift in the reduction peak positions to higher temperatures, as well as the appearance of numerous peaks in the samples containing silica (compared to **100/0 Fe/SiO$_2$**, which only exhibits two peaks).

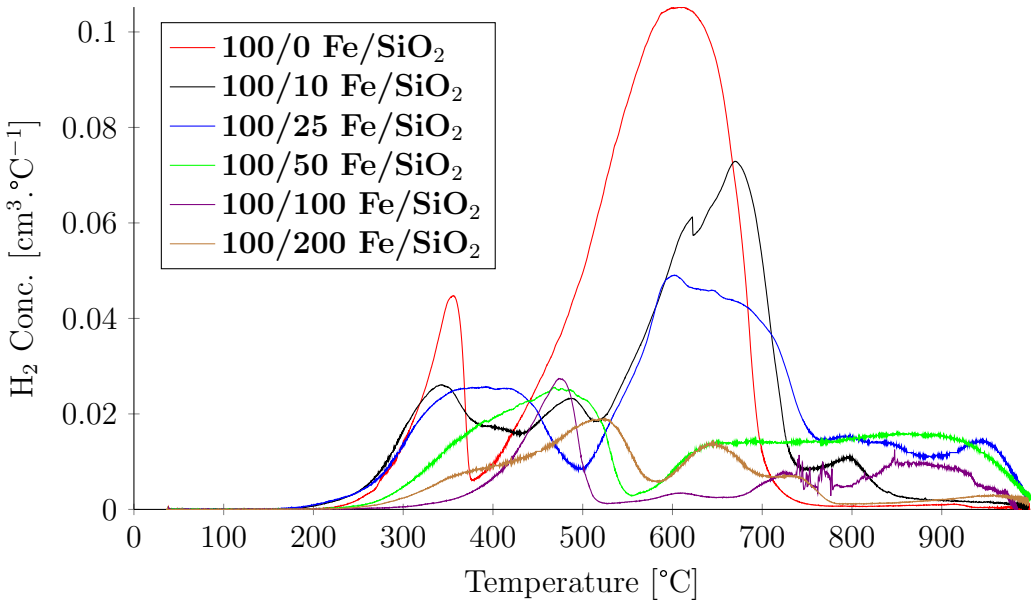

Figure 5.1: *Hydrogen TPR profile of samples with increasing silica content. Heating rate = 10°C.min^{-1}.*

The hydrogen TPR profile for **100/0 Fe/SiO$_2$** is shown in Figure 5.2. It exhibits two distinct peaks. The first (labeled A) has a maximum at 356°C (onset at approximately 210°C). It overlaps slightly with the second peak (labeled B), which has a maximum at 600°C (onset somewhere below 370°C). This suggests that the reduction occurs via a two-step process.

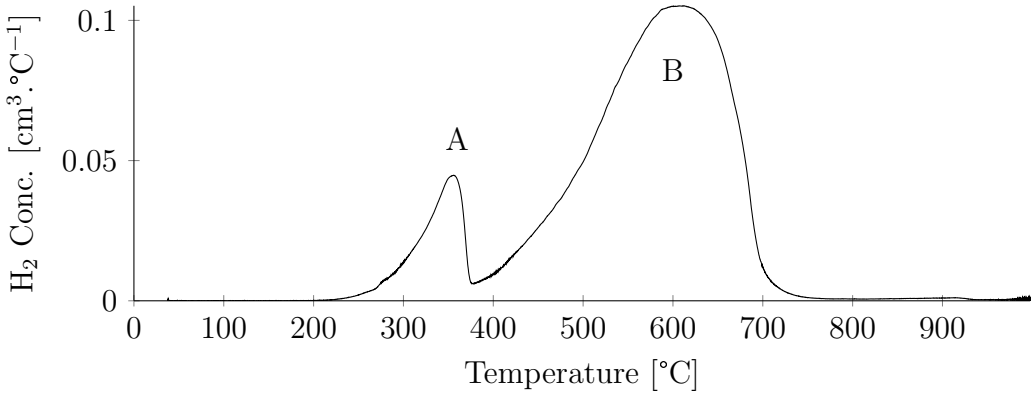

Figure 5.2: *Hydrogen TPR profile of **100/0 Fe/SiO$_2$**. Heating rate = 10°C.min^{-1}.*

The total areas beneath each peak have been calculated in order to determine the hydrogen consumption for each reduction process. As a result of peak B tailing into peak A, the calculated area is higher for peak A, and slightly lower for peak B than is actually the case. The calculated peak areas, corresponding to the total hydrogen consumption for each reduction step are 2.54 $cm^3.g^{-1}$ and 19.49 $cm^3.g^{-1}$ respectively, given a ratio of peak A to peak B (A:B) of 1.0:7.7.

The initial iron oxide phase present in **100/0 Fe/SiO$_2$** is hematite (α-Fe_2O_3), as confirmed by XRPD, TEM-SAED, MS and Raman data. This 2-step reduction process observed here is well documented in the literature and corresponds to the reduction of hematite to magnetite, followed by the subsequent reduction of magnetite to metallic iron[75,80,82,279]. The associated balanced equations are:

$$3Fe_2O_3 + H_2 \longrightarrow 2Fe_3O_4 + H_2O \qquad n(H_2)/n(Fe) = 0.17$$
$$Fe_3O_4 + 4H_2 \longrightarrow 3Fe + 4H_2O \qquad n(H_2)/n(Fe) = 1.33$$

$$Fe_2O_3 + 3H_2 \longrightarrow 2Fe + 3H_2O \qquad n(H_2)/n(Fe) = 1.50$$

This suggests that for every one mole of hydrogen consumed during reduction process A, there are 8 moles consumed during reduction process B. The experimental data has a ratio of peak A to peak B of 1.0:7.7. This is in good agreement with the above theoretical model, especially considering that the hydrogen consumption for A has been over estimated and B has been under estimated.

Based on the total reduction equation, a total hydrogen consumption of 1.5 moles per mole of iron is expected. The total hydrogen consumption per mole of iron for **100/0 Fe/SiO$_2$** is determined experimentally as 1.47. This is in excellent agreement with the proposed theoretical model. It thus seems reasonable to conclude that the reduction of **100/0 Fe/SiO$_2$** occurs via the above mechanism.

The hydrogen TPR profile for **100/10 Fe/SiO$_2$** is shown in Figure 5.3. Unlike **100/0 Fe/SiO$_2$** where only two reduction peaks are visible, 5 reduction peaks are clearly visible in this case, labelled A to E. The first peak, A, has its onset at 190°C and a maximum at 342°C. A smaller peak, B, appears soon after and has a maximum at approximately 400°C, while peak C has a maximum at 488°C. Peak D is similar in shape and size to the Fe_3O_4 to Fe reduction peak of **100/0 Fe/SiO$_2$**,

and has a maximum in this case of 670°C. Finally, there is an additional peak E with a maximum at 800°C. It must also be noted that the hydrogen consumption tends very gradually to zero after peak E without ever reaching it, suggesting continued reduction even at temperatures approaching 1000°C.

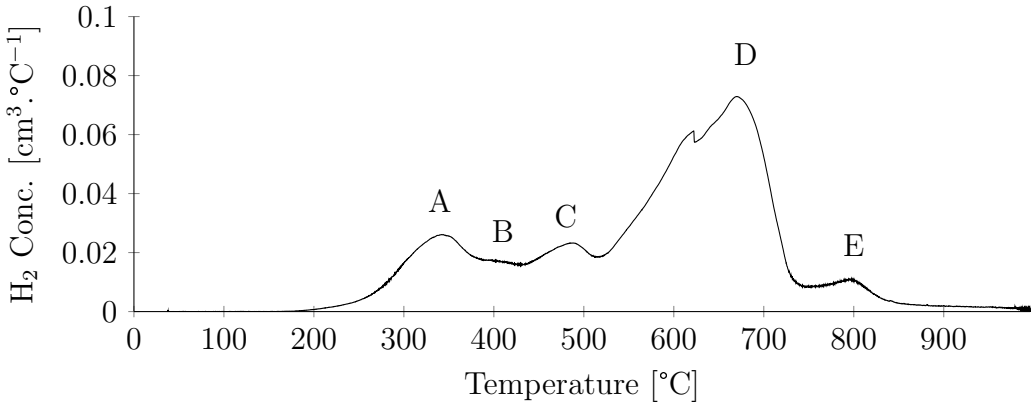

Figure 5.3: *Hydrogen TPR profile of* ***100/10 Fe/SiO$_2$****. Heating rate = 10°C.min^{-1}.*

There exists a large degree of overlap between peaks A, B and C, which prevents calculations of the total hydrogen consumption (area under the peak) for each reduction step. However, the total hydrogen consumption for peak A, B and C together is 5.26 $cm^3.g^{-1}$, while the total hydrogen consumption for the remainder of the profile (peak D and E) is 11.22 $cm^3.g^{-1}$. This gives a peak ratio of (A+B+C):(D+E) of 1.0:2.1. This suggests the reduction of the ferrihydrite particles to magnetite (peak A) and subsequently to wüstite by the end of peak C. Reduction step D corresponds to the reduction of wüstite to metallic iron. The appearance of a well-defined wüstite reduction step is indicative of this normally meta-stable phase being stabilised by the presence of silica. This reduction process is summarised in the following equations (by simply writing ferrihydrite as Fe_2O_3):

$$3Fe_2O_3 + H_2 \longrightarrow 2Fe_3O_4 + H_2O \qquad n(H_2)/n(Fe) = 0.17$$

$$Fe_3O_4 + H_2 \longrightarrow 3FeO + H_2O \qquad n(H_2)/n(Fe) = 0.33$$

$$FeO + H_2 \longrightarrow Fe + H_2O \qquad n(H_2)/n(Fe) = 1.00$$

$$Fe_2O_3 + 3H_2 \longrightarrow 2Fe + 3H_2O \qquad n(H_2)/n(Fe) = 1.50$$

This also suggests a ratio of peak (A+B+C) to peak (D+E) of 1:2, somewhat similar to the calculated 1.0:2.1. There are multiple reasons for this deviation however. Firstly, the continued reduction of a small portion of the sample even at 1000°C suggests that not all the iron has been reduced. Indeed, the molar ratio of consumed hydrogen to iron is only 1.3, less than the expected 1.5. This is indicative of strong Fe-O-Si bonds forming within the sample which are very difficult to reduce.

The presence of 5 peaks, when only 3 are expected for the proposed mechanism, are also indicative of the same reduction step occurring at different temperatures within different regions of the sample. This is attributed to subtle variations in the silicon-concentration and the nature of the existing Fe-O-Si bonds. As a result, the reduction steps are very poorly defined, which prevents accurate determination of the total hydrogen consumption.

Suo *et al.* and Masina *et al.* have reported TPR results of similar iron-silica composites[86,239]. A similar shift in reduction to higher temperatures was observed, as well as total hydrogen consumption less than expected from theory. The presence of stabilised wüstite was also observed. While there were slight differences in the temperature and hydrogen consumption values obtained in this work and those in the literature, this is attributed to the strong influence of different experimental parameters on the resulting TPR profile, such as heating rate, particle morphology and the water to hydrogen molar ratio[73,82].

The hydrogen TPR profile for **100/25 Fe/SiO$_2$** is shown in Figure 5.4. The further increase in silica content from 10 weight parts to 25 has resulted in an increase in reduction temperature. Four peaks are distinctly visible. Peak A has its onset at 190°C, a maximum at 390°C and contains a shoulder at 420°C. The largest peak, B, appears at 500°C and has a maximum at approximately 650°C. It does, however, have a number of peaks superimposed upon it, suggesting that it is the sum of a multitude of different reduction steps. Finally, peak C and D correspond to reduction peaks at higher temperatures, likely the reduction of iron incorporated in strong Fe-O-Si bonding networks. The relative proportion of these peaks is greater in **100/25 Fe/SiO$_2$** than in **100/10 Fe/SiO$_2$**, since the silica content is greater.

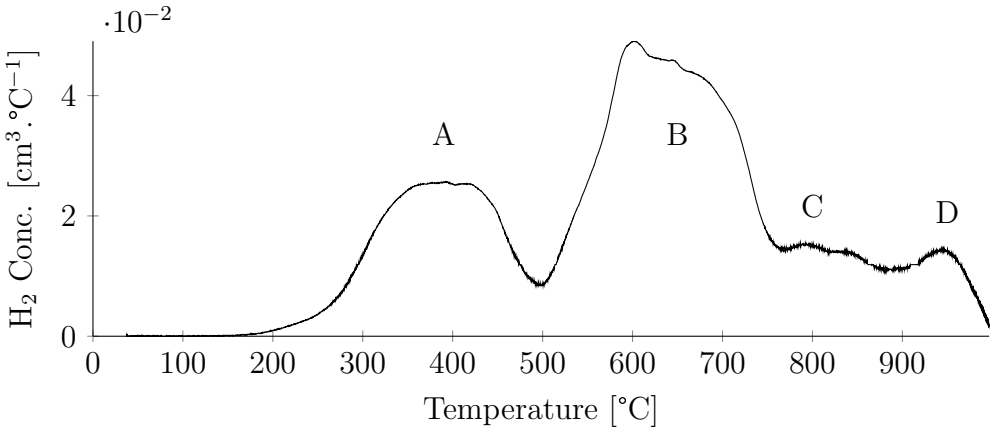

Figure 5.4: *Hydrogen TPR profile of* ***100/25 Fe/SiO$_2$****. Heating rate = 10°C.min^{-1}.*

The reduction process follows the same three-step reduction observed in **100/10 Fe/SiO$_2$** of ferrihydrite to magnetite, magnetite to wüstite and wüstite to iron. However, these reduction steps are much broader, and the peak overlap prevents any attempt at reliably quantifying the hydrogen consumption. However, the broadness of these peaks does indicate the presence of slight inhomogeneities in the silica distribution, with regions of higher silica concentration reducing only at higher temperatures. As before, not all the iron was reduced from Fe^{3+} to Fe^0, as indicated by a calculated n(H_2)/n(Fe) ratio of 1.3.

Zhang *et al.* have reported on the TPR of similar 25 weight parts silica incorporated into iron oxides[140]. The TPR profile exhibited a similar increase in reduction temperature versus those observed in their control sample without any silica. They also observed incomplete reduction of the Fe^{3+} species present initially. However, the maximum temperature attained during the TPR run was only 830°C.

This effect of silica is further exemplified by the TPR profile of **100/50 Fe/SiO$_2$** in Figure 5.5. When compared to **100/25 Fe/SiO$_2$**, the first reduction peak (labeled A) has shifted to higher temperatures, having an onset at 230°C and a maximum at 485°C. It also demonstrates a shoulder at approximately 400°C, indicated by the arrow. This is then followed by a very broad reduction peak. It exhibits two obvious maxima, labeled B (at 630°C) and C (at 900°C), however it is clearly the net sum of a large number of broad, overlapping peaks.

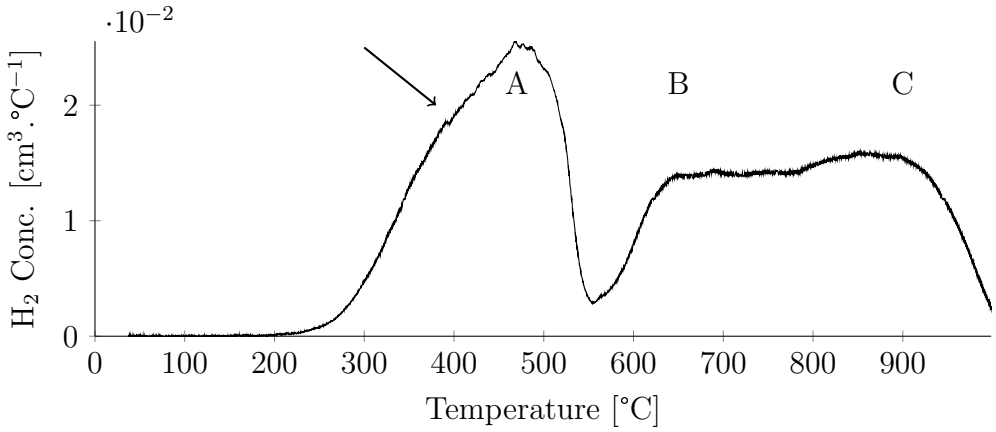

Figure 5.5: *Hydrogen TPR profile of* ***100/50 Fe/SiO$_2$****. Heating rate = 10°C.min^{-1}.*

Peak B in **100/50 Fe/SiO$_2$** corresponds directly with peak B in **100/25 Fe/SiO$_2$**. However, in this case it is smaller and shifted to a higher temperature. This reduction is believed to be the reduction of Fe^{2+} in wüstite to Fe^0. At the same time, peak C of **100/50 Fe/SiO$_2$** corresponds with peaks C and D of **100/25 Fe/SiO$_2$**. However, the relative peak area of C in this case is larger. This reduction is believed to be that of Fe^{2+} in Fe-O-Si bonded networks. The increase in the amount of silica results in a further increase in the amount of difficult to reduce Fe-O-Si bonds forming. As a result, this peak C increases in area, while peak B decreases in intensity. Once more, the broadness of each peak suggests a complex reduction behaviour governed by varying local concentrations of silica within the original ferrihydrite framework.

The TPR profile of **100/100 Fe/SiO$_2$** demonstrates 2 distinct peaks, A and B, with maxima at 480°C and 610°C respectively. These are shown in Figure 5.6. Thereafter, the signal of the TCD detector is very noisy. This is a result of the quartz reactor tube breaking. This breaking has been attributed to significant volumes of gas released from the sodium nitrate trapped in the silica matrix causing a localised pressure sufficient to break the reactor tube.

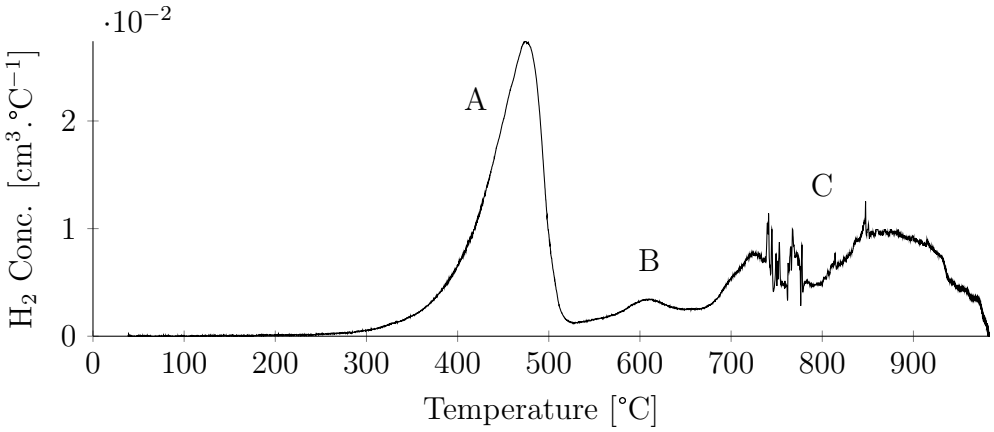

Figure 5.6: *Hydrogen TPR profile of* ***100/100 Fe/SiO$_2$****. Heating rate = 10°C.min^{-1}.*

However, the TPR profile of **100/100 Fe/SiO$_2$** may still be interpreted qualitatively. The initial reduction peak at 480°C likely corresponds to the reduction of some Fe^{3+} to Fe^{2+} to form small magnetite and wüstite domains. The noisy region C, has its major peak area shifted to higher temperature than the lower silica-content samples, further evidence of the increased amount of Fe-O-Si bonds forming in the sample during reduction.

Finally, the TPR profile of **100/200 Fe/SiO$_2$** is shown in Figure 5.7. It demonstrates a peak at 520°C (labeled B) with a shoulder on the low temperature side (labeled A). A third reduction peak (C) attains a maximum at 650°C and a fourth peak (D) shoulders it at 735°C. There is continued hydrogen consumption (reduction of Fe-species) until 1000°C, indicating not all the iron is reduced.

This incomplete reduction is a result of the large relative amount of silica present in the sample. Indeed, the calculated n(H_2)/n(Fe) ratio is only 0.96, compared to the expected value of 1.5 for complete reduction of Fe^{3+} to Fe^0. This suggests, on average, the iron-species are all reduced to monovalent iron cation, Fe^+. This is unlikely however, and the more likely possibility is the reduction of half the Fe^{3+} species to Fe^0, while the other half is only reduced to Fe^{2+} species at 1000°C. This strongly suggests the formation of an iron silicate such as fayalite, which is known to only reduce at temperatures in excess of 1000°C[141]. No attempt was made to relate each identified reduction peak with a particular reduction reaction, since the

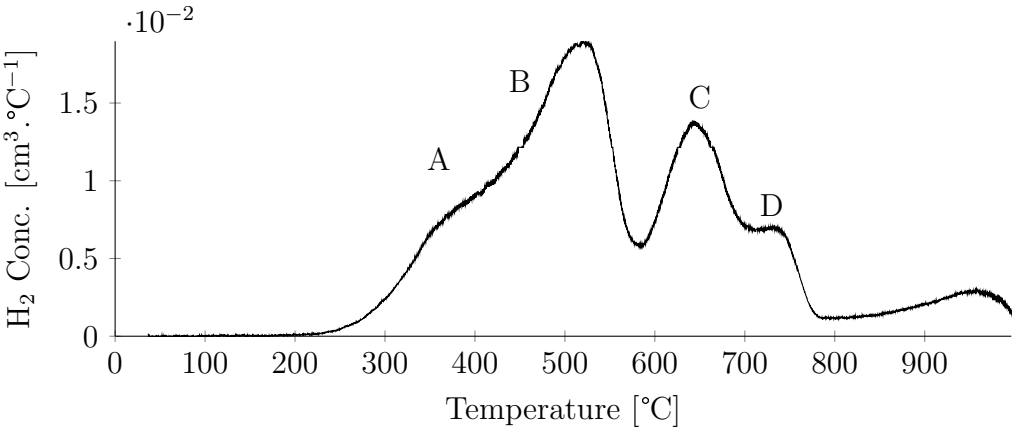

Figure 5.7: *Hydrogen TPR profile of* ***100/200 Fe/SiO$_2$****. Heating rate = 10°C.min^{-1}.*

local environment of the iron is very varied as a result of the large silica content, which causes reduction reactions to overlap significantly.

Finally, it must be noted that the silica matrix which is known to incorporate the iron oxide domains in both **100/100 Fe/SiO$_2$** and **100/200 Fe/SiO$_2$** will inhibit the reduction by hydrogen simply by limiting the hydrogen supply, since the hydrogen needs to diffuse through the matrix in order to react with the iron species. It is known that this rate of diffusion is dependent on temperature, increasing to a maximum only at 1000°C[280]. Hydrogen is also known to react with silica at temperatures below 1000°C to form hydroxide groups at free oxygen sites[281,282]. Thus hydrogen consumption in all the silica-bearing samples may not be entirely a result of the reduction of Fe^{3+} species.

5.3 *In Situ* X-Ray Powder Diffraction

The *in situ* X-ray powder diffractograms of **100/0 Fe/SiO$_2$** in 1 bar hydrogen and heated from 40°C to 380°C are shown in Figure 5.8. Rietveld refinement using the fundamental parameter, full pattern approach was performed at each temperature and the crystallite size and relative phase abundance of each phase present at each temperature are summarised in Table 5.1 (page 172).

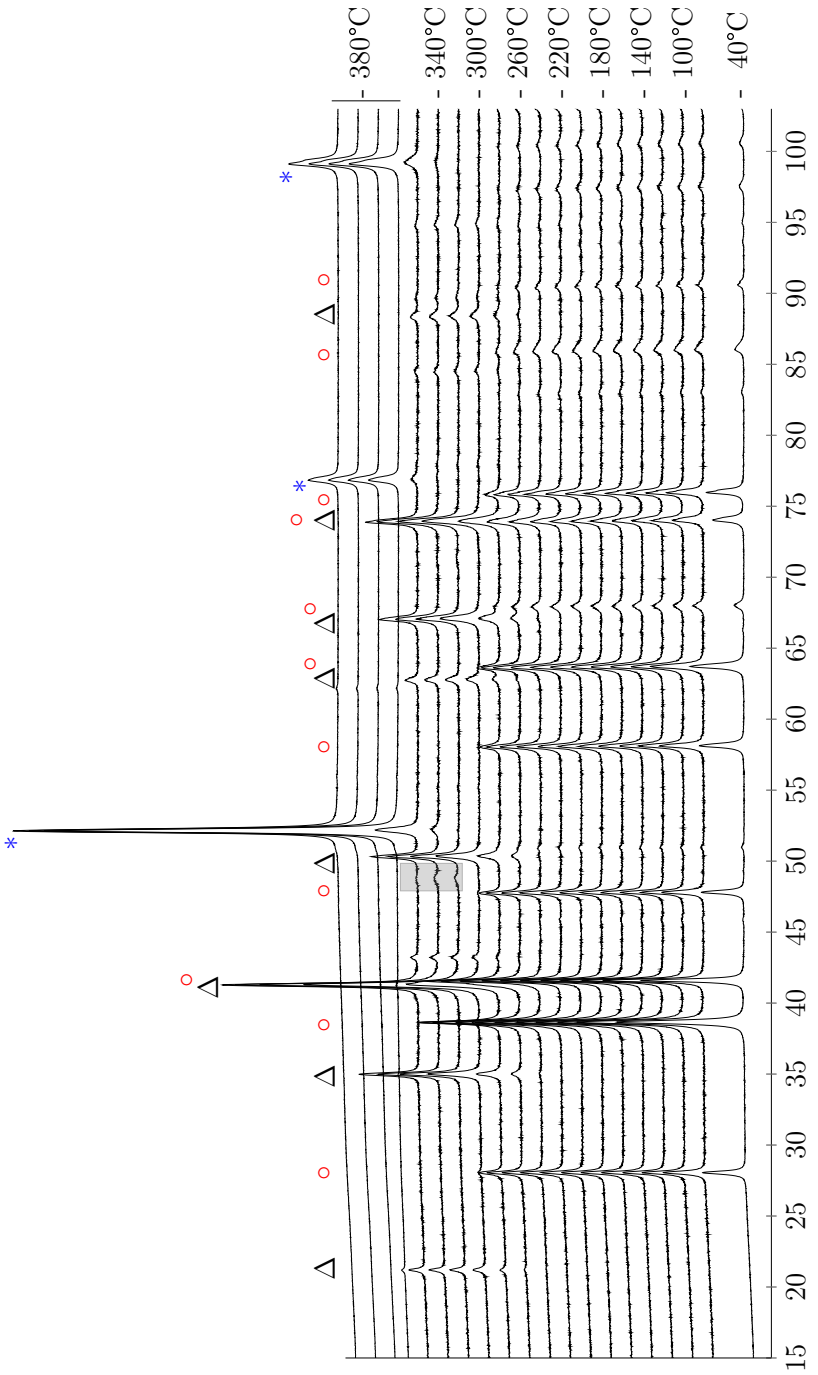

Figure 5.8: *In situ XRPD data for* ***100/0 Fe/SiO$_2$*** *in 1 bar hydrogen, heated from 40°C to 380°C. The most intense reflections of hematite (○), magnetite (Δ) and α-iron (*) are indicated. The reflections enclosed in the gray box are those of wüstite.*

Table 5.1: *Mean crystallite size and relative phase abundances obtained using Rietveld refinement, fundamental parameter, full pattern approach for* ***100/0 Fe/SiO$_2$*** *XRPD patterns when heated from 40°C to 380°C in 1 bar hydrogen.*

Temperature [°C]	**Phase**	**Crys. Size [nm]**	**Abundance [%]**
40	$\alpha-Fe_2O_3$	54.7(0.1)	100
80	$\alpha-Fe_2O_3$	56.1(0.2)	100
100	$\alpha-Fe_2O_3$	55.5(0.2)	100
120	$\alpha-Fe_2O_3$	55.0(0.2)	100
140	$\alpha-Fe_2O_3$	55.4(0.2)	100
160	$\alpha-Fe_2O_3$	56.5(0.2)	100
180	$\alpha-Fe_2O_3$	55.1(0.2)	100
200	$\alpha-Fe_2O_3$	55.5(0.2)	100
220	$\alpha-Fe_2O_3$	56.5(0.2)	100
240	$\alpha-Fe_2O_3$	57.8(0.3)	94.2(0.2)
	Fe_3O_4	30.7(1.0)	5.8(0.2)
260	$\alpha-Fe_2O_3$	59.1(0.3)	78.4(0.1)
	Fe_3O_4	35.4(0.5)	21.6(0.1)
280	$\alpha-Fe_2O_3$	61.1(0.5)	50.2(0.1)
	Fe_3O_4	43.0(0.3)	49.8(0.1)
300	$\alpha-Fe_2O_3$	65.2(5.1)	4.6(0.2)
	Fe_3O_4	49.4(0.2)	95.4(0.2)
320	Fe_3O_4	60.2(0.2)	95.0(0.2)
	FeO	15.1(0.9)	5.0(0.2)
340	Fe_3O_4	64.0(0.3)	93.1(0.2)
	FeO	29.6(1.3)	4.0(0.2)
	α-Fe	28.2(1.3)	2.9(0.1)
360	Fe_3O_4	72.6(0.3)	82.4(0.2)
	FeO	20.7(4.3)	1.3(0.2)
	α-Fe	43.5(0.5)	16.3(0.1)
380a	Fe_3O_4	59.4(10.2)	1.1(0.1)
	α-Fe	71.6(0.2)	98.9(0.1)
380b	α-Fe	70.4(0.2)	100
380c	α-Fe	69.0(0.2)	100
380d	α-Fe	68.0(0.2)	100

The sample initially consists of hematite (α-Fe_2O_3, most intense reflections indicated by ○ in Figure 5.8), with a mean crystallite diameter of 54.7 ± 0.1 nm. This is consistent with the *ex situ* XRPD data (Chapter 4.6) which suggests a mean crystallite diameter of 52.7 ± 0.2 nm. Upon increasing the temperature, there is no additional phase present until 240°C, where reflections corresponding to a small amount of magnetite (Fe_3O_4, most intense reflections indicated by Δ in Figure 5.8) are observed. The hematite crystallite size does not change an appreciable amount in this interval.

The initial magnetite phase formed at 240°C constitutes only 5.8 ± 0.2 % of the sample, and refinement results calculate a mean crystallite diameter of 30.7 ± 1.0 nm. The mean crystallite diameter of the hematite phase is calculated at 57.8 ± 0.3 nm. At 260°C and 280°C, the phase abundance of magnetite increases to 21.6 ± 0.1 % and 49.8 ±0.1 %, while the mean crystallite size increases to 35.4 ± 0.5 nm and 43.0 ± 0.3 nm respectively. The corresponding hematite mean crystallite diameter at these two temperatures is calculated as 59.1 ± 0.3 and 61.1 ± 0.5 nm respectively. Finally, by 300°C, the sample consists of 95.4 ± 0.2 % magnetite with a mean crystallite diameter of 49.4 ± 0.2 nm, while the hematite crystallite diameter has increased to 65.2 ± 5.1 nm.

This simultaneous increase in magnetite and hematite crystallite size suggests that the effect of crystallite size is an important parameter in determining the activation energy (E_a) for the reduction of hematite to magnetite in hydrogen, with smaller particles being reduced more easily (lower E_a). This would leave the larger hematite crystallites unreduced initially, resulting in the observed increase in mean crystallite size. The reduction of hematite to magnetite in hydrogen is typically described by a unimolecular reduction model[75,81,82,252,283,284], with activation energies ranging between 80 and 120 $kJ.mol^{-1}$.

At a temperature of 320°C, reflections are visible that indicate the presence of wüstite. It is unlikely that this wüstite is an intermediate species undergoing its known disproportionation below 570°C, since this would result in the formation of α-Fe[285]. It is thus likely that the wüstite (with a mean crystallite diameter of 15.1 ± 0.9 nm) is stabilised by some other factor, likely a high water to hydrogen molar ratio within the reactor[77–80].

A temperature increase to 340°C results in the formation of a small quantity of iron together with a small quantity of wüstite. It is uncertain whether this iron is a result of disproportionation or reduction of the wüstite, or a result of direct reduction of magnetite. At 360°C, only a very small fraction of wüstite remains (1.3 ± 0.3 %), with a larger fraction of iron (16.3 ± 0.1 %). The magnetite present has continued to grow in size as a result of sintering, with a mean crystallite diameter of 49.4 ± 0.3 nm at 300°C to 72.6 ± 0.3 nm at 360°C.

At the final temperature of 380°, very little magnetite remains, and that remaining has a smaller crystallite diameter of 49.4 ± 0.3 nm. Additionally, the iron crystallites are shown to increase in size as the magnetite reduces. This fits with the accepted two-dimensional reduction model proposed for the reduction of magnetite to iron,[75,81]. The absence of significant quantities of wüstite suggests that the reduction of magnetite to iron occurs directly for the most part, with the small observed quantities of wüstite at lower temperatures likely stabilised by high, localised water to hydrogen molar ratios. The final iron crystallites have mean diameters of approximately 70 nm. The phase composition of **100/0 Fe/SiO$_2$** between 200°C and 380°C is summarised graphically in Figure 5.9.

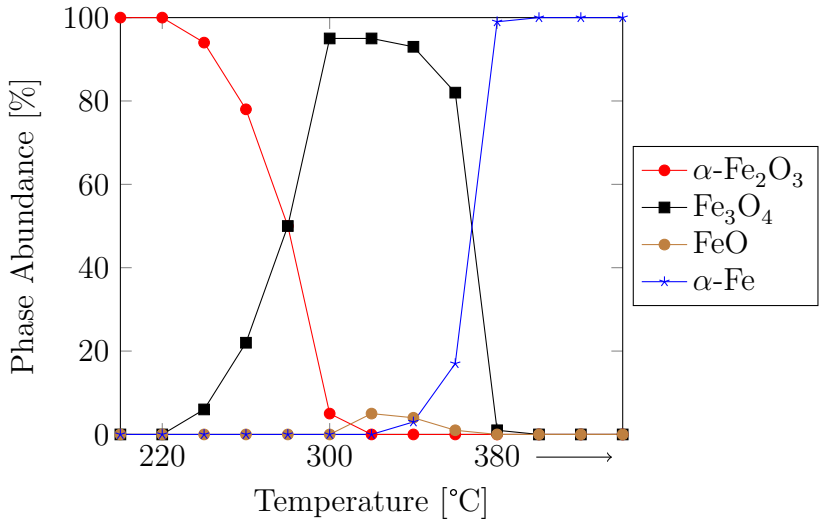

Figure 5.9: *Phase composition of* ***100/0 Fe/SiO$_2$*** *determined from Rietveld refinement of in situ XRPD patterns between 200°C and 380°C.*

The *in situ* X-ray powder diffractograms of **100/10 Fe/SiO_2** in 1 bar hydrogen and heated from 40°C to 380°C are shown in Figure 5.10. Rietveld refinement using the fundamental parameter, full pattern approach was performed at each temperature where crystalline phases were present, and the crystallite size and relative phase abundance of each phase present at each temperature are summarised in Table 5.2. It is important to note that at all temperatures, broad reflections corresponding to amorphous material were present, but not quantified. These were described in the Rietveld fit by broad peaks at d-spacings of approximately 2.5 Å and 1.5 Å that were necessary to ensure a satisfactory refinement. This suggests that the poorly crystalline phase attributed to ferrihydrite is present at all temperatures, and all quoted compositions reflect only that of the crystalline content within the sample. This data is reported as relative crystalline phase abundances.

At 40°C, the XRPD pattern of **100/10 Fe/SiO_2** exhibits two broad reflections at d-spacings of approximately 2.5 Å and 1.5 Å, consistent with the 2-line ferrihydrite phase initially present. On heating in the hydrogen atmosphere, there is no change in the reflection at 2.5 Å until 240°C, where the reflection begins to grow sharper. This is further exemplified at 260°C, while at 280°C, the appearance of a magnetite {311} reflection at this d-spacing is clearly evident. The peak at 1.5 Å appears to gradually shift on heating to lower degrees 2θ, until at 280°C it presents as a crystalline {440} reflection of magnetite.

This change in the amorphous reflections from 40°C till 280°C suggests that there is a slow reduction of Fe^{3+} cations in the 2-line ferrihydrite which is linked to an increase in crystallinity. The shift in the 1.5 Å reflection to lower degrees 2θ (higher d-spacing) is further evidence of this. The ionic radius of Fe^{3+} is known to be smaller than that of Fe^{2+}, resulting in slightly greater bond lengths and the observed shift to a higher d-spacing[2]. The poorly-ordered iron-oxygen clusters in ferrihydrite simultaneously begin rearrangement into a poorly ordered form of magnetite and slowly increase in crystallinity, until 280°C, where they have sufficient energy to arrange into a considerably more crystalline structure. The reduction of unpromoted synthetic 2-line ferrihydrite exhibits crystalline reflections of magnetite by 250°C, thus it is clear that the presence of silica is inhibiting the formation of this crystalline magnetite[239].

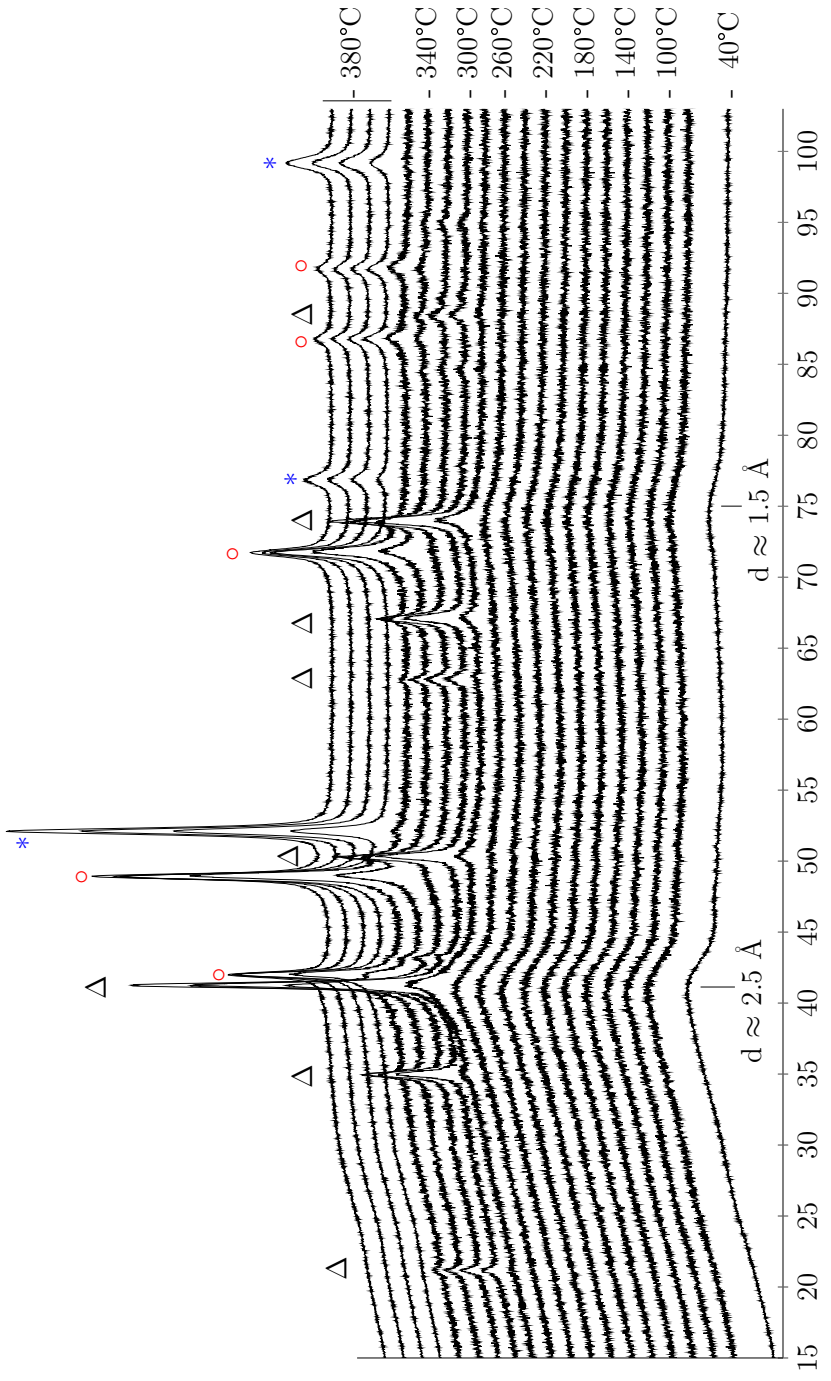

Figure 5.10: *In situ XRPD data for* ***100/10 Fe/SiO$_2$*** *in 1 bar hydrogen, heated from 40°C to 380°C. The most intense reflections of magnetite (Δ), wüstite (○) and α-iron (*) are indicated. The amorphous reflections at d ≈ 2.5 Å and d ≈ 1.5 Å are from 2-line ferrihydrite.*

Table 5.2: *Mean crystallite size and relative phase abundance obtained using Rietveld refinement, fundamental parameter, full pattern approach for* ***100/10 Fe/SiO$_2$*** *XRPD patterns when heated from 40°C to 380°C in 1 bar hydrogen.*

Temperature [°C]	**Phase**	**Crys. Size [nm]**	**Abundance [%]**
280	Fe_3O_4	8.5(0.2)	100
300	Fe_3O_4	26.4(0.3)	100
320	Fe_3O_4	30.7(0.4)	100
340	Fe_3O_4	31.9(0.6)	66.2(0.5)
	FeO	17.6(0.4)	33.8
360	Fe_3O_4	32.7(1.0)	27.8(0.4)
	FeO	26.4(0.5)	71.3(0.4)
	α-Fe	46.1(12.6)	0.8(0.1)
380a	FeO	31.0(0.2)	84.6(0.1)
	α-Fe	26.8(0.3)	15.4(0.1)
380b	FeO	25.7(0.1)	72.1(0.1)
	α-Fe	25.6(0.1)	27.9(0.1)
380c	FeO	26.1(0.1)	63.5(0.1)
	α-Fe	27.2(0.1)	36.5(0.1)
380d	FeO	26.2(0.1)	57.4(0.1)
	α-Fe	28.4(0.1)	42.6(0.1)

Thereafter, the magnetite reflections continue to narrow, indicating an increase in crystallinity of the magnetite crystallites. However, the calculated crystallite size never exceeds 33 nm. The presence of silica prevents further sintering to larger crystallite sizes. Upon heating to 340°C, reflections characteristic of wüstite become evident. The relative abundance of wüstite continues to increase from 33.8 ± 0.5 % at 340°C to 84.6 ± 0.1 % at 380°C, while the calculated crystallite size increases from 17.6 ± 0.4 nm to 31.0 ± 0.2 nm. Iron only begins to form at 380°C

once a significant amount of wüstite is present in the sample.

This suggests that the presence of just 10 weight parts silica is able to alter the reduction pathway of the resulting magnetite phase. The magnetite first reduces to a stable phase of wüstite, which is itself reduced to iron. There does not appear to be a direct reduction of the magnetite to iron, nor a disproportionation of the wüstite. The resulting iron crystallites are significantly smaller than those formed in **100/0 Fe/SiO$_2$**, with a maximum calculated size of 28.4 ± 0.1 nm at the end of the reduction experiment. The crystalline phase composition of **100/10 Fe/SiO$_2$** between 280°C and 380°C is summarised graphically in Figure 5.11.

The silicon present in the ferrihydrite structure prevents sintering of the α-Fe particles, while the formation of Fe-O-Si bonds also inhibits the reduction of the Fe-species to Fe^0 in the iron oxide structure. Work reported by Masina *et al.* shows that a similar 2-line ferrihydrite promoted with 10 weight silica was reduced to magnetite at 300°C, but no further reduction to wüstite or iron was observed[87]. However, the *in situ* XRPD experiment, while heated to a maximum temperature of 450°C, recorded considerably fewer scans (27 min scans every 50°C while heating to the maximum temperature). As a result, there was insufficient time spent at an elevated temperature to reduce magnetite to wüstite and iron. Similarly, Suo *et al.* reported the presence of magnetite after reduction, however they employed a H_2/CO gas ratio of 2.0 for the reduction which was performed isothermally at 300°C for 20 hours, thus the energy available was insufficient to reduce magnetite to wüstite and iron[86].

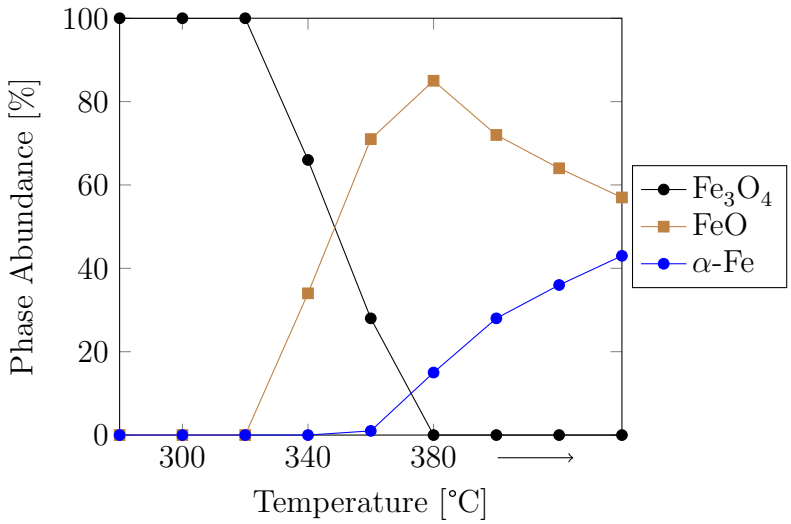

Figure 5.11: *Phase composition for the crystalline content of* ***100/10 Fe/SiO$_2$*** *calculated from in situ XRPD patterns from 280°C to 380°C. Amorphous reflections corresponding to 2-line ferrihydrite are present at all temperatures and were excluded from the quantification.*

The *in situ* X-ray powder diffractograms of **100/25 Fe/SiO$_2$** in 1 bar hydrogen and heated from 40°C to 380°C are shown in Figure 5.12. Rietveld refinement using the fundamental parameter, full pattern approach was performed at each temperature where crystalline phases were present.

At 40°C, the XRPD pattern of **100/25 Fe/SiO$_2$** exhibits two broad reflections at d-spacings of approximately 2.5 Å and 1.5 Å, consistent with the 2-line ferrihydrite phase initially present. On heating in the hydrogen atmosphere, there is no observable change in either reflection until 320°C, where the reflection at 2.5 Å begins to grow sharper and the reflection at 1.5 Å also grows sharper and shifts to lower degrees 2θ. This suggests the formation of extremely small/disordered crystallites of magnetite (marked Δ in Figure 5.12) and wüstite (marked $\circ$ in Figure 5.12). Attempts were made to perform Rietveld refinement on the patterns at 320°C and higher, but any results were heavily influenced by starting parameters as a result of the significant contribution of the 2-line ferrihydrite still present. In all cases, however, mean crystallite sizes for magnetite were approximately 5 nm and for wüstite were approximately 3 nm in diameter.

At 360°C, the formation of a small amount of iron is observed, and this increases on heating to 380°C. The relative amount of iron in the sample continues to grow, as evidenced by the increase in reflection intensity. The mean crystallite diameter of the iron remains constant at 80 nm for all scans at 380°C. This is remarkably different to **100/10 Fe/SiO$_2$**, which reduced to approximately 30 nm iron crystallites and a very well-defined three-step reduction of ferrihydrite → magnetite → wüstite → iron.

Suo *et al.* reported the formation of magnetite after reduction[86]. This sample also contained a large quantity of amorphous material after isothermal reduction in hydrogen for 20 hours. The silica precursor, however, was TEOS, and the initial iron oxide particles were considerably larger than those of this study. Zhang *et al.* also reported on the reduction of a similar iron-silica catalyst sample[140]. However, they demonstrated the presence of a single crystalline phase after isothermal reduction in 5% H_2/95% Ar mixture at 500°C for 10 hours which was the ferrosilicate material fayalite. Complementary Mössbauer spectroscopy data did demonstrate the presence of wüstite, likely too small (less than 3 nm) or too disordered to appear in the XRPD pattern.

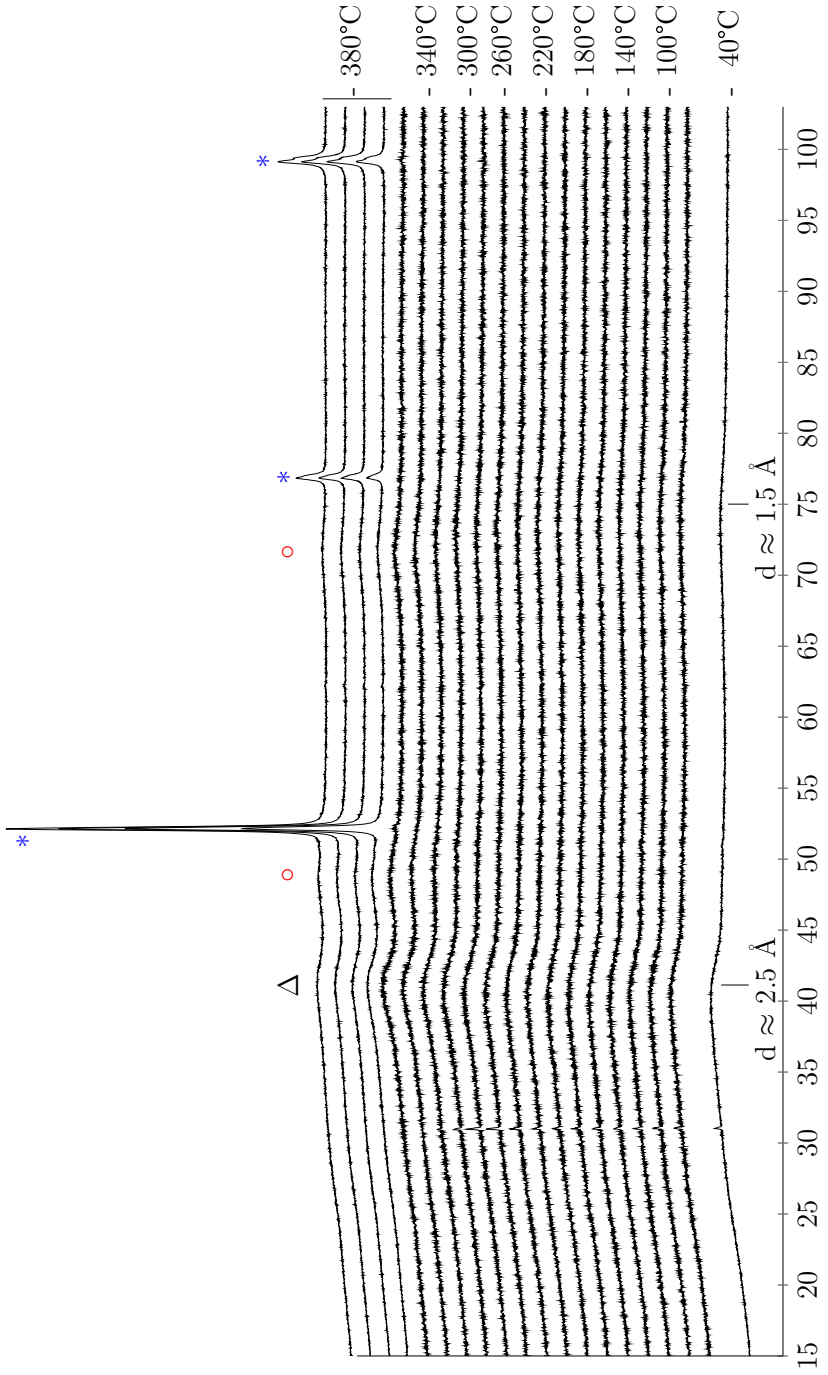

Figure 5.12: *In situ XRPD data for* ***100/25 Fe/SiO$_2$*** *in 1 bar hydrogen, heated from 40°C to 380°C. The most intense reflections of α-iron (*) are indicated. Broad reflections at d-spacings consistent with magnetite (Δ) and wüstite (○) are also indicated. The amorphous reflections at d ≈ 2.5 Å and d ≈ 1.5 Å are from 2-line ferrihydrite.*

The *in situ* X-ray powder diffractograms of **100/50 Fe/SiO$_2$** in 1 bar hydrogen and heated from 40°C to 380°C are shown in Figure 5.13. Rietveld refinement using the fundamental parameter, full pattern approach was performed at each temperature where crystalline phases were present.

Similar to **100/25 Fe/SiO$_2$**, the XRPD pattern of **100/50 Fe/SiO$_2$** exhibits two broad reflections at d-spacings of approximately 2.5 Å and 1.5 Å at 40°C, consistent with the 2-line ferrihydrite phase initially present. On heating in the hydrogen atmosphere, there is no observable change in either reflection until 320°C, where the reflection at 2.5 Å begin to grow sharper and the reflection at 1.5 Å also grows sharper and shifts to lower degrees 2θ. This suggests the formation of extremely small/disordered crystallites of magnetite (marked Δ in Figure 5.13) and wüstite (marked ○ in Figure 5.13). As with **100/25 Fe/SiO$_2$** attempts were made to perform Rietveld refinement on the patterns at 320°C and higher, but any results were heavily influenced by starting parameters as a result of the significant contribution of the 2-line ferrihydrite still present. In all cases, however, mean crystallite sizes for magnetite were approximately 5 nm and for wüstite were approximately 3 nm in diameter.

At 360°C, the formation of a small amount of iron is observed, and this increases on heating to 380°C. The relative amount of iron in the sample continues to grow, as evidenced by the increase in reflection intensity. The mean crystallite diameter of the iron remains constant at 80 nm for all scans at 380°C. This is very similar to **100/25 Fe/SiO$_2$**. Additionally, a very broad, amorphous reflection is visible between 20° and 30° 2θ at all temperatures, which indicates the presence of amorphous silica in the sample. For comparison, Figure 5.14 shows an XRPD pattern typical of amorphous silica[286] acquired using Cu-K$_\alpha$ radiation. In this example, the broad reflection has most of its intensity between 17° and 25° 2θ. Using Co-K$_\alpha$ radiation (as in this work) would shift this reflection to between 20° and 29° 2θ, consistent with the reflection described above.

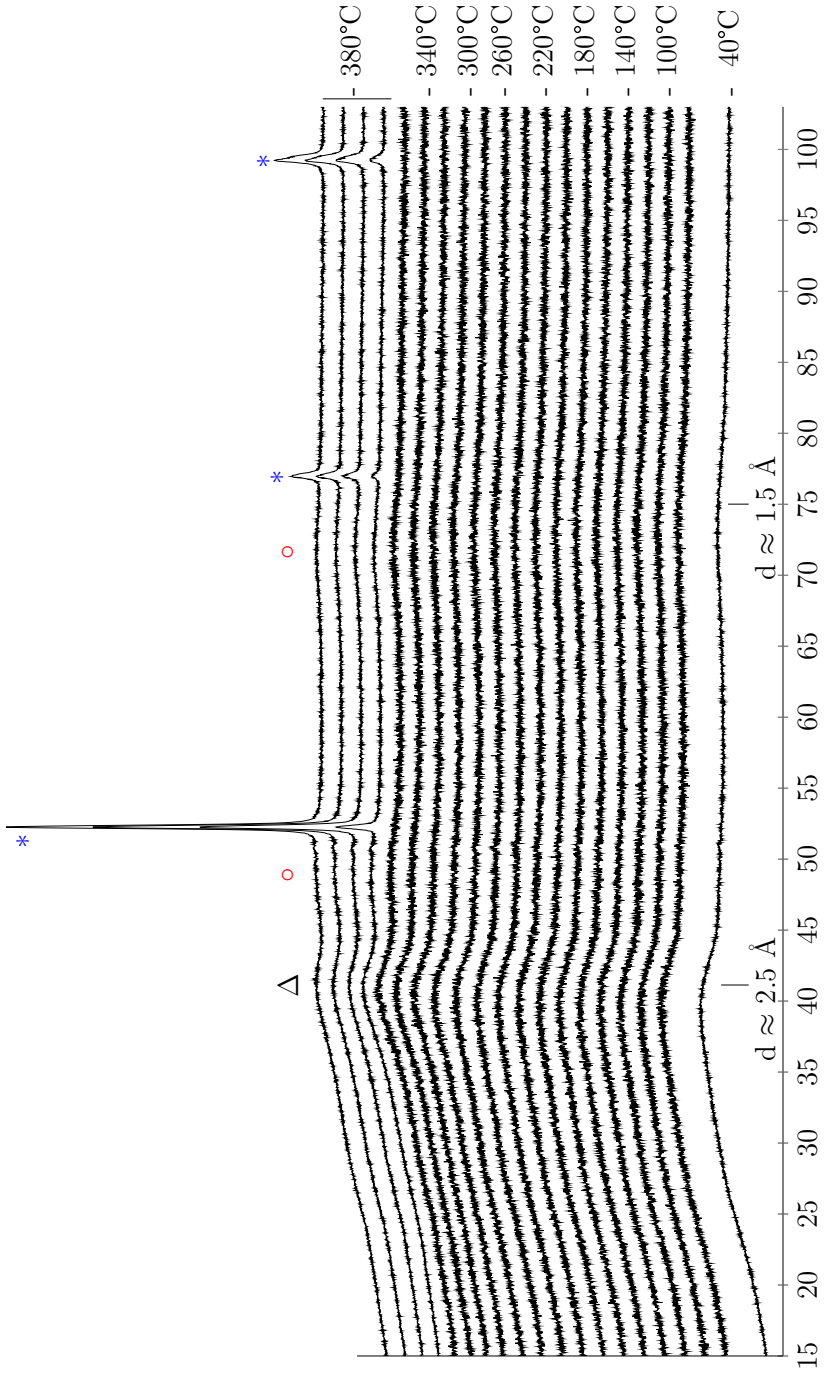

Figure 5.13: *In situ XRPD data for* ***100/50 Fe/SiO$_2$*** *in 1 bar hydrogen, heated from 40°C to 380°C. The most intense reflections of α-iron (*) are indicated. Broad reflections at d-spacings consistent with magnetite (Δ) and wüstite (○) are also indicated. The amorphous reflections at d ≈ 2.5 Å and d ≈ 1.5 Å are from 2-line ferrihydrite.*

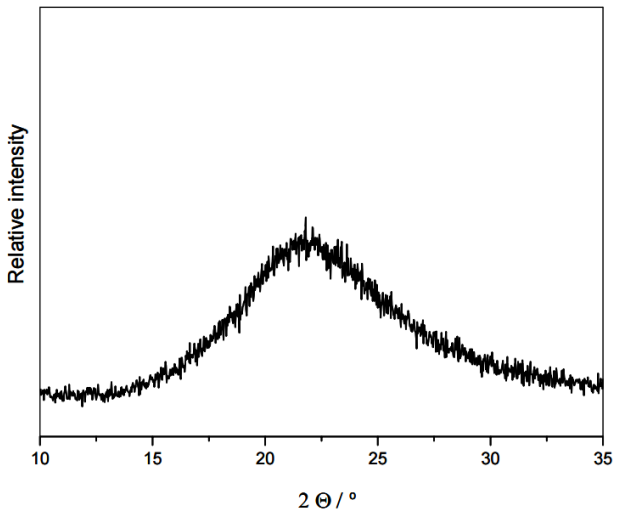

Figure 5.14: *XRPD pattern of amorphous silica using Cu-K_α radiation (λ=1.54 Å), demonstrating a broad reflection between 17 ° and 25 ° 2θ. Using Co-K_α radiation (λ=1.79 Å) would shift this reflection to between 20 ° and 29 ° 2θ. XRPD pattern taken from Musić et. al. (2011)*[286].

The formation of such large crystallites of iron in **100/25 Fe/SiO$_2$** and **100/50 Fe/SiO$_2$** is curious. This crystallite size is also observed in the *ex situ* reduced samples analysed using TEM (Chapter 5.4). For **100/10 Fe/SiO$_2$**, the addition of silica resulted in iron particles smaller than the silica-free **100/0 Fe/SiO$_2$**. However, this trend was not continued when the silica content was increased in **100/25 Fe/SiO$_2$** and **100/50 Fe/SiO$_2$**, even though all three samples initially exist as silicon-substituted ferrihydrite particles.

The proposed reason for this is that the increased amount of SiO_4 tetrahedra incorporated within the ferrihydrite material results in a considerably more defective structure for **100/25 Fe/SiO$_2$** and **100/50 Fe/SiO$_2$** when compared to **100/10 Fe/SiO$_2$**. It is well known that the amount of defects present in a solid affects the rate of diffusion through that material[287,288]. Thus the more defective structure allows reduced Fe^0 atoms to readily diffuse through the disordered material, resulting in the formation of larger iron particles than with **100/10 Fe/SiO$_2$**.

The only literature work reported for the reduction of a similar iron-silica sample in hydrogen was once again by Suo *et al.* who, after 20 hours at 300°C, still observed the two broad reflections corresponding to ferrihydrite[86].

The *in situ* X-ray powder diffractograms of **100/100 Fe/SiO$_2$** in 1 bar hydrogen and heated from 40°C to 380°C are shown in Figure 5.15. Rietveld refinement using the fundamental parameter, full pattern approach was performed at each temperature where crystalline phases were present.

100/100 Fe/SiO$_2$ demonstrates two broad reflections at 40°C. The first at 3.7 Å corresponds to amorphous silica, while the second at 2.5 Å corresponds to two-line ferrihydrite. A small amount of sodium nitrate is visible in the sample, indicated by the gray box in Figure 5.15. The sodium nitrate was also evident in Raman and *ex situ* XRPD data (Chapter 4.5 and Chapter 4.6). On heating, the sodium nitrate is reduced by the hydrogen, disappearing completely by 140°C through the release of NO_x gas. The shape of the reflection at 2.5 Å begins to change slightly at 360°C, indicating the formation of poorly crystalline magnetite. This is clearer in the first XRPD pattern collected at 380°C. There are no broad reflections to indicate the presence of any wüstite, as was the case with **100/25 Fe/SiO$_2$** and **100/50 Fe/SiO$_2$**.

Reflections corresponding to iron begin to form at 380°C, and as the temperature remains steady, the relative amount of iron also increases. The mean crystallite diameter of the iron particles is initially 41.9± 1.5 nm in the first scan at 380°C, but increases to 55.3 ± 0.5 nm, 56.6 ± 0.4 nm and 59.8 ± 0.4 nm in the subsequent scans.

There is no literature data available involving the reduction of such an iron-silica composite material with which to compare this data with.

The *in situ* X-ray powder diffractograms of **100/200 Fe/SiO$_2$** in 1 bar hydrogen and heated from 40°C to 380°C are shown in Figure 5.16. Rietveld refinement using the fundamental parameter, full pattern approach was performed at each temperature where crystalline phases were present.

100/200 Fe/SiO$_2$ demonstrates two broad reflections at 40°C. The first at 3.7 Å corresponds to amorphous silica, while the second at 2.5 Å corresponds to two-line ferrihydrite. However, the reflection at 3.7 Å is considerably more pronounced than in **100/100 Fe/SiO$_2$**, a result of the increased silica content within the sample. The shape of the reflection at 2.5 Å begins to change slightly at 340°C, indicating

the formation of poorly crystalline magnetite. There are no broad reflections to indicate the presence of any wüstite, as was the case with **100/25 Fe/SiO_2** and **100/50 Fe/SiO_2**.

A weak reflection, corresponding to the formation of a small amount of iron, is visible in the second scan recorded at 380°C. This reflection increases in intensity with subsequent scans at this temperature. The initial calculated average crystallite size measured in the second scan at 380°C is 13.7 ± 7.0 nm, but this increases slightly to 16.7 ± 4.9 nm and 18.8 ± 2.0 nm in the third and fourth scans respectively.

An additional reflection, common to all XRPD patterns, is visible at 51° 2θ. Comparison with the *ex situ* data presented in Figure 4.21 reveals that is not characteristic of the sample. Indeed, it may be matched with an Austenite stainless steel ($FeCr_{0.29}Ni_{0.16}C_{0.06}$) which is the material used in the sample holder. An appreciable number of X-rays are able to penetrate through the sample (mean-free path is higher as a result of increased silica content) and be scattered from the sample holder below.

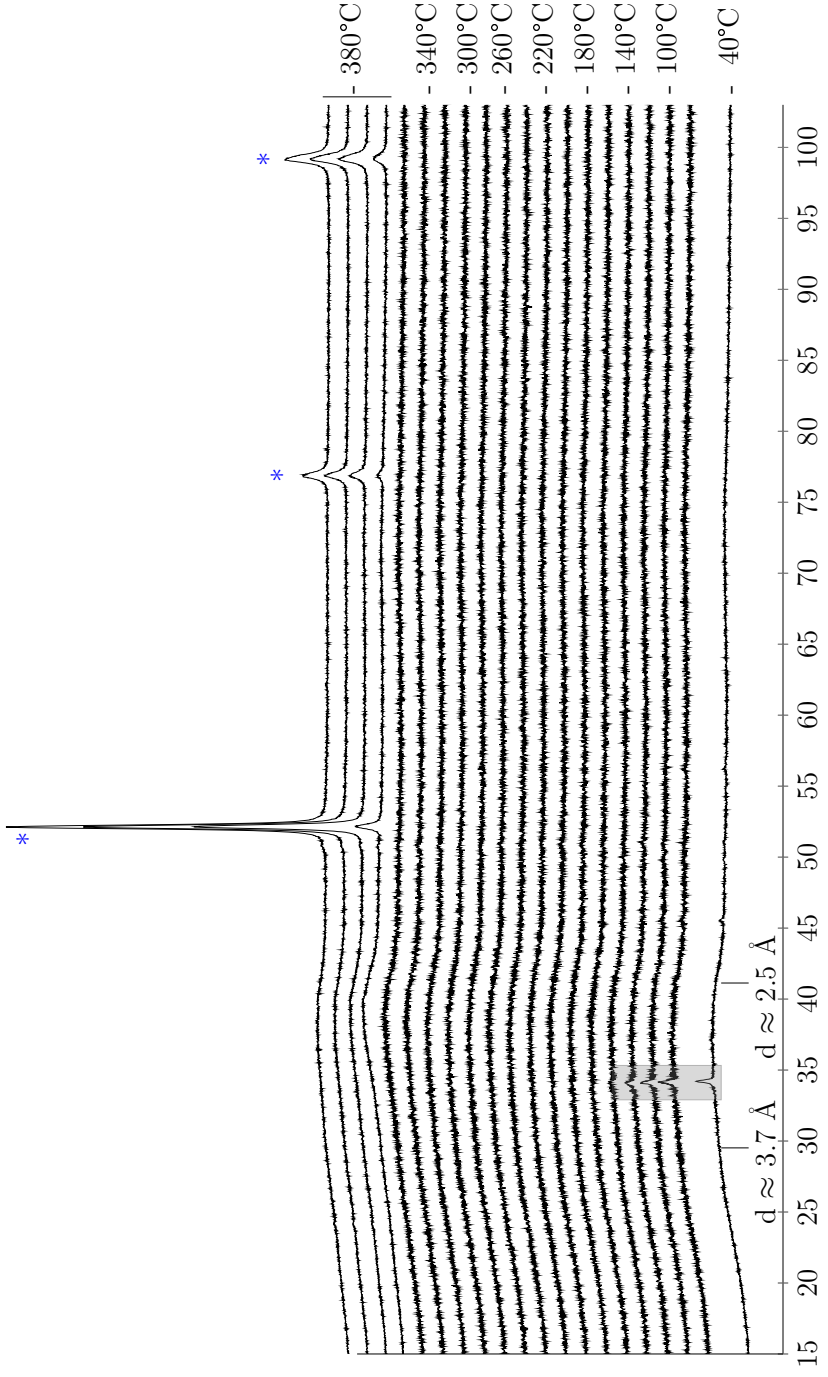

Figure 5.15: *In situ XRPD data for* ***100/100 Fe/SiO$_2$*** *in 1 bar hydrogen, heated from 40 °C to 380 °C. The most intense reflections of α-iron (*) are indicated. The amorphous reflections at d ≈ 2.5 Å are from 2-line ferrihydrite and those at d ≈ 3.7 Å are from vitreous silica. Reflections enclosed in the gray box are from sodium nitrate.*

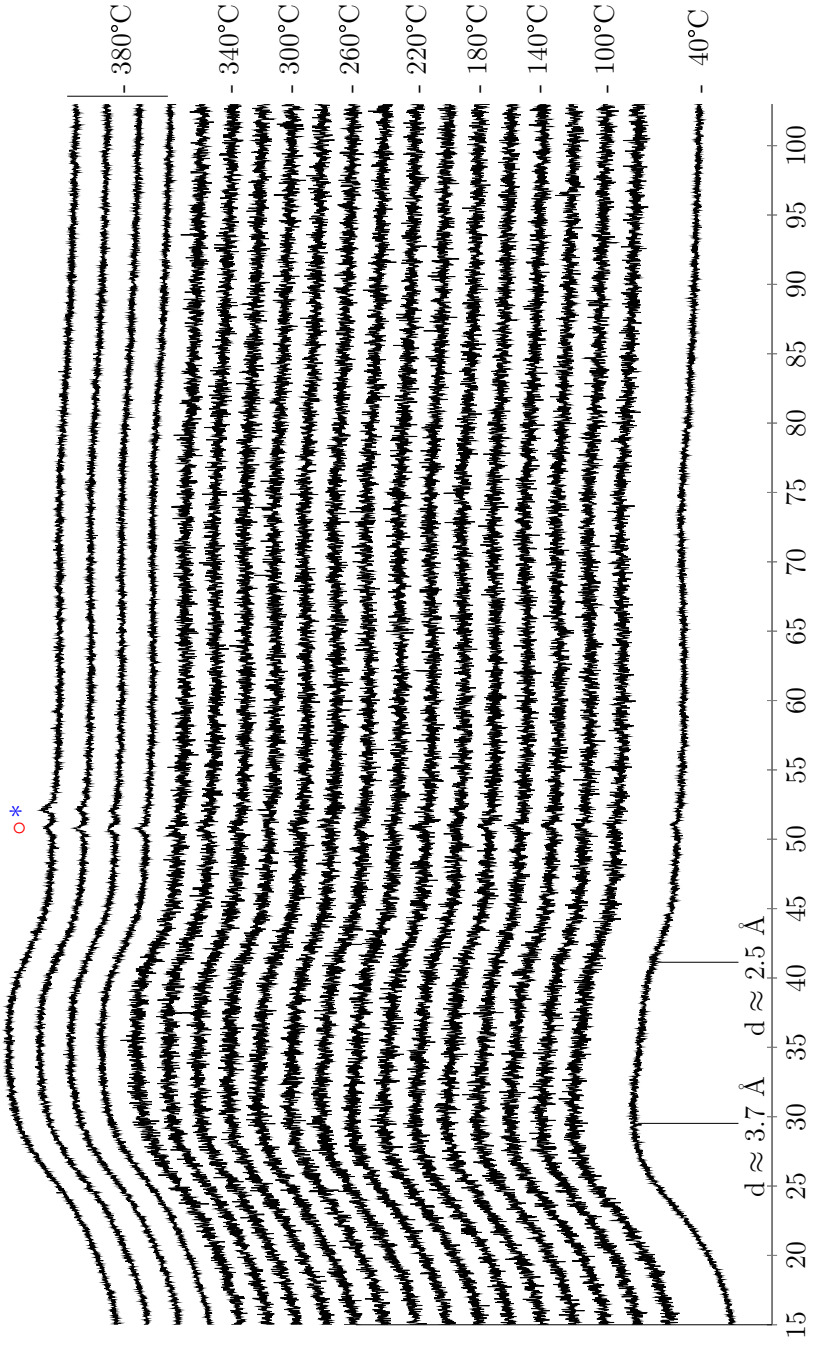

Figure 5.16: *In situ XRPD data for* ***100/200 Fe/SiO$_2$*** *in 1 bar hydrogen, heated from 40°C to 380°C. The most intense reflections of α-iron (*) are indicated. The amorphous reflections at d ≈ 2.5 Å and those at d ≈ 3.7 Å are from vitreous silica. The reflections at 51° 2θ (○) are from the stainless steel sample holder.*

5.4 Transmission Electron Microscopy

TEM micrographs of **100/0 Fe/SiO$_2$** after reduction at 400°C in hydrogen for 20 hours reveal the presence of very large, crystalline particles. A micrograph illustrating several of these particles is shown on the left of Figure 5.17. The corresponding SAED pattern of this region is shown on the right. It exhibits a number of diffraction spots in concentric rings and was subsequently rotationally averaged and the resulting line pattern used to index the reflections.

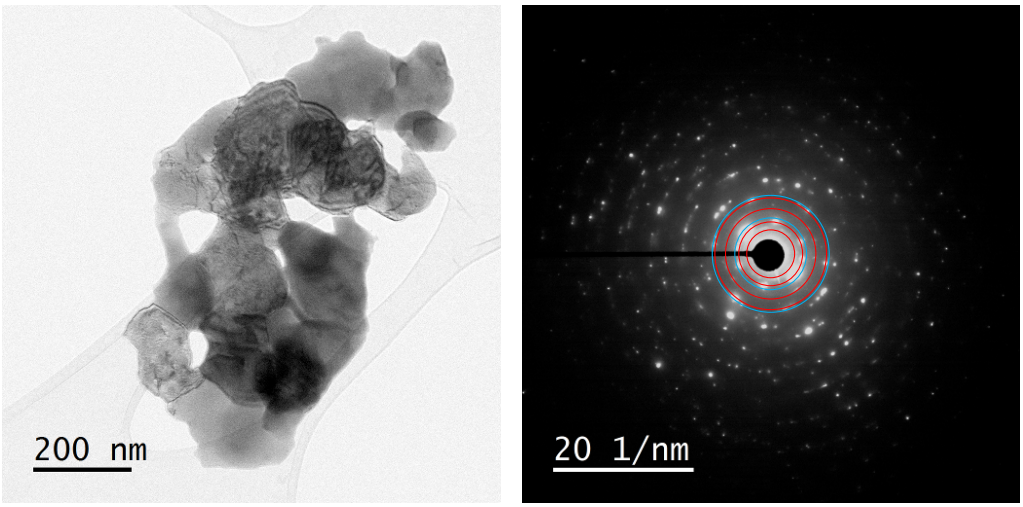

Figure 5.17: *TEM micrograph of* ***100/0 Fe/SiO$_2$*** *(left) and corresponding SAED pattern (right). Red concentric rings correspond to magnetite {311} (d = 2.53 Å), {440} (d = 2.10 Å),{511} (d = 1.62 Å) and {440} (d = 1.48 Å) reflections, while blue concentric rings are iron {110} (d=2.02 Å) and {200} (d = 1.43 Å) reflections.*

100/0 Fe/SiO$_2$ consists of a mixture of magnetite and metallic iron. A few of the lower order, more intense reflections of magnetite and iron are shown on the the SAED pattern as red and blue concentric rings, respectively. The red rings, working outwards from the center, correspond to the magnetite {311} (d = 2.53 Å), {440} (d = 2.10 Å), {511} (d = 1.62 Å) and {440} (d = 1.48 Å) reflections, while the blue rings correspond to the iron {110} (d=2.02 Å) and 200 (d = 1.43 Å) reflections. The particles visible in the BF-STEM micrograph exhibit diffraction contrast, a result of defects forming in the reduced particles. The co-existence of

magnetite and iron could be a result of incomplete reduction, or it could be the result of oxidation of iron particles when transferring from the quartz tube reactor to the electron microscope.

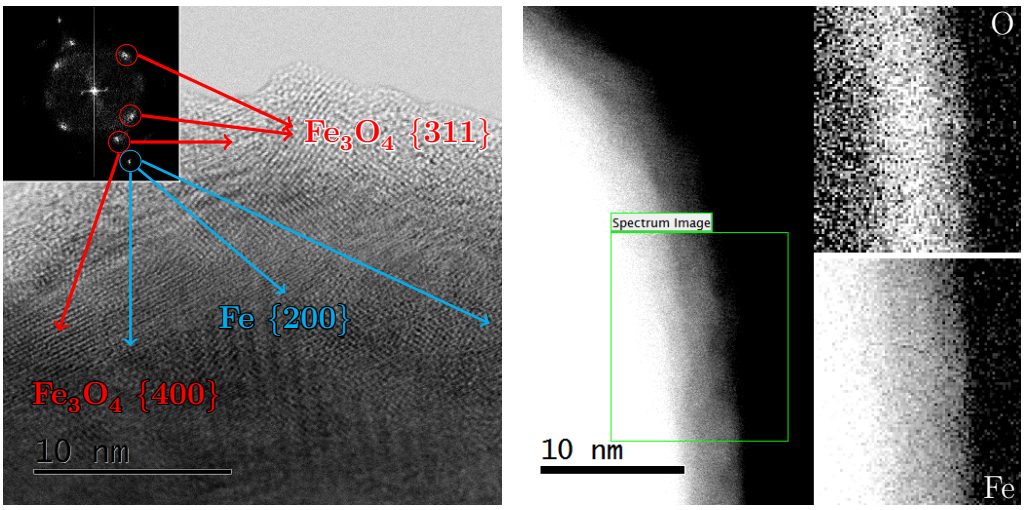

Figure 5.18: *High resolution BF-STEM micrograph of reduced* ***100/0 Fe/SiO$_2$*** *(left). The FFT of the BF-STEM micrographs is shown as an inset, with the regions of the particle responsible for the observed reflections in the FFT indicated in blue (iron) and red (magnetite). An EELS survey image of a particle edge (right) shows an oxygen concentration at the edge of the particle.*

HAADF STEM images (Figure 5.18 right) exhibit contrast at the particle edge. Lattice information obtained from a BF STEM image (Figure 5.18 left) reveals d-spacings corresponding to magnetite {311} and {400} lattice planes and iron {200} lattice planes. By applying a circular mask over selected spots in the FFT and performing an inverse FFT, the location of the individual d-spacings could be determined. Magnetite {311} and {400} d-spacings are located both at the particle surface and at its interior, while the iron {200} d-spacings are located only in the center of the particle. The magnetite is thus located as a shell around the particle, with an iron core, indicating that the magnetite is a result of oxidation, since incomplete reduction would result in an oxide core, with a reduced-metal shell.

This is further exemplified by the EELS data in Figure 5.18 right. The iron and oxygen compositional maps show clearly the concentration of oxygen at the surface of the particle, while the iron concentration increases towards the interior. The iron oxide shell that is formed is approximately 6 nm in thickness.

TEM micrographs of **100/10 Fe/SiO$_2$** after reduction at 400°C in hydrogen for 20 hours reveal a vastly different resulting particle morphology to those of **100/0 Fe/SiO$_2$**. A BF- and HAADF-STEM micrograph are shown in Figure 5.19. An SAED pattern of this region is also shown. It exhibits a number of diffraction spots in concentric rings and was subsequently rotationally averaged and the resulting line pattern used to index the reflections.

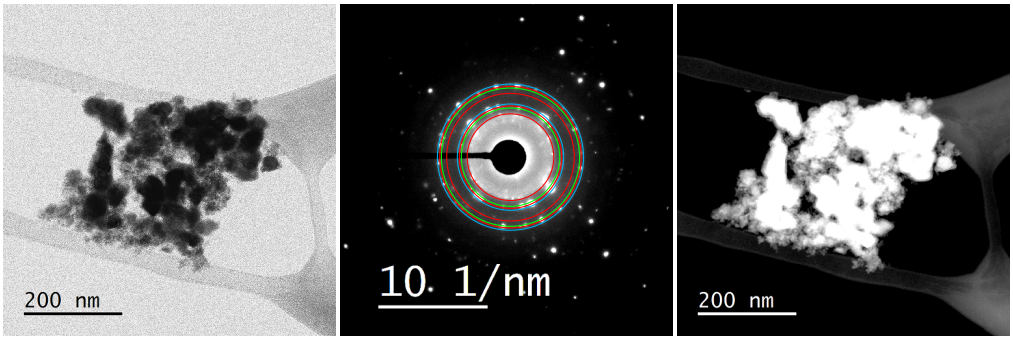

Figure 5.19: *BF-STEM micrograph of **100/10 Fe/SiO$_2$** (left) and corresponding HAADF-STEM micrograph (right). The SAED pattern is shown in the center. Red concentric rings correspond to magnetite {311} (d = 2.53 Å), {440} (d = 2.10 Å),{511} (d = 1.62 Å) and {440} (d = 1.48 Å) reflections, green concentric rings correspond to wüstite {200} (d = 2.15 Å) and {220} (d = 1.52 Å) reflections, while blue concentric rings are iron {110} (d=2.02 Å) and {200} (d = 1.43 Å) reflections.*

100/10 Fe/SiO$_2$ consists of a mixture of magnetite, wüstite and metallic iron. A few of the lower order, more intense reflections of magnetite, wüstite and iron are shown on the the SAED pattern as red, green and blue concentric rings, respectively. The red rings, working outwards from the center, correspond to the magnetite {311} (d = 2.53 Å), {440} (d = 2.10 Å), {511} (d = 1.62 Å) and {440} (d = 1.48 Å) reflections, the green correspond to wüstite {200} (d = 2.15 Å) and {220} (d = 1.52 Å) reflections, while the blue rings correspond to the iron {110} (d=2.02 Å) and {200} (d = 1.43 Å) reflections. The particles observed in the STEM micrographs are smaller than those in **100/0 Fe/SiO$_2$**, a result of the silica stabilising the formation of smaller crystallites of iron. Additionally, there are regions of poorly crystalline material. An SAED pattern recorded from an area with predominantly poorly crystalline material is shown in Figure 5.20.

It consists of several diffraction spots, which correspond to wüstite {200}, {220}

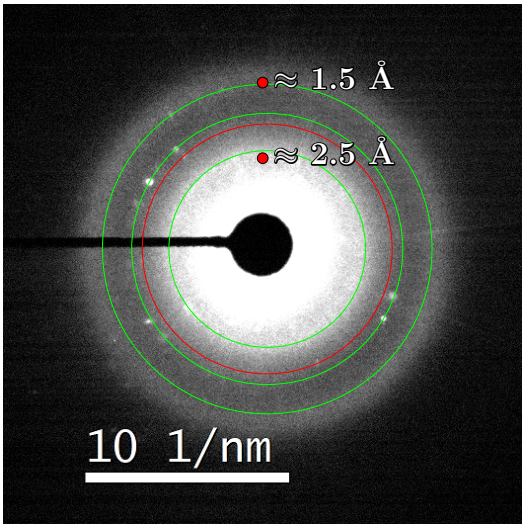

Figure 5.20: *SAED pattern recorded from a region of* ***100/10 Fe/SiO$_2$*** *consisting largely of poorly crystalline material. It contains two broad rings at approximately 2.5 Å and 1.5 Å, as well as diffraction spots correpsonding to wüstite (green circles) and magnetite (red circle).*

and {311} reflections (green rings, working outwards) and a {511} reflection of magnetite (red ring). It also exhibits two broad rings which are located at approximately 2.5 Å and 1.5 Å, characteristic of a poorly-crystalline iron oxide. This is in agreement with the *in situ* XRPD data, which suggests poorly crystalline material is present even after reduction at 380°C.

This poorly crystalline region also contains a significantly higher proportion of silicon than the larger particles. Figure 5.21 shows a HAADF-STEM image on the left. A mixture of well-defined particles and poorly crystalline regions are visible. EDS spectra were collected from the regions shown, and this data (normalised to the Fe-intensity) is shown in Figure 5.21 (right). Area A (red) which is a region of poorly crystalline material, has a much higher silicon content relative to iron, when compared with area B (blue). This inhomogeneity was not observed in the unreduced sample, and suggests that there is a migration of iron or silica during the reduction process. As a result, regions of iron oxide which have a lower silicon content are able to reduce and form well-defined iron particles, while those with a high silicon-content might reduce, but the high amount of silica structural units inhibits the formation of crystallised particles.

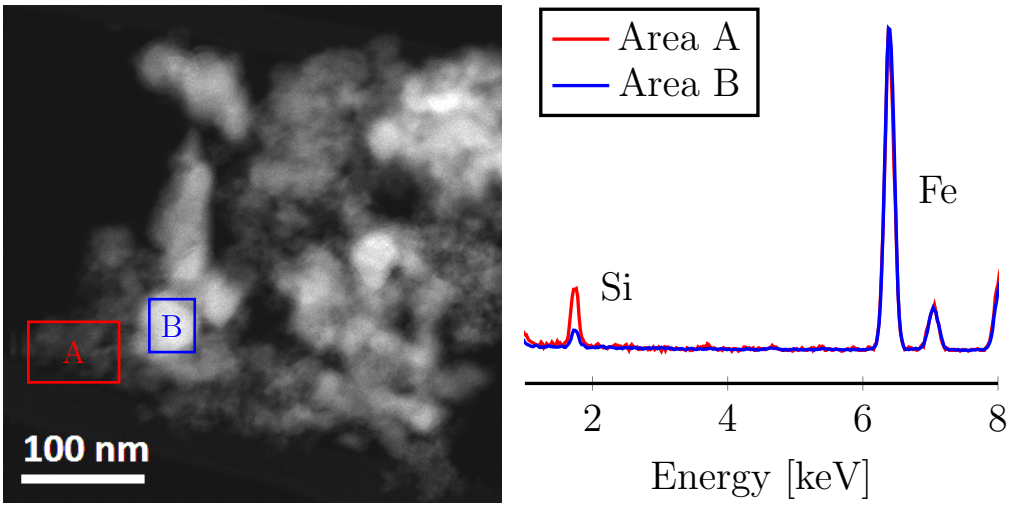

Figure 5.21: *HAADF-STEM micrograph (left) indicating the areas scanned by the electron beam. Area A corresponds to a poorly crystalline region, while area B corresponds to a well-defined, large particle. The corresponding EDS spectra (normalised to Fe-intensity) are shown on the right.*

As with **100/0 Fe/SiO$_2$**, HAADF micrographs of reduced **100/10 Fe/SiO$_2$** also exhibit a contrast variation at the particle edges. An EELS survey image, shown in Figure 5.22 (right) with the generated oxygen and iron compositional maps show once again the presence of an iron-rich core surrounded by an iron oxide shell. This is a result of oxidation on transferring from the reactor to the electron microscope. The Si-EELS signal was too weak to generate a compositional map, however EDS was able to provide insight into the distribution of silicon within these particles.

Figure 5.22 (left) is a HAADF micrograph of a single particle in reduced **100/10 Fe/SiO$_2$**. A linescan ($\approx$ 20 nm long) was performed from point A in the vacuum region, to point B in the interior of the particle. The corresponding EDS data collected is shown in Figure 5.22 (center). The iron counts have been suppressed by a factor of 5 to facilitate easier comparison of the data. Initially, the oxygen- (blue), iron- (red) and silicon-signals (green) are zero. Moving along the line, the iron- and oxygen-signals increase once the particle edge is reached and the electron beam comes into contact with the oxidation shell. Thereafter, the silicon-signal also begins to increase. However, the oxygen and silicon signals decrease on moving further towards the interior of the particle, while the iron continues to increase.

This not only suggests the presence of an iron oxide shell encapsulating metallic iron, but also that the silicon, likely in the form of silica (SiO_4) tetrahedra, is preferentially concentrated at the surface of the reduced iron particles.

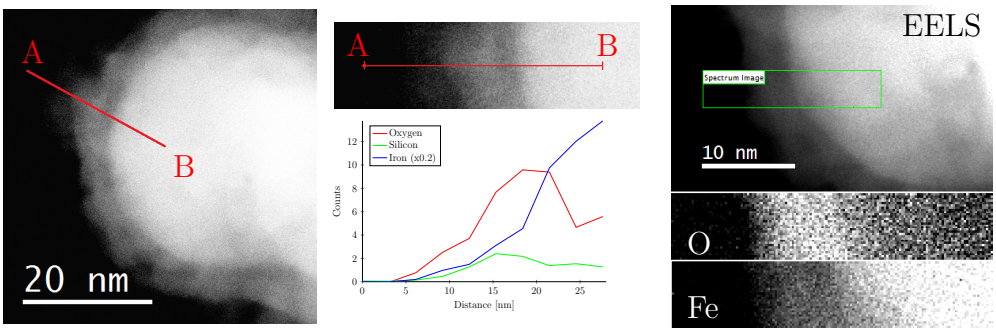

Figure 5.22: *HAADF-STEM micrograph (left) indicating the line scanned by the electron beam, starting at A and ending at B. The EDS counts for Fe, Si and O along line AB are shown (center). The Fe-signal has been suppressed by a factor of 5 to facilitate easier visualisation. EELS survey image (right) and corresponding Fe- and O-compositional maps illustrating the distribution of iron and oxygen in the scanned region.*

This has implications for FTS, which requires the dissociation of syngas onto active metal sites. The presence of a large concentration of silica at surface sites translates to a reduction in the number of available metal sites available for dissociation of syngas. Consequently, the expected catalytic activity will drop. Secondly, an increase in concentration of silica likely results in a higher density of Fe-O-Si bonds at the surface. This will greatly influence the surface energy of a catalyst particle, affecting the various steps involved in FTS.

Increasing the silica content in **100/25 Fe/SiO_2** once again results in different morphology after reduction at 400°C in hydrogen for 20 hours when compared to **100/0 Fe/SiO_2** and **100/10 Fe/SiO_2**. Representative HAADF-STEM micrographs are shown in Figure 5.23. The additional silica has not had the effect of stabilising smaller crystallites compared to **100/10 Fe/SiO_2**. Instead, the reduced sample consists of large particles located amongst very small particles. Some regions of sample consisted entirely of the small nanoparticle agglomerates.

Figure 5.23 (right) is a HAADF-STEM micrograph which reveals several large particles, between 110 nm and 170 nm in diameter scattered amongst very poorly

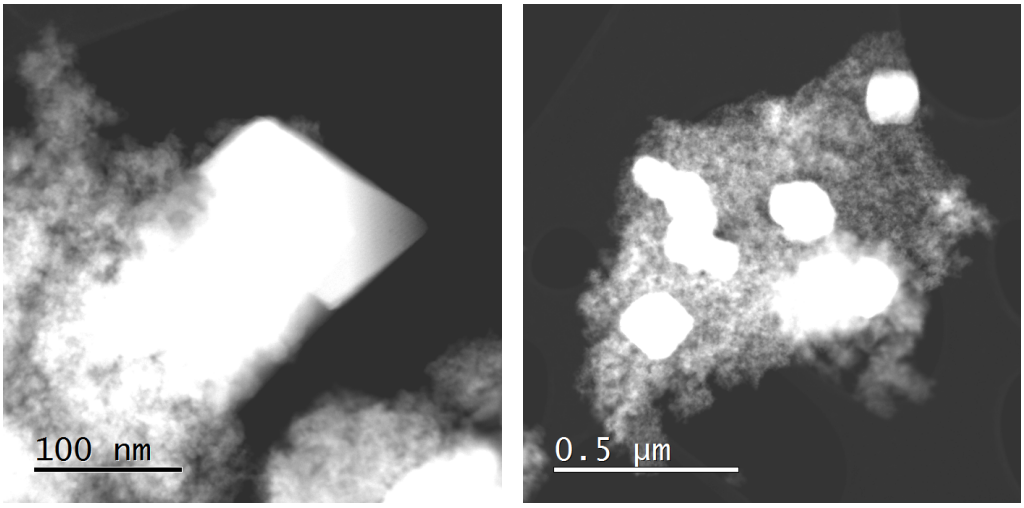

Figure 5.23: *HAADF-STEM microgprahs of reduced* ***100/25 Fe/SiO$_2$.***

crystalline material. The HAADF-STEM micrograph on the left is a large, single particle amongst the much smaller nanoparticles. These small nanoparticle resemble ferrihydrite in appearance, with diffraction patterns revealing two broad rings at approximately 2.5 Å and 1.5 Å. An SAED pattern taken from the region shown in Figure 5.23 (left) is shown on the left in Figure 5.24.

The SAED pattern reveals several distinct features. Firstly, the appearance of the two broad rings characteristic of poorly crystalline iron oxide are evident. Secondly, reflections are visible that correspond to a large single crystal grain oriented close to a zone axis. These are indicated by red rings around the reflections and originate from the large particle. Comparison with simulated spot patterns was performed using JEMS, and it was found that this large grain is that of magnetite oriented close to a <322> zone axis. The simulated spot pattern is shown on the right in Figure 5.24. Comparison with the EELS data (5.25) suggests that is the the right corner of the visible bright particle that is the magnetite grain. Finally, individual reflections are visible in the SAED pattern which originate from magnetite, wüstite and iron crystallites. Some of the lower order reflections are shown as red, green and blue quarter-circles respectively. The iron crystallites occur within the large particles, while wüstite and magnetite are present in the form of the small nanoparticles.

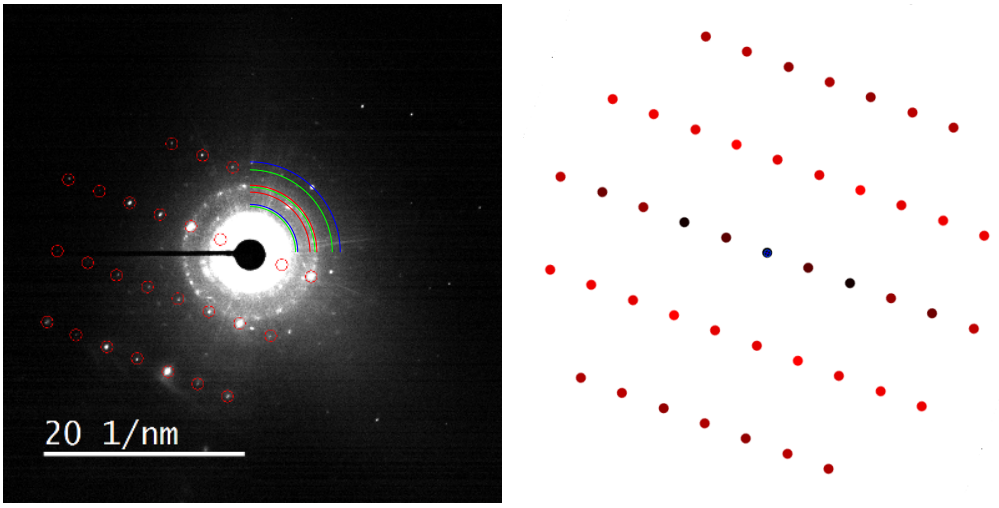

Figure 5.24: *SAED pattern of* ***100/25 Fe/SiO$_2$****. A large particle of magnetite oriented close to a <322> zone axis gives rise to the spot pattern shown in red circles. The theoretical magnetite <322> spot pattern is shown on the right. Two broad rings characteristic of amorphous iron oxide are visible, while reflections corresponding to magnetite (red), wüstite (green) and iron (blue) are indicated.*

As was observed in **100/10 Fe/SiO$_2$**, the large particles of **100/25 Fe/SiO$_2$** contain an oxide shell that is rich in silicon, while the interior is predominantly iron. This suggests the migration of SiO_4 units to the surface of the iron particles during reduction. The oxide layer is a result of oxidation of α-Fe when transferring from the quartz tube reactor to the electron microscope. An EELS survey image and corresponding Fe- Si- and O-compositional maps of the region shown in Figure 5.25.

The Fe-EELS map reveals that the bright particles in the HAADF-STEM image are composed of iron, while the O-EELS map shows very little oxygen at the center of these particles. It is concentrated at the edges of the particles. This is a result of an iron oxide shell forming around the large iron particles. Additionally the Si-EELS map shows a thin layer of silica surrounding the large particle in the top right of the micrograph, once again indicating a concentration of silica at the surface of the iron particles that form. The regions consisting of poorly crystalline to small nanoparticles of iron oxide consist of a uniform distribution of iron, silicon and oxygen.

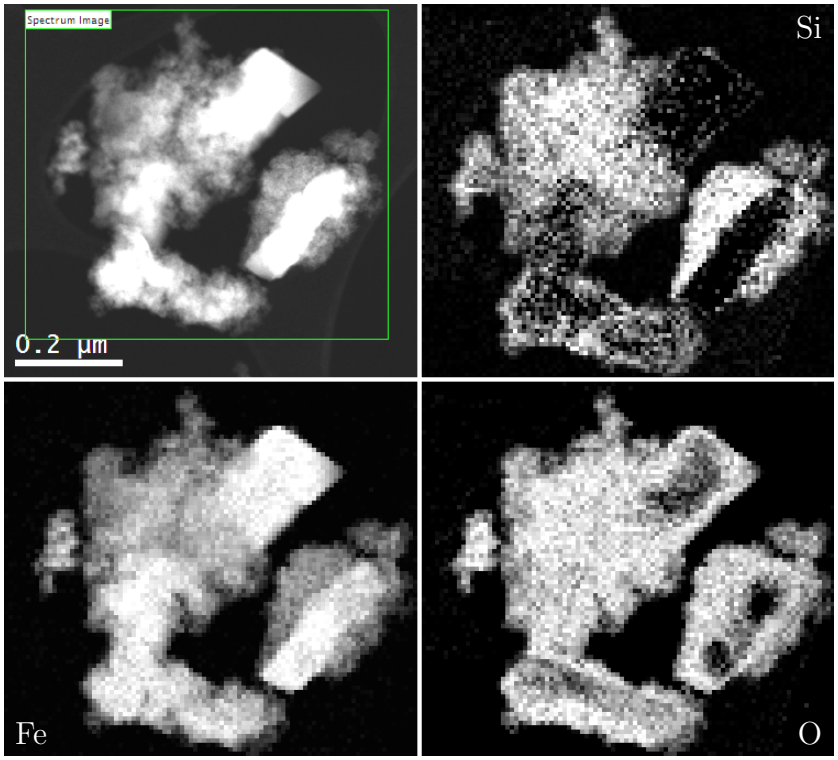

Figure 5.25: *EELS survey image of* ***100/25 Fe/SiO$_2$*** *and corresponding Si-, O- and Fe-compositional maps.*

100/50 Fe/SiO$_2$ reduced at 400°C for 20 hours in hydrogen is very similar to the equivalently reduced **100/25 Fe/SiO$_2$**. It consists of several large particles scattered amongst a collection of very small nanoparticles and poorly crystalline material. The BF-STEM micrograph shown in Figure 5.26 demonstrates such a particle in the bottom right, while the top left of the micrograph contains the poorly crystalline nanoparticle component that is prevalent throughout the sample. A qualitative inspection reveals fewer large particles than what was observed in **100/25 Fe/SiO$_2$**. An EDS spectrum (center inset), acquired from the large particle in Figure 5.26 (blue), reveals the presence of very little silicon (silica) while the EDS spectrum of the small, poorly crystalline nanoparticles (red) contains a significant amount of silicon. This is indicative of segregation between the iron and silica during reduction, as was observed for **100/25 Fe/SiO$_2$**.

A typical SAED pattern for **100/50 Fe/SiO$_2$** is shown on the right of Figure 5.26. It contains a large number of reflections located in concentric rings around

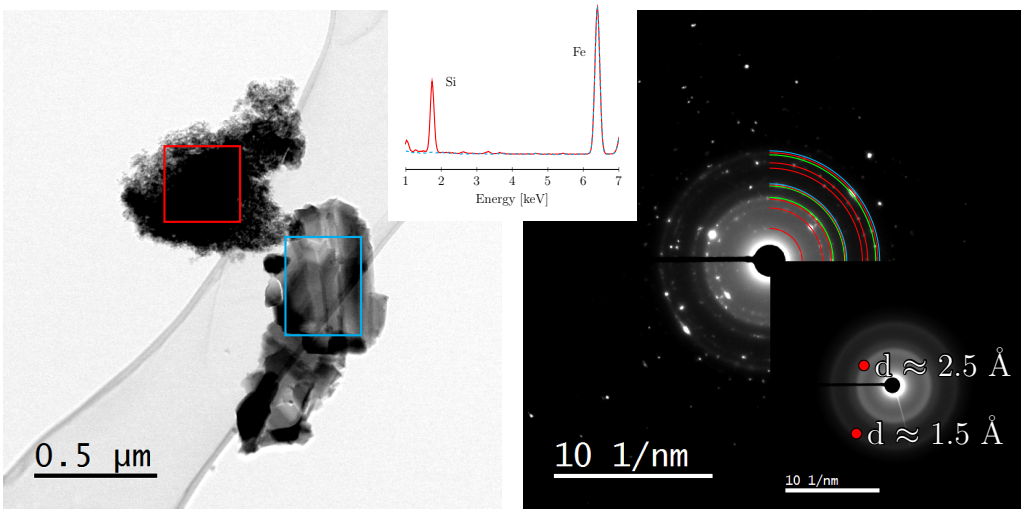

Figure 5.26: *BF-STEM micrograph of reduced* ***100/50 Fe/SiO$_2$*** *(left). An SAED pattern recorded from reduced* ***100/50 Fe/SiO$_2$*** *(right), while a second SAED pattern recorded from a region containing only small, poorly crystalline nanoparticles is also shown (inset).*

the center. The d-spacings of these rings suggest a mixture of magnetite (red), wüstite (green) and iron (blue) is present in the sample. Additionally, the SAED pattern shown as an inset was recorded from an area of the sample where only small, poorly crystalline nanoparticles were visible. It reveals the presence of the two broad rings at approximately 2.5 Å and 1.5 Å, corresponding to a collection of poorly crystalline iron oxides.

The elemental distribution of iron, silicon and oxygen is similar to **100/10 Fe/SiO$_2$** and **100/25 Fe/SiO$_2$**. Figure 5.27 contains two EELS survey images and the corresponding Fe-, Si- and O-maps. On the left is a lower resolution data set of large particles. They are composed of iron and oxygen. The particles contain very little silicon.

There are, however, two regions high in silicon. These are inscribed by blue and red rectangles. The weaker iron signal in these areas suggests a lower iron content than elsewhere on the surveyed region, while the simultaneous presence of oxygen suggests that these regions are poorly crystalline iron oxide-silica composites.

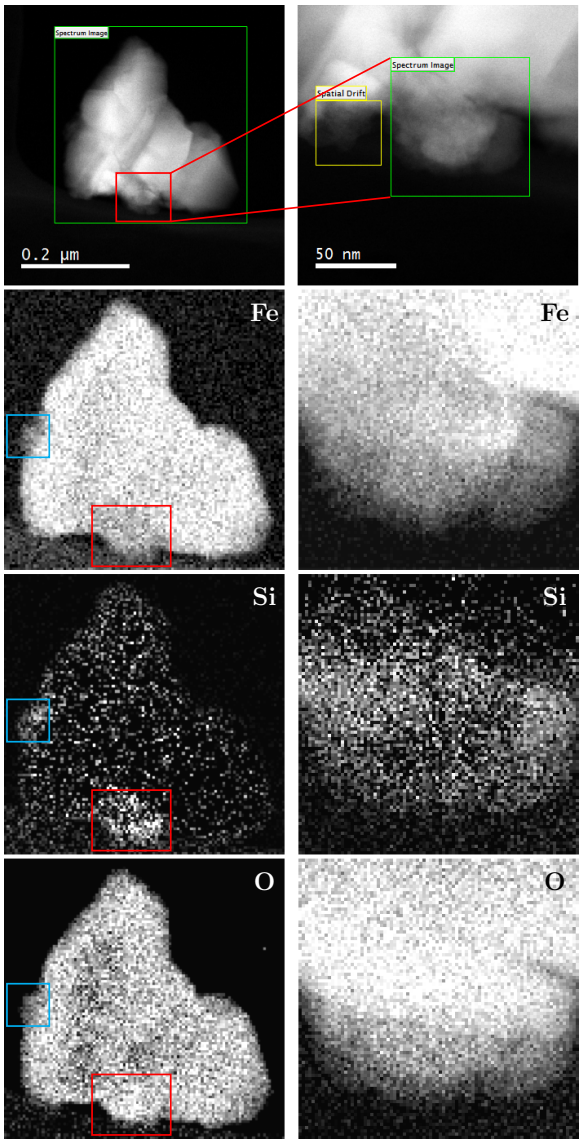

Figure 5.27: *EELS survey image of* ***100/50 Fe/SiO$_2$*** *and corresponding Si-, O- and Fe-compositional maps (left). A secondary EELS survey image of the region inscribed by the red rectangle (right).*

A second EELS survey scan was performed on the area inscribed by the red rectangle and this data is shown on the right of Figure 5.27. The HAADF-STEM micrographs reveal some contrast variation. The EELS-compositional maps reveal that this is the result of segregation between silicon- and iron-bearing phases. The oxygen signal is fairly uniform across the EELS survey region, however the

silicon is located around the edge of large bright particle visible in the center of the micrograph, and the particle at the top of the micrograph. This suggests that the silicon has once again migrated to the edge of the iron particles, tending to concentrate at the surface. A small amount of poorly crystalline iron oxide-silica material is present on the bottom right of the survey image.

As discussed in Chapter 4.4, the initial product of **100/100 Fe/SiO$_2$** is very different to **100/10 Fe/SiO$_2$**, **100/25 Fe/SiO$_2$** and **100/50 Fe/SiO$_2$**, consisting of a mixture of iron-infused vitreous silica and very small iron oxide domains encapsulated in the silica matrix. After reduction at 400°C for 20 hours in hydrogen, the resulting product is also different to reduced forms of the lower silica content samples. The left of Figure 5.28 is a HAADF-STEM micrograph of **100/100 Fe/SiO$_2$**. It does not contain any large, individual particle. Rather it is an agglomeration of poorly crystalline material.

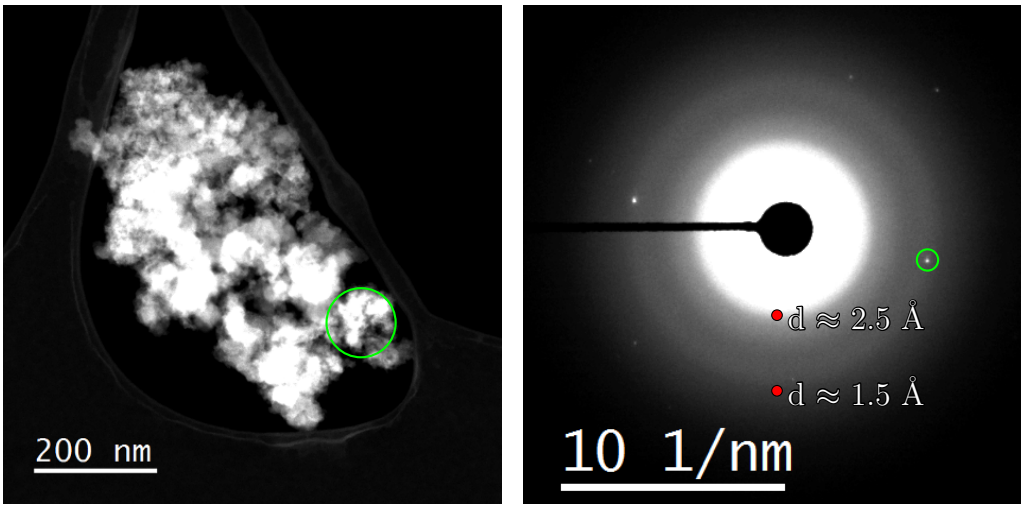

Figure 5.28: *HAADF-STEM micrographs of **100/100 Fe/SiO$_2$** (right). SAED pattern of the same region (left). The reflection inscribed by the green ring originates from the corresponding region shown in the HAADF-STEM micrograph.*

However, the SAED pattern, shown on the right of Figure 5.28, does exhibit a few reflections, with d-spacings corresponding to those of magnetite, which correspond to more crystalline domains within the sample. A HCDF micrograph generated using the reflections at the d-spacing of the reflection inscribed by the green ring

was used to identify the region of the sample containing the more crystalline material. Two broad rings at d-spacings of approximately 2.5 Å and 1.5 Å are also visible, corresponding to poorly crystalline iron oxide, most likely two-line ferrihydrite, although the existence of poorly crystalline magnetite and wüstite may not be excluded.

A high resolution HAADF-STEM micrograph of **100/100 Fe/SiO$_2$** is shown in Figure 5.29. The contrast in the micrograph is a result of small iron-rich domains within the silica matrix, which give rise to the broad rings in the SAED pattern. A single, crystalline particle is visible at the edge of the silica, and reveals lattice spacings (measured using the FFT shown as an inset) which identify this particle as magnetite. While it is possible that this magnetite particle is the result of partial reduction of the initial iron oxide, it is also possible that it is the result of oxidation of iron particles that formed during reduction. Correlation with the *in situ* XRPD data, which suggests the only crystalline phase to form is iron, supports the latter hypothesis. While **100/10 Fe/SiO$_2$**, **100/25 Fe/SiO$_2$** and **100/50 Fe/SiO$_2$** all had partially reduced iron particles (iron oxide shell, metal iron interior), the small size of the iron particle in this case resulted in complete oxidation of the particle to magnetite.

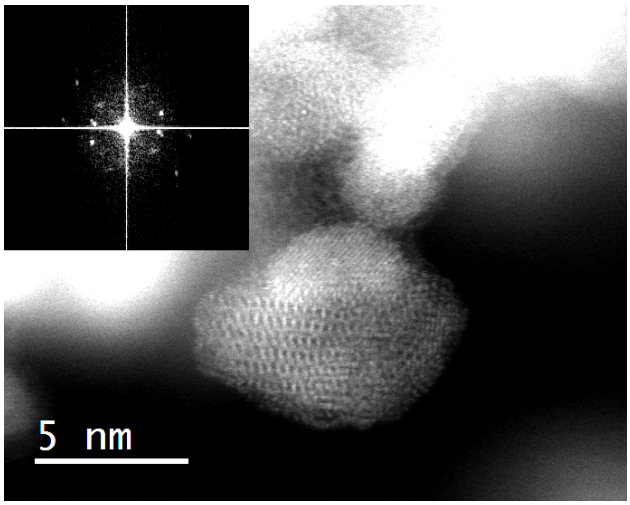

Figure 5.29: *High resolution HAADF-STEM micrograph of* ***100/100 Fe/SiO$_2$*** *showing a crystalline particle. FFT (insert) reveals lattice spacings consistent with those of magnetite.*

Elemental compositional maps obtained from STEM-EELS and STEM-EDS data are shown in Figure 5.30. They show an almost-homogeneous distribution of iron, oxygen and silicon. This is very different from the large degree of elemental-segregation observed in the samples with a lower silica content. The Fe-EELS map does, however, reveal some concentrations of iron - a result of the small iron oxide domains which give rise to the crystalline reflections in the SAED patterns.

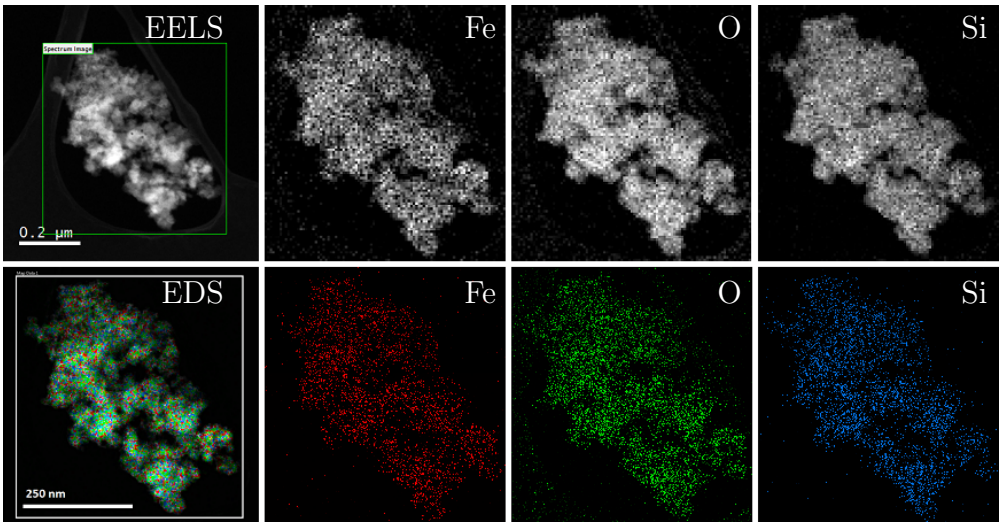

Figure 5.30: *STEM-EELS and STEM-EDS data for* ***100/100 Fe/SiO$_2$*** *and the resulting Fe-, O- and Si-compositional maps.*

100/200 Fe/SiO$_2$, similar to **100/100 Fe/SiO$_2$**, demonstrates the presence of amorphous silica containing small iron-rich domains. A HAADF-STEM micrograph of **100/200 Fe/SiO$_2$** is shown on the left in Figure 5.31. A large amount of contrast variation is evident in the micrograph, which suggests localised iron-rich regions (brighter regions) in amongst the darker, silica-rich regions. An SAED pattern is shown on the right of Figure 5.31. It contains the two-broad reflections common to two-line ferrihydrite, although once again the presence of poorly crystalline magnetite and wüstite is also a possibility. Several low intensity reflection spots are visible at three unique d-spacings, corresponding to magnetite {400}, {511} and {440} reflections. Correlating this with the *in situ* XRPD data suggests that these magnetite domains initially exist as iron, but are oxidised to magnetite on transferring the sample from reactor to microscope.

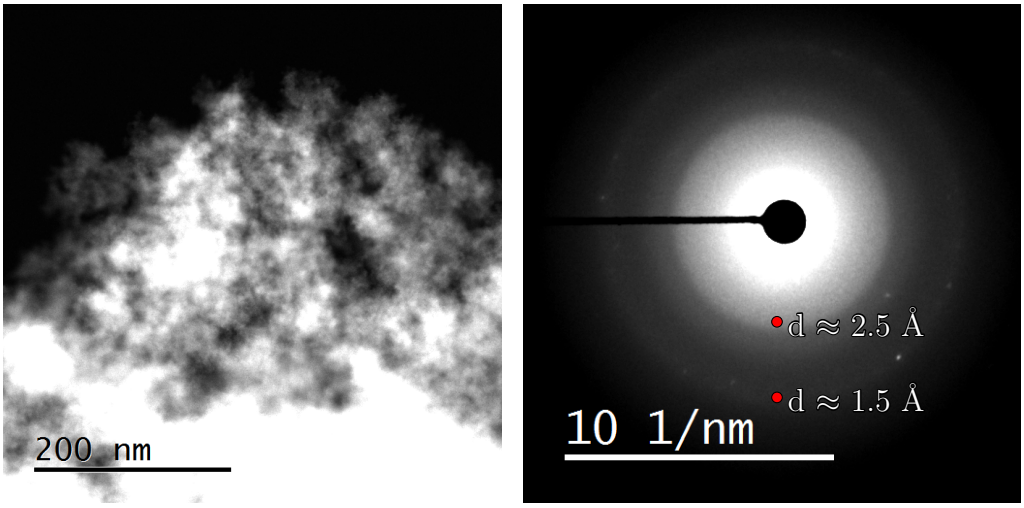

Figure 5.31: *HAADF-STEM micrograph of* ***100/200 Fe/SiO$_2$*** *(left) and the corresponding SAED pattern (right). The few diffraction spots visible correspond to magnetite.*

Elemental compositional maps obtained from STEM-EELS are shown in Figure 5.32. They show a distribution of oxygen that correlates well with the HAADF micrograph. The Fe-compositional map shows very small concentrations of iron throughout the matrix, while the Si-map reveals silicon distributed almost over the entirety of the scanned area, with silicon-deficient regions corresponding to regions with localised iron concentrations. This strongly suggests the formation of very small crystalline iron-containing domains during reduction which give rise to the reflection spots visible in the SAED patterns.

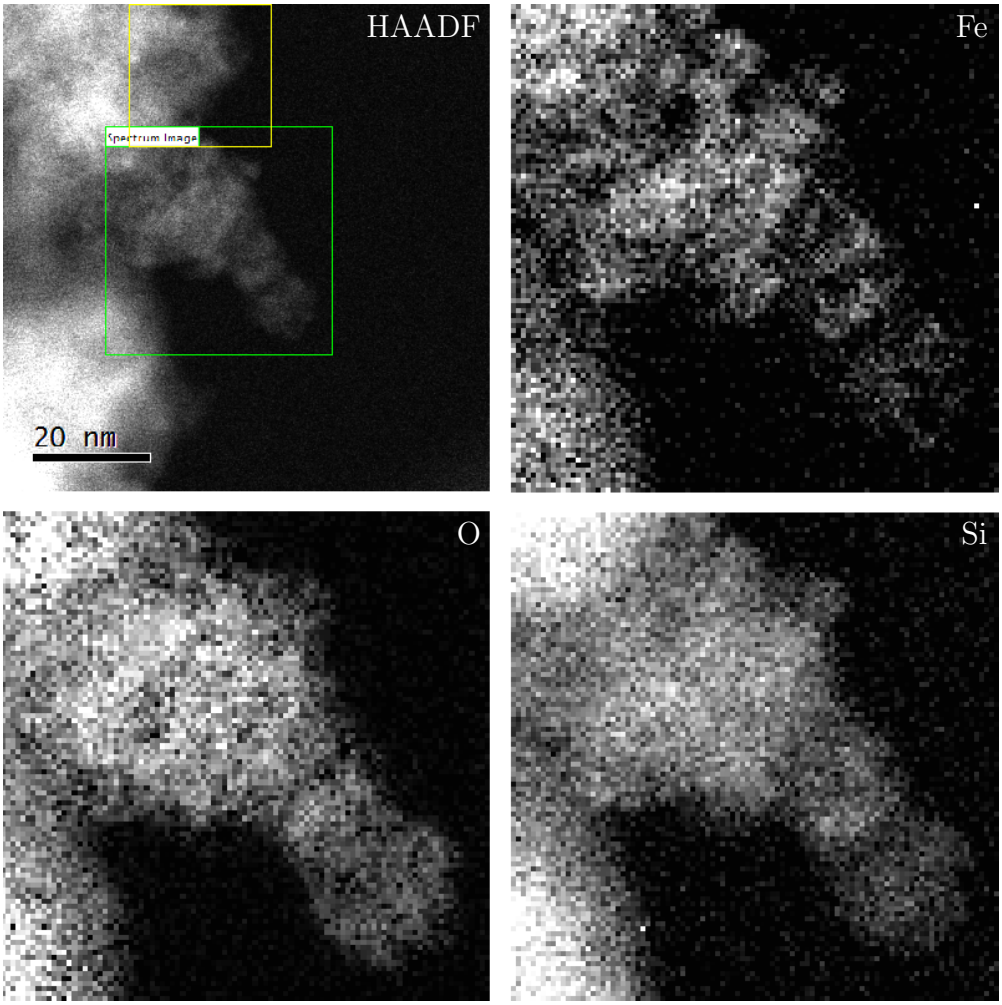

Figure 5.32: *STEM-EELS data for* ***100/200 Fe/SiO$_2$*** *and the resulting Fe-, O- and Si-compositional maps.*

5.5 Chapter Conclusions

This chapter discusses the reduction of the iron oxides prepared in Chapter 4. The reduction was characterised using TPR, *in situ* XRPD and electron microscopy techniques.

TPR data revealed a regular trend on increasing silica content within each of the samples. With **100/0 Fe/SiO$_2$**, the reduction is a two-step process of hematite

→ magnetite → iron, confirmed by comparison of theoretical and experimental hydrogen consumptions at each reduction step. The addition of silica has four effects on the various samples.

Firstly, it causes the reduction to shift to higher temperatures, a result of Fe-O-Si bonds which are more difficult to reduce than standard Fe-O bonds. Secondly, it stabilises the formation of a wüstite phase in the reducing atmopshere, which would otherwise dissociate or reduce immediately to α-Fe. This splits the reduction of magnetite to iron into two distinct steps *viz.* magnetite → wüstite and wüstite → iron.

Thirdly, the presence of silica causes the reduction peaks to continually broaden. This is a result of local concentration variations of silicon with the initial sample, leading to varying concentrations of Fe-O-Si bonds. A direct consequence of this is that regions with lower Fe-O-Si bond density are more easily reduced, while the opposite is true for those with a higher density of such bonds. This prevented the calculation of hydrogen consumption at each step, since it was not possible to deconvolute the various reduction peaks. Finally, the addition of silica results in a certain percentage of the Fe^{3+} in the sample that did not completely reduced to metallic iron (Fe^0). This percentage increased with increasing silica content, and is the result of small domains of iron silicates forming during reduction.

The *in situ* XRPD data for **100/0 Fe/SiO$_2$** shows the same two-step reduction that was observed in the TPR measurements. Hematite begins to reduce to magnetite at 260°C, which itself begins to reduce to iron from 340°C. A small amount of wüstite appeared between 320 and 360 °C, but was readily reduced to iron. Mean crystallite diameter of the final iron domains, determined using a full pattern, fundamental parameter Rietveld refinement, was 68 nm.

The addition of silica in **100/10 Fe/SiO$_2$** resulted in a shift in reduction to higher temperatures. The XRPD data shows clearly the existence of a stable wüstite phase forming between magnetite and iron, highlighting the change from a two-step to a three-step reduction pathway. Even after 8 hours at 380 °C, the amount of wüstite exists in appreciable quantities. The mean crystallite diameter of the final iron domains was 28 nm. Amorphous reflections were still visible at the end of the experiment.

100/25 Fe/SiO$_2$ and **100/50 Fe/SiO$_2$** demonstrated very different behaviour to **100/10 Fe/SiO$_2$**. The reduction still occurs in a three-step process, however, crystalline magnetite and wüstite are not formed. Instead, broad reflections at d-spacings of the most intense reflections of these two phases suggest that they exist as very small, disordered particles. The reduction to iron, which occurs at 380 °C in both samples, results in particles with a mean crystallite diameter of 80 nm. Significant quantities of small, disordered magnetite, wüstite and ferrihydrite-like material remains at the end of the reduction experiment.

100/100 Fe/SiO$_2$ and **100/200 Fe/SiO$_2$** both exhibit two broad reflections throughout the entirety of the reduction experiment, with some crystalline iron reflections appearing at 380°C. The mean crystallite size is 60 nm in **100/100 Fe/SiO$_2$** and 14 nm in **100/200 Fe/SiO$_2$**. The much smaller mean particle size in the highest silica-content sample is the result of the encapsulating silica isolating the initial iron oxide domains, preventing access to additional iron atoms to allow for the growth of larger particles.

The samples were reduced *ex situ* at 400°C for 20 hours in hydrogen, prior to TEM analysis. The process of transferring the sample from the reactor to the microscope caused the iron particles to oxidize. Larger iron particles still contained an iron interior, while smaller particles were completely oxidised to magnetite.

100/0 Fe/SiO$_2$ consists of very large particles consisting of an iron core with an encapsulating iron-oxide (magnetite) shell. It is believed that during reduction, iron particles are formed, but the edges of these particles are oxidised to magnetite when transferring from the reactor to the electron microscope.

100/10 Fe/SiO$_2$ consists of large iron particles scattered amongst poorly crystalline material. STEM-EDS linescans reveal a small amount of silicon located at the edge of iron particles, but not at the interior. This suggests a small amount of silicon is contained at or near the surface of the iron particles that form during reduction. This has implications for catalysis since it will alter the surface energies and also decrease the number of active metal sites.

The iron particles formed during reduction of **100/25 Fe/SiO$_2$** and **100/50 Fe/SiO$_2$** are larger than those formed in **100/10 Fe/SiO$_2$**, consistent with the

data obtained from *in situ* XRPD. SAED diffraction patterns reveal reflections at d-spacings consistent with magnetite, wüstite and iron. A large amount of poorly crystalline material is also evident across the entirety of the sample. STEM-EDS elemental analysis of there poorly crystalline regions shows a much higher silicon content when compared to the iron particles. The iron particles once again contain a small amount of silicon at the surface. This suggests that during reduction, Fe^{3+} is reduced to Fe^{0} atoms which diffuse out of the particle framework and come together to form the final iron particles.

100/100 Fe/SiO$_2$ and **100/200 Fe/SiO$_2$** both consist of small crystallite domains of iron oxide within a vitreous silica network. These iron oxide domains were likely iron metal prior to oxidation on exposure to atmospheric conditions during transferal from the reactor to the microscope.

6 Reduction in Hydrogen - *In Situ* TEM Gas Flow Holders

6.1 Experimental Details

6.1.1 Protochips Atmosphere^{TM} Gas Flow Cell

This work was performed in collaboration with the University of Manchester. TEM micrographs, BF and HAADF STEM images, SAED patterns, EDS and EELS data were acquired using an FEI Titan G2 operated at 200 kV.

Initially, the small silicon chip used in the gas cell construction (described in Chapter 3.3.2) was soaked in acetone for 1 minute to remove a protective polymer coating. It was then soaked in methanol for a further minute to remove the acetone. The large chip was blown with compressed air to remove any particulates. Both chips were plasma cleaned in a 25%/75% oxygen/argon mixture for 10 minutes, using a Fischione 1070 at 100 % power and 40 $cm^3.min^{-1}$ flow rate. The sample was placed in a small volume of ethanol and ultrasonicated to thoroughly disperse it. A small drop of this solution was placed on the silicon nitride membrane of the large chip. Both chips were plasma cleaned for a further 10 minutes using the same conditions.

The gas cell was assembled on the tip of the sample holder, and the system placed in a vacuum chamber with the gas connections of the holder exposed to the atmosphere. This was to test for leaks. If the vacuum pressure reached a value below 10^{-6} bar, a good seal was present and pressures of approximately 1 atm of experimental gas would not leak into the microscope column. The gas flow holder was then transferred to the microscope, and gas lines connected.

Samples were reduced in high purity hydrogen gas (99.999 %) between 700 and 950 mbar, while temperatures ranged from room temperature to 750°C. After exposure to hydrogen at a given temperature for a sufficient period of time to ensure reduction, the gas cell was evacuated to quench the reduction process. Regions of

interest on the sample were constantly probed at various temperatures to study any changes that had occurred. At various stages of the analyses, additional regions of interest that had not been exposed to any electron beam dose were also analysed in order to evaluate the effect of the electron beam on the reduction process. This is particularly important since not only is the electron beam a reduction source, it can also damage the sample[170]and ionize the experimental gas[289,290], altering the reduction conditions.

The samples were heated at relatively fast rates, but there was a large amount of sample drift on changing the temperature. This is a result of the thermal expansion of the heating mantle and the silicon nitride membrane. It took approximately 30 min for the sample drift to be sufficiently low for analysis to proceed. For lengthly analysis times, the cell was evacuated in order to quench any reductive process. Hydrogen was reintroduced prior to increasing the temperature. All these results are thus snapshots of the reduction processes occurring within each sample.

6.1.2 Hummingbird Gas Flow Cell

This work was performed in collaboration with Hummingbird Scientific. TEM micrographs were obtained using a JEOL JEM-2100 operated at 200 kV. The microscope is equipped with a Direct Electron DE-capture camera, which allows for high resolution, real-time imaging of samples. This allowed real-time video of dynamical changes within the systems to be captured.

Initially, both small and large chips were plasma cleaned for 5 minutes in air. The sample was placed in a small volume of ethanol and ultrasonicated to thoroughly disperse it. A small drop of this solution was placed on the silicon nitride membrane of the large chip.

The gas cell was assembled at the tip of the holder and the system placed in a vacuum chamber with the gas connections exposed to the atmosphere. This was to test for leaks in the gas flow cell. The gas flow holder was finally transferred to the microscope and the gas lines connected.

Isothermal experiments were performed by heating the samples to 400°C in high

purity hydrogen and air, and monitoring changes to particle size and morphology. Samples were heated at a very fast rate (100°C.s^{-1}) and there was very little sample drift upon heating.

It must also be mentioned that during analysis in air, a gas flow cell did burst. This was a result of concentrating the electron beam too much, resulting in a thinning out the silicon nitride membrane. The resulting rise in pressure within the microscope column was immediately detected by the control software, and the microscope switched itself off, suffering no damage.

6.2 Protochips Atmosphere^{TM} Gas Flow Cell

The reduction of two of the samples prepared in this study was investigated using the Protochips Amosphere^{TM} gas flow cell. The first sample investigated was **100/0 Fe/SiO$_2$**, the hematite control sample, while the second was **100/10 Fe/SiO$_2$**. Time-constraints prevented the study of the remaining silica-bearing samples.

6.2.1 100/0 Fe/SiO$_2$

The sample was initially imaged under vacuum at room temperature. This allowed distinct regions of interest (ROIs) to be identified on the sample. These ROIs, named ROI A, B and C, were constantly examined at different stages of reduction for changes in particle size, phase and morphology. HAADF-STEM micrographs for all three ROIs identified for **100/0 Fe/SiO$_2$** are shown in Figure 6.1. All 3 ROIs exhibit irregularly shaped hematite particles. The bright particles visible in the top left of ROI C are SiC from the heating mantle.

The hydrogen gas was introduced at a pressure of 800 mbar, and the temperature raised to 220°C. This temperature was chosen based on *in situ* XRPD data (Chapter 5.3), which suggests the reduction of hematite to magnetite begins at this temperature. The presure of hydrogen used in the *in situ* XRPD experiments (1 bar) is also comparable to the hydrogen pressures used during the TEM reduction. No change was observed in the ROIs, and the sample was subsequently

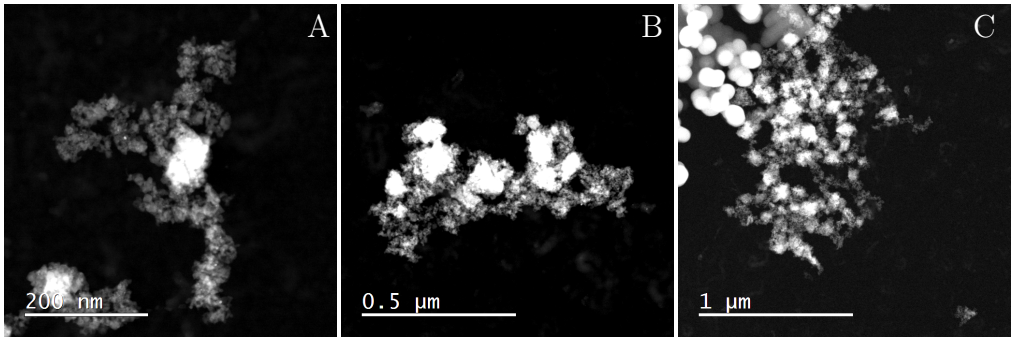

Figure 6.1: *HAADF-STEM micrographs of ROI A(left), B (middle) and C (right) for in situ reduction of* ***100/0 Fe/SiO$_2$*** *recorded at room temperature in vacuum.*

heated to 240°C to account for deviations in set temperature from actual temperature (which is quoted as being within 10% error). No change in the ROIs was observed. Further heating to 260°C, 280°C and 310°C continued to exhibit no change in the ROIs. SAED patterns recorded at 310°C contain reflections in concentric circles, at d-spacings of hematite, consistent with the notion that no reduction has occurred up till 310°C. A HAADF-STEM micrograph of ROI C, with its SAED pattern, is shown in Figure 6.2.

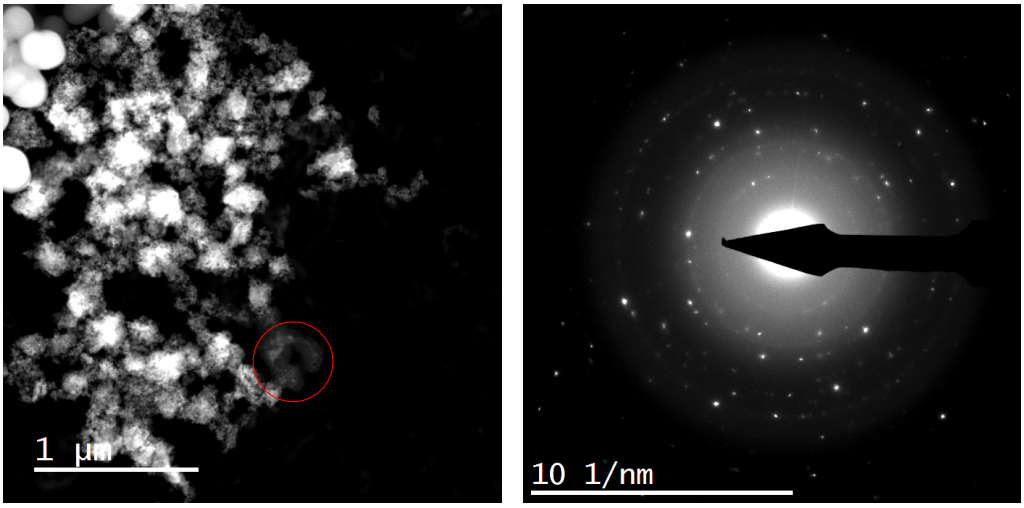

Figure 6.2: *HAADF-STEM micrographs of ROI C(left) and its corresponding SAED pattern (right). Red circle highlights an area of ROI C that suffered electron beam damage.*

The red circle in the HAADF-STEM micrograph shown in Figure 6.2 shows some morphology change. However, this is not a result of reduction. It is electron beam damage induced during the acquisition of STEM-EELS and STEM-EDS survey images. One such data set is shown in Figure 6.3. The compositional maps of iron and oxygen correspond with one another, which indicates that no metallic iron has been formed, nor regions with reduced oxygen content (reduced iron oxide).

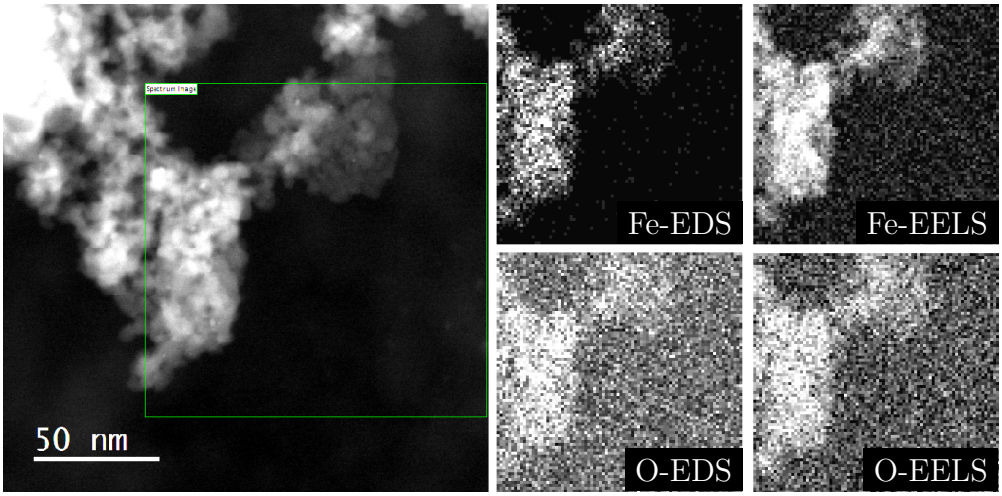

Figure 6.3: *HAADF-STEM micrographs of ROI C (left) and the region used to generate EDS- and EELS-compositional maps (green rectangle). The corresponding Fe- and O-EDS (middle) and EELS (right) compositional maps are shown on the right.*

While the compositional maps do not contribute additional information about the sample, this serves as an excellent example of the analytical capabilities that are possible with a gas flow cell. Even considering the approximately 100 nm thick silicon nitride layer, and the 1 atm of gas, that the electrons (or X-rays) must travel through, there is sufficient signal collected using both techniques to generate the appropriate compositional maps. An oxygen signal was also observed in the regions of the silicon nitride membrane that contained no sample. This is attributed to Si-O bonds likely present in the silicon nitride membrane[§].

The gas cell was further heated to 350°C. The hydrogen pressure at this point

[§]The presence of oxygen in the Si_3N_4 membrane is believed to be a result of oxygen bonding to free silicon sites on the membrane surface during synthesis. These exist because the membrane is nitrogen-deficient.

decreased from 800 mbar to 770 mbar. This was a result of reintroducing hydrogen into the cell after removing it to quench any potential reactions during prolonged periods of imaging. It is at this point that some small changes were observed: there was a slight increase in particle size as a result of the increase in temperature. The areas damaged by the electron beam have also reconstructed themselves, transforming from a poorly crystalline region to one of well-defined, crystalline particles - a result of the elevated temperature. This increase in particle size and reconstruction is shown in Figure 6.4. The sample still consists of hematite.

A HAADF-STEM micrograph on the left of Figure 6.4 shows the well-defined particles in the previously damaged region of ROI C. The SAED pattern (inset) contains reflections at d-spacings consistent with hematite. On the right is a high resolution BF-STEM micrograph of an individual particle in the same area showing lattice fringes. An FFT of this micrograph reveals these lattice spacings to be those of hematite. These subtle morphology changes are thus not a result of reduction, rather they are a product of the elevated temperature of the gas cell.

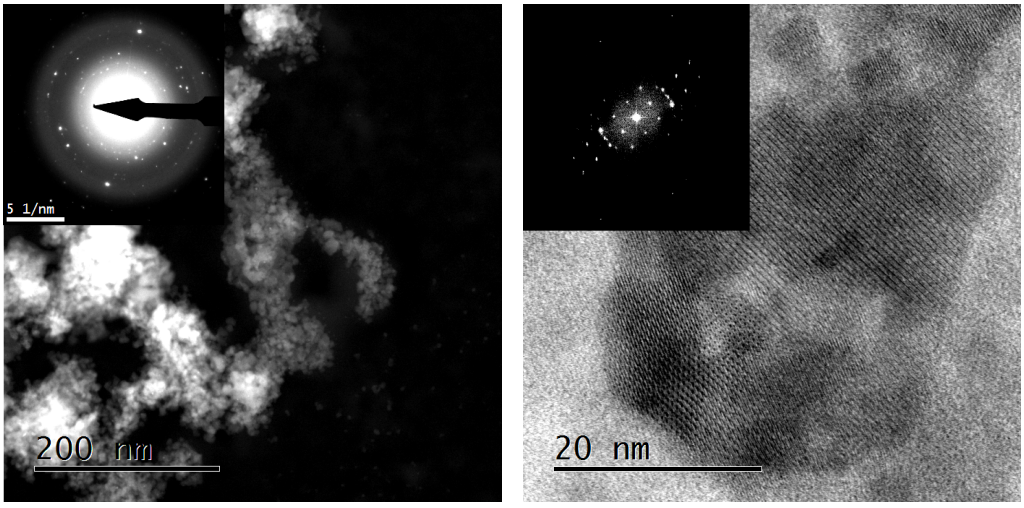

Figure 6.4: *HAADF-STEM micrograph showing reconstruction of previously electron-beam damaged region (left), with SAED pattern showing reflections of hematite (left inset). High-resolution BF-STEM (left) reveals lattice fringes of hematite. The FFT of the BF-STEM micrograph is also shown (left inset).*

Larger morphological changes are observed when the gas cell is heated to 400°C.

ROI A, B and C are shown in Figure 6.5 left, middle and right respectively. The micrographs exhibit more clearly defined particles, with more space visible between the individual particles. This is indicative of a reduction of the hematite particles to magnetite, since this involves a reduction in sample volume. An SAED pattern recorded in ROI C is shown in Figure 6.6.

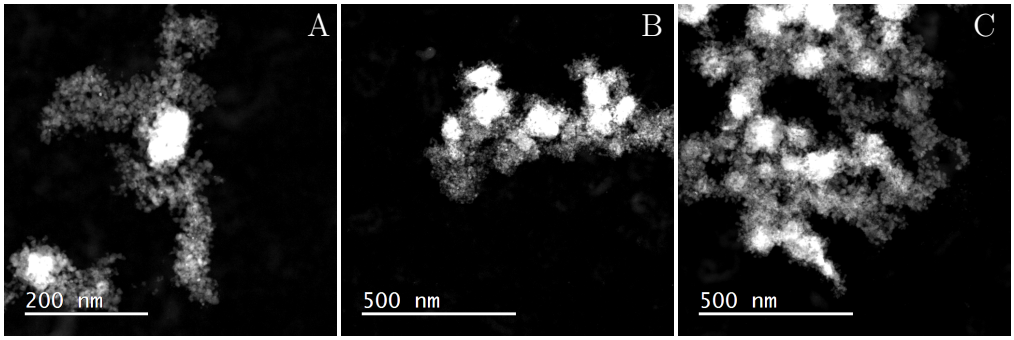

Figure 6.5: *HAADF-STEM micrographs of ROI A(left), B (middle) and C (right) for in situ reduction of* ***100/0 Fe/SiO$_2$*** *recorded at 400°C in 770 mbar hydrogen.*

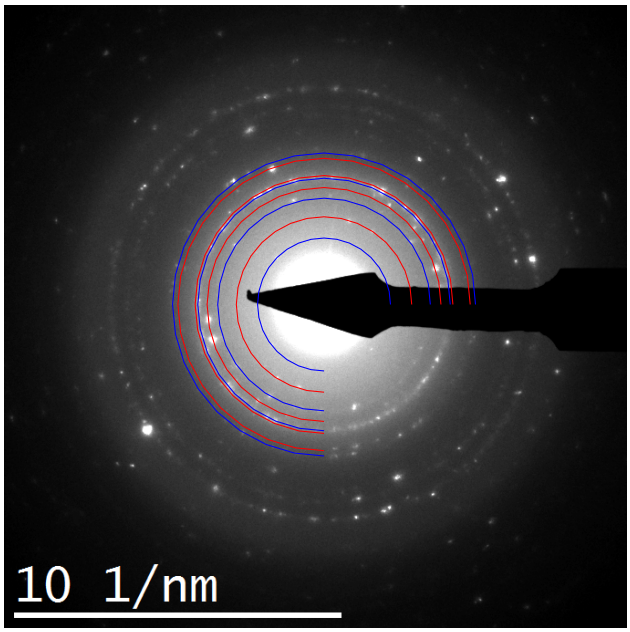

Figure 6.6: *SAED pattern of ROI C recorded at 400°C in 770 mbar hydrogen. Lower order reflections of hematite (red) and magnetite (blue) are indicated by the rings.*

In addition to the crystalline reflections corresponding to hematite (red rings indicate hematite (012), (104), (110) and (113) reflections), it also exhibits reflections of lower intensity. These reflections form diffraction rings located at d-spacings consistent with magnetite (blue rings indicate magnetite {111}, {220}, {311} and {400} reflections). This suggests the sample consists of hematite, with many small crystallites of magnetite forming at regions where reduction has begun.

The appearance of magnetite only at 400°C is 180°C higher than when it was first observed using *in situ* XRPD. Even performing at the extreme of the 10% error of the gas cell temperature (40°C at 400°C), this is a 140°C discrepancy. The most plausible explanation for this is that the hydrogen gas removes a large amount of heat from the system. The current versus temperature of the gas cell is calibrated *in vacuo*. Introducing hydrogen will conduct some of the heat away (but the current will remain constant), hence the temperature of the cell will drop to a lower than expected value. This is especially severe for hydrogen, which has the highest thermal conductivity of the gases. The dilute gas thermal conductivity of hydrogen is 230.4 $mW.m^{-1}.K^{-1}$ at 400°C and 186.9 $mW.m^{-1}.K^{-1}$ at 300°C[291]. The values for nitrogen, air, oxygen and argon at 300°C are 17.9 $mW.m^{-1}.K^{-1}$, 18.5 $mW.m^{-1}.K^{-1}$, 20.6 $mW.m^{-1}.K^{-1}$ and 22.7 $mW.m^{-1}.K^{-1}$ respectively[292].

The gas cell was further heated, this time by a larger increment of 100°C, to 500°C. Even more radical changes were observed, and these are illustrated in the HAADF-STEM micrographs shown in Figure 6.7. ROI A at 400°C and at 500°C are shown. There is a very noticeable increase in particle size when heating from 400°C to 500°C. The SAED pattern on the right of Figure 6.7 contains reflections at d-spacings of magnetite and iron, and does not contain any reflections of hematite. The {220}, {311}, {400}, {511} and {440} reflections of magnetite are indicated by blue rings, while the {110} and {200} reflections of iron are shown by the red rings.

A large number of small nanoparticles of 2 nm to 3 nm in size are also visible across the entirety of the ROIs. These nanoparticles are shown in Figure 6.8. An EELS compositional map over an individual particle shows no local concentration of oxygen, but a concentration of iron the same size as the particle, which identifies this particular particle as iron.

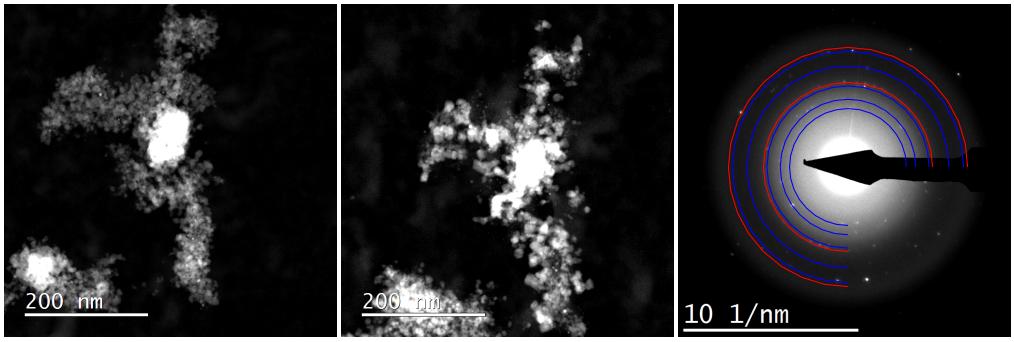

Figure 6.7: *HAADF-STEM micrographs of* ***100/0 Fe/SiO$_2$*** *ROI A in 770 mbar hydrogen at 400°C (left) and 500°C (middle). The SAED pattern at 500°C is shown on the right. Blue rings are the reflections from magnetite, red rings are reflection from iron.*

The presence of these small iron nanoparticles suggests that there is a migration of iron during the reduction process. It is likely that atomic layers of iron are liberated from the surface of the iron oxide particles during reduction and migrate across the surface of the silicon nitride window, agglomerating to form very small metallic iron nanoparticles.

Heating the gas cell further to 600°C results in a further increase in particle size, as well as an apparent decrease in sample volume, all indicative of further reduction. This is confirmed by SAED patterns in all three ROIs which demonstrate remarkably fewer reflections than previously. Only reflections at d-spacings that correspond to iron are visible in the diffraction patterns, an indication that the reduction of all the iron oxide material to metallic iron is fully completed. Figure 6.9 shows a high resolution BF-STEM micrograph of an individual particle in ROI B on the left, while the right is an SAED pattern of ROI C. Lattice fringes visible in the BF-STEM micrograph are spaced 2.02 Å apart (FFT inset), which correspond to iron {110} planes. The SAED pattern shows reflections located at d-spacings of metallic iron. The {110}, {200} and {211} reflections of iron are indicated.

The gas cell was then heated to 700°C. No additional phase changes were observed in the sample, however a slight increase in particle size was observed. Final HAADF-STEM micrographs of all three ROIs are shown in Figure 6.10. The HAADF-STEM micrographs, when compared with the same ROIs at lower temperatures, illustrate the morphological changes that have occurred on reduction.

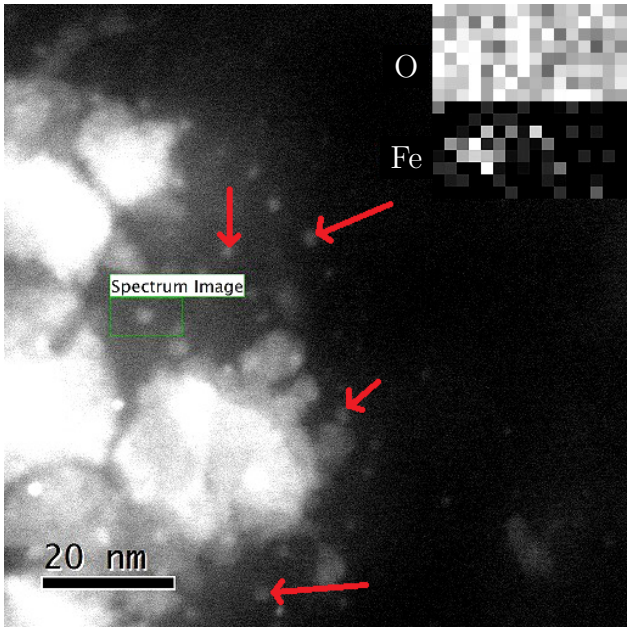

Figure 6.8: *HAADF-STEM images of* ***100/0 Fe/SiO$_2$*** *showing the small nanoparticles, some of which are indicated by red arrows. O-EELS (top) and Fe-EELS (bottom) compositional maps reveal that these naoparticles are iron.*

There is both an increase in the size of the iron particles compared to the hematite particles, as well as a decrease in sample volume as a result of the reduction.

The presence of such large iron particles would seem to contradict the hypothesis that the iron forms through agglomeration of iron atoms that migrate towards each other after being liberated from the surface of iron oxide particles during reduction. However, with the increase in temperature, the rate of this liberation process has increased to a sufficiently high value that each layer of iron is released rapidly after the previous one. As a result, there are much larger local concentrations of iron atoms located on the silicon nitride membrane, encouraging the formation of larger particles. Additionally, the iron nanoparticles already present act as seeding sites for the liberated atomic iron, themselves growing larger as a result.

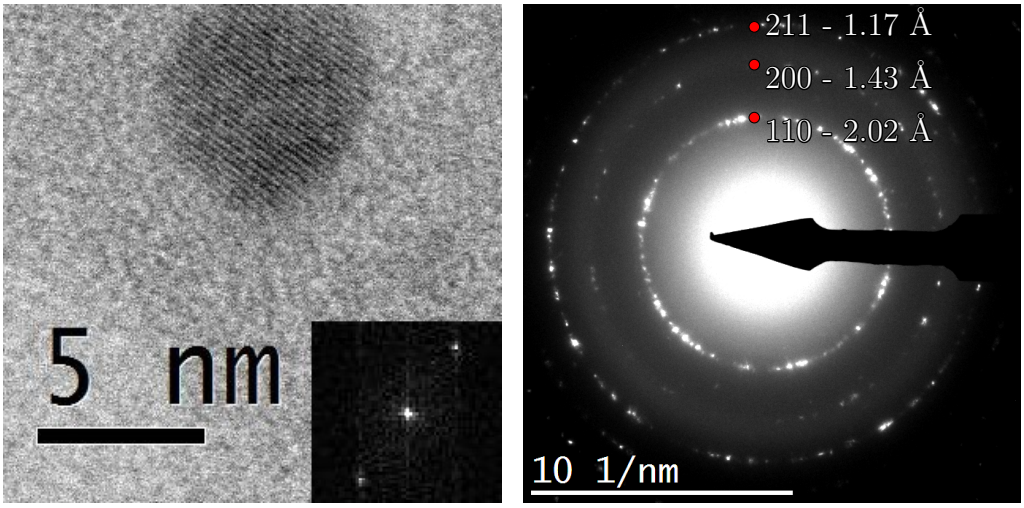

Figure 6.9: *BF-STEM micrograph of an individual particle in ROI B in 770 mbar hydrogen at 600°C (left). The SAED pattern contains reflections of metallic iron (right).*

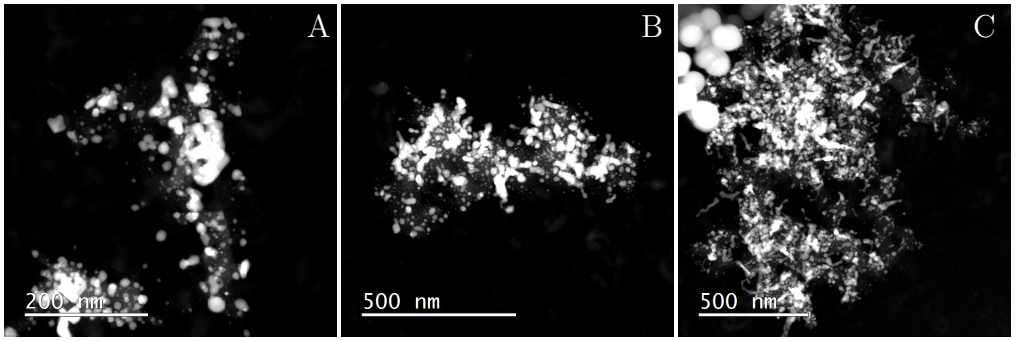

Figure 6.10: *HAADF-STEM micrographs of ROI A(left), B (middle) and C (right) for in situ reduction of* ***100/0 Fe/SiO$_2$*** *recorded at 700°C after reduction in hydrogen.*

6.2.2 100/10 Fe/SiO$_2$

100/10 Fe/SiO$_2$ was initially imaged under vacuum at a temperature of 200°C. As with **100/0 Fe/SiO$_2$**, this was done for the purpose of identifying several distinct ROIs that would be monitored for phase, size and morphology changes on a regular basis. The elevated temperature was preferred to room temperature

as it prevented beam-induced contamination forming on the sample. The three ROIs are shown in Figure 6.11. They are named A (left), B (middle) and C (right). There are no well-defined particles visible in the micrographs, a result of the approximately 3.5 nm ferrihydrite nanoparticles that are present in this sample. The small, bright particles (one visible in each STEM image) are gold nanoparticles. The entire silicon nitride membrane is sparsely populated with these gold nanoparticles, which originate from the electrical contacts.

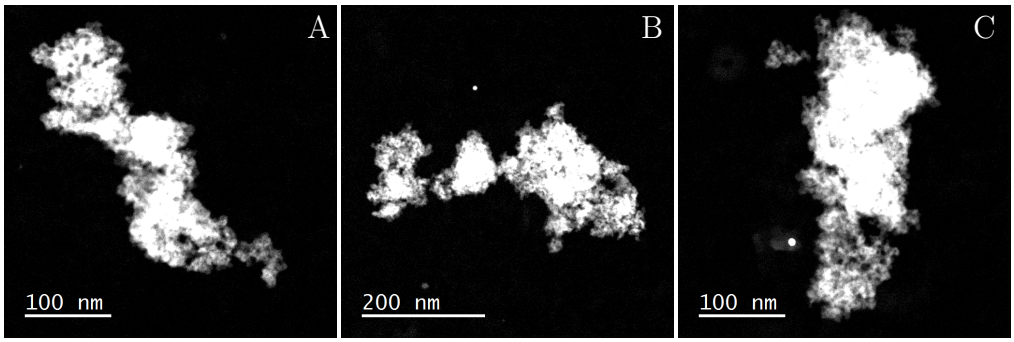

Figure 6.11: *HAADF-STEM micrographs of ROI A(left), B (middle) and C (right) for in situ reduction of* ***100/10 Fe/SiO_2*** *recorded at 200°C in vacuum.*

Hydrogen was introduced at a pressure of 740 mbar, while the temperature was maintained at 200°C. Since it is known that the initial reduction of these ferrihydrite particles involves an increase in crystallinity coupled with a reduction to magnetite, the SAED patterns of each ROI were monitered while heating. Based on *in situ* XRPD data, the appearance of crystalline magnetite is expected at approximately 260°C. The point at which this initial reduction begins to occur was determined by monitoring the appearance of crystalline reflection spots in the SAED pattern, in addition to the two broad rings of ferrihydrite. No changes in the diffraction patterns were observed at 200°C, and the gas cell was subsequently heated in 50°C increments to 250°C, 300°C, 350°C and 400°C.

None of these temperatures resulted in any changes in the SAED pattern. SAED patterns of ROI B recorded at 200°C, 250°C, 300°C, 350°C, 400°C and 450°C are shown in Figure 6.12.

All the SAED patterns between 200°C and 400°C reveal two broad rings corresponding to the poorly crystalline reflections of 2-line ferrihydrite, located at

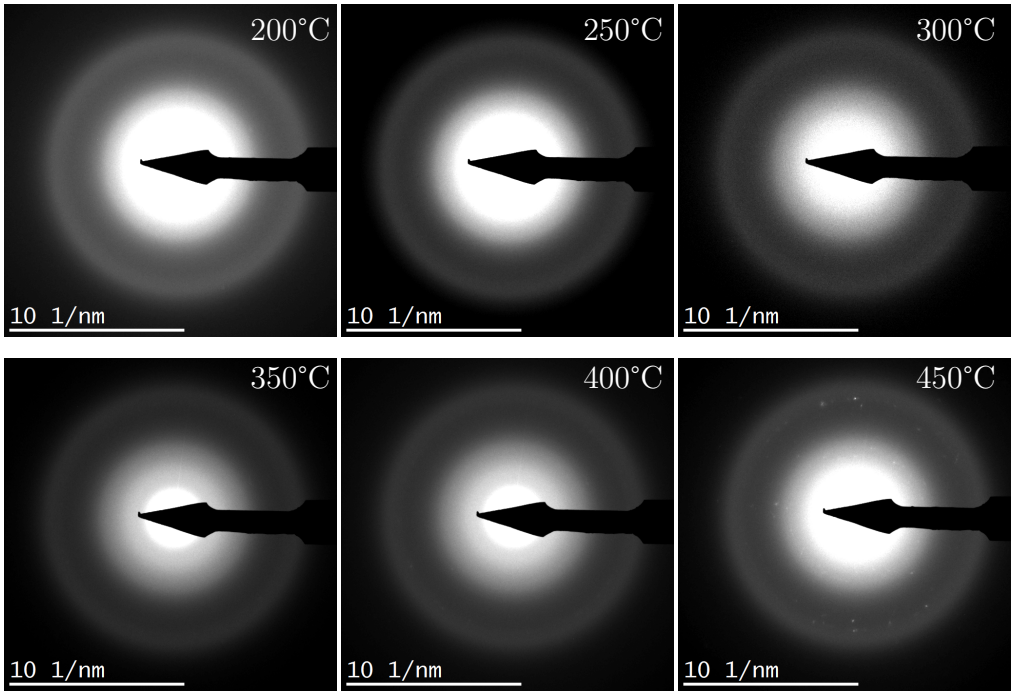

Figure 6.12: *SAED patterns of ROI B recorded in 740 mbar hydrogen at temperatures of 200°C to 450°C. Crystalline reflections of magnetite are visible at 450°C.*

d-spacings of 2.5 Å and 1.5Å. The SAED pattern at 450°C also reveals these two broad reflections, however it also contains individual reflection spots characteristic of crystalline domains. These are located at d-spacings which correspond to a magnetite phase and indicate the reduction from ferrihydrite to magnetite is proceeding. Once again, there is a temperature discrepancy of approximately 150°C between this data and the *in situ* XRPD data as a result of the hydrogen gas conducting heat away from the system.

Hollow cone dark-field (HCDF) micrographs were recorded in ROI B to determine which regions of the sample were reducing and which regions of the sample were still ferrihydrite-containing. Figure 6.13 shows a HCDF micrograph. The micrograph on the left is conventional BF TEM. Large particles are clearly observed, and these are likely the magnetite particles giving rise to the diffraction spots observed in the SAED pattern at 450°C. The electron beam was tilted at an angle of 0.871° from the optic axis and precessed about the optic axis. An objective aperture was inserted, and the corresponding HCDF micrograph recorded. This HCDF image is

shown on the right of Figure 6.13. The center image is the SAED pattern of ROI B. The circle in red corresponds to the relative position of the objective aperture in the diffraction plane (assuming the beam is not rotating). By rotating the beam at this fixed angle about the optic axis, the diffraction pattern rotates and the entire region inscribed by the two concentric yellow circles will pass through the red objective aperture circle at some point. The result is that electrons scattered at angles that correspond to distances between 5.76 nm^{-1} and 8.41 nm^{-1}, shown by the yellow circles, are used to form the HCDF micrograph. Any particles that give rise to reflections (in this case magnetite) thus appear bright. These bright particles are located across the entirety of ROI B.

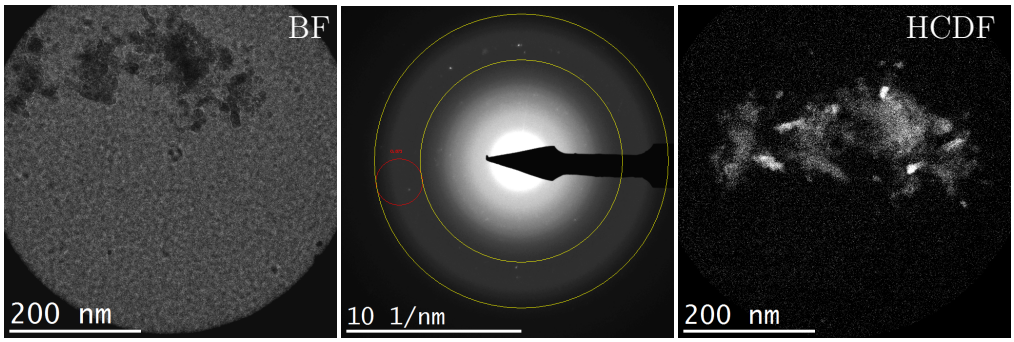

Figure 6.13: *BF TEM micrograph of ROI B in 740 mbar hydrogen at 450°C (left). The SAED pattern (middle) shows the reflections used to generate the HCDF micrograph (right). Bright regions correspond to magnetite particles.*

The result of this analysis shows that reduction is occurring in all areas of the sample, as evidenced by the spread of bright areas that are visible in the HCDF. These bright areas also correspond to the larger particles observed in the BF TEM micrographs, which lends support to the suggestion that the larger particles are indeed the magnetite. It seems reasonable to conclude that reduction of ferrihydrite to magnetite is closely associated with an initial agglomeration and sintering of ferrihydrite particles. The gas cell was heated from 450°C to 500°C and a further increase in particle size was observed. Once more, HCDF images suggested that these regions correspond to the formation of magnetite, however there are still regions present that contain ferrihydrite. This is evidenced by the two broad rings in the SAED patterns, as well as the characteristic small nanoparticles visible in TEM micrographs. Two HCDF micrographs of ROI C, generated using different d-spacing ranges in the diffraction pattern reveal bright particles (of magnetite)

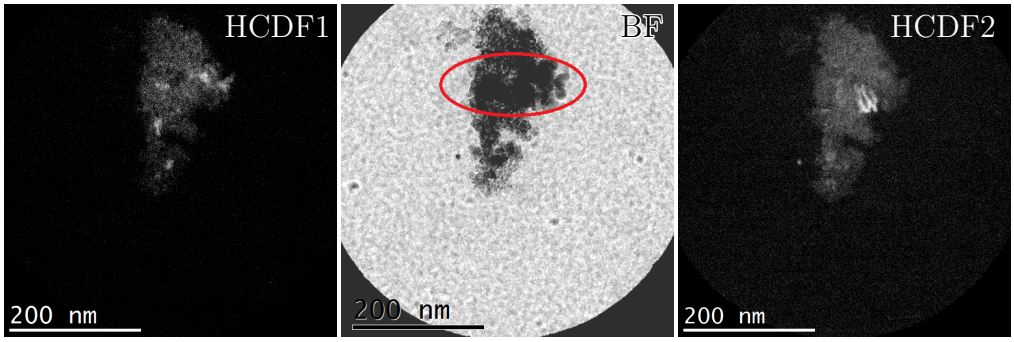

Figure 6.14: *BF TEM micrograph of ROI C in 740 mbar hydrogen at 500°C (middle). HCDF micrographs generated using different d-spacings (left and right) show that the large particles in the BF micrograph (red ellipse) cooresponds to magnetite.*

that correspond to the large particles visible in the center of the cluster in ROI C (see BF micrograph - red ellipse). These are shown in Figure 6.14.

HAADF STEM micrographs of each ROI recorded at 500°C are shown in Figure 6.15. Each ROI is a mixture of large, bright particles and the poorly crystalline ferrihydrite observed initially. It also appears that ROI B is in a more advanced stage of the reduction process, since it contains comparatively less ferrihydrite (and more larger magnetite particles) than ROI A and ROI B. This might be a result of a slightly higher temperature or hydrogen concentration in this ROI. However, it is also possible that the electron beam has assisted with the reduction process, since ROI B has been exposed to a higher electron dose than the ROI A and B.

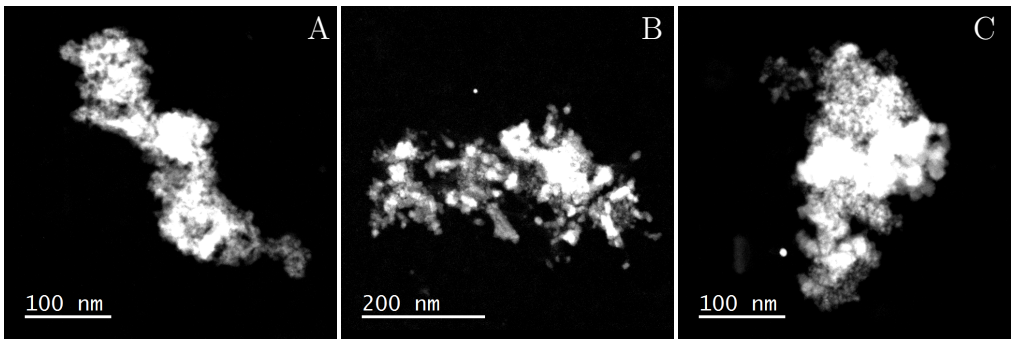

Figure 6.15: *HAADF-STEM micrographs of ROI A(left), B (middle) and C (right) for in situ reduction of* ***100/10 Fe/SiO$_2$*** *recorded at 500°C in 740 mbar hydrogen.*

STEM-EELS and STEM-EDS data were also collected for each ROI to determine the distribution of iron, oxygen and silicon. A HAADF-STEM micrograph of ROI C is shown in Figure 6.16 with the corresponding Fe-, O- and Si-EDS compositional maps.

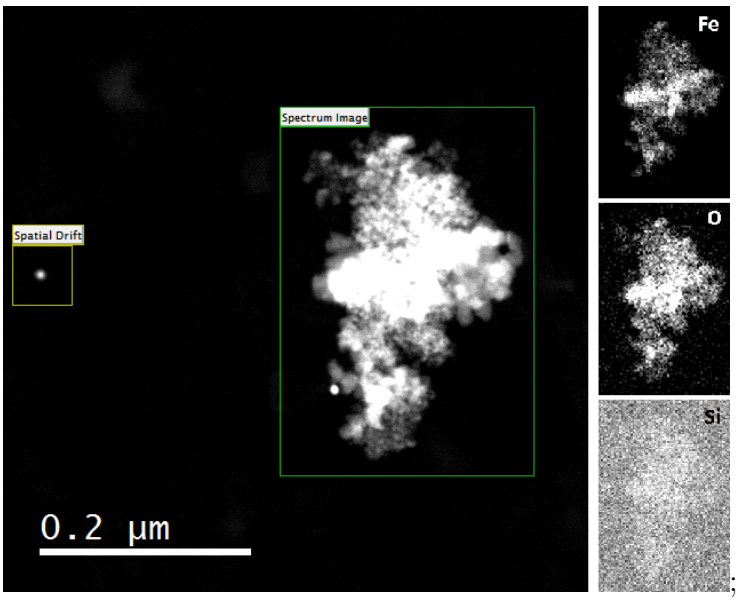

Figure 6.16: *HAADF-STEM micrographs of ROI C and corresponding Fe-, O- and Si-EDS compositional maps.*

The iron and oxygen are strongly associated to each other, suggesting no concentrations of silica or iron. Thus these particles present are all still silicon-containing iron oxides (magnetite and ferrihydrite). The silicon EDS compositional map provides very little information. This is a combination of the low amount of silicon present giving a weak signal, and the silicon nitride membrane contributing a large signal of silicon across the entirety of the scan region.

On heating to 550°C, the sample demonstrated a similar increase in crystallinity and decrease in the quantity of poorly-crystalline ferrihydrite regions. This change is illustrated in Figure 6.17 which shows ROI B at temperatures of 200°C, 500°C and 550°C. There is a very large change observable on heating by just 50°C, from 500°C to 550°C. The particles grow considerably in size and all the ferrihydrite areas appear to have been reduced.

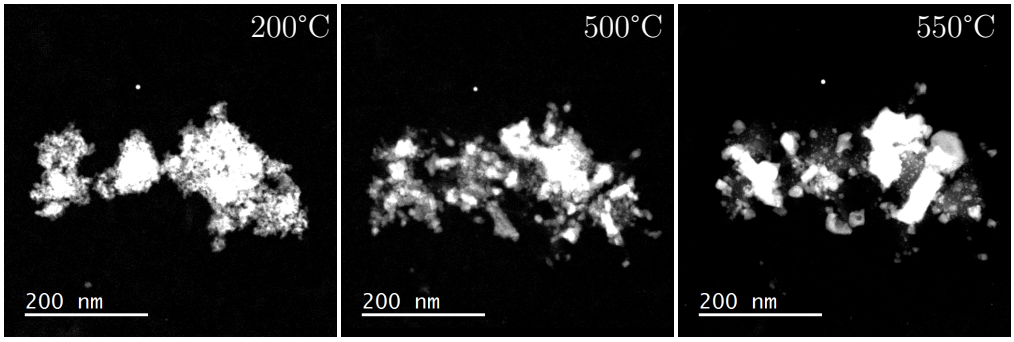

Figure 6.17: *HAADF-STEM micrographs of ROI B for in situ reduction of* ***100/10 Fe/SiO$_2$*** *recorded at 200°C (left), 500°C (middle) and 550°C (right) in 740 mbar hydrogen.*

Additionally, a large number of small nanoparticles (2 - 4 nm in diamter) are scattered in the iron oxide cluster of ROI B. These small nanoparticles were also observed in **100/0 Fe/SiO$_2$** and are formed from atomic iron species liberated from the surface of the iron oxides during the earlier stages of reduction. While these nanoparticles were observed at 500°C in **100/0 Fe/SiO$_2$**, it is not possible to conclude whether this temperature difference is an effect of the silica, since 500°C and 550°C are within the 10% temperature error of each other. A HAADF-STEM micrograph with the corresponding Fe- and O-EELS compositional maps across one of the larger of such nanoparticles is shown in Figure 6.18. The oxygen intensity is uniform over the scanned region (from the silicon nitride membrane) while the iron is located at a position corresponding to the particle, revealing that this particle consists of iron.

Curiously, only ROI B contains these small nanoparticles of iron; these small nanoparticles are not visible in ROI A and C. A HAADF-STEM micrograph of ROI C at 550° is shown on the left in Figure 6.19. This region (and ROI A) is still a mixture of ferrihydrite (the poorly defined regions which corresponds to the two broad rings visible in the SAED pattern in Figure 6.19 left inset) and magnetite particles (larger particles which give rise to the few reflection spots visible in the SAED pattern).

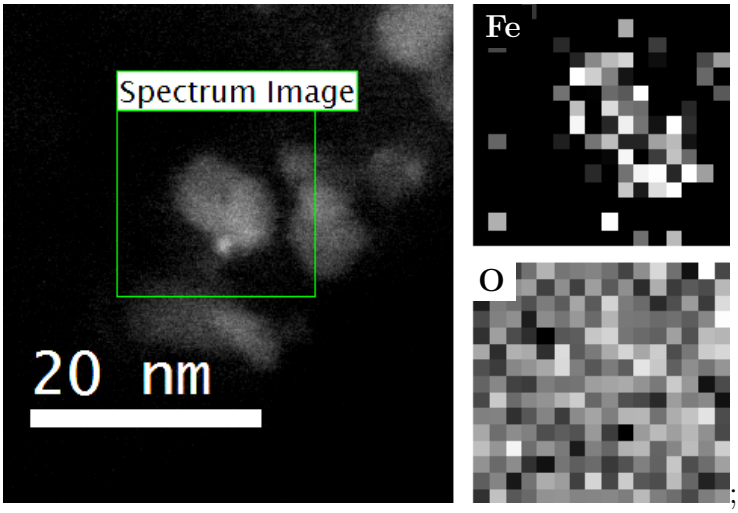

Figure 6.18: *HAADF-STEM micrographs of several small nanoparticles in ROI B. Fe- and O-EELS compositional maps of the scanned region (green rectangle) reveal these nanoparticles to be iron.*

A BF-STEM micrograph of an individual, larger particle in ROI C is shown on the right in Figure 6.19. This particle reveals lattice fringes that correspond to magnetite {111} planes. In addition, there is a hollow region in the center of the sample, which is characteristic of iron oxyhydroxides that undergo dehydration, as is the case with the reduction of ferrihydrite to magnetite. Similar hollow regions have been observed in geothite systems during their transformation to hematite [293].

The gas cell was heated a further 50°C to 600°C. ROI A, B and C are shown in Figure 6.20. ROI A and C have both increased in crystallinity and contain a large number of well-defined particles (all magnetite as evidenced by SAED patterns). However, they still contain regions of poorly crystalline ferrihydrite. ROI B exhibits fewer small iron nanoparticles, and those observed are larger, having grown at the expense of the smaller ones through sintering processes. ROI A and C do not demonstrate any small iron nanoparticles.

The gas cell was heated to a final temperature of 750°C. This large jump from 600°C to 750°C was necessary, since the remaining experimental time was fast approaching zero. It was decided that reduction and characterisation of the iron end-product was preferable to an incomplete reduction.

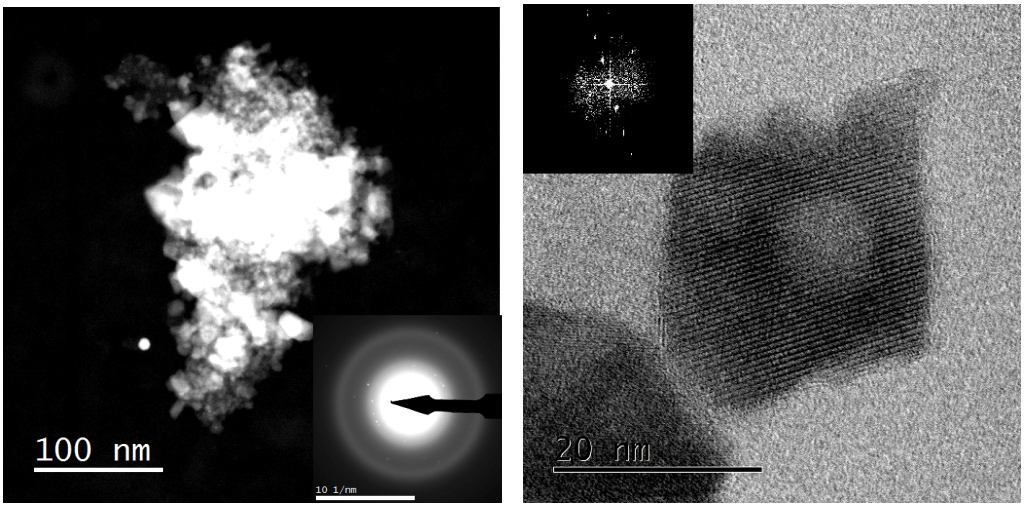

Figure 6.19: *HAADF-STEM micrograph of ROI C at 550°C in 740 mbar hydrogen (left). A BF-STEM micrograph of an individual particle in ROI C (right) with lattice fringes corresponding to magnetite {111} lattice planes.*

ROI A, B and C after reduction in hydrogen at 750°C are shown in Figure 6.21. All regions consist of large, well defined particles of iron, while ROI A and C also contain magnetite, as well as some areas that are almost ferrihydrite-like. The presence of ferrihydrite-like material still present at such an elevated temperature is consistent with TPR data which suggested there was incomplete reduction of the iron in the silica-containing samples.

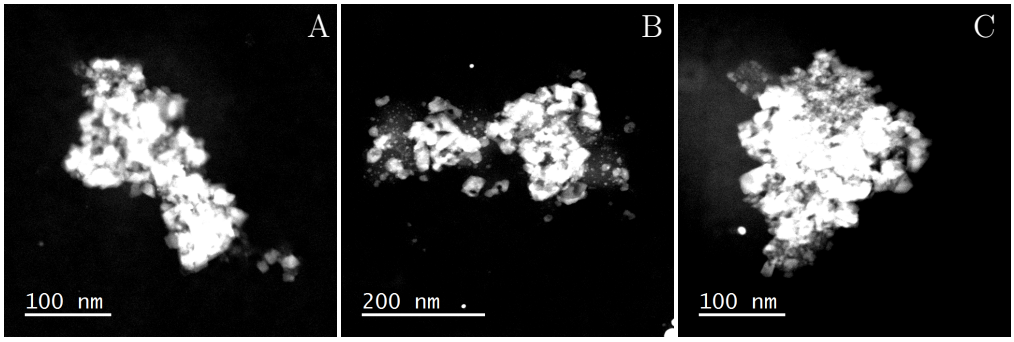

Figure 6.20: *HAADF-STEM micrographs of ROI A (left), ROI B (middle) and ROI C (right) for in situ reduction of* ***100/10 Fe/SiO_2*** *recorded at 600°C (right) in 740 mbar hydrogen.*

However, this weakens the hypothesis that the "hastened" reduction observed in ROI B is a result of electron beam damage. Rather, it seems more likely that ROI B simply contains a lower local concentration of silicon within the initial ferrihydrite material, thus allowing complete reduction, while the increased silicon concentration in ROI A and ROI C prevent a complete reduction of the ferrihydrite particles.

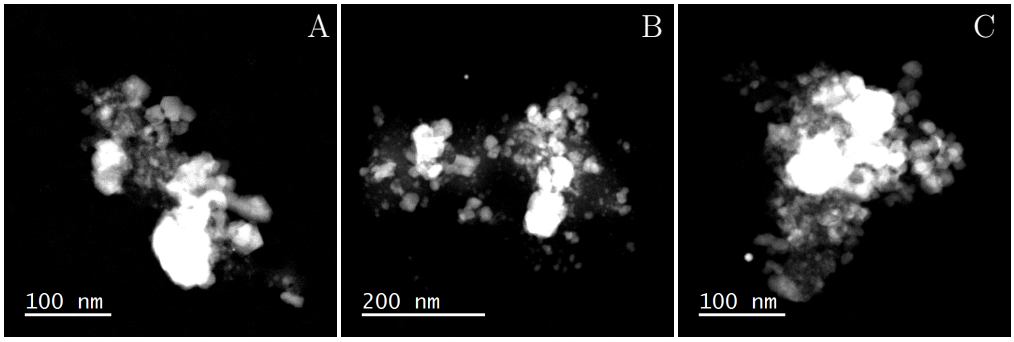

Figure 6.21: *HAADF-STEM micrographs of ROI A (left), ROI B (middle) and ROI C (right) for in situ reduction of* ***100/10 Fe/SiO$_2$*** *recorded at 600°C (right) in 740 mbar hydrogen.*

The SAED patterns of ROI A at 750°C is shown in Figure 6.22. It reveals a large number of reflections at a wide variety of d-spacings. Some of these are shown as concentric rings in Figure 6.22. This SAED pattern demonstrates a complex mixture of phases.

Initially, reflections at the d-spacings of magnetite, wüstite and iron were easily identified. However, a large number of reflections remained unindexed, suggesting the presence of at least 1 additional phase. These unindexed reflections are located at d-spacings consistent with the more intense reflections of the iron silicate phase fayalite. Thus the reflections in the SAED pattern located at d-spacings indicated by the red rings correspond to those of fayalite. The reflections at d-spacings indicated by the yellow, green and blue rings correspond to reflections of magnetite, wüstite and iron respectively. These reflections are summarised in Table 6.1.

The mixture of magnetite, wüstite and iron is expected when considering the *in situ* XRPD and TPR data. However, the observation of fayalite reflections provides more direct evidence that this phase does indeed form at a certain point of the

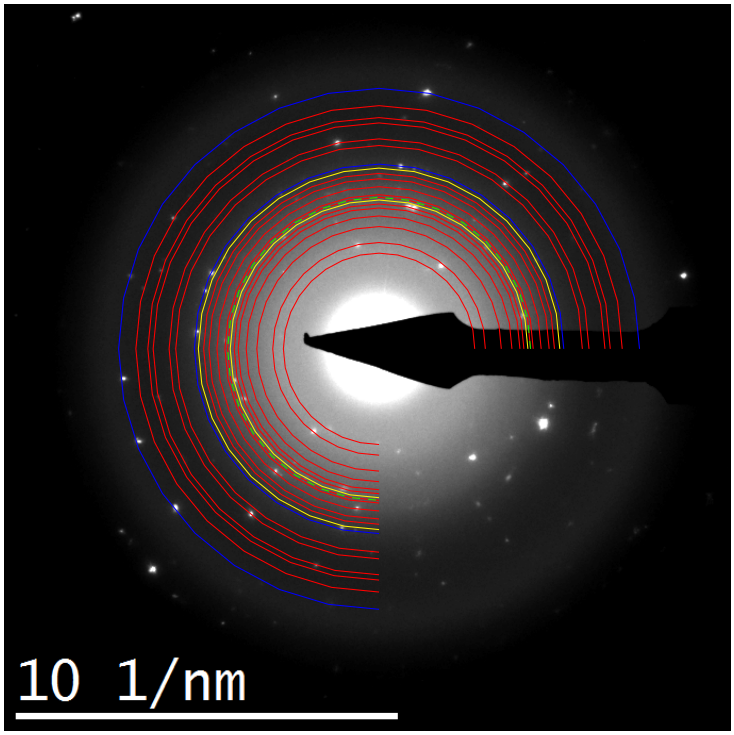

Figure 6.22: *SAED diffraction pattern of ROI A at 750°C. Red rings correspond to reflections at d-spacings of fayalite, green rings to reflections at d-spacings of wüstite, yellow rings to reflections of magnetite and blue rings to reflections at d-spacings of iron.*

reduction of silica-promoted iron oxides to metallic iron.

These SAED patterns were recorded at 750°C. Assuming a 10% error in temperature reading, and hydrogen gas withdrawing approximately 150°C worth of heat from the system (based on the temperature discrepancy between the *in situ* TEM and XRPD data), this suggests the actual temperature of the cell was between 525°C and 825°C. Even at the coolest extreme of this range, it is still 145°C hotter than the highest temperature reached during *in situ* XRPD experiment. This increased temperature provides the additional energy needed for the amorphous or poorly crystalline iron oxide regions (observed from the *ex situ* TEM analysis) to crystallise into fayalite domains.

The presence of this fayalite phase (and even magnetite and wüstite) at such an elevated temperature supports the TPR data which suggested that the reduction

steps were very broad and prevented quantitative analysis of the hydrogen consumption. The presence of fayalite also explains the incomplete reduction of initial iron oxide to iron, even at temperatures of 1000°C.

Table 6.1: *D-spacings of measured and expected reflections in the SAED pattern of ROI A at 750°C. Fa = fayalite, M = magnetite, W = wustite, Fe = iron.*

$\mathbf{d_{measured}}$ [nm]	$\mathbf{d_{theory}}$ [nm]	Reflection
0.397	0.397	Fa (021)
0.356	0.355	Fa (111)
0.307	0.306	Fa (121)
0.284	0.283	Fa (130)
0.264	0.263	Fa (022)
0.259	0.256	Fa (131)
0.251	0.253	M {311}
0.248	0.250, 0.248	Fa (112), W {111}
0.243	0.241, 0.240	Fa (200), Fa (041)
0.231	0.231, 0.230	Fa (122), Fa (140)
0.219	0.219	Fa (211)
0.215	0.215	W {200}
0.209	0.209	M {400}
0.203	0.203	Fe {110}
0.183	0.184, 0.183	Fa (113), Fa (151)
0.178	0.178, 0.177	Fa (222), Fa (240)
0.165	0.165	Fa (133)
0.161	0.162	Fa (152)
0.152	0.152, 0.152, 0.151	W {220}, Fa (004), Fa (062)
0.143	0.143	Fe {200}

6.2.3 Comments

Since the temperature dependence of the reduction process is readily available through bulk techniques such as XRPD and temperature-programmed reduction (TPR), it is not essential that the temperature of the gas flow cell agree with these techniques. The principle purpose of *in situ* TEM in these experiments is to understand what is happening to individual particles and their surfaces during reduction. This data can always be correlated with bulk techniques when considering the process as a whole.

However, it is a factor to be considered when performing similar experiments, especially should the experiments involve temperatures close to the limit of the system (the upper limit for Atmosphere is quoted at 1000°C). By way of example, consider the hypothetical scenario that an experiment was looking to study a particular process at 900°C in hydrogen, it might not be possible to actually reach this temperature, even though the system is rated for it.

6.3 Hummingbird Gas Flow Cell

As mentioned in the experimental section (Chapter 6.1.2), the JEOL 2100 was not equipped with EDS, EELS or STEM capabilities. As such, the work was limited to TEM imaging and electron diffraction. However, electron diffraction was limited to the fluorescent screen of the microscope. The electron capture camera could not record SAED patterns. However, owing to the low drift of the gas cell on heating and the high speed electron capture camera, it was possible to record morphological changes occurring within the samples in real time.

A large majority of the data was obtained in the form of video recordings. As a result, most micrographs presented in this chapter section are image frames extracted from these video recordings. Each micrograph is labeled with the name of the video (in mp4 format) that it was extracted from and a timestamp corresponding to the time in that video will also be given. The videos are available at 640x480 resolutions. These videos are attached in Appendix B on the attached DVD. While an attempt is made in this section to discuss the results from each video with ref-

erence to the extracted image frames, the results are best read alongside a viewing of the relevant video recording.

6.3.1 100/0 Fe/SiO$_2$

Two separate experiments were performed for **100/0 Fe/SiO$_2$**. The first experiment involved heating the gas cell to 400°C in 1 atm of air (this was done by simply leaving the gas lines open, exposed to the air in the room) and observing the changes in the particles over time. All the data is contained in one video named "Hematite Heating.mp4".

The first series of micrographs, taken from "Hematite Heating.mp4" and shown in Figure 6.23, focuses on a particular particle of hematite. Over time, the particle grows in size, likely at the expense of smaller particles in the vicinity. The contrast in the images is constantly changing, as a result of the dynamic movement of atoms occurring within the individual particles. While not evident in the images, lattice fringes and thickness contrast fringes are also visible, and constantly appear and disappear as the particles rotate close to and move away from zone axes.

At 2:26, the camera is moved slightly and focuses on a smaller particle that is visible in the top left of Figure 6.23 (image recorded at 1:30). Some images taken from this point in the video are shown in Figure 6.24. What is of particular interest is how the surface facets of the particle are well-defined, but continually changing over time. Note how the lengths of the various facets are constantly changing as the particle in question grows/shrinks or just changes shape slightly, a result of energetically favoured surfaces forming as the sample remains at this elevated temperature. This process is conventional crystal growth of the hematite particles present in **100/0 Fe/SiO$_2$**.

From about 4:10 in "Hematite Heating.mp4", it may seem like the particles are changing shape fairly rapidly. However, this is actually a result of the membrane window moving in such a way as to cause the particles to rotate. This movement of the window is a result of it being particularly thin in this area, since the electron beam was focused down to too small a spot, which etched away some silicon nitride material. This is likely the membrane being pushed by the gas within the cell,

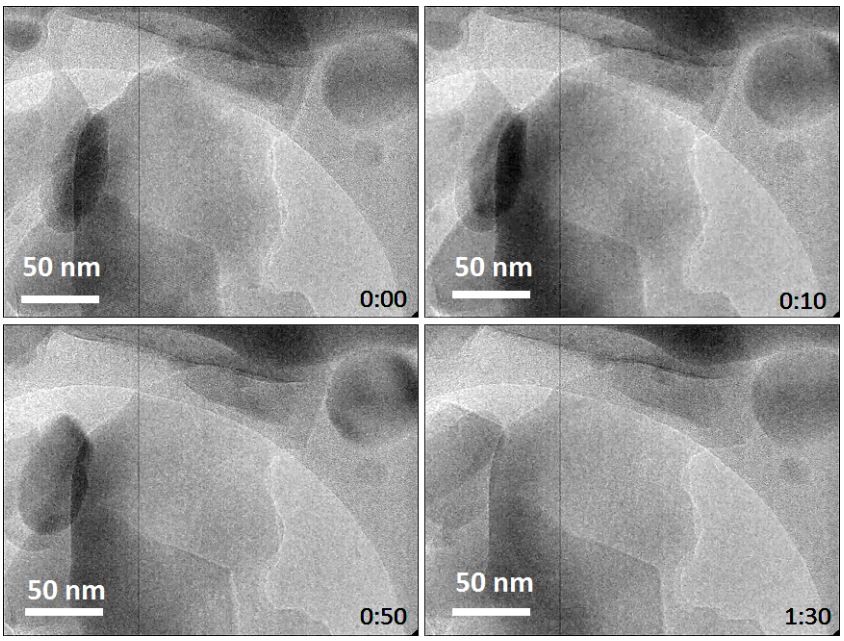

Figure 6.23: *TEM micrographs taken from "Hematite Heating.mp4". As the particles remain at 400°C in air, they increase in size, and the edges of the particles are constantly changing.*

since there comes a point where the cell membrane ruptures, and the microscope switches control software automatically switches the microscope off. This occurred just after the video recording ended. This process is probably best compared with piercing a thin material with a pin. The material in the vicinity of the pin is pushed outwards, and any objects sitting on the material would appear to rotate when looking along the same direction as the pin's axis.

The TEM micrograph shown below (Figure 6.25) is one of the few still-frame micrographs recorded. As such, it was subject to a longer exposure, and considerably more detail is visible in the particles. It was recorded at 400°C in air. Lattice fringes are visible which correspond to the d-spacings of hematite (FFT shown as an inset). This serves as an excellent example of the resolution achievable in such a gas flow cell, even with a LaB_6 electrons source.

The second experiment performed on **100/0 Fe/SiO$_2$** was an isothermal reduction and involved leaving the sample at 400°C in 1.2 atm of hydrogen gas and observing changes to the morphology. The gas cell holder reached the desired temperature

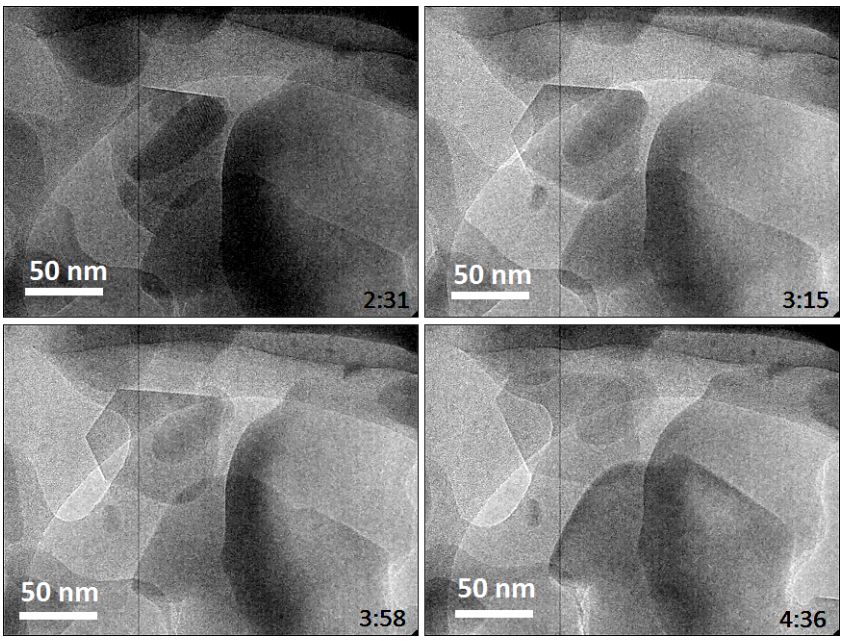

Figure 6.24: *TEM micrographs taken from "Hematite Heating.mp4". Of note is how the surface facets of the particle in the top left quadrant of the micrographs are dynamically changing.*

in a few seconds, heated at a rate of 100°C.s^{-1}. Video recordings of the sample at these conditions total approximately 31.5 min, while the actual period of time that the sample was exposed to these conditions was slightly longer. The images appear fairly dark since the electron beam was spread as much as possible to minimize the total electron dose received by the sample, while still providing sufficient intensity to enable imaging of the particles.

The first series of micrographs are extracted from "SA_hem_h2_2.mp4". They are shown in Figure 6.26. Three distinct clusters of particle are visible in the micrographs. Over the course of the 9 minute video, there is very little change in the particles. The particles do not grow larger, nor is there evidence to suggest reduction has begun to take place. The inability to record diffraction patterns at various times is a severe disadvantage, since this would provide a quick method of determining when reduction was occurring (since the reduction of hematite to magnetite will result in a change in position of reflections in the SAED patterns). "SA_hem_h2_3.mp4" shows the same information as "SA_hem_h2_2.mp4" *viz.* very little to no change in the three particles clusters. As such, micrographs from this

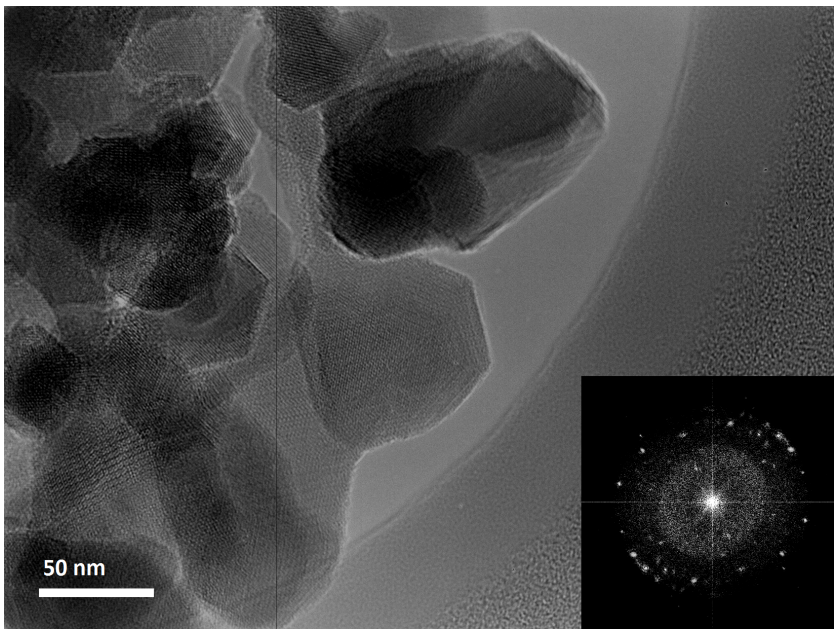

Figure 6.25: *HRTEM micrograph of* ***100/0 Fe/SiO$_2$*** *in 1 atm air. Facets of particles are very well defined and lattice fringes of hematite are clearly visible.*

region are not presented.

Micrographs extracted from "SA_hem_h2_4.mp4" are shown in Figure 6.27. Unlike the previous recordings, changes begin to occur within the sample. This is evidenced by movement of particles and a darkening towards the center of the top cluster. It is believed that this marks the start of the reduction of hematite to magnetite.

The final video recording of the sample in 1.2 atm hydrogen at 400°C is named "SA_hem_h2_5.mp4" and micrographs from this video are shown in Figure 6.28. The most noticeable changes in the particle morphology are observed during this recording. Initially, there is no obvious change, but from 1:20, a needle-like particle can be observed to be growing from the top cluster in the image (highlighted by the red circle). It continues to grow over time and reaches its maximum length after 2:30. Thereafter, there is a sharp increase in crystallinity in all three clusters, marked by an increase in particle size and definition. Comparison with Figure 6.26 and Figure 6.27 shows this contrast quite clearly. SAED patterns (not recorded) viewed on the fluorescent screen suggest that this is the beginning of iron formation,

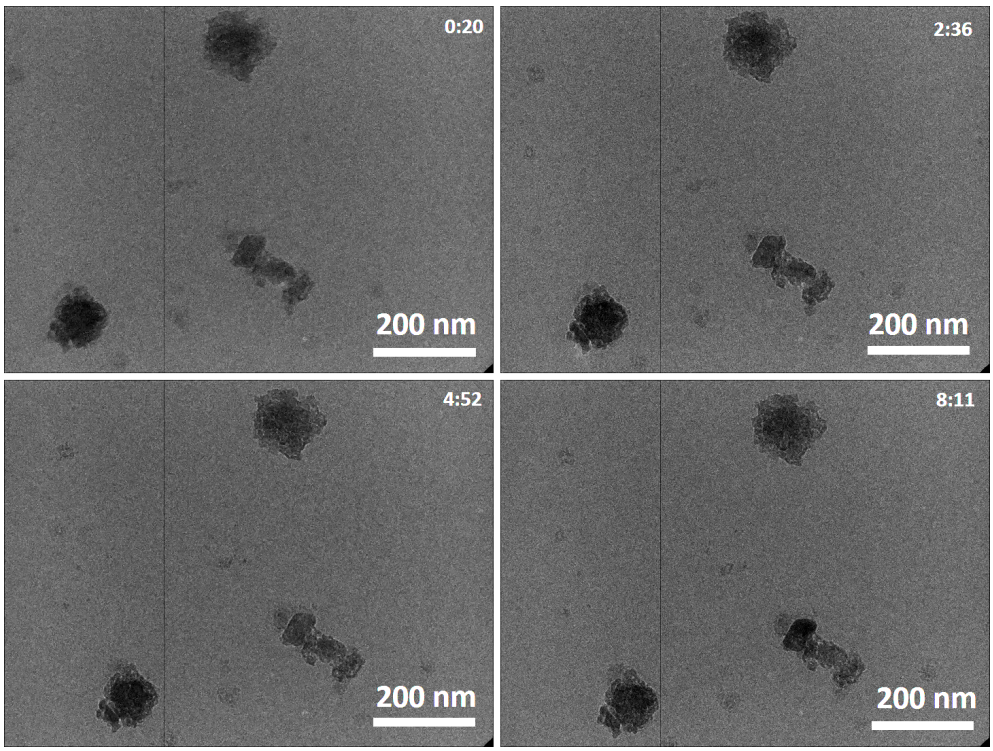

Figure 6.26: *Series of micrographs extracted from "SA_hem_h2_2.mp4". The sample was exposed to 1.2 atm hydrogen at 400°C. The most noticeable change in particle morphology occurs over the 6 min duration of this video. There is very little change in the video after the 9 min recording period.*

however large amounts of magnetite are still present.

The reduction did not continue beyond this point, since the alloted experimental time was fast coming to an end. If this experiment were continued, it is believed that the complete reduction to metallic iron particles would have been observed and recorded.

6.3.2 100/10 Fe/SiO$_2$

Only one experiment was performed **100/10 Fe/SiO$_2$**. The experiment was also an isothermal reduction, and involved holding the gas cell temperature at 400°C in the presence of 1.2 atm of hydrogen, similar to the isothermal reduction experiment performed for **100/0 Fe/SiO$_2$**. A 20 minute video of the sample was recorded

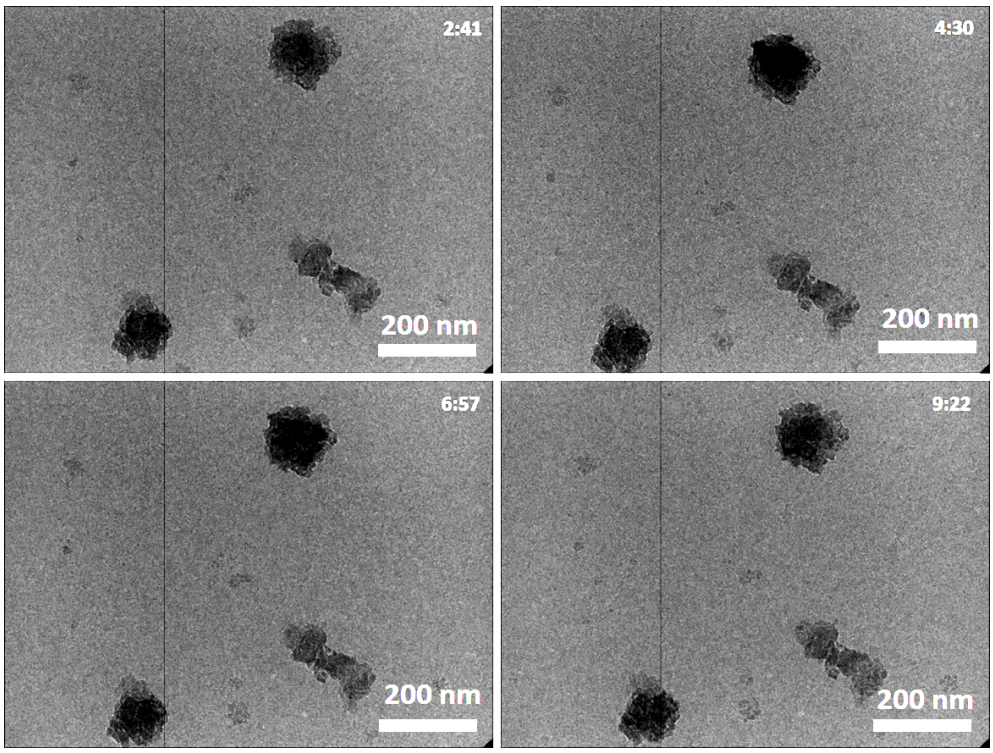

Figure 6.27: *Series of micrographs extracted from "SA_hem_h2_4.mp4". The sample was exposed to 1.2 atm hydrogen at 400°C. There is some change in particle morphology over the 10 min period of the video. The start of this video begins approximately 16 minutes after the sample was first exposed to hydrogen.*

and named "SA_ferrihydrite_H2_Heating_4.mp4". At certain points the video goes dark. There are periods when the fluorescent screen of the microscope was lowered so that an SAED pattern could be viewed. This was done to determine when reduction from ferrihydrite began to occur, since this change is most easily seen in the SAED pattern as the appearance of diffraction spots, rather than the two broad rings associated with 2-line ferrihydrite.

Figure 6.29 contains images extracted from the first 9 minutes of the video labelled "SA_ferrihydrite_H2_Heating_4.mp4". Initially, the sample consists of very small, poorly crystalline nanoparticles that are characteristic of the initial 2-line ferrihydrite phase. Over time, the particles begin to agglomerate and increase in size and crystallinity. The image taken at 9:04 just begins to illustrate the initial formation of magnetite particles.

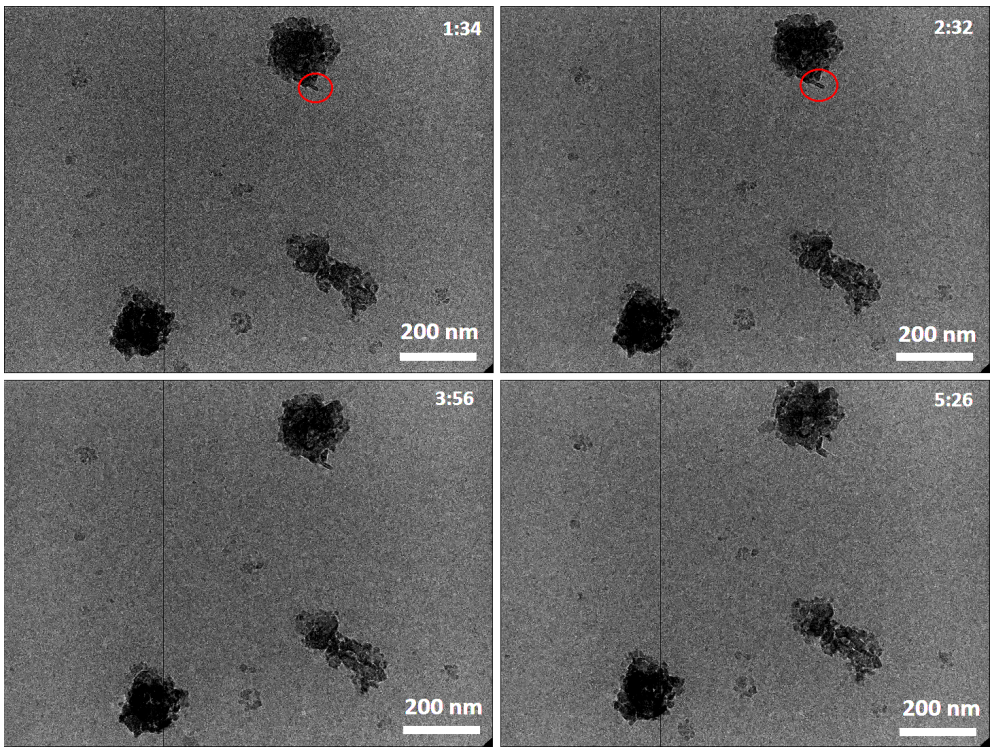

Figure 6.28: *Series of micrographs extracted from "SA_hem_h2_5.mp4". The sample was exposed to 1.2 atm hydrogen at 400°C. The most noticeable changes in particle morphology occurs over the 6 min duration of this video. The start of this video begins approximately 26 minutes after the sample is first exposed to hydrogen. There is a sharp increase in crystallinity in all three clusters, marked by an increase in particle size and definition.*

While it took just over 9 minutes for ferrihydrite to begin reducing to magnetite, the full transformation is comparatively much quicker. Figure 6.30 contains further micrographs extracted from "SA_ferrihydrite_H2_Heating_4.mp4" and shows how the agglomeration of ferrihydrite particles is quickly associated with the formation of larger particles. These larger particles of magnetite grow at the expense of remaining ferrihydrite particles.

Upon complete reduction of ferrihydrite to magnetite, the magnetite particles continue to grow, so much so that the area of the sample in view increases. At first thought, this seems counterintuitive, since reduction of an iron oxide to iron involves a decrease in volume as the oxygen is expelled from the lattice as water. However, TEM micrographs are 2D projections of 3D objects. Thus, since the

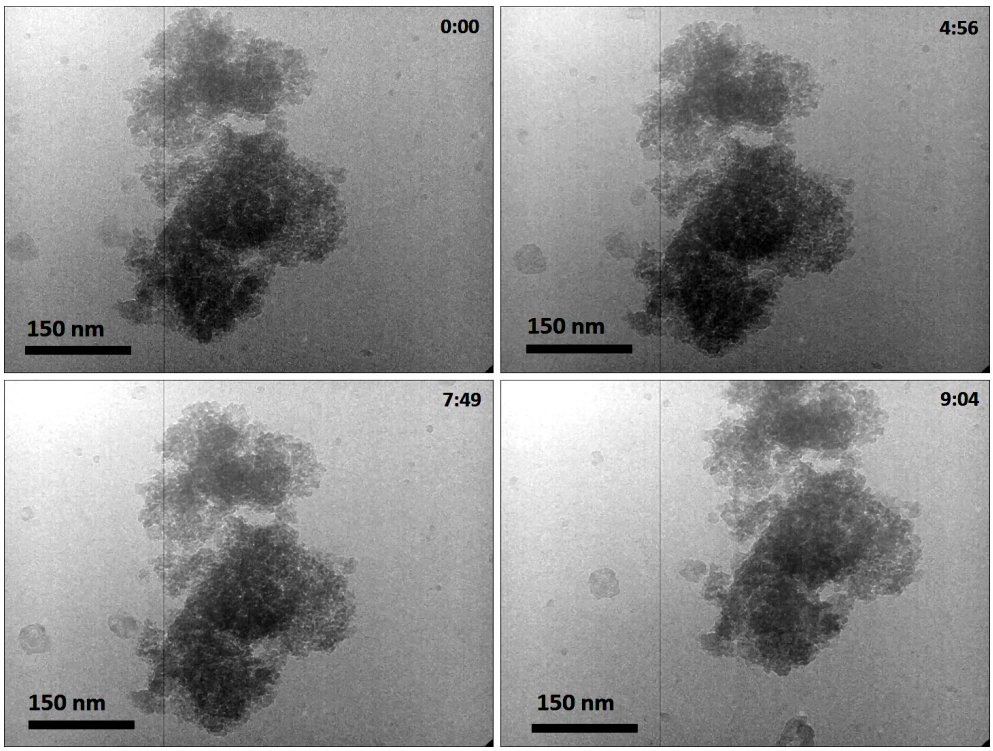

Figure 6.29: *Series of micrographs extracted from "SA_ferrihydrite_H2_Heating-_4.mp4". The sample was exposed to 1.2 atm hydrogen at 400°C. The initial size and shape of the particles is characteristic of ferrihydrite nanoparticles. Over the duration of the recording, the particles agglomerate and increase in size.*

area is growing in size in the TEM image and it must be decreasing in volume as a result of reduction, it follows that the height (or thickness) of the sample is decreasing, resulting in the formation of flattened crystals. In the frame taken at 10:29, some considerably thinner regions are visible as the particles continue to flatten.

This region continues to grow and flatten over time, as evidenced by the images in Figure 6.31. More distinct particles begin appearing in the cluster and the edges of the particles become sharper and more defined over time. Closer observation shows that new particles are forming at various points on the cluster. Additionally, there are areas appearing within the cluster where the silicon nitride membrane is visible. This suggests that the reduction process is occurring across the entirety of the cluster, and not initiating at any particular point. The appearance of these particles appears random and occurs very quickly. The frame taken at 12:47 begins

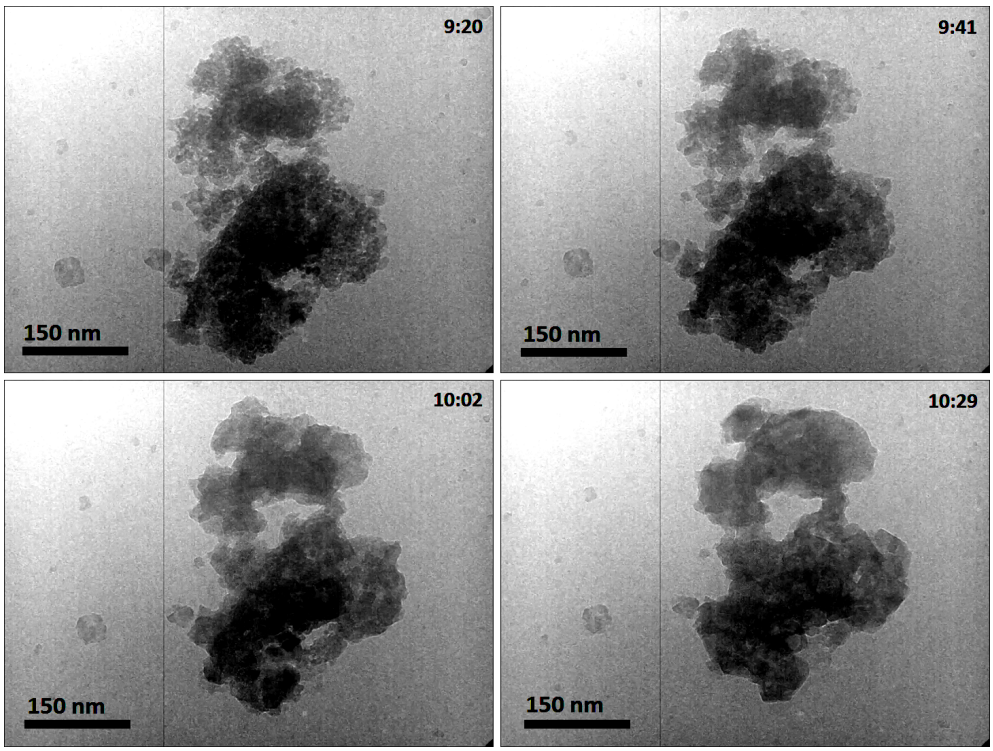

Figure 6.30: *Series of micrographs extracted from "SA_ferrihydrite_H2_Heating-_4.mp4". The sample was exposed to 1.2 atm hydrogen at 400°C. The ferrihydrite nanoparticles quickly agglomerate and form larger particles as they are reduced to magnetite. These magnetite particles then increase in crystallinity, all within a comparatively short period of time.*

to demonstrate a few of these particles that are beginning to form. The cluster continues to slowly increase in size as particles flatten out. It is not known what form of oxide these crystals are in (owing once again to a lack of ED patterns). However, based on *in situ* XRPD data, it is believed that the crystals present are a mix of magnetite and wüstite phases.

A sudden change is observed in the cluster at 14:40 onwards as the iron oxides are fully reduced to metallic iron. The micrographs in Figure 6.31 highlight key points in this reduction. At 14:40, the sample is at its maximum size. At 14:55, the top left-hand side of the cluster begins to form smaller particles which rapidly contract towards the center of the cluster. The appearance is analogous to a spherical object collapsing in on itself. This is likely a result of the magnetic interaction between adjacent iron particles. This reduction is preceded by small,

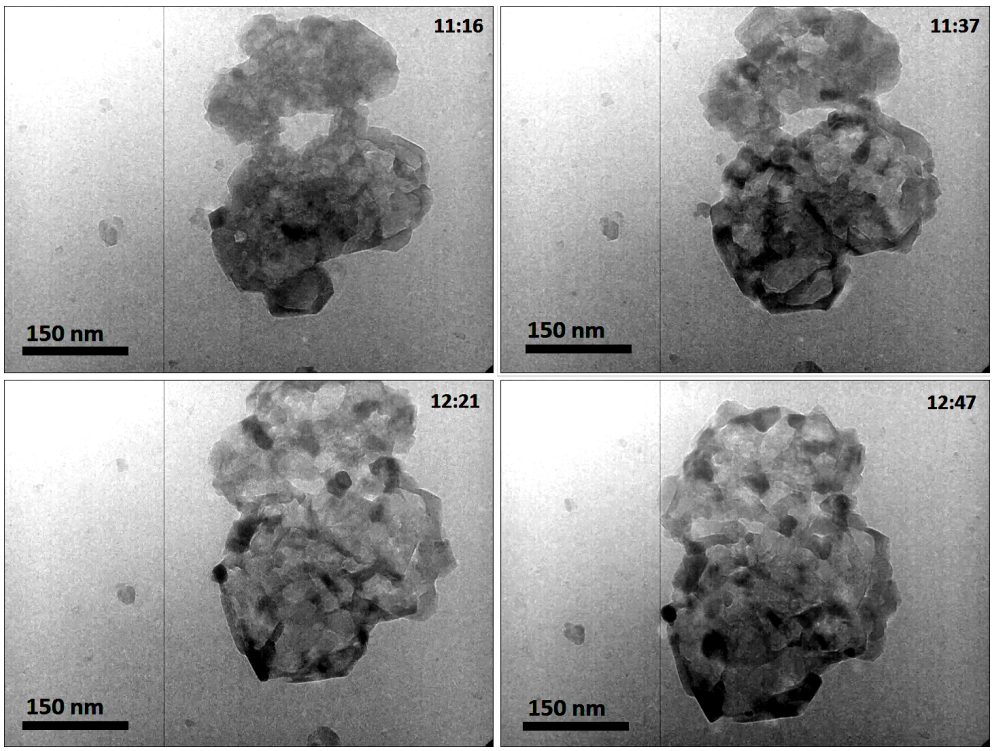

Figure 6.31: *Series of micrographs extracted from "SA_ferrihydrite_H2_Heating-_4.mp4". The sample was exposed to 1.2 atm hydrogen at 400°C. The agglomeration of newly formed magnetite particles continues to grow in size and flatten over time.*

dark crystallites appearing randomly within the iron oxide cluster. These are the first iron domains forming.

By 14:57, small particles have formed all around the cluster, and are attracted towards each other. At 15:01, the process is largely complete, with smaller particles of iron being prevalent throughout the cluster. The total area of the cluster in the micrographs is considerably less than initially, suggesting a decrease in volume as expected with reduction of iron oxide to iron.

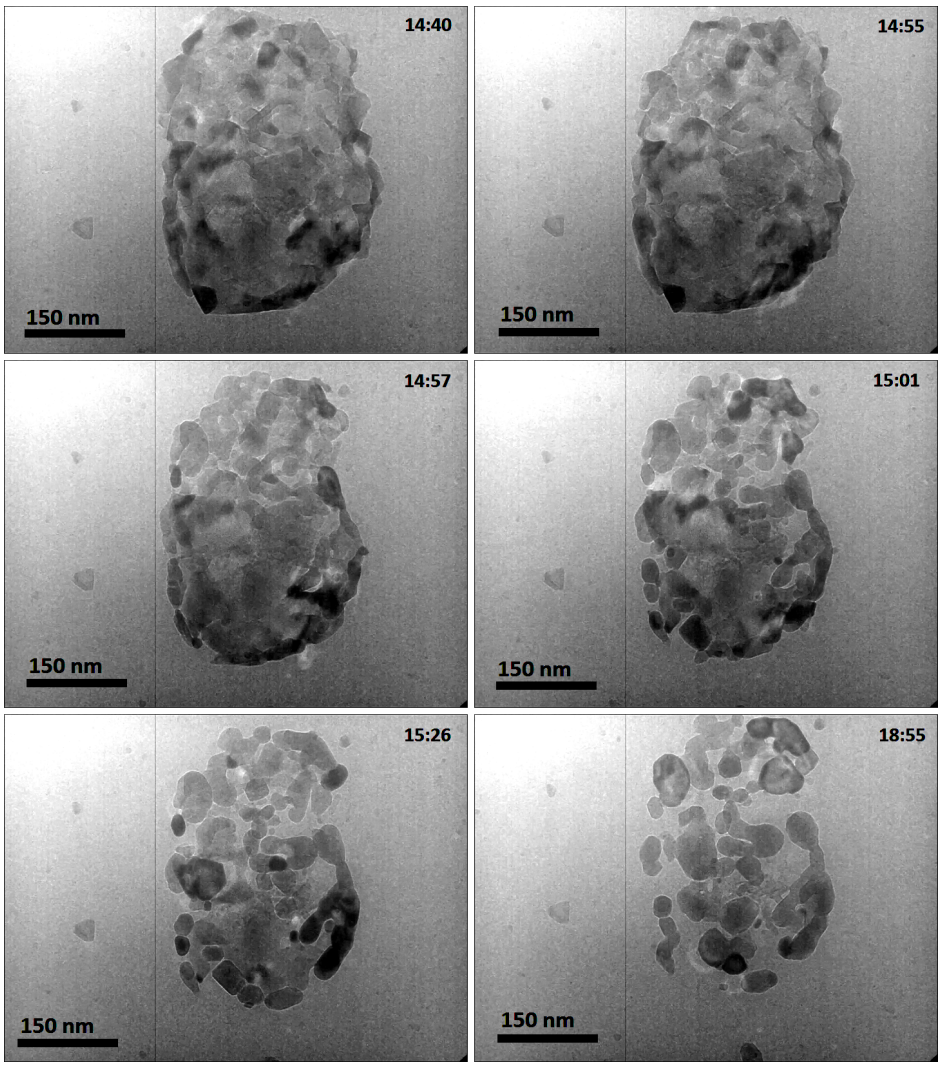

Figure 6.32: *Series of micrographs extracted from "SA_ferrihydrite_H2_Heating-_4.mp4". The sample was exposed to 1.2 atm hydrogen at 400°C. These micrographs reveal the final stage of reduction to metallic iron. The process is rapid, with iron particles forming throughout the cluster. Thereafter iron particles grow larger at the expense of smaller particles and increase in crystallinity.*

Thereafter, the few remaining magnetite/wüstite particles reduce to iron, while the already present iron particles continue to grow larger at the expense of smaller ones. As the particles increase in size, they start presenting very well-defined surface facets. The micrograph extracted at 15:26 demonstrates several iron particles with very well-defined facets visible. The total number of particles has decreased

by this point, and particles are much larger.

The final image at 18:55 is towards the end of the video recording and illustrates the morphology of the cluster 4 minutes after the rapid formation of iron. The particle sizes continue to increase while the number of particles decrease. There is a region in the center of the cluster that contains particles that are considerably smaller and less-defined. These are the poorly-crystalline ferrihydrite-like regions containing a higher concentration of silica.

A condensed video (8:42 in duration), entitled "Ferrihydrite Reduction - action.mp4", showing just the reduction from ferrihydrite to magnetite and then the reduction to iron, is also included in Appendix B.

Upon completion of the video recording, the temperature was reduced to 200°C and the hydrogen removed from the gas cell, to be replaced by nitrogen. This quenched the reaction. Other regions of the sample were surveyed to evaluate the effects of electron beam. The results were fairly surprising.

Areas on the sample consisted of well-defined agglomerates of flat crystals, similar to what was observed after the reduction of ferrihydrite to magnetite. In other areas, unreduced ferrihydrite particles were present. However, it is unlikely that the electron beam caused the complete reduction of the area that was recorded, since other areas consisted entirely of particles of the same morphology as those present at the end of the reduction, suggesting the complete reduction to iron.

This might be a result of hydrogen concentration variation across the surface of the gas cell during reduction, or it might be a result of subtle silicon concentration variations within the ferrihydrite precursors, as is observed with TPR and *in situ* XRPD.

At no area on the gas cell window was there any evidence to suggest that the silicon and iron had segregated, forming metal particles and vitreous silica respectively, suggesting the silica was still associated with the iron/iron oxide during reduction. This is consistent with the *ex situ* TEM analyses which suggested a migration of silicon to the surface of the resulting iron particles.

6.4 Additional Considerations

As mentioned in Chapter 3.3, the two options currently available in order to conduct *in situ* experiments in a TEM are gas flow holders or dedicated differentially-pumped ETEMs. The only apparent advantage that an E-TEM has over the gas flow holders is that the electron beam need only be transmitted through a thin layer of low pressure gas, and not through approximately 100 nm of silicon nitride material as with the gas cells. However, it is evident from these results that high resolution images may easily be obtained through the silicon nitride membranes of these gas cells. The gas cells are considerably cheaper than an ETEM, more mobile and can perform experiments at much greater pressures (1000 mbar in a gas flow cell versus 20-30 mbar in an ETEM). There is no doubt that as the technology (which is currently in its infancy) continues to grow, the attainable pressures within these cells will also increase. This will likely be accompanied by increasing temperature limits and finer, more accurate temperature control.

As an aside, a single *in situ* reduction on **100/0 Fe/SiO$_2$** was also performed using an FEI DP-ETEM at Pacific Northwest National Laboratory. The sample was suspended in ethanol and drop-cast onto a silicon nitride membrane. A Gatan heating holder was employed. Since hydrogen was the experimental gas, a partial pressure of 0.6 mbar was the highest possible pressure of gas that the sample could safely be exposed to. This is 2000 times less pressure than that available in either of the gas flow holders. The holder also drifts by an amount similar to the Atmosphere gas flow system. Over the course of two hours, there was no evidence to suggest that reduction had begun to occur, even with heating to a temperature of 750°C. This is attributed to the very low partial pressure of hydrogen.

Another consideration to take into account is the type of experiment that is needed. It takes approximately two hours to prepare a gas cell and ensure it is adequately sealed to prevent gas leaking into the microscope column and compromising the integrity of the vacuum. More importantly, they are not reusable. Additionally, the particular process under investigation might be fully reversible in some cases, but in others, such as the reduction experiments performed in this work, the process is not completely reversible. As a result, there is no returning to a previous state after passing a certain point in the experiment. It is thus important to ensure all

the requisite data has been collected prior to reaching this critical point.

The particular questions that the experiment is looking to answer will dictate the type of experiment. By way of example, this work was able to probe the reduction of iron oxides in hydrogen by analyzing the sample at various points in the reduction process. Quenching the reaction allows access to chemical and high resolution information that is difficult to obtain while the reaction is on-going. By contrast, this study was also able to study the general morphology changes occurring within the different iron oxide systems over a period of time through the use of lower magnification imaging and video recording using a high speed camera. A combination of these two approaches will yield the most information regarding a particular process when considering catalytic systems of this nature

It is possible to spend several days on a given sample, depending on the level of detail required in the analysis. This is an appreciable period of microscope time and as such, the time should be spent as efficiently as possible. This is only possible with thorough planning. Directly related to long microscope times is the issue of total electron dose. It is always important to try minimize the electron dose received by a sample, and with long observation times or constant probing of a particular region of a sample, the total electron dose can be significant enough to damage the sample. For meaningful conclusions to be drawn from an experiment, it is important that the effects of the electron beam can be separated from those of the gas and temperature environment. This is easiest performed by periodically examining areas of the sample that have been exposed to considerably lower electron doses. This becomes particularly important during high resolution work, where electron dose rates are considerably higher.

A final set of considerations is not related to the actual experiment, but to the post-processing of the data. Each experiment may potentially generate an enormous amount of data, which will need to be processed, interpreted and reported. This may take a fair amount of time. Additionally, the data generated can be significant in terms of size, and requires a suitable amount of storage. The actual size of the dataset varies vastly depending on numerous factors. These include the number of micrographs recorded and the resolution of each, with higher resolution micrographs being considerably larger. Additionally, any EDS/EELS survey data sets will also be considerably larger than a standard image (the actual size will

depend on the size of the region of interest). These datasets however are still small enough to be stored on modern PCs using conventional storage methods (internal/external hard drives etc).

It is the real-time imaging of a process that requires special data storage considerations. It easily generates the largest amount of data. The actual size of the generated data will depend on the resolution of the camera and the framerate at which the process is recorded. Using this work to illustrate, the total amount of data generated is summarized in Table 6.2 and Table 6.3.

Table 6.2 contains a summary of the data generated using the Atmosphere^{TM} gas flow system at the University of Manchester. It took approximately two days of microscope time (approximately 22 hours) per sample to generate each data set. Owing to the sample drift in the Atmosphere^{TM} system, there were long periods of waiting for the system to stabilize before any imaging was performed. A total of 783 images were obtained across both samples, totaling 8.23 GB. A further 4.78 GB worth of EELS/EDS survey images (46 in total) were generated, bringing the total amount of data collected within 4 days to 13 GB. This is not a particularly large data set, but the number of micrographs recorded required a significant amount of time to adequately post-process and interpret.

Table 6.2: *Summary of the number of micrographs and EDS/EELS survey data sets generated using the Atmosphere^{TM} gas flow system at the University of Manchester and their respective sizes. It took approximately 22 hours to generate the data for each sample.*

Sample	Micrographs	EELS/EDS maps	Size [GB]
100/0 Fe/SiO_2	538	31	8.41
100/10 Fe/SiO_2	245	15	4.60

Table 6.3 contains a summary of the data generated using the Hummingbird gas flow system at Hummingbird Scientific. While a few images were recorded, their size is insignificant when compared to the size of data generated for the real-time video recordings. Over the course of approximately 4 hours, a total of 62 minutes and 38 seconds worth of video was recorded. This was comprised of 54982 individual frames, with each frame recorded as a lossless TIF file with dimensions

2048 x 1536. The total size of this data set is 363 GB. It is entirely possible that similar experiments can generate several terabytes of data within as little as a one week period. As such, careful consideration must be made regarding the storage of such large amount of data prior to actual collection of the data.

Should the data need to be transferred over large distances, a large amount of bandwidth is required. Assuming an upload speed of 3072 kbps (the fastest upload speed offered by South Africa's leading broadband supplier in 2015), it would take 269 hours (a little over 11 days) to transfer the 363 GB of data generated in approximately 4 hours. This is an extremely long period of time, as such alternative methods of data transfer, such as posting of hard drives, should be considered prior to conducting these experiments.

Table 6.3: *Summary of the video data generated using the Hummingbird gas flow system at Hummingbird Scientific and their respective data sizes. The data set for each sample was collected in approximately 2 hours.*

Sample	Videos	Frames	Length [min:sec]	Size [GB]
100/0 Fe/SiO_2	6	38161	42:58	264
100/10 Fe/SiO_2	1	16821	18:41	98.6

6.5 Chapter Conclusions

These *in situ* TEM experiments studied the reduction of two model FT catalysts in an electron microscope under realistic operating conditions using two different, commercially available *in situ* gas flow systems. A large variety of techniques, including TEM imaging (with real-time video recording), selected area electron diffraction, hollow cone dark-field imaging and bright-field and high angle annular dark-field STEM imaging were employed in analysing the reduction process. These data were complemented with EDS and EELS data. The silicon nitride membrane windows have very little influence on the achievable resolution.

100/0 Fe/SiO_2, which begins as the hematite phase, is initially reduced to magnetite. The initial stages of reduction are characterised by the formation of small magnetite domains which rapidly increase in particle size and definition. As the

temperature increases to 500°C, small iron nanoparticles are visible across the entirety of the sample. It is proposed that iron atoms are liberated slowly from surface layers of the magnetite, and migrate towards each other across the surface of the silicon nitride window. These nanoparticles grow at the expense of smaller ones via sintering mechanisms, resulting in larger particles of iron.

100/10 Fe/SiO$_2$, which is initially a silicon-substituted 2-line ferrihydrite phase, has a similar reduction behavior. The ferrihydrite particles initially agglomerate, forming larger particles. This is accompanied by the simultaneous reduction to magnetite. As with **100/0 Fe/SiO$_2$**, the formation of small iron nanoparticles at lower temperatures is observed, as liberated atomic iron species of iron migrate across the surface of the silicon nitride window. At higher temperatures, these nanoparticles grow, forming larger iron particles. The magnetite particles grow and flatten prior to reduction to iron. Amorphous regions co-exist alongside the iron particles after reduction. They consist of much less crystalline particles, which SAED patterns suggest are a mixture of magnetite, wüstite. At a temperature of 750°C, crystallite domains of fayalite (Fe_2SiO_4) are also observed to form. The formation of this fayalite provides direct evidence of Fe-O-Si networks that have formed at lower temperatures.

It is difficult to directly compare the two gas flow systems used in this work, since each was involved in a different type of experiment, and each was used in a different microscope. The Atmosphere^{TM} gas flow system by Protochips has a fairly large temperature discrepancy between the actual temperature at the sample and the set temperature in the control software. It also tends to drift considerably when the temperature is adjusted. The temperature of the sample appears to be very uniform however, and the cell is very reliable if assembled correctly.

The temperature of the sample in the Hummingbird gas flow system is in much closer agreement to that set using the control software. There is a definite advantage to temperature control by monitoring the resistivity of the heating material, rather than using a set current for a cell pre-calibrated in vacuum, as this largely eliminates the heat-withdrawing effects of gases (particularly hydrogen). There is also minimal drift upon changing the temperature of the sample. The heating cells do appear to be less stable, with several cells rupturing during experiments.

As with any electron microscope investigation, the total sample size probed is extremely small. It is always important to correlate data obtained in a TEM with bulk analysis techniques to more rigorously understand the properties or behavior of the sample of interest. This is especially important with gas flow cells, with the uncertainty regarding the temperature at the sample and no way to accurately measure the actual gas flow over the sample itself.

The electron microscope has long been an invaluable tool for analyzing the shape, size and structure of catalyst materials owing to its superior resolution when compared to other techniques. However it has always required the sample to be in a vacuum, conditions far removed from those experienced during a reaction. Gas flow TEM holders remove this limitation to electron microscope analysis, and allow dynamic changes in the catalyst material, in a realistic temperature and gaseous environment, to be studied. This is all possible without compromising the resolution of the microscope. As this technology, still in its infancy, continues to grow and develop, there is no doubt that understanding of catalytic processes will greatly benefit from the knowledge generated using this and similar *in situ* TEM techniques.

7 Conclusions

This chapter summarises the key findings of this study, and provides recommendations for future work.

The six iron oxide samples investigated in this study were prepared via a co-precipitation technique from an $Fe(NO_3)_3 \cdot 9H_2O$ precursor in the presence of varying amounts of silica. Their structural and magnetic properties were characterised using a variety of experimental techniques.

The reduction of these iron oxides in hydrogen was also investigated. This provided insight into the role of silica in such reduction processes and the mechanism responsible for the reduction.

7.1 Structural and Magnetic Properties of Oxide Precursors

For the purposes of this discussion, the six samples may be collectively described by three-different groups, owing to the similarities between the various samples within each group. The first group is the sample with no silica, containing only **100/0 Fe/SiO$_2$**. The second group is referred to as the low silica samples and contains **100/10 Fe/SiO$_2$**, **100/25 Fe/SiO$_2$** and **100/50 Fe/SiO$_2$**. Finally, **100/100 Fe/SiO$_2$** and **100/200 Fe/SiO$_2$** together make up the high-silica group.

7.1.1 No Silica

The particle phase and morphology were evaluated using a combination of TEM, XRPD, MS and Raman spectroscopy. The sample precipitated without any silica (**100/0 Fe/SiO$_2$**) consists of irregular-shaped hematite nanoparticles, with a mean particle diameter (determined from TEM) of 39 ± 12 nm. SAED and XRPD patterns, as well as the Raman spectrum, revealed that the sample is phase-pure. Rietveld refinement of the XRPD pattern using the fundamental parameter ap-

proach revealed a mean crystallite diameter of 52.7 ± 0.2 nm.

The RTMS and LTMS spectra of **100/0 Fe/SiO$_2$** were each fitted with a single sextet. The hyperfine values obtained from the fits are δ = 0.39 mm.s^{-1}, ΔE_Q = -0.20 mm.s^{-1}, B_{hf} = 51.7 T for the spectrum recorded at 300 K and δ = 0.49 mm.s^{-1}, ΔE_Q = 0.40 mm.s^{-1}, B_{hf} = 53.9 T for the spectrum at 4.2 K. These values are consistent with hematite.

The magnetic behaviour of **100/0 Fe/SiO$_2$** was studied using χ_{DC}(T) curves. They reveal a magnetic transition at $\approx$ 230 K ascribed to the Morin transition. This temperature value is consistent with nano-hematite particles of $\approx$ 50 nm.

Nitrogen physisorption data revealed a surface area and pore size distribution consistent with nano-hematite particles. The surface area data was used to calculate the mean particle size, and this was determined to be 49.5 nm, in excellent agreement with the particle diameters determined using TEM and XRPD.

7.1.2 Low Silica Content

The addition of 10, 25 and 50 weight silica for every 100 weight iron in **100/10 Fe/SiO$_2$**, **100/25 Fe/SiO$_2$** and **100/50 Fe/SiO$_2$** resulted in the formation of very different iron oxide particles when compared to **100/0 Fe/SiO$_2$**. BSE-SEM micrographs, with complementary SEM-EDS elemental maps, revealed a very strong association of iron with silica. This was necessary for iron-silica interactions to manifest during reduction and confirms a successful synthesis.

The particle phase and morphology was evaluated using TEM, XRPD, MS and Raman spectroscopy. TEM revealed that the resulting particles are very small, approximately spherical nanoparticles. The particle sizes determined from the TEM images are 3.1 ± 0.4 nm, 2.4 ± 0.3 nm and 2.4 ± 0.3 nm for **100/10 Fe/SiO$_2$**, **100/25 Fe/SiO$_2$** and **100/50 Fe/SiO$_2$** respectively. SAED patterns revealed two broad rings at approximately 2.5 and 1.5 Å, while XRPD patterns revealed two broad reflections at the same d-spacings. These confirm that the stable iron oxide phase formed in the presence of silica is the poorly crystalline oxyhydroxide known as 2-line ferrihydrite. Raman spectra of all three samples exhibit peaks

characteristic of 2-line ferrihydrite, as well as an additional peak consistent with a ν_3 ${SiO_4}^{4-}$ vibrational mode. Shifts in these peaks with increasing silica content is a result of changes in the reduced mass, which is an indication of Fe-O-Si bonds forming even prior to reduction.

STEM-EELS and STEM-EDS data revealed a very homogeneous distribution of silicon within the ferrihydrite particles. This suggests that, during synthesis, the silica is fully incorporated within the ferrihydrite framework. As a result, each of these samples consists of silicon-substituted 2-line ferrihydrite nanoparticles within a very narrow size range. Nitrogen physisorption data reveals surface areas and pore size distributions consistent with very small nanoparticle powders, while the calculated particle sizes are 9.0, 6.5 and 6.7 nm for **100/10 Fe/SiO$_2$**, **100/25 Fe/SiO$_2$** and **100/50 Fe/SiO$_2$** respectively. These are larger than those determined using TEM, but this is a result of a portion of the surface sites being inaccessible to nitrogen as a result of particle agglomeration.

The MS spectra of these samples all exhibited a doublet at room temperature and were fitted with a distribution of ΔE_Q. The values of $\delta \approx 0.35$ mm.s^{-1} are consistent with super paramagnetic Fe^{3+} cations in an octahedral environment, while the large values of ΔE_Q distributions (maximum intensity greater than 0.90 mm.s^{-1} for all samples) is indicative of a large degree of distortion in the octahedral environment. At 4.2 K, each sample exhibited a broad sextet which was fitted with a distribution of B_{hf}. There was a regular decrease in the median position of the B_{hf} distribution on increasing silica content (49.0 T, 48.0 T and 46.9 T for **100/10 Fe/SiO$_2$**, **100/25 Fe/SiO$_2$** and **100/50 Fe/SiO$_2$** respectively). These B_{hf} values are characteristic of ferrihydrite particles, with a decrease in the field distribution indicative of a decrease in particle size or an increase in disorder. Additionally, in a 10 T applied field, the distribution of B_{hf} merely broadened as a result of particles randomly orienting themselves in the field. There was also a slight increase in intensity in lines 2 and 5. This behaviour is characteristic of ferrihydrite.

The χ_{DC}(T) curves allowed the temperature-dependent magnetisation of each of these samples to be studied. They are characteristic of an assembly of superparamagnetic nanoparticles. The blocking temperature decreased with increased silica content with T_B=68 K for **100/10 Fe/SiO$_2$**, 42 K for **100/25 Fe/SiO$_2$** and 39 K for **100/50 Fe/SiO$_2$**. Using these blocking temperatures, the mean particle

sizes for each sample were calculated as 4.2 nm for **100/10 Fe/SiO$_2$** and 3.6 nm for **100/25 Fe/SiO$_2$** and 3.5 nm for **100/50 Fe/SiO$_2$**. These are in excellent agreement with those obtained using TEM.

7.1.3 High Silica Content

The addition of 100 and 200 weight silica for every 100 weight iron in **100/100 Fe/SiO$_2$** and **100/200 Fe/SiO$_2$** results in the formation of two distinct phases. This is a result of the increased amount of silica being too great to fully incorporate in the iron oxide framework. While BSE-SEM micrographs, together with SEM-EDS maps, show an association between iron and silicon, there is a large degree of inhomogeneity present in each sample, suggesting that local concentrations of iron and silica vary.

TEM data revealed that the samples consist of large pieces of amorphous silica. STEM-EELS elemental composition maps revealed that iron is substituted throughout this silica material, likely as atomic domains. Within the iron-infused silica network, small iron oxide domains are found. SAED and XRPD patterns revealed two broad reflections at 2.5 and 1.5 Å characteristic of 2-line ferrihydrite. The XRPD pattern also contains a reflection at $\approx$ 3.7 Å which is ascribed to amorphous silica. The Raman spectra for each sample show the same peaks as the low silica content samples, with an additional vibrational mode appearing at 1050 cm^{-1}. This is characteristic of pure silica vibrations.

The nitrogen physisorption data revealed lower surface areas, since a large number of iron oxide particles are encapsulated by the iron-infused amorphous silica. The pore size distributions also indicate the presence of macropores which is characteristic of amorphous silica.

The MS spectra of these samples both exhibit a doublet at room temperature and were fitted with a distribution of ΔE_Q. The values of $\delta \approx 0.35$ mm.s^{-1} are consistent with super paramagnetic Fe^{3+} cations in an octahedral environment, while the large values of the ΔE_Q distributions (maximum intensity greater than 0.90 mm.s^{-1} for all samples) is indicative of a large amount of distortion in the octahedral environment. The LTMS spectra are complex and best fitted with two

distributions of B_{hf}. The high-field distribution has a median B_{hf} value of 44.8 T for both samples and is attributed to ferrihydrite domains within each sample. This further continues the trend observed for the low silica-content samples i.e. an increase in silica results in a decrease in B_{hf}. This is a result of an increasing amount of distortion introduced into the Fe^{3+} environment as increasing amounts of silica tetrahedra are incorporated into the oxide framework. The low-field distribution (whose contribution to the total spectrum is greater in **100/200 Fe/SiO$_2$** than **100/100 Fe/SiO$_2$**) is attributed to isolated Fe^{3+} domains encapsulated in a silica matrix. In a 10 T applied field, the high-field distribution merely broadens as the ferrihydrite domains orient themselves randomly with respect to the field, while the low-field distribution is shifted to higher values as the magnetic moments of the isolated Fe^{3+} domains orient themselves parallel to the applied field.

The χ_{DC}(T) of these samples are distinctly different to those with lower silica content. **100/100 Fe/SiO$_2$** exhibits a small bump corresponding to the blocked state of the larger iron oxide domains, while this is not even evident in the χ_{DC}(T) curve for **100/200 Fe/SiO$_2$**. The presence of this increased amount of silica results in a much broader particle size distribution which results in a very broad distribution of blocking temperatures.

7.2 Reduction in Hydrogen

The reduction of each sample in hydrogen was studied using a combination of TPR, *in situ* XRPD and TEM analyses of samples reduced *ex situ*.

TPR data for **100/0 Fe/SiO$_2$** shows two reduction peaks indicative of a two-step reduction process, confirmed by comparison of theoretical and experimental hydrogen consumptions at each reduction step. This reduction process occurs as:

$$\alpha\text{-}Fe_2O_3 \rightarrow Fe_3O_4 \rightarrow Fe$$

This reduction is greatly altered on addition of silica and follows a very regular trend. A total of four changes are observed in the TPR profiles of the silica-promoted samples.

Firstly, the reduction shifts to higher temperatures. This is indicative of Fe-O-Si bonds that have formed during synthesis. Secondly, the reduction proceeds via three-steps as a wüstite phase is stabilised. This phase typically disproportionates to iron and magnetite at temperatures below 570 K, but the presence of silica helps to stabilise it. The reduction of magnetite is now split into two distinct steps and the total reduction now reads:

$$\text{Ferrihydrite} \rightarrow Fe_3O_4 \rightarrow FeO \rightarrow Fe$$

The third effect of the silica-addition is that the reduction peaks continually broaden with increasing silica content. This is a result of local concentration variations of silica within the initial iron oxide material. As a result of this, those regions with lower amounts of silicon are able to reduce more easily since they contain less Fe-O-Si which inhibit reduction. This peak broadening prevented the quantification of hydrogen consumption, since peak overlap was too severe.

Finally, the addition of silica prevents all the Fe^{3+} from being reduced to Fe^0, at least up to temperatures of 1000°C. This was determined by comparing the calculated total hydrogen consumption for each sample with the theoretically expected value. The percentage of Fe^{3+} that was not fully reduced increased with increasing silica content, once more a result of an increased amount of Fe-O-Si bonds.

The two-step reduction in hydrogen of **100/0 Fe/SiO$_2$** is confirmed by *in situ* XRPD. Hematite begins to reduce to magnetite at 260°C, which itself begins to reduce to iron from 340°C. A small amount of wüstite appeared between 320 and 360 °C, but was readily reduced to iron. Mean crystallite diameter of the final iron crystallite domains, determined using a full pattern, fundamental parameter Rietveld refinement, was 68.0 ± 0.2 nm.

The *in situ* XRPD patterns for **100/10 Fe/SiO$_2$** show clearly the existence of a stable wüstite phase forming between magnetite and iron, highlighting the change from a two-step to a three-step reduction pathway. Even after 8 hours at 380°C, the amount of wüstite exists in appreciable quantities. The mean crystallite diameter of the final iron domains was 28.4 ± 0.1 nm. Amorphous reflections were still visible at the end of the experiment, which indicated the Fe-O-Si material contains unreduced or partially reduced Fe^{3+} species.

100/25 Fe/SiO$_2$ and **100/50 Fe/SiO$_2$** demonstrated the formation of different crystalline material when compared to **100/10 Fe/SiO$_2$**. The reduction still occurs in a three-step process, however, crystalline magnetite and wüstite are not formed. Instead, broad reflections at d-spacings of the most intense reflections of these two phases suggest that they exist as very small, disordered particles. The reduction to iron, which occurs at 380 °C in both samples, results in particles with a mean crystallite diameter of approximately 80 nm. Significant quantities of small, disordered magnetite, wüstite and ferrihydrite-like material remain at the end of the reduction experiment, a result of incompletely reduced Fe^{3+} species.

The *in situ* XRPD patterns for **100/100 Fe/SiO$_2$** and **100/200 Fe/SiO$_2$** both exhibit two broad reflections throughout the entirety of the reduction experiment, with some crystalline iron reflections appearing at 380°C. The mean crystallite size is 60 nm in **100/100 Fe/SiO$_2$** and 14 nm in **100/200 Fe/SiO$_2$**. The much smaller mean particle size in the highest silica-content sample is the result of the encapsulating silica isolating the initial iron oxide domains, preventing access to additional iron atoms to allow for the growth of larger particles.

Each of the samples was reduced *ex situ* at 400°C for 20 hours in hydrogen, prior to TEM analysis. The process of transferring the sample from the reactor to the microscope caused the iron particles to oxidize. Larger iron particles still contained an iron interior, while smaller particles were completely oxidised to magnetite.

100/0 Fe/SiO$_2$ consists of very large particles consisting of an iron core with an encapsulating iron-oxide (magnetite) shell. It is believed that during reduction, iron particles are formed, but the edges of these particles are oxidised to magnetite when transferring from the reactor to the electron microscope.

100/10 Fe/SiO$_2$ consists of large iron particles scattered amongst poorly crystalline material. STEM-EDS linescans revealed a small amount of silicon located at the edge of iron particles, but not at the interior. This suggests a small amount of silicon is contained at or near the surface of the iron particles that form during reduction. This has implications for catalysis since it will alter the surface energies and also decrease the number of active metal sites.

The iron particles formed during reduction of **100/25 Fe/SiO$_2$** and **100/50**

Fe/SiO$_2$ are larger than those formed in **100/10 Fe/SiO$_2$**, consistent with the data obtained from *in situ* XRPD. SAED diffraction patterns revealed reflections at d-spacings consistent with magnetite, wüstite and iron. A large amount of poorly crystalline material is also evident across the entirety of the sample. STEM-EDS elemental analysis of these poorly crystalline regions showed a much higher silicon content when compared to the iron particles. The iron particles once again contain a small amount of silicon at the surface. This suggests that during reduction, Fe^{3+} is reduced to Fe^0 atoms which diffuse out of the particle framework and come together to form the final iron particles.

100/100 Fe/SiO$_2$ and **100/200 Fe/SiO$_2$** both consist of small crystallite domains of iron oxide within a vitreous silica network. These iron oxide domains were likely iron metal prior to oxidation on exposure to atmospheric conditions during transferal from the reactor to the microscope.

7.3 *In Situ* Gas Flow TEM

The reduction of two samples in hydrogen *viz.* **100/0 Fe/SiO$_2$** and **100/10 Fe/SiO$_2$** was investigated using two different, commercially available gas flow TEM holders. These are the Atmopshere^{TM} gas flow cell produced by Protochips and the Hummingbird Scientific gas flow cell. A large variety of techniques, including TEM imaging (with real-time video recording), selected area electron diffraction, hollow cone dark-field imaging and bright-field and high angle annular dark-field STEM imaging were employed in analysing the reduction. These data were complemented with EDS and EELS data. The enclosing silicon nitride membrane windows have very little influence on the achievable resolution.

100/0 Fe/SiO$_2$, which begins as the hematite phase is initially reduced to magnetite. The initial stages of reduction are characterised by the formation of small magnetite domains which rapidly increase in particle size and definition. As the temperature increases to 500°C, small iron nanoparticles are visible across the entirety of the sample. It is proposed that iron atoms are liberated slowly from surface layers of the magnetite, and migrate towards each other across the surface of the silicon nitride window. These nanoparticles grow at the expense of smaller

ones via sintering mechanisms, resulting in larger particles of iron.

100/10 Fe/SiO$_2$, which is initially a silicon-substituted 2-line ferrihydrite phase, has a similar reduction behavior. The ferrihydrite particles initially agglomerate, forming larger particles. This is accompanied by the simultaneous reduction to magnetite. As with **100/0 Fe/SiO$_2$**, the formation of small iron nanoparticles at lower temperatures is observed, as liberated atomic iron species of iron migrate across the surface of the silicon nitride window. At higher temperatures, these nanoparticles grow, forming larger iron particles. Amorphous regions coexist alongside the iron particles after reduction. They consist of much less crystalline particles, which SAED patterns suggested are a mixture of magnetite and wüstite. At a temperature of 750°C, the formation of crystalline domains of fayalite (Fe_2SiO_4) is also observed. The formation of these fayalite crystallites provided direct evidence of Fe-O-Si networks existing at lower temperatures.

Complementary real-time video of an isothermal reduction at 400°C in hydrogen reveals that the reduction of ferrihydrite in **100/10 Fe/SiO$_2$** to magnetite is directly linked to a growth of the ferrihydrite particles. These magnetite particles slowly increase in size and flatten as they reduce to wüstite. The final reduction to iron is very rapid, and the iron particles are magnetically attracted towards each other.

The reduction in hydrogen using Atmosphere^{TM} may best be described as a "snapshot" approach. The samples were heated in a hydrogen atmosphere (750 - 950 mbar) for fixed periods of time, and then the temperature was lowered and the hydrogen removed. This gave insight into the reduction at various stages, or "snapshots", throughout the entirety of the reduction.

Reduction using the Hummingbird gas flow cell involved the isothermal reduction of the iron oxides in 1.2 atm hydrogen gas and an isothermal study of **100/0 Fe/SiO$_2$** at 400°C in 1 atm of air, allowing the dynamical process to be studied. This did not allow for any EELS/EDS elemental maps to be constructed, nor diffraction patterns recorded.

It is recommend that a combination of these two approaches be employed if possible, as this will provide the maximum amount of information regarding the re-

duction.

7.3.1 Comparison of Gas Flow Cells

Since each of the different holders was used for a different type of experiment and in different microscopes (Atmosphere^{TM} was used for "snapshot" experiments in an FEI Titan G2, Hummingbird gas flow cell was used in real-time isothermal experiments in a JEOL JEM-2100), it is not easy to compare the two.

The temperature of the sample in the Hummingbird gas flow system is in much closer agreement to that set using the control software, compared to Atmosphere^{TM}. There is a definite advantage to temperature control by monitoring the resistivity of the heating material, rather than using a set current for a cell pre-calibrated in vacuum, as this largely eliminates the heat-withdrawing effects of gases (particularly hydrogen). There is also minimal drift upon changing the temperature of the sample when compared with Atmosphere^{TM} which is subject to a fair amount of sample drift.

The Hummingbird gas flow cells do appear to be less stable, with several cells rupturing during experiments, while the Atmosphere^{TM} cells that passed the leak test never ruptured. However the sample sizewas very low, hence no real conclusions may be drawn from this owing to very limited sampling statistics. Atmosphere^{TM} cells are also rated to much higher temperatures (1000°C) when compared to the Hummingbird gas flow cell (400°C), which is hugely advantageous when studying processes that require such elevated temperatures.

7.4 Final Comments and Future Work

It has been shown in this work that the effect of silica is to inhibit the reduction of the iron oxide precursors. This is through the formation of Fe-O-Si bonding networks in the silicon-substituted 2-line ferrihydrite particles that form during co-precipitation. These make the silicon-substituted precursors considerably more difficult to reduce than pure iron oxides. Thus this inhibitory behaviour of silica is very intimately related to the synthesis conditions and further studies should

investigate the effect of various synthesis conditions (temperature, iron/silica precursors, precipitation time, pH, point when silica is added etc.).

Literature has suggested that there is a formation of encapsulating iron silicate layers that inhibit reduction and subsequent catalytic activity. However, this work has shown that atomic iron species are liberated from the Fe-O-Si networks during reduction, and it is these iron atoms that grow to form the final iron particles. Only a small amount of silicon is located at the edge of the particles, with most of the silicon remaining in the Fe-O-Si bonded material. Thus the overall reduction is considerably more heterogeneous than has previously been suggested. This leaves a final, reduced product that is a complex mixture of iron particles and poorly crystalline Fe-O-Si bonded material with the iron in a variety of oxidation states. The effects of the silica promoter on the iron oxide precursors and their subsequent reductions are neatly summarised in Figure 7.1.

Since these iron-FT catalysts are often prepared with additional promoters (such as copper) which assist in the reduction of the iron oxide precursor, further work should also include a study on the effect of these different promoters. More importantly, their distribution within the particles at the various stages of reduction should be studied i.e. do they associate quite strongly with the liberated iron, do they remain a part of the Fe-O-Si throughout the entirety of the reduction or do they segregate into their own separate phase?

This work has also employed *in situ* gas flow TEM to study the reduction at temperature and pressure conditions approaching those that the catalyst materials experience in an FT reactor. These experiments allow the same region to be monitored, and hence any deductions regarding the reduction pathway are less ambiguous than when a number of different TEM samples at varying degrees of reduction are prepared.

While this work involved the study of iron-FT model catalyst materials, the extension and subsequent value of these TEM gas flow experiments to any catalytic system is immediately obvious. Indeed, any dynamic process on the micrometer scale (and below) that occurs as a result of temperature and pressure effects may be readily studied using these TEM gas flow cells.

Co-precipitated iron oxides

0 ⟶ Silica content ⟶ 200

Hematite → Si-Ferrihydrite → Si-Ferrihydrite and Fe-infused silica

⟶ Increased number of Fe-O-Si bonds
Increased distortion in Fe^{3+} environment
Decrease in crystallinity
Suppresion of blocking temperature ⟶

⇩

Reduction in Hydrogen

⇩

⟶ Increase in reduction temperature
Reduction temperature range
Degree of incomplete reduction at 1000°C ⟶

Mechanism:

No Silica			Silica		
Fe_2O_3	⟶	Fe_3O_4	Ferrihydrite	$\xrightarrow{sintering}$	Fe_3O_4
Fe_3O_4	⟶	Fe	Fe_3O_4	⟶	FeO
			FeO	⟶	Fe

Final reduction step involves liberation of Fe^0 atoms from Fe-O-Si networks. Fe particles grow via sintering process.

Some silicon substitutes at Fe particle edges → implications for catalysis

At elevated temperature, remaining poorly crystalline Fe-O-Si networks crystallise into fayalite (Fe_2SiO_4) domains.

Figure 7.1: *Graphical summary of the effect of silica in co-precipitated, silica-promoted iron oxides and their subsequent reductions in hydrogen.*

A Nitrogen Physisorption Data

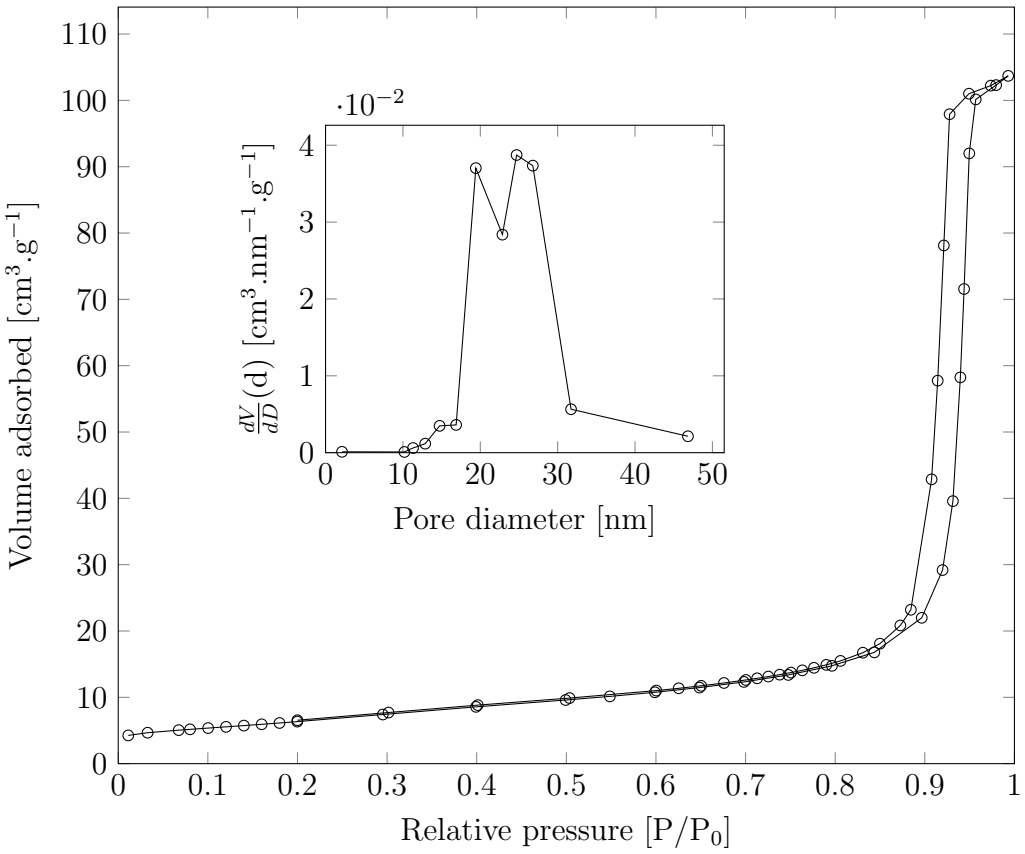

Figure A.1: *Nitrogen physisorption curve and pore size distribution (inset) for* ***100/0 Fe/SiO$_2$****.*

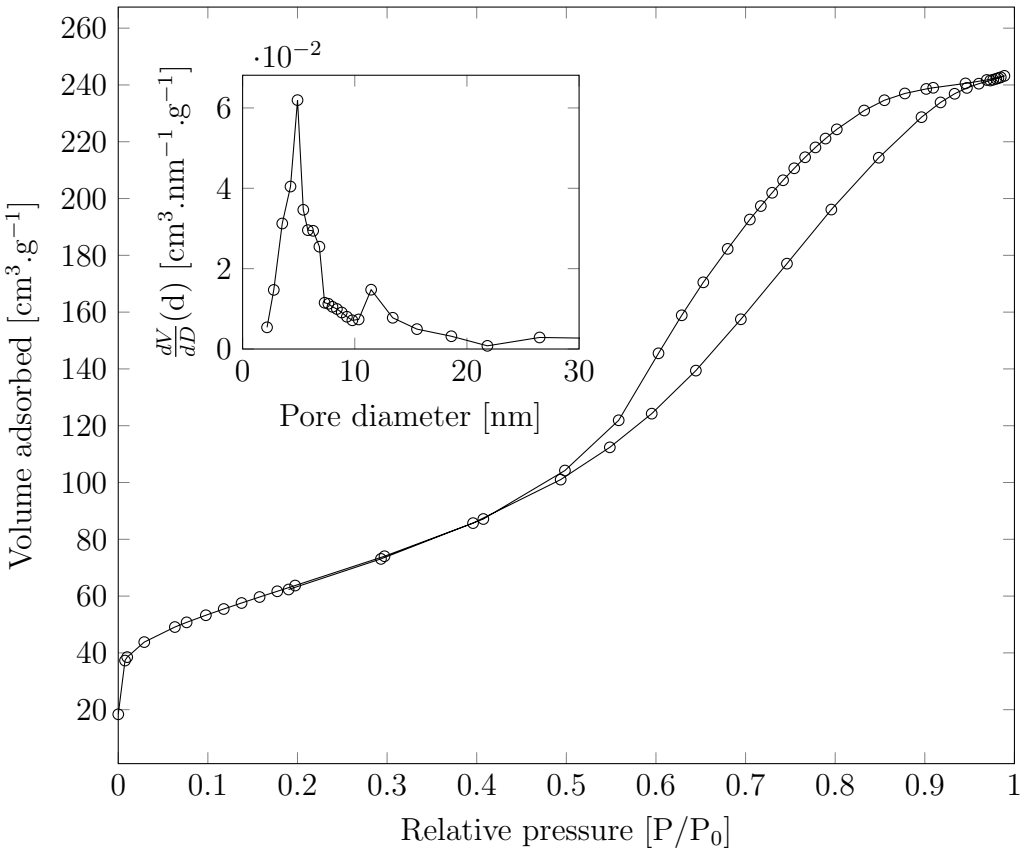

Figure A.2: *Nitrogen physisorption curve and pore size distribution (inset) for* ***100/10 Fe/SiO$_2$****.*

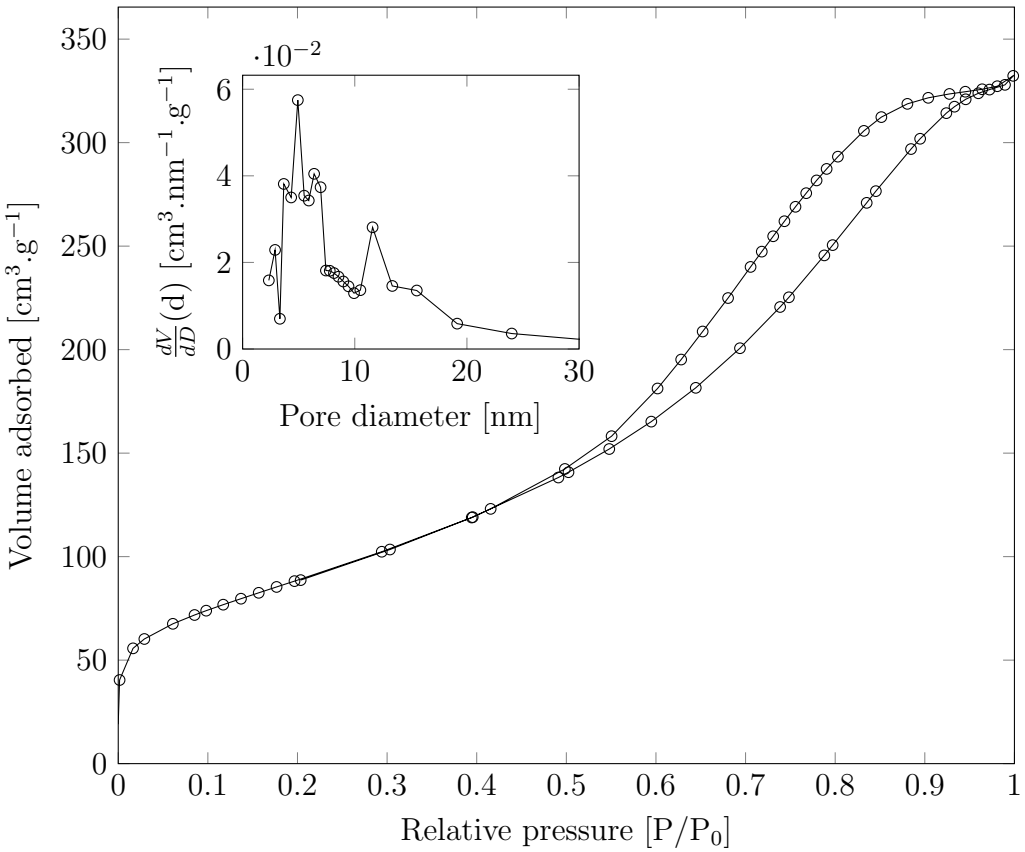

Figure A.3: *Nitrogen physisorption curve and pore size distribution (inset) for* ***100/25 Fe/SiO$_2$****.*

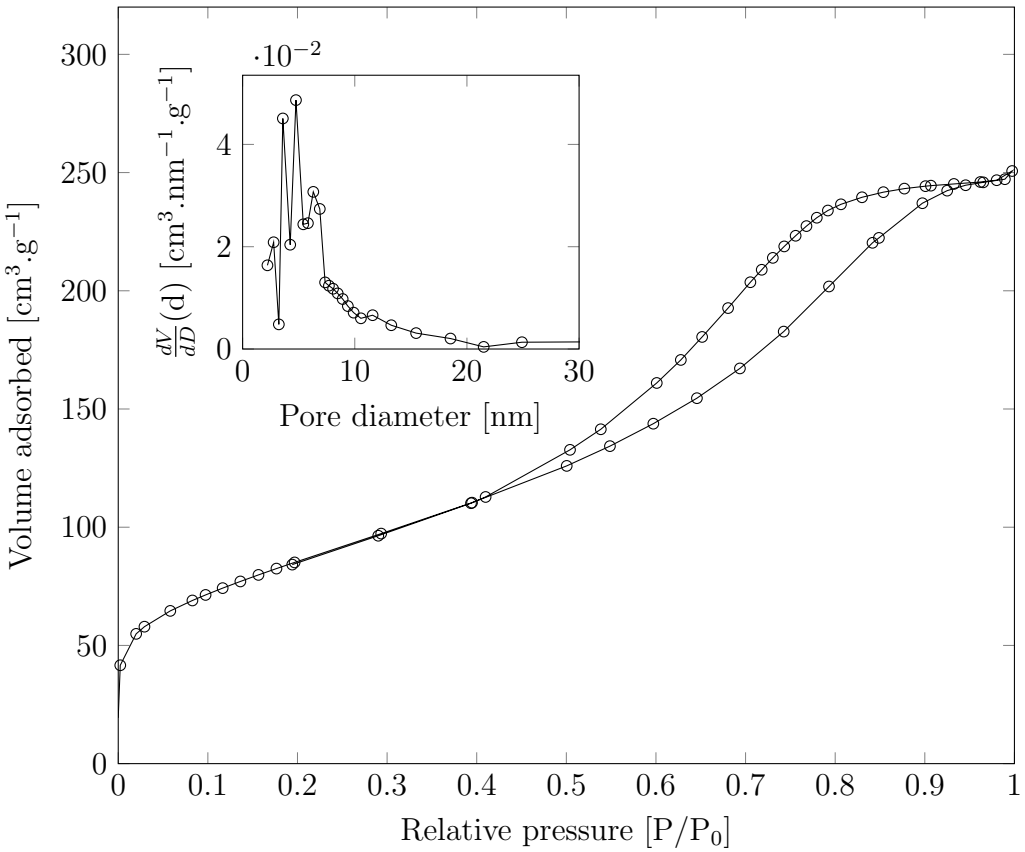

Figure A.4: *Nitrogen physisorption curve and pore size distribution (inset) for* ***100/50 Fe/SiO$_2$****.*

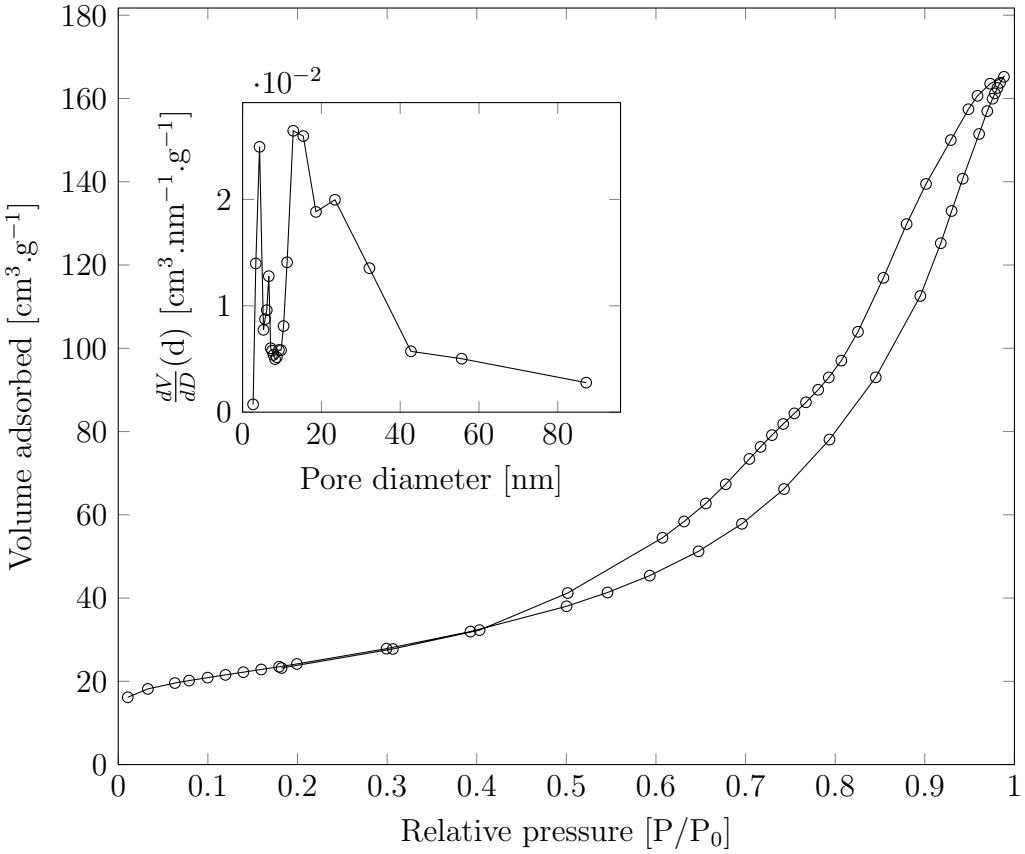

Figure A.5: *Nitrogen physisorption curve and pore size distribution (inset) for* ***100/100 Fe/SiO$_2$****.*

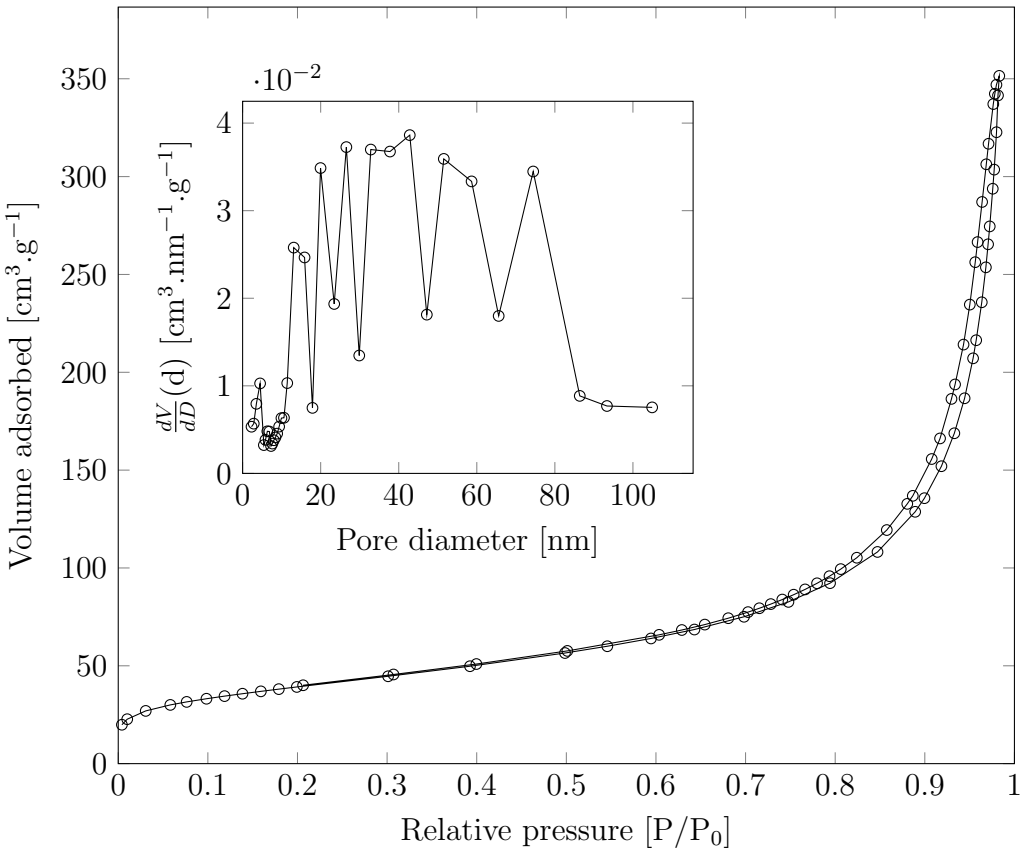

Figure A.6: *Nitrogen physisorption curve and pore size distribution (inset) for* ***100/200 Fe/SiO$_2$****.*

B *In Situ* TEM video recordings

All video recordings mentioned in Chapter 6.3 are stored on the attached data DVD.

References

[1] **N. N. Greenwood and A. Earnshaw**. *Chemistry of the Elements*. Second edition. Butterworth-Heinemann, Oxford (1997).

[2] **R. M. Cornell and U. Schwertmann**. *The Iron Oxides: Structure, Properties, Reactions, Occurences and Uses*. Second edition. Wiley-VCH GmbH & Co. KGaA, Weinheim (2003).

[3] **T. Jones**. *Steel Industry and the Environment: Technical and Management Issues*. UNEP/Earthprint, Paris (1997).

[4] **G. Buxbaum and G. Pfaff**. *Industrial Inorganic Pigments*. Third edition. Wiley-VCH Verlag GmbH & Co. KGaA (2005).

[5] **A. S. Teja and P.-Y. Koh**. "Synthesis, properties, and applications of magnetic iron oxide nanoparticles". *Prog. Cryst. Growth Charact. Mater.* **55**(1-2) (2009) 22–45.

[6] **R. Jurgons, C. Seliger, A. Hilpert, L. Trahms, S. Odenbach and C. Alexiou**. "Drug loaded magnetic nanoparticles for cancer therapy". *J. Phys. Condens. Matter* **18**(38) (2006) S2893–S2902.

[7] **L. Cabrera, S. Gutierrez, N. Menendez, M. P. Morales and P. Herrasti**. "Magnetite nanoparticles: Electrochemical synthesis and characterization". *Electrochim. Acta* **53**(8) (2008) 3436–3441.

[8] **M. Mohapatra and S. Anand**. "Synthesis and applications of nanostructured iron oxides/hydroxides a review". *Int. J. Eng. Sci. Technol.* **2**(8) (2010) 127–146.

[9] **A. Navrotsky, L. Mazeina and J. Majzlan**. "Size-driven structural and thermodynamic complexity in iron oxides". *Science* **319**(5870) (2008) 1635–1638.

[10] **U. Schwertmann**. "Solubility and dissolution of iron-oxides". *Plant Soil* **130** (1991) 1–25.

[11] **F. dos Santos Coelho, J. D. Ardisson, F. C. C. Moura, R. M. Lago, E. Murad and J. D. Fabris**. "Potential application of highly reactive Fe(0)/Fe_3O_4 composites for the reduction of Cr(VI) environmental contaminants". *Chemosphere* **71**(1) (2008) 90–96.

[12] **X. Li and W. Zhang**. "Iron nanoparticles: the core-shell structure and unique properties for Ni(II) sequestration". *Langmuir* **22**(10) (2006) 4638–4642.

[13] **J. A. Rodriguez, J. C. Hanson, D. Stacchiola and S. D. Senanayake**. "*In situ/operando* studies for the production of hydrogen through the water-gas shift on metal oxide catalysts." *Phys. Chem. Chem. Phys.* **15**(29) (2013) 12004–25.

[14] **A. D. Abid, M. Kanematsu, T. M. Young and I. M. Kennedy**. "Arsenic removal from water using flame-synthesized iron oxide nanoparticles with variable oxidation states". *Aerosol Sci. Technol. J. Am. Assoc. Aerosol Res.* **47**(2) (2013) 169–176.

[15] **A. G. Roca, R. Costo, A. F. Rebolledo, S. Veintemillas-Verdaguer, P. Tartaj, T. González-Carreño, M. P. Morales and C. J. Serna**. "Progress in the preparation of magnetic nanoparticles for applications in biomedicine". *J. Phys. D. Appl. Phys.* **42**(22) (2009) 224002.

[16] **Z. P. Xu, Q. H. Zeng, G. Q. Lu and A. B. Yu**. "Inorganic nanoparticles as carriers for efficient cellular delivery". *Chem. Eng. Sci.* **61**(3) (2006) 1027–1040.

[17] **Y. Sun, S. Walspurger, J.-P. Tessonnier, B. Louis and J. Sommer**. "Highly dispersed iron oxide nanoclusters supported on ordered mesoporous SBA-15: A very active catalyst for Friedel-Crafts alkylations". *Appl. Catal. A Gen.* **300**(1) (2006) 1–7.

[18] **A. L.-T. Pham, C. Lee, F. M. Doyle and D. L. Sedlak**. "A silica-supported iron oxide catalyst capable of activating hydrogen peroxide at neutral pH values". *Environ. Sci. Technol.* **43**(23) (2009) 1–6.

[19] **M. Hermanek, R. Zboril, I. Medrik, J. Pechousek and C. Gregor**. "Catalytic efficiency of iron(III) oxides in decomposition of hydrogen peroxide: competition between the surface area and crystallinity of nanoparticles". *J. Am. Chem. Soc.* **129**(35) (2007) 10929–10936.

[20] **C. Li, Y. Shen, M. Jia, S. Sheng, M. O. Adebajo and H. Zhu**. "Catalytic combustion of formaldehyde on gold/iron-oxide catalysts". *Catal. Commun.* **9**(3) (2008) 355–361.

[21] **A. Kayo**. "The effect of preparation method on the acidic and catalytic properties of iron oxide". *J. Catal.* **83**(1) (1983) 99–106.

[22] **M. Baldi, V. S. Escribano, J. M. G. Amores, F. Milella and G. Busca**. "Characterization of manganese and iron oxides as combustion catalysts for propane and propene". *Appl. Catal. B Environ.* **17**(3) (1998) 175–182.

[23] **F. Fischer and H. Tropsch**. "The synthesis of petroleum at atmospheric pressures from gasification products of coal". *Brennst. Chemie* **7** (1926) 97.

[24] **M. E. Dry**. "The Fischer-Tropsch process: 1950-2000". *Catal. Today* **71**(3-4) (2002) 227–241.

[25] **H. Dlamini, T. Motjope, G. Joorst, G. ter Stege and M. Mdleleni**. "Changes in physico-chemical properties of iron-based Fischer-Tropsch catalyst induced by SiO_2 addition". *Catal. Letters* **78**(1-4) (2002) 201–207.

[26] **K. Jothimurugesan, J. J. Spivey, S. K. Gangwal and J. G. Goodwin Jr.** "Effect of silica on iron-based Fischer-Tropsch catalysts". *Stud. Surf. Sci. Catal.* **119** (1998) 215–220.

[27] **C. R. F. Lund and J. A. Dumesic**. "Strong oxide-oxide interactions in silica-cupported magnetite catalysts. 1. X-ray diffraction and Mössbauer spectroscopy evidence for interaction". *J. Phys. Chem.* **85**(21) (1981) 3175–3180.

[28] **G. Bergerhoff and I. D. Brown**. *Crystallographic Databases*. International Union of Crystallography, Chester (1987).

[29] **A. Belkly, M. Helderman, V. L. Karen and P. Ulkch**. "New developments in the Inorganic Crystal Structure Database (ICSD): Accessibility in support of materials research and design". *Acta Crystallogr. Sect. B Struct. Sci.* **58**(3) (2002) 364–369.

[30] **K. Momma and F. Izumi**. "VESTA 3 for three-dimensional visualization of crystal, volumetric and morphology data". *J. Appl. Crystallogr.* **44**(6) (2011) 1272–1276.

[31] **T. Danno, D. Nakatsuka, Y. Kusano, H. Asaoka, M. Nakanishi, T. Fujii, Y. Ikeda and J. Takada**. "Crystal structure of β-Fe_2O_3 and topotactic phase transformation to α-Fe_2O_3". *Cryst. Growth & Des.* **13**(2) (2013) 770–774.

[32] **J. R. Smyth**. "High temperature crystal chemistry of fayalite". *Am. Minerol.* **60**(2) (1975) 1092–1097.

[33] **L. Pauling and S. B. Hendricks**. "The crystal structures of hematite and corundum". *J. Am. Chem. Soc.* **47**(3) (1925) 781–790.

[34] **R. L. Blake, R. E. Hessevick, T. Zoltai and L. W. Finger**. "Refinement of the hematite structure". *Am. Minerol.* **51**(1-2) (1966) 123–129.

[35] **K. Kelm and W. Mader**. "Synthesis and structural analysis of ϵ-Fe_2O_3". *Zeitschrift für Anorg. und Allg. Chemie* **631**(12) (2005) 2383–2389.

[36] **C. G. Shull, W. A. Strauser and E. O. Wollan**. "Neutron diffraction by paramagnetic and antiferromagnetic substances". *Phys. Rev.* **83**(2) (1951) 333–345.

[37] **J. O. Artman, J. C. Murphy and S. Foner**. "Magnetic anisotropy in antiferromagnetic corundum-type sesquioxides". *Phys. Rev.* **138**(3A) (1965) A912–A917.

[38] **J. M. D. Coey and G. A. Sawatzky**. "A study of hyperfine interactions in the system $(Fe_{1-x}Rh_x)_2O_3$, using the Mössbauer effect". *J. Phys. C Solid State Phys.* **4** (1971) 2386–2407.

[39] **F. Bødker, M. Hansen, C. Koch, K. Lefmann, S. Mørup, F. Bødker and S. Mørup**. "Magnetic properties of hematite nanoparticles". *Phys. Rev. B* **61**(10) (2000) 6826–6838.

[40] **J. D. Bernal, D. R. Dasgupta and A. L. Mackay**. "The oxides and hydroxides of iron and their structural inter-relationships". *Clay Miner. Bull.* **4**(21) (1959) 15–30.

[41] **G. W. van Oosterhout and C. J. M. Rooijmans**. "A new superstructure in gamma-ferric oxide". *Nature* **181**(4601) (1958) 44.

[42] **J.-E. Jørgensen, L. Mosegaard, L. E. Thomsen, T. R. Jensen, J. C. Hanson and J.-E. Jørgensen**. "Formation of γ-Fe_2O_3 nanoparticles and vacancy ordering: An in situ X-ray powder diffraction study". *J. Solid State Chem.* **180**(1) (2007) 180–185.

[43] **E. Murad**. "Magnetic properties of microcrystalline iron(III) oxides and related materials as reflected in their Mössbauer spectra". *Phys. Chem. Miner.* **23**(4-5) (1996) 248–262.

[44] **S. S.-J. Lee**. "The spin structure of maghemite investigated by ^{57}Fe NMR". *New J. Phys.* **8**(6) (2006) 98–98.

[45] **J. M. D. Coey and D. Khalafalla**. "Superparamagnetic γ-Fe_2O_3". *Phys. Status Solidi* **11**(1) (1972) 229–241.

[46] **J. L. Jambor and J. E. Dutrizac**. "Occurrence and constitution of natural and synthetic ferrihydrite, a widespread iron oxyhydroxide". *Chem. Rev.* **98**(7) (1998) 2549–2586.

[47] **D. Janney, J. Cowley and P. Buseck**. "Structure of synthetic 2-line ferrihydrite by electron nanodiffraction". *Am. Mineral.* **85**(8-9) (2000) 1180–1187.

[48] **D. E. Janney, J. M. Cowley and P. R. Buseck**. "Transmission electron microscopy of synthetic 2- and 6-line ferrihydrite". *Clays Clay Miner.* **48**(1) (2000) 111–119.

[49] **D. Janney, J. Cowley and P. Buseck**. "Structure of synthetic 6-line ferrihydrite by electron nanodiffraction". *Am. Mineral.* **86**(2-3) (2001) 327–335.

[50] **K. M. Towe and W. F. Bradley**. "Mineralogical constitution of colloidal "hydrous ferric oxides"". *J. Colloid Interface Sci.* **24**(3) (1967) 384–392.

[51] **F. V. Chukhov, B. B. Zvyagin, A. I. Gorshkov, L. P. Yermilova and V. V. Balashova**. "Ferrihydrite". *Int. Geol. Rev.* **16**(10) (1974) 1131–1143.

[52] **V. A. Drits, B. A. Sakharov, A. L. Salyn and A. Manceau**. "Structural model for ferrihydrite". *Clay Miner.* **28**(2) (1993) 185–207.

[53] **F. M. Michel, L. Ehm, S. M. Antao, P. L. Lee, P. J. Chupas, G. Liu, D. R. Strongin, M. A. A. Schoonen, B. L. Phillips and J. B. Parise**. "The structure of ferrihydrite, a nanocrystalline material". *Science* **316**(5832) (2007) 1726–1729.

[54] **W. H. Casey**. "Large aqueous aluminum hydroxide molecules." *Chem. Rev.* **106**(1) (2006) 1–16.

[55] **S. Bali, G. Bali, F. E. Huggins, M. S. Seehra, V. Singh, J. M. Hancock, R. Harrison, G. P. Huffman, R. J. Pugmire, R. D. Ernst and E. M. Eyring**. "Synthetic doped amorphous ferrihydrite for the Fischer-Tropsch synthesis of alternative fuels". *Ind. Eng. Chem. Res.* **51**(12) (2012) 4515–4522.

[56] **M. B. Madsen, S. Mørup and C. J. W. Koch**. "Magnetic properties of ferrihydrite". *Hyperfine Interact.* **27** (1986) 329–332.

[57] **M. Seehra, V. Babu, A. Manivannan and J. Lynn**. "Neutron scattering and magnetic studies of ferrihydrite nanoparticles". *Phys. Rev. B* **61**(5) (2000) 3513–3518.

[58] **R. J. Hill, J. R. Craig and G. V. Gibbs**. "Systematics of the spinel structure type". *Phys. Chem. Miner.* **4**(4) (1979) 317–339.

[59] **W. H. Bragg**. "The structure of magnetite and the spinels". *Nature* **95**(2386) (1915) 561.

[60] **Z. Cvejic, S. Rakic, A. Kremenovic, B. Antic, C. Jovalekic and P. Colomban**. "Nanosize ferrites obtained by ball milling: crystal structure, cation distribution, size-strain analysis and Raman investigations". *Solid State Sci.* **8**(8) (2006) 908–915.

[61] **R. W. G. Wyckoff and E. D. Crittenden**. "The preparation and crystal structure of ferrous oxide". *J. Am. Chem. Soc.* **47**(12) (1925) 2876–2882.

[62] **H. Fjellvåg, F. Grønvold, S. Stølen and B. Hauback**. "On the crystallographic and magnetic structures of nearly stoichiometric iron monoxide". *J. Solid State Chem.* **124**(1) (1996) 52–57.

[63] **L. von Bogdandy and H. Engell**. *The Reduction of Iron Ores: Scientific Basis and Technology.* First edition. Springer-Verlag Berlin Heidelberg GmbH, Düsseldorf (1971).

[64] **P. D. Battle and A. K. Cheetham**. "The magnetic structure of non-stoichiometric ferrous oxide". *J. Phys. C Solid State Phys.* **12**(2) (1979) 337.

[65] **F. Princivalle and L. Secco**. "Crystal structure refinement of 13 olivines in the forsterite-fayalite series from volcanic rocks and ultramafic nodules". *TMPM Tschermaks Mineral. und Petrogr. Mitteilungen* **34**(2) (1985) 105–115.

[66] **Y. Matsui and Y. Syono**. "Unit cell dimensions of some synthetic olivine group solid solutions". *Geochem. J.* **2** (1968) 51–59.

[67] **G. Nover and G. Will**. "Structure refinements of seven natural olivine crystals and the influence of the oxygen partial pressure on the cation distribution". *Zeitschrift für Krist.* **155**(1-2) (1981) 27–45.

[68] **R. Santoro, R. Newnham and S. Nomura**. "Magnetic properties of Mn_2SiO_4 and Fe_2SiO_4". *J. Phys. Chem. Solids* **27**(4) (1966) 655–666.

[69] **M. Cococcioni, A. Dal Corso and S. de Gironcoli**. "Structural, electronic, and magnetic properties of Fe_2SiO_4 fayalite: Comparison of LDA and GGA results". *Phys. Rev. B* **67**(9) (2003) 094106.

[70] **J. D. Bernal and A. L. Mackay**. "Topotaxy". *Tschermaks Mineral. und Petrogr. Mitteilungen* **10**(1-4) (1965) 331–340.

[71] **M. A. Blesa and E. Matijević**. "Phase transformations of iron oxides, oxohydroxides, and hydrous oxides in aqueous media". *Adv. Colloid Interface Sci.* **29**(3-4) (1989) 173–221.

[72] **M. Sastri, R. Viswanath and B. Viswanathan**. "Studies on the reduction of iron oxide with hydrogen". *Int. J. Hydrogen Energy* **7**(12) (1982) 951–955.

[73] **O. J. Wimmers, P. Arnoldy and J. A. Moulijn**. "Determination of the reduction mechanism by temperature-programmed reduction: application to small Fe_2O_3 particles". *J. Phys. Chem* **90**(1963) (1986) 1331–1337.

[74] **Y. Jin and A. K. Datye**. "Phase transformations in iron Fischer-Tropsch catalysts during temperature-programmed reduction". *J. Catal.* **196**(1) (2000) 8–17.

[75] **H.-Y. Lin, Y.-W. Chen and C. Li**. "The mechanism of reduction of iron oxide by hydrogen". *Thermochim. Acta* **400**(1-2) (2003) 61–67.

[76] **P. Pourghahramani and E. Forssberg**. "Reduction kinetics of mechanically activated hematite concentrate with hydrogen gas using nonisothermal methods". *Thermochim. Acta* **454**(2) (2007) 69–77.

[77] **W. Jozwiak, E. Kaczmarek, T. Maniecki, W. Ignaczak and W. Maniukiewicz**. "Reduction behavior of iron oxides in hydrogen and carbon monoxide atmospheres". *Appl. Catal. A Gen.* **326**(1) (2007) 17–27.

[78] **C. Messi, P. Carniti and A. Gervasini**. "Kinetics of reduction of supported nanoparticles of iron oxide". *J. Therm. Anal. Calorim.* **91**(1) (2008) 93–100.

[79] **G. Munteanu, L. Ilieva and D. Andreeva**. "Kinetic parameters obtained from TPR data for α-Fe_2O_3 and Au/α-Fe_2O_3 systems". *Thermochim. Acta* **291**(1-2) (1997) 171–177.

[80] **G. Munteanu, L. Ilieva and D. Andreeva**. "TPR data regarding the effect of sulfur on the reducibility of α-Fe_2O_3". *Thermochim. Acta* **329**(2) (1999) 157–162.

[81] **A. Pineau, N. Kanari and I. Gaballah**. "Kinetics of reduction of iron oxides by H_2. Part I: Low temperature reduction of hematite". *Thermochim. Acta* **447**(1) (2006) 89–100.

[82] **J. Zieliński, I. Zglinicka, L. Znak and Z. Kaszkur**. "Reduction of Fe_2O_3 with hydrogen". *Appl. Catal. A Gen.* **381**(1-2) (2010) 191–196.

[83] **A. J. H. M. Kock, H. M. Fortuin, J. W. Geus and O. F. Catalysis**. "The reduction behavior of supported iron catalysts in in hydrogen or carbon monoxide atmospheres". *J. Catal.* **96**(1) (1985) 261–275.

[84] **A. F. H. Wielers, A. J. H. M. Kock, C. E. C. A. Hop, J. W. Gues and A. M. van der Kraan**. "The reduction behavior of silica-supported and alumina-supported iron catalysts: A Mössbauer and infrared spectroscopic study". *J. Catal.* **117**(1) (1989) 1–18.

[85] **D. B. Bukur and C. Sivaraj**. "Supported iron catalysts for slurry phase Fischer-Tropsch synthesis". *Appl. Catal. A Gen.* **231**(1-2) (2002) 201–214.

[86] **H. Suo, S. Wang, C. Zhang, J. Xu, B. Wu, Y. Yang, H. Xiang and Y.-W. Li**. "Chemical and structural effects of silica in iron-based Fischer-Tropsch synthesis catalysts". *J. Catal.* **286** (2012) 111–123.

[87] **C. J. Masina**. *Structural analysis of synthetic ferrihydrite nanoparticles and its reduction in a hydrogen atmosphere.* Ph.D. thesis, Nelson Mandela Metropolitan University (2014).

[88] **S. Shafiee and E. Topal**. "When will fossil fuel reserves be diminished?" *Energy Policy* **37**(1) (2009) 181–189.

[89] **D. O. Uner**. "A sensible mechanism of alkali promotion in Fischer-Tropsch synthesis: adsorbate mobilities". *Ind. Eng. Chem. Res.* **37**(6) (1998) 2239–2245.

[90] **M. E. Dry**. "The Fischer-Tropsch process - commercial aspects". *Catal. Today* **6**(3) (1990) 183–206.

[91] **M. E. Dry**. "Practical and theoretical aspects of the catalytic Fischer-Tropsch process". *Appl. Catal. A Gen.* **138**(2) (1996) 319–344.

[92] **A. Steynberg and M. Dry**. *Fischer-Tropsch Technology.* First edition. Elsevier B.V., Amsterdam (2004).

[93] **L. C. Browning and P. H. Emmett**. "Equilibrium measurements in the NiC-Ni-CH-H and CoC-Co-CH-H systems". *J. Am. Chem. Soc.* **74**(7) (1952) 1680.

[94] **J. Kummer and P. H. Emmett**. "Fischer-Tropsch synthesis mechanism studies. The addition of radioactive alcohols to the synthesis gas". *J. Am. Chem. Soc.* **75**(21) (1953) 5177–5183.

[95] **M. Dry**. "Catalytic aspects of industrial Fischer-Tropsch synthesis". *J. Mol. Catal.* **17**(2-3) (1982) 133–144.

[96] **P. Biloen, J. N. Helle and W. M. H. Sachtler**. "Incorporation of surface carbon into hydrocarbons during Fischer-Tropsch synthesis: mechanistic implications". *J. Catal.* **58**(1) (1979) 95–107.

[97] **M. Ojeda, R. Nabar, A. U. Nilekar, A. Ishikawa, M. Mavrikakis and E. Iglesia**. "CO activation pathways and the mechanism of Fischer-Tropsch synthesis". *J. Catal.* **272**(2) (2010) 287–297.

[98] **D. Bibby, C. Chang, R. Howe and S. Yurchak** (editors). *Methane Conversion.* First edition. Elsevier Science Publishers B.V., Amsterdam (1988).

[99] **J. S. Jung, S. W. Kim and D. J. Moon**. "Fischer-Tropsch synthesis over cobalt based catalyst supported on different mesoporous silica". *Catal. Today* **185**(1) (2012) 168–174.

[100] **M. D. Shroff, D. S. Kalakkad, K. E. Coulter, S. D. Köhler, M. S. Harrington, N. B. Jackson, A. G. Sault and A. K. Datye**. "Activation of precipitated iron Fischer-Tropsch synthesis catalysts". *J. Catal.* **156**(2) (1995) 185–207.

[101] **D. S. Kalakkad, M. D. Shroff, S. Köhler, N. Jackson and A. K. Datye**. "Attrition of precipitated iron Fischer-Tropsch catalysts". *Appl. Catal. A, Gen.* **133**(2) (1995) 335–350.

[102] **D. B. Bukur, X. Lang and Y. Ding**. "Pretreatment effect studies with a precipitated iron Fischer-Tropsch catalyst in a slurry reactor". *Appl. Catal. A Gen.* **186**(1-2) (1999) 255–275.

[103] **D. B. Bukur, L. Nowicki, R. K. Manne and X. Lang**. "Activation studies with a precipitated iron catalyst for Fischer-Tropsch synthesis II. Reaction studies". *J. Catal.* **155**(2) (1995) 366–375.

[104] **D. B. Bukur, X. Lang, J. A. Rossin, W. H. Zimmerman, M. P. Rosynek, E. B. Yeh and C. Lil**. "Activation studies with a promoted precipitated iron Fischer-Tropsch catalyst". *Ind. Eng. Chem. Res.* **28**(8) (1989) 1130–1140.

[105] **H. Hayakawa, H. Tanaka and K. Fujimoto**. "Studies on precipitated iron catalysts for Fischer-Tropsch synthesis". *Appl. Catal. A Gen.* **310** (2006) 24–30.

[106] **W. Ngantsoue-Hoc, Y. Zhang, R. J. O. Brien, M. Luo and B. H. Davis**. "Fischer-Tropsch synthesis: activity and selectivity for group I alkali promoted iron-based catalysts". *Appl. Catal. A Gen.* **236**(1-2) (2002) 77–89.

[107] **S. Li, S. Krishnamoorthy, A. Li, G. D. Meitzner and E. Iglesia**. "Promoted iron-based catalysts for the FischerTropsch synthesis: design, synthesis, site densities, and catalytic properties". *J. Catal.* **206**(2) (2002) 202–217.

[108] **D. S. Newsome**. "The water-gas shift reaction". *Catal. Rev.* **21**(2) (1980) 275–318.

[109] **C. H. Bartholemew, R. B. Pannell and J. L. Butler**. "Support and crystallite size effects in CO hydrogenation on nickel". *J. Catal.* **65**(2) (1980) 335–347.

[110] **G. Zhao, C. Zhang, S. Qin, H. Xiang and Y. Li**. "Effect of interaction between potassium and structural promoters on Fischer-Tropsch performance in iron-based catalysts". *J. Mol. Catal. A Chem.* **286**(1-2) (2008) 137–142.

[111] **G. Maiti, R. Malessa and M. Baerns**. "Iron/manganese oxide catalysts for Fischer-Tropsch synthesis". *Appl. Catal.* **5**(2) (1983) 151–170.

[112] **H. Hayakawa, H. Tanaka and K. Fujimoto**. "Studies on catalytic performance of precipitated iron/silica catalysts for Fischer-Tropsch synthesis". *Appl. Catal. A Gen.* **328**(2) (2007) 117–123.

[113] **Y. Yang, H. W. Xiang, L. Tian, H. Wang, C. H. Zhang, Z. C. Tao, Y. Y. Xu, B. Zhong and Y. W. Li**. "Structure and Fischer-Tropsch performance of iron-manganese catalyst incorporated with SiO_2". *Appl. Catal. A Gen.* **284**(1-2) (2005) 105–122.

[114] **M. Luo, R. O'Brien and B. H. Davis**. "Effect of palladium on iron Fischer-Tropsch synthesis catalysts". *Catal. Letters* **98**(1) (2004) 17–22.

[115] **R. J. O'Brien, L. Xu, R. L. Spicer, S. Bao, D. R. Milburn and B. H. Davis**. "Activity and selectivity of precipitated iron Fischer-Tropsch catalysts". *Catal. Today* **36**(3) (1997) 325–334.

[116] **J. Xu, C. H. Bartholomew, J. Sudweeks and D. L. Eggett**. "Design, synthesis, and catalytic properties of silica-supported, Pt-promoted iron Fischer-Tropsch catalysts". *Top. Catal.* **26**(1-4) (2003) 55–71.

[117] **G. Zhao, C. Zhang, S. Qin, H. Xiang and Y. Li**. "Effect of interaction between potassium and structural promoters on Fischer-Tropsch performance in iron-based catalysts". *J. Mol. Catal. A Chem.* **286**(1-2) (2008) 137–142.

[118] **A. P. Raje, R. J. O'Brien and B. H. Davis**. "Effect of potassium promotion on iron-based catalysts for Fischer-Tropsch synthesis". *J. Catal.* **180**(1) (1998) 36–43.

[119] **T. Riedel, M. Claeys, H. Schulz, G. Schaub, S.-S. Nam, K.-W. Jun, M.-J. Choi, G. Kishan and K.-W. Lee**. "Comparative study of

Fischer-Tropsch synthesis with H_2/CO and H_2/CO_2 syngas using Fe- and Co-based catalysts". *Appl. Catal. A Gen.* **186**(1-2) (1999) 201–213.

[120] **S. Li, A. Li, S. Krishnamoorthy and E. Iglesia**. "Effects of Zn, Cu, and K promoters on the structure and on the reduction, carburization, and catalytic behavior of iron-based Fischer-Tropsch synthesis catalysts". *Catal. Letters* **77**(4) (2001) 197–205.

[121] **S. J. Tauster, S. C. Fung and R. L. Garten**. "Strong metal-support interactions. Group 8 noble metals supported on TiO_2". *J. Am. Chem. Soc.* **100**(1) (1978) 170–175.

[122] **J. Santos, J. Phillips and J. A. Dumesic**. "Metal-support interactions between iron and titania for catalysts prepared by thermal decomposition of iron pentacarbonyl and by impregnation". *J. Catal.* **81**(1) (1983) 147–167.

[123] **R. T. K. Baker, E. B. Prestridge and R. L. Garten**. "Electron microscopy of supported metal particles: I. Behavior of Pt on titanium oxide, aluminum oxide, silicon oxide, and carbon". *J. Catal.* **56**(3) (1979) 390–406.

[124] **E. J. Braunschweig, A. D. Logan, A. K. Datye and D. J. Smith**. "Reversibility of strong metal-support interactions on Rh/TiO_2". *J. Catal.* **118**(1) (1989) 227–237.

[125] **T. Komaya, A. Bell, Z. Wengsieh, R. Gronsky, F. Engelke, T. King and M. Pruski**. "The influence of metal-support interactions on the accurate determination of Ru dispersion for Ru/TiO_2". *J. Catal.* **149**(1) (1994) 142–148.

[126] **A. K. Datye, D. S. Kalakkad, M. H. Yao and D. J. Smith**. "Comparison of metal-support interactions in Pt/TiO_2 and Pt/CeO_2". *J. Catal.* **155**(1) (1995) 148–153.

[127] **J. Cunningham, D. Culinane, F. Farell, M. A. Morris, A. Datye and D. Lalakkad**. "Changes in microstructure and catalytic activity effected by redox cycling of rhodium upon CeO_2 and Al_2O_3". *Stud. Surf. Sci. Catal.* **96** (1995) 237–248.

[128] **K. Sun, J. Liu, N. Nag and N. D. Browning**. "Studying the metal-support interaction in Pd/γ-Al_2O_3 catalysts by atomic-resolution electron energy-loss spectroscopy". *Catal. Letters* **84**(3-4) (2002) 193–199.

[129] **M. Kohyama, S. Kose, M. Kinoshita and R. Yamamoto**. "Electronic structure calculations of transition metal-alumina interfaces". *J. Phys. Chem. Solids* **53**(3) (1992) 345–354.

[130] **A. Katrib, C. Petit, P. Légaré, L. Hilaire and G. Maire**. "An investigation of metal-support interaction in bimetallic Pt-Mo catalysts deposited on silica and alumina". *Surf. Sci.* **189-190** (1987) 886–893.

[131] **R. Lamber**. "On the metal-support interaction in the Ni-SiO_2 system". *Surf. Sci.* **227**(3) (1990) 268–272.

[132] **R. Lamber and W. Romanowski**. "Dispersion changes of platinum supported on silica glass during thermal treatment in oxygen and hydrogen atmospheres". *J. Catal.* **105**(1) (1987) 213–226.

[133] **L.-L. Sheu, Z. Karpinksi and W. M. H. Sachtler**. "Effects of palladium particle size and palladium silicide formation on fourier transform infrared spectra of CO adsorbed on Pd/SiO_2 catalysts". *J. Phys. Chem.* **93**(12) (1989) 4890–4894.

[134] **W. Juszczyk and Z. Karpiński**. "Characterization of supported palladium catalysts: II. Pd/SiO_2". *J. Catal.* **117**(2) (1989) 519–532.

[135] **C. R. F. Lundt and J. A. Dumeslc**. "Strong oxide-oxide interactions In silica-supported magnetite catalysts. 2. The core/shell nature of the interaction". *J. Phys. Chem.* **86**(1) (1982) 130–135.

[136] **C. R. F. Lund and J. A. Dumesic**. "Strong oxide-oxide interactions in silica-supported magnetite catalysts: IV. Catalytic consequences of the interaction in water-gas shift". *J. Catal.* **76**(1) (1982) 93–100.

[137] **C. R. F. Lund and J. A. Dumesic**. "Strong oxide-oxide interactions in silica-supported Fe_3O_4: III. Water-induced migration of silica on geometrically designed catalysts". *J. Catal.* **72**(1) (1981) 21–30.

[138] **S. Yuen, Y. Chen, J. E. Kubsh and J. A. Dumeslc**. "Metal oxide-support interactions in silica-supported iron oxide catalysts probed by nitric oxide adsorption". *J. Phys. Chem.* **86**(15) (1982) 3022–3032.

[139] **M. V. Cagnoli, S. G. Marchetti, N. G. Gallegos, A. M. Alvarez, R. C. Mercader and A. A. Yeramian**. "Influence of the support on the activity and selectivity of high dispersion Fe catalysts in the Fischer-Tropsch reaction". *J. Catal.* **123**(1) (1990) 21–30.

[140] **C.-H. Zhang, H.-J. Wan, Y. Yang, H.-W. Xiang and Y.-W. Li**. "Study on the iron-silica interaction of a co-precipitated Fe/SiO_2 Fischer-Tropsch synthesis catalyst". *Catal. Commun.* **7**(9) (2006) 733–738.

[141] **C. C. Massieon, A. H. Cutler and F. Shadman**. "Hydrogen reduction of iron-bearing silicates". *Ind. Eng. Chem. Res.* **32**(6) (1993) 1239–1244.

[142] **E. de Smit, I. Swart, J. F. Creemer, G. H. Hoveling, M. K. Gilles, T. Tyliszczak, P. J. Kooyman, H. W. Zandbergen, C. Morin, B. M. Weckhuysen and F. M. F. de Groot**. "Nanoscale chemical imaging of a working catalyst by scanning transmission X-ray microscopy". *Nature* **456**(7219) (2008) 222–225.

[143] **M. Qing, Y. Yang, B. Wu, J. Xu, C. Zhang, P. Gao and Y. Li**. "Modification of Fe-SiO_2 interaction with zirconia for iron-based Fischer-Tropsch catalysts". *J. Catal.* **279**(1) (2011) 111–122.

[144] **S. Qin, C. Zhang, J. Xu, Y. Yang, H. Xiang and Y. Li**. "Fe-Mo interactions and their influence on Fischer-Tropsch synthesis performance". *Appl. Catal. A Gen.* **392**(1-2) (2011) 118–126.

[145] **P. Fabrizioli, T. Bürgi, M. Burgener, S. van Doorslaer and A. Baiker**. "Synthesis, structural and chemical properties of iron oxidesilica aerogels". *J. Mater. Chem.* **12**(3) (2002) 619–630.

[146] **S. Bruni, F. Cariati, M. Casu, A. Lai, A. Musinu, G. Piccaluga, S. Solinas, S. Chimiche and C. Cagliari**. "IR and NMR study of nanoparticle-support interactions in a Fe_2O_3-SiO_2 nanocomposite prepared by a sol-gel method". *Nanostructured Mater.* **11**(5) (1999) 573–586.

[147] **J. Zhan, T. Zheng, G. Piringer, C. Day, G. L. Mcpherson, Y. Lu, K. Papadopoulos and V. T. John**. "Transport characteristics of nanoscale functional zerovalent iron/silica composites for in situ remediation of trichloroethylene". *Environ. Sci. Technol.* **42**(23) (2008) 8871–8876.

[148] **S. Kato, C. Kobayashi, T. Kakegawa and A. Yamagishi**. "Microbial communities in iron-silica-rich microbial mats at deep-sea hydrothermal fields of the Southern Mariana Trough". *Environ. Microbiol.* **11**(8) (2009) 2094–2111.

[149] **P. R. Anderson and M. M. Benjamin**. "Effects of silicon on the crystallization and adsorption properties of ferric oxides". *Environ. Sci. Technol.* **19**(11) (1985) 1048–1053.

[150] **K. O. Konhauser and F. G. Ferris**. "Diversity of iron and silica precipitation by microbial mats in hydrothermal waters, Iceland: implications for precambrian iron formations". *Geology* **24**(4) (1996) 323–326.

[151] **L. Carlson and U. Schwertmann**. "Natural ferrihydrites in surface deposits from Finland and their association with silica". *Geochim. Cosmochim. Acta* **45**(3) (1981) 421–429.

[152] **R. N. Sylva**. "Hydrolysis of iron(III)". *Rev. Pure Appl. Chem.* **22**(Dec) (1972) 115–132.

[153] **U. Schwertmann and R. M. Cornell**. *Iron Oxides in the Laboratory.* Second edition. Wiley-VCH Verlag GmbH, Weinheim (1993).

[154] **G. S. Pokrovski, J. Schott, F. Farges and J.-L. Hazemann**. "Iron (III)-silica interactions in aqueous solution: insights from X-ray absorption fine structure spectroscopy". *Geochim. Cosmochim. Acta* **67**(19) (2003) 3559–3573.

[155] **L. Dyer, P. D. Fawell, O. M. G. Newman and W. R. Richmond**. "Synthesis and characterisation of ferrihydrite/silica co-precipitates". *J. Colloid Interface Sci.* **348**(1) (2010) 65–70.

[156] **A. C. Cismasu, F. M. Michel, A. P. Tcaciuc and G. E. Brown**. "Properties of impurity-bearing ferrihydrite III. Effects of Si on the structure of 2-line ferrihydrite". *Geochim. Cosmochim. Acta* **133** (2014) 168–185.

[157] **M. M. Woolfson**. *An Introduction to X-ray Crystallography*. Second edition. Cambridge University Press, Cambridge (1997).

[158] **Ervin Hartmann**. *An Introduction to Crystal Optics*. First edition. University College Cardiff Press, Cardiff (1984).

[159] **P. P. Ewald** (editor). *X-Ray Years of Diffraction*. First edition. N. V. A. Ossthoek's Uitgeversmaatschappij, Utrecht (1962).

[160] **J. P. Glusker**. *Elementary X-Ray Diffraction For Biologists*. First edition. University College Cardiff Press, Cardiff (1984).

[161] **B. D. Cullity**. *Elements of X-ray Diffraction*. First edition. Addison-Wesley Publishing Company Inc., Reading (1978).

[162] **D. B. Williams and B. Carter**. *Transmission Electron Microscopy*. First edition. Plenum Publishing Corporation, New York (1996).

[163] **M. de Graef**. *Introduction to Conventional Transmission Electron Microscopy*. First edition. Cambridge University Press, Cambridge (2003).

[164] **L. Reimer and H. Kohl**. *Transmission Electron Microscopy: Physics of Image Formation*. Fifth edition. Springer Science+Business Media, LLC, New York (2008).

[165] **R. Brydson** (editor). *Aberration-Corrected Analytical Transmission Electron Microscopy*. First edition. John Wiley & Sons Ltd. (2011).

[166] **M. Haider, G. Braunshausen and E. Schwan**. "Correction of the spherical aberration of a 200 kV TEM by means of a hexapole-corrector". *Optik (Stuttg)*. **99**(4) (1995) 167–179.

[167] **M. Haider, H. Rose, S. Uhlemann, E. Schwan, B. Kabius and K. Urban**. "A spherical-aberration-corrected 200kV transmission electron microscope". *Ultramicroscopy* **75**(1) (1998) 53–60.

[168] **J. B. Wagner, F. Cavalca, C. D. Damsgaard, L. D. L. Duchstein and T. W. Hansen**. "Exploring the environmental transmission electron microscope". *Micron* **43**(11) (2012) 1169–1175.

[169] **R. F. Egerton, P. Li and M. Malac**. "Radiation damage in the TEM and SEM". *Micron* **35**(6) (2004) 399–409.

[170] **R. F. Egerton**. "Mechanisms of radiation damage in beam-sensitive specimens, for TEM accelerating voltages between 10 and 300 kV." *Microsc. Res. Tech.* **75**(11) (2012) 1550–6.

[171] **R. F. Egerton**. "Control of radiation damage in the TEM". *Ultramicroscopy* **127** (2013) 100–108.

[172] **E. Boyes and P. Gai**. "Environmental high resolution electron microscopy and applications to chemical science". *Ultramicroscopy* **67**(1-4) (1997) 219–232.

[173] **R. Sharma and K. Weiss**. "Development of a TEM to study *in situ* structural and chemical changes at an atomic level during gas-solid interactions at elevated temperatures". *Microsc. Res. Tech.* **42**(4) (1998) 270–280.

[174] **E. P. Butler and K. F. Hale**. *Dynamic Experiments in the Electron Microscope*. First edition. North-Holland Publishing Company, Amsterdam (1981).

[175] **T. W. Hansen and J. B. Wagner**. "Environmental transmission electron microscopy in an aberration-corrected environment". *Microsc. Microanal.* **18**(4) (2012) 684–690.

[176] **H. L. Xin, K. Niu, D. H. Alsem and H. Zheng**. "*In situ* TEM study of catalytic nanoparticle reactions in atmospheric pressure gas environment". *Microsc. Microanal.* **19**(6) (2013) 1558–1568.

[177] **N. de Jonge, W. C. Bigelow and G. M. Veith**. "Atmospheric pressure scanning transmission electron microscopy". *Nano Lett.* **10**(3) (2010) 1028–1031.

[178] **W. Chuang and T. Luger**. "Mechanical property characterization of LPCVD silicon nitride thin films at cryogenic temperatures". *J. Microelectromechanical Syst.* **13**(5) (2004) 870–879.

[179] **R. F. Egerton**. *Electron Energy-Loss Spectroscopy in the Electron Microscope*. Third edition. Springer Science+Business Media, LLC, New York (2011).

[180] **H. Ibach and D. Mills**. *Electron Energy Loss Spectroscopy and Surface Vibrations*. First edition. Academic Press, Inc., New York (1982).

[181] **R. F. Egerton**. "Electron energy-loss spectroscopy in the TEM". *Reports Prog. Phys.* **72**(1) (2009) 016502.

[182] **D. E. Newbury, D. C. Joy, P. Echlin, C. E. Fiori and J. I. Goldstein**. *Advanced Scanning Electron Microscopy and X-ray Microanalysis*. First edition. Springer Science+Business Media, LLC, New York (1986).

[183] **A. J. Garratt-Reed and D. C. Bell**. *Energy-dispersive X-ray analysis in the electron microscope*. First edition. BIOS Scientific Publishers Limited, Oxford (2003).

[184] **V. Kazmiruk** (editor). *Scanning Electron Microscopy*. First edition. Intech, Rijeka (2012).

[185] **T. G. Rochow and E. G. Rochow**. *An Introduction to Microscopy by Means of Light, Electrons, X-rays, or Ultrasound*. Second edition. Plenum Press, New York (1979).

[186] **R. L. Mössbauer**. "Kernresonanzfluoreszenz von Gammastrahlung in Ir191". *Zeitschrift für Phys.* **151**(2) (1958) 124–143.

[187] **G. K. Wertheim**. *Mössbauer Effect: Principles and Applications*. First edition. Academic Press, New York (1964).

[188] **H. R. H. Goldanskii**. *Chemical Applications of Mössbauer Spectroscopy*. First edition. Academic Press, New York (1968).

[189] **H. Lustig**. "The Mössbauer Effect". *Am. J. Phys.* **29**(1) (1961) 1.

[190] **G. J. Long**. *Mössbauer Spectroscopy Applied to Inorganic Chemistry*. First edition. Springer US, New York (1984).

[191] **E. Murad and J. Cashion**. *Mössbauer spectroscopy of Enviromental Materials and their Industrial Utilization.* First edition. Springer Science+Business Media, LLC, New York (2004).

[192] **L. May** (editor). *An Introduction to Mössbauer Spectroscopy.* Plenum Press, New York (1971).

[193] **G. Neyens**. "Nuclear magnetic and quadrupole moments for nuclear structure research on exotic nuclei". *Reports Prog. Phys.* **66**(4) (2003) 633–689.

[194] **M. Darby Dyar, D. G. Agresti, M. W. Schaefer, C. A. Grant and E. C. Sklute**. "Mössbauer spectroscopy of earth and planetary materials". *Annu. Rev. Earth Planet. Sci.* **34** (2006) 83–125.

[195] **E. Murad and J. Cashion**. *Mössbauer Spectroscopy of Environmental Materials and Their Industrial Utilization.* Springer Science+Business Media, LLC, New York (2004).

[196] **G. Osmond**. "Characterization of FeOOH polymorphs and ferrihydrite using low-temperature, applied-field, Mössbauer spectroscopy". *Clay Miner.* **27** (1992) 57–71.

[197] **O. C. Kistner and A. W. Sunyar**. "Excited states of Fe^{57} populated in Co^{57} decay". *Phys. Rev.* **139**(2B) (1964) B295–B299.

[198] **R. Subramanian**. *Mössbauer spectroscopy , nuclear inelastic scattering and density functional theory studies on oxobridged iron complexes and their reaction under Gif-type conditions.* Ph.D. thesis, Universität Stuttgart (2010).

[199] **R. Gerber, C. D. Wright and G. Asti** (editors). *Applied Magnetism.* First edition. Springer-Science+Business Media, B.V., Dordrecht (1994).

[200] **D. Wagner**. *Introduction to the Theory of Magnetism.* First edition. Pergamon Press, Oxford (1972).

[201] **K. H. J. Buschow and F. R. de Boer**. *Physics of Magnetism and Magnetic Materials.* First edition. Kluwer Academic Publishers, New York (2004).

[202] **R. L. Carlin**. *Magnetochemistry*. First edition. Springer-Verlag Berlin Heidelberg GmbH, Berlin (1986).

[203] **B. D. Cullity and C. D. Graham**. *Introduction to Magnetic Materials*. Second edition. John Wiley & Sons, Inc., Hoboken (2009).

[204] **L. Néel**. "Theory of magnetic viscosity of fine grained ferromagnetics with application to baked clays". *Ann. Geophys* **5**(41) (1949) 99–136.

[205] **J. B. Condon**. *Surface Area and Porosity Determinations by Physisorption Measurements and Theory*. First edition. Elsevier B.V., Amsterdam (2006).

[206] **K. H. J and Z. W. Gortel**. *Springer Series in Surface Sciences Volume 1: Physisorption Kinetics*. First edition. Springer-Verlag Berlin Heidelberg GmbH, Heidelberg (1986).

[207] **K. S. W. Sing**. "Reporting physisorption data for gas/solid systems with special reference to the determination of surface area and porosity (Recommendations 1984)". *Pure Appl. Chem.* **57**(4) (1985) 603–619.

[208] **S. Brunauer, P. H. Emmett and E. Teller**. "Adsorption of gases in multimolecular layers". *J. Am. Chem. Soc.* **60**(2) (1938) 309–319.

[209] **I. Langmuir**. "The constitution and fundamental properties of solids and liquids. Part I. Solids." *J. Am. Chem. Soc.* **252** (1916) 2221–2295.

[210] **D. J. Fabian**. *Solid-State Spectroscopy*. First edition. Springer-Verlag Berlin Heidelberg GmbH, New York (1998).

[211] **D. R. Vij**. *Handbook of Applied Solid State Spectroscopy*. First edition. Springer Science+Business Media, LLC, New York (2006).

[212] **J. Chalmers, H. Edwards and M. Hargreaves**. *Infrared and Raman Spectroscopy in Forensic Science*. First edition. John Wiley & Sons Ltd., Chichester (2012).

[213] **I. R. Lewis and H. G. M. Edwards** (editors). *Handbook of Raman Spectroscopy From the Research Laboratory to the Process Line*. First edition. Marcel Dekker, Inc, New York (2001).

[214] **C. V. Raman and K. S. Krishnan**. "A new type of secondary radiation". *Nature* **121**(3048) (1928) 501–502.

[215] **P. J. Haines**. *Thermal Methods of Analysis: Principles, Applications and Problems*. First edition. Blackie Academic and Professional, an imprint of Chapman & Hall, Glasgow (1995).

[216] **M. E. Brown** (editor). *Handbook of Thermal Analysis and Calorimetry Volume 1: Principles and Practice*. Elsevier Science B.V., Amsterdam (1998).

[217] **T. Hatakeyama and Z. Liu** (editors). *Handbook of Thermal Analysis*. First edition. John Wiley & Sons Ltd., Chichester (1998).

[218] **M. Brown and P. Gallagher** (editors). *Handbook of Thermal Analysis and Calorimetry Volume 2: Applications to Inorganic and Miscellaneous Materials*. First edition. Elsevier B.V., Amsterdam (2003).

[219] **W. M. Groenewoud**. *Characterisation of Polymers by Thermal Analysis*. First edition. Elsevier B.V., Amsterdam (2001).

[220] **M. A. Reiche, M. Maciejewski and A. Baiker**. "Characterization by temperature programmed reduction". *Catal. Today* **56**(4) (2000) 347–355.

[221] **S. Bhatia, J. Beltramini and D. Do**. "Temperature programmed analysis and its applications in catalytic systems". *Catal. Today* **7**(3) (1990) 309–438.

[222] **A. Jones and B. D. McNicol**. *Temperature programmed reduction for solid materials characterization*. First edition. Marcel Dekker, Inc, New York (1986).

[223] **F. Pinna**. "Supported metal catalysts preparation". *Catal. Today* **41**(1-3) (1998) 129–137.

[224] **P. Malet and A. Caballero**. "The selection of experimental conditions in temperature-programmed reduction experiments". *J. Chem. Soc. Faraday Trans. 1* **84**(7) (1988) 2369.

[225] **J. H. Sharp, G. W. Brindley and B. N. Narahari Achar**. "Numerical data for some commonly used solid state reaction equations". *J. Am. Ceram. Soc.* **49**(7) (1966) 379–382.

[226] **K. Go, S. Son and S. Kim**. "Reaction kinetics of reduction and oxidation of metal oxides for hydrogen production". *Int. J. Hydrogen Energy* **33**(21) (2008) 5986–5995.

[227] **G. Munteanu, P. Budrugeac and L. Ilieva**. "Kinetics of temperature programmed reduction of Fe_3O_4 promoted with copper: application of isoconversional methods". *J. Mater. Sci.* **8** (2003) 1995–2000.

[228] **H.-Y. Lin and Y.-W. Chen**. "The mechanism of reduction of cobalt by hydrogen". *Mater. Chem. Phys.* **85**(1) (2004) 171–175.

[229] **C. Gammer, C. Mangler, C. Rentenberger and H. P. Karnthaler**. "Quantitative local profile analysis of nanomaterials by electron diffraction". *Scr. Mater.* **63**(3) (2010) 312–315.

[230] **M. D. Abràmoff, P. J. Magalhães and S. J. Ram**. "Image processing with ImageJ". *Biophotonics Int.* **11**(7) (2004) 36–41.

[231] **E. P. Barrett, L. G. Joyner and P. P. Halenda**. "The determination of pore volume and area distributions in porous substances. I. Computations from nitrogen isotherms". *J. Am. Chem. Soc.* **73**(1) (1951) 373–380.

[232] **R. Brand**. "Improving the validity of hyperfine field distributions from magnetic alloys". *Nucl. Instruments Methods Phys. Res. Sect. B Beam Interact. with Mater. Atoms* **28**(3) (1987) 398–416.

[233] **P. Hovington, D. Drouin and R. Gauvin**. "CASINO: A new monte carlo code in C language for electron beam interaction -part I: Description of the program". *Scanning* **19**(1) (2006) 1–14.

[234] **J. J. Friel and C. E. Lyman**. "X-ray mapping in electron-beam instruments." *Microsc. Microanal.* **12**(1) (2006) 2–25.

[235] **Y. Pan, a. Brown and R. Brydson**. "Electron Beam Damage Studies on 6-Line Ferrihydrite". *J. Phys. Conf. Ser.* **26** (2006) 46–49.

[236] **Y. Guyodo, S. K. Banerjee, R. L. Penn, D. Burleson, T. S. Berquo, T. Seda and P. Solheid**. "Magnetic properties of synthetic six-line ferrihydrite nanoparticles" **154** (2006) 222–233.

[237] **R. A. Buhrman and C. G. Granqvist**. "Log-normal size distributions from magnetization measurements on small superconducting Al particles". *J. Appl. Phys.* **47**(5) (1976) 2220–2222.

[238] **J. Zhao, Z. Feng, G. P. Huffman and F. E. Huggrns**. "Ferihydrite: surface structure and its effects on phase transformation". *Clay Clay Miner.* **42**(6) (1994) 737–746.

[239] **C. Masina, J. Neethling, E. Olivier, E. Ferg, S. Manzini, L. Lodya, P. Mohlala and M. Ngobeni**. "Mechanism of reduction in hydrogen atmosphere and thermal transformation of synthetic ferrihydrite nanoparticles". *Thermochim. Acta* **599** (2015) 73–83.

[240] **Z. Karim**. "Characteristics of ferrihydrites formed by oxidation of $FeCl_2$ solutions containing different amounts of silica". *Clay Clay Miner.* **32**(3) (1984) 181–184.

[241] **D. L. A. de Faria, S. Venâncio Silva and M. T. de Oliveira**. "Raman microspectroscopy of some iron oxides and oxyhydroxides". *J. Raman Spectrosc.* **28**(11) (1997) 873–878.

[242] **M. Hanesch**. "Raman spectroscopy of iron oxides and (oxy)hydroxides at low laser power and possible applications in environmental magnetic studies". *Geophys. J. Int.* **117**(3) (2009) 941–948.

[243] **L. Mazzetti and P. J. Thistlethwaite**. "Raman spectra and thermal transformations of ferrihydrite and schwertmannite". *J. Raman Spectrosc.* **33**(2) (2002) 104–111.

[244] **A. Chopelas**. "Single crystal Raman spectra of forsterite, fayalite, and monticellite". *Am. Mineral.* **76**(7-8) (1991) 1101–1109.

[245] **P. McMillan, B. Poe, P. Gillet and B. Reynard**. "A study of SiO_2 glass and supercooled liquid to 1950 K via high-temperature Raman spectroscopy". *Geochim. Cosmochim. Acta* **58**(17) (1994) 3653–3664.

[246] **A. Ianoul, T. Coleman and S. A. Asher**. "UV resonance Raman spectroscopic detection of nitrate and nitrite in wastewater treatment processes". *Anal. Chem.* **74**(6) (2002) 1458–1461.

[247] **R. K. Kukkadapu, J. M. Zachara, J. K. Fredrickson, S. C. Smith, A. C. Dohnalkova and C. K. Russel**. "Transformation of 2-line ferrihydrite to 6-line ferrihydrite under oxic and anoxic conditions". *Am. Minerol.* **88**(11-12) (2003) 1903–1914.

[248] **D. Carta, M. Casula, A. Corrias, A. Falqui, G. Navarra and G. Pinna**. "Structural and magnetic characterization of synthetic ferrihydrite nanoparticles". *Mater. Chem. Phys.* **113**(1) (2009) 349–355.

[249] **M. D. Alcalá and C. Real**. "Synthesis based on the wet impregnation method and characterization of iron and iron oxide-silica nanocomposites". *Solid State Ionics* **177**(9-10) (2006) 955–960.

[250] **S. Britto, S. Joseph and P. V. Kamath**. "Distinguishing crystallite size effects from those of structural disorder on the powder X-ray diffraction patterns of layered materials". *J. Chem. Sci.* **122**(5) (2010) 751–756.

[251] **M. Zhou, Z. Wei, H. Qiao, L. Zhu, H. Yang and T. Xia**. "Particle size and pore structure characterization of silver nanoparticles prepared by confined arc plasma". *J. Nanomater.* **968058** (2009) 1–5.

[252] **J. P. Gaviría, A. Bohé, A. Pasquevich and D. M. Pasquevich**. "Hematite to magnetite reduction monitored by Mössbauer spectroscopy and X-ray diffraction". *Phys. B Condens. Matter* **389**(1) (2007) 198–201.

[253] **J. Jacob and M. Abdul Khadar**. "VSM and Mössbauer study of nanostructured hematite". *J. Magn. Magn. Mater.* **322**(6) (2010) 614–621.

[254] **S. A. Fysh and P. E. Clark**. "Aluminous hematite : a Mössbauer study". *Phys. Chem. Miner.* **8**(6) (1982) 257–267.

[255] **E. D. Grave and R. E. Vandenberghe**. "Mössbauer Effect Study of the Spin Structure in Natural Hematites". *Phys Chem Miner.* **17**(4) (1990) 344–352.

[256] **E. Murad and U. Schwertmann**. "Influence of Al substitution and crystal size on the room-temperature Mössbauer spectrum of hematite". *Clays Clay Miner.* **34**(1) (1986) 1–6.

[257] **E. Murad**. "High-precision determination of magnetic hyperfine fields by Mössbauer spectroscopy using an internal standard". *J. Phys. E Sci. Instrum.* **17**(9) (1984) 736–737.

[258] **E. Murad and U. Schwertmann**. "The Mössbauer spectrum of ferrihydrite and its relations to those of other iron oxides". *Am. Mineral.* **65** (1980) 1044–1049.

[259] **C. M. Cardile**. "Tetrahedral Fe^{3+} in ferrihydrite; ^{57} Fe Mössbauer spectroscopic evidence". *Clays Clay Miner.* **36**(6) (1988) 537–539.

[260] **E. Murad, L. H. Bowen, G. J. Long and T. G. Quin**. "The influence of crystallinity on magnetic ordering in natural ferrihydrites". *Clay Miner.* **23**(2) (1988) 161–173.

[261] **W. J. Schuele, S. Shtrikman and D. Treves**. "Observation of superparamagnetism by the Mössbauer Effect". *J. Appl. Phys.* **36**(3) (1965) 1010.

[262] **D. Rancourt and J. Daniels**. "Influence of unequeal magnetization direction probabilities on the Mössbauer spectra of superparamegnetic particles". *Phys. Rev. B* **29**(5) (1984) 2410.

[263] **C. W. Jung and P. Jacobs**. "Physical and chemical properties of superparamagnetic iron oxide MR contrast agents: ferumoxides, ferumoxtran, ferumoxsil." *Magn. Reson. Imaging* **13**(5) (1995) 661–674.

[264] **I. Suzdalev, V. Buravtsev, V. Imshennik, Y. Maksimov, V. Matveev, S. Novichikhin, A. Trautwein and H. Winkler**. "Magnetic properties of ultrafine ferrihydrite clusters studied by Mössbauer spectroscopy and by thermodynamical analysis". *Zeitschrift für Phys. D Atoms, Mol. Clust.* **37**(1) (1996) 55–61.

[265] **J. M. D. Coey and P. W. Readman**. "New spin structure in an amorphous ferric gel". *Nature* **246** (1973) 476–478.

[266] **G. J. Long and F. Grandjean** (editors). *Mössbauer Spectroscopy Applied to Magnetism and Materials Science Volume 1.* First edition. Springer Science+Business Media, LLC, New York (1993).

[267] **Q. A. Pankhurst and R. J. Pollard**. "Structural and magnetic properties of ferrihydrite". *Clay Clay Miner.* **40**(3) (1992) 268–272.

[268] **R. A. Brand and H. Georges-Gibert**. "Magnetic properties of the spin glass $Pd_{1-y}Fe_yH_x$: hyperfine and susceptibility studies in a magnetic field". *J. Phys. F Met. Phys.* **10** (1980) 2501–2513.

[269] **W. T. Herrera, Y. T. Xing, S. M. Ramos, P. Munayco, M. B. Fontes, E. M. Baggio-Saitovitch and F. J. Litterst**. "Kondo effect and spin-glass behavior of dilute iron clusters in silver films". *Phys. Rev. B* **84**(1) (2011) 014430.

[270] **F. Morin**. "Magnetic susceptibility of α-Fe_2O_3 and α-Fe_2O_3 with added titanium". *Phys. Rev.* **78** (1950) 819.

[271] **Ö. Özdemir, D. J. Dunlop and T. S. Berquó**. "Morin transition in hematite: size dependence and thermal hysteresis". *Geochemistry, Geophys. Geosystems* **9**(10) (2008) 1–12.

[272] **T. Nakamura, T. Seinjo, Y. Endoh, N. Yamamoto, M. Shiga and Y. Nakamura**. "Fe^{57} Mössbauer effect in ultra fine particles of α-Fe_2O_3". *Phys. Lett.* **12**(3) (1964) 178–179.

[273] **M. Sorescu, R. Brand, D. Mihaila-Tarabasanu and L. Diamandescu**. "Synthesis and magnetic properties of haematite with different particle morphologies". *J. Alloys Compd.* **280**(1-2) (1998) 273–278.

[274] **M. I. Dar and S. A. Shivashankar**. "Single crystalline magnetite, maghemite, and hematite nanoparticles with rich coercivity". *RSC Adv.* **4**(8) (2014) 4105.

[275] **R. Zysler, D. Fiorani, A. M. Testa, L. Suber and E. Agostinelli**. "Size dependence of the spin-slop transition in hematite nanoparticles". *Phys. Rev. B* **68** (2003) 212408–1 – 212408–4.

[276] **E. L. Duarte, R. Itri, E. Lima, M. S. Baptista, T. S. Berquo and G. F. Goya**. "Large magnetic anisotropy in ferrihydrite nanoparticles synthesized from reverse micelles". *Nanotechnology* **17**(22) (2006) 5549–5555.

[277] **R. A. Eggleton, R. W. Fitzpatrick and G. Osmond**. "New data and a revised structural model for ferrihydrite". *Clays and Clay Minerals* **36**(2) (1988) 111–124.

[278] **W. Xu, D. B. Hausner, R. Harrington, P. L. Lee, D. R. Strongin and J. B. Parise**. "Structural water in ferrihydrite and constraints this provides on possible structure models". *Am. Mineral.* **96**(4) (2011) 513–520.

[279] **A. Venugopal and M. S. Scurrell**. "Low temperature reductive pretreatment of Au/Fe_2O_3 catalysts, TPR/TPO studies and behaviour in the water-gas shift reaction". *Appl. Catal. A Gen.* **258**(2) (2004) 241–249.

[280] **V. Lou, R. Sato and M. Tomozawa**. "Hydrogen diffusion in fused silica at high temperatures". *J. Non. Cryst. Solids* **315**(1-2) (2003) 13–19.

[281] **J. M. Wiesenfeld, J. Stone, D. Marcuse, C. A. Burrus and S. Yang**. "Temperature dependence of hydroxyl formation in the reaction of hydrogen with silica glass". *J. Appl. Phys.* **61**(12) (1987) 5447.

[282] **J. E. Shelby**. "Reaction of hydrogen with hydroxyl-free vitreous silica". *J. Appl. Phys.* **51**(5) (1980) 2589.

[283] **P. Pourghahramani and E. Forssberg**. "Reduction kinetics of mechanically activated hematite concentrate with hydrogen gas using nonisothermal methods". *Thermochim. Acta* **454**(2) (2007) 69–77.

[284] **J. F. Lu and C. J. Tsai**. "Reduction kinetics of hematite to magnetite under hydrothermal treatments". *RSC Adv.* **5**(22) (2015) 17236–17244.

[285] **L. Broussard**. "The disproportionation of wüstite". *J. Phys. Chem.* **73**(6) (1969) 1848–1854.

[286] **S. Musić, N. Filipović-Vinceković and L. Sekovanić**. "Precipitation of amorphous SiO_2 particles and their properties". *Brazilian J. Chem. Eng.* **28**(1) (2011) 89–94.

[287] **R. Oppermann**. "Diffusion in and through solids". *J. Franklin Inst.* **232**(5) (1941) 505.

[288] **G. E. Murch and A. S. Nowick**. *Diffussion in Crystalline Solids*. First edition. Academic Press, Inc., Orlando (1984).

[289] **S. Takeda and H. Yoshida**. "Atomic-resolution environmental TEM for quantitative *in-situ* microscopy in materials science". *Microscopy* **62**(1) (2013) 193–203.

[290] **L. Sun, K. W. Noh, J. G. Wen and S. J. Dillon**. "*In situ* transmission electron microscopy observation of silver oxidation in ionized/atomic gas". *Langmuir* **27** (2011) 14201–14206.

[291] **M. J. Assael, S. Mixafendi and W. A. Wakeham**. "Viscosity and thermal conductivity of normal hydrogen". *J. Phys. Chem. Ref. Data* **15**(4) (1986) 1315–1322.

[292] **E. W. Lemmon and R. T. Jacobsen**. "Viscosity and thermal conductivity equations for nitrogen, oxygen, argon, and air". *Int. J. Thermophys.* **25**(1) (2004) 21–69.

[293] **M. Pomiès, M. Menu and C. Vignaud**. "TEM observations of goethite dehydration: application to archaeological samples". *J. Eur. Ceram. Soc.* **19**(8) (1999) 1605–1614.